Investigation of Reaction Intermediates and Ion Structures in the Gas-Phase

Inaugural Dissertation

Zur

Erlangung des Doktorgrades

der Mathematisch-Naturwissenschaftlichen Fakultät

der Universität zu Köln

vorgelegt von

Dennis Zeh

aus Herrenberg,

Köln, 2022

1.Berichterstatter:

Prof. Dr. Mathias Schäfer

Department für Chemie

Institut für Organische Chemie

Universität zu Köln

2. Berichterstatter:

Prof. Dr. Axel Griesbeck

Department für Chemie

Institut für Organische Chemie

Universität zu Köln

Tag der mündlichen Prüfung:

Dedicated to my family and friends.

"The saddest aspect of life right now is
that science gathers knowledge faster than society gathers wisdom."

- Isaac Asimov, 1988

Acknowledgements

Abstract

The present work comprises three independent studies in which novel infrared ion spectroscopy data sets as well as extensive theoretical computational data and EI/ESI mass spectrometry results were acquired. In these studies, we mainly used methods of cryogenic messenger and IRMPD ion spectroscopy at room temperature combined with sophisticated computational chemistry based on ions formed by mass spectrometry to characterize and identify ion structures of important species in the gas-phase.

The molecular ions of phenol and aniline as well as the common fragment ion at *m/z* 66 formed by electron ionization were examined with cryogenic messenger ion spectroscopy. According to our data, aromatic ground state molecular ions of phenol and aniline are clearly identified. However, as reported in the literature, our data set supports the assumption that tautomeric molecular ions of phenol and aniline are only short-lived intermediates on the reaction pathway towards the final loss of CO in case of phenol and the loss of HNC in the case of aniline. The potential energy surfaces of their reaction trajectories further indicate that once they isomerized, they possess more than enough energy to directly decompose, showing that the isomerization is the kinetic bottleneck of these reactions. We further showed that the common fragment ion at *m/z* 66 is indeed the cyclopentadiene radical cation in both cases as proposed in the literature.[1, 2]

The present work also provides independent evidence for the structures of the product ions formed by the intriguing 2H and 3H rearrangement reactions and subsequent fragmentation in EI and ESI-MS with IRMPD ion spectroscopy discovered by Kuck *et al.* several decades ago.[3] In the early reports it was pointed out that the proposed mechanisms and ion structures remain speculative and need further evidence, which is what motivated us to investigate and clarify these interesting reactions with modern techniques, that have not been available at the time. We found that the 2H rearrangement product $C_9H_{14}N^+$ at *m/z* 136 is *N,N*-dimethyl-4-toluidine, however, protonated at the position 2 instead of the *ipso* position 4 as reported earlier. The structure of the 3H rearrangement had to be revised, because our data proofs that the rearranged fragment ion $C_8H_{13}N^{•+}$ present at *m/z* 123 is the radical cationic *N,N*-dimethyl-2,3-dihydro-4-toluidine. Our calculations also showed that this isomer is the most stable one in the ion series tested in this work. We furthermore propose revised mechanisms for the 2H and 3H rearrangement reactions based on the new data sets from computational chemistry and IRMPD ion spectroscopy.

The last part of this work reports the investigation of the Claisen and Aza-Claisen rearrangement in the gas-phase with ESI-MS, IRMPD ion spectroscopy and computational chemistry. Our data indicates that before the Claisen rearrangement occurs, the molecular ion $[M+H]^+$ of allyl-2,4,6-trimethylphenylether is protonated in *ortho*-position to the ether-group, which is an interesting finding and different from most common textbook literature, in which such species are usually protonated at the oxygen. Upon collision activation of this molecular ion the sidechain migrates to the ortho position and is not transferred further to the *para*-position as the Claisen-Cope-Tandem reaction would suggest. In addition, we found that the rearrangement already occurred without any activation in case of the Aza-Claisen, reflecting the lower energy needed for the Aza-Claisen rearrangement to be triggered. We also proposed a new mechanism in this case for the Claisen rearrangement in the gas-phase.

Kurzzusammenfassung

In der vorliegenden Arbeit werden drei unabhängige Studien dargestellt, in welchen neuen Daten via Infrarot Ionen Spektroskopie, theoretischer Chemie und EI sowie ESI Massenspektrometrie gesammelt wurden. In den Studien wurden die spektroskopischen Methoden der kryogenen Messenger-Ionenspektroskopie sowie Infrarot Multiphotonen Dissoziation Ionenspektroskopie eingesetzt, welche zusammen mit computergestützten Rechnungen und Massenspektrometrie verwendet wurden, um Ionenstrukturen in der Gasphase zu charakterisieren und Reaktionsmechanismen aufzuklären.

Die aus Elektronenstoß-Ionisation gebildeten Molekularionen von Phenol und Aniline und das gemeinsame Fragment bei *m/z* 66 wurden mit kryogener Messenger-Ionenspektroskopie untersucht. Unsere Daten identifizieren die Grundzustandsionen von Phenol und Aniline. Die wahrscheinlich sehr kurzlebigen tautomeren Strukturen von Anilin und Phenol, wie sie als Reaktionsintermediate zu den Fragmentierungsprodukten CO für Phenol und HNC für Aniline in der Literatur beschrieben werden, konnten wir jedoch nicht nachweisen. Die gerechneten Potentialhyperflächen des Reaktionsverlaufs zeigen, dass nach der Isomerisierung mehr als genug Energie zur Verfügung steht, um schnell vollständig zu fragmentieren, dass also die Isomerisierung der kinetische Flaschenhals der Fragmentierungsreaktionen ist. Unsere Daten identifizieren das gemeinsame Fragment bei *m/z* 66 klar als Cyclopentadien für beide Analyten, wie auch schon in der Literatur vorgeschlagen.[1, 2]

Die vorliegende Arbeit gibt auch unabhängige Beweise via IRMPD Ionenspektroskopie für die Strukturen der Produktionen, welche in seltenen 2H und 3H Umlagerungsreaktionen in EI- und ESI-MS gebildet werden und das erste Mal vor über 30 Jahren von Kuck *et al.* beschrieben wurden.[3] Die alten Studien schlagen einen Mechanismus vor, welcher allerdings nicht direkt bewiesen wurde. Dies gab uns den Ansporn diese interessanten Umlagerungsreaktionen mit modernen Methoden, welche damals nicht verfügbar waren, genauer zu untersuchen. Diese Arbeit zeigt dass das Produktion der 2H Umlagerung, $C_9H_{14}N^+$ bei *m/z* 136, tatsächlich *N,N*-Dimethyl-4-toluidin ist, allerdings nicht in Position 2 (*ortho*) protoniert, sondern in Position 4 (*ipso*). Das Produktion der 3H Umlagerung, $C_8H_{13}N^{\bullet+}$ bei *m/z* 123, musste revidiert werden, da unsere Daten eine andere Struktur nachweisen, und zwar das Radikalkation von *N,N*-Dimethyl-2,3-dihydro-4-toluidin. Unsere Rechnungen zeigen, dass dieses Ion auch das Stabilste von allen in dieser Arbeit getesteten ist. Basierend auf diesen neuen IRMPD Spektroskopie und

theoretischen Daten schlagen wir in unserer Studie einen neuen Mechanismus für die 2H und 3H Umlagerung vor.

Der letzte Teil dieser Arbeit beschreibt eine Studie zur Analyse der Claisen und Aza-Claisen Umlagerung in der Gasphase mittels ESI-MS, IRMPD Ionenspektroskopie und theoretische Chemie. Die neuen Daten zeigen, dass das Molekularion $[M+H]^+$ von Allyl-2,4,6-trimethylphenylether vor der Claisen Umlagerung in der *ortho*-Position protoniert ist und nicht am Sauerstoff wie in den meisten Textbüchern und Literatur beschrieben. Nach Kollisionsaktivierung der Molekularionen wandert die Seitenkette zur *ortho*-Position und nicht weiter zur para-Position wie man nach der Claisen-Cope-Tandem Reaktion erwarten würde. Wir zeigen auch dass bei der Aza-Claisen Umlagerung die Wanderung der Seitenkette bereits vor Aktivierung der Molekularionen stattgefunden hat, was die niedrigere Schwellenenergie dieses Stickstoffanalogs wieder gibt. In dieser Studie zeigen wir auch einen neuen Mechanismus für die Claisen Umlagerung in de Gasphase auf.

Table of Contents

VIII

1 Introduction

1.1 Ion Structures and Reaction Mechanisms in the Gas-Phase

Studies of molecular ions in the gas-phase have become a general and important tool for identifying and assigning molecular structures and clarifying reaction mechanisms via characterizing their sometimes very elusive intermediates, which is often not easily feasible in regular solution mixtures.[4-9] This achievement of gas-phase analytics is mainly due to the technical developments in mass spectrometry (MS) and especially ion spectroscopy, as well as the rapidly increasing processing power of computers applied for sophisticated theoretical calculations, during the last couple decades. Mass spectrometry has been used to investigate reaction mechanisms and short-lived intermediates for quite some time,[10-17] however, it was always difficult to unambiguously assign ion structures. This has massively changed over the last two decades since the rise of specific infrared (IR) ion spectroscopy methods in combination with mass spectrometry and computational chemistry.

One big advantage of this approach is that the results are not affected by many effects such as solvation, counter ions, aggregation, salts und others. These effects in general are often not well defined, hard to control and even more difficult to take them into consideration all at once in the condensed phase. Therefore, we can investigate ion energetics or reaction kinetics experimentally on a pure molecular basis without any disruptive influences. Now, most would say that this does not reflect the reality, but it does on the molecular level and with the nowadays very sophisticated theoretical models and concepts for computation, we can still apply the influences mentioned above in our theoretical calculations, making this approach extremely versatile. The main difference of gas-phase reactions versus reactions in solution are the states of aggregation and a different rate of reaction due to differing mass-transfer abilities.[18] Furthermore, usually a higher selectivity is observed, and the electrostatic interactions are stronger in the gas-phase.[18]

Next to the identification of reaction intermediates, where ion spectroscopy is broadly used, is the identification of isomeric structures in general and the characterization of the coordination sphere in complexes, which can be difficult to achieve in the liquid phase. There are quite a lot of studies, where elusive tautomers were unambiguously characterized with this analytical strategy.[19-24] For these reasons we made choice of the approach of ion spectroscopy to investigate the reactions and the uncertainty of the described reaction pathways and

intermediates. The methods and procedures used in this approach as well as the selected model studies will be discussed and presented in the following chapters.

1.2 Mass Spectrometry

1.2.1 General

Mass spectrometry (MS) is an analytical tool, which has rapidly developed over the several past decades and has become probably the most important analytical method in modern chemistry, biochemistry, pathology, forensics, environmental science, and many other fields.[25, 26] In mass spectrometry the mass-to-charge ratio (*m/z*) of ions is measured, which can be done with very high resolution in beam-type instruments (e.g., TOF, electrostatic and magnetic sectors) and in ion trapping devices (e.g., FTICR, Orbitrap).[27, 28] Mass spectrometry has become extremely versatile and enables us to characterize analytes and intermediates as well as fragments yielded from those; meaning we can clarify reaction mechanisms or find structural features of unknown samples. The ions investigated in mass spectrometry are usually generated in an ion source from their neutral analytes. There are many different ionization methods, two of them were used in the studies of this work and are going to be discussed in the following.

1.2.2 EI-MS

Electron ionization (EI) is indisputably the mostly used and one of the oldest ionization techniques in mass spectrometry, which is mainly used for low molecular weight (<800 Da) and non-polar analytes.[26] In EI, formerly known as electron impact ionization, a beam of energetic electrons is utilized to produce the ions. The analyte is evaporated in a heated vacuum chamber and able to pass that electron beam running through this chamber (see Figure 1). Collisions of the high energetic electrons with the gaseous neutral analyte molecules induces ionization in the gas-phase according to the following oxidation reaction:

$$M \ + \ e^- \ \rightarrow \ [M]^{\bullet+} \ + \ 2e^-$$
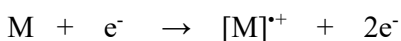
The resulting open shell molecular ions [M]$^{\bullet+}$ are then accelerated and focused through lenses with an electrostatic potential resulting in an ion beam, which can be guided and detected. The highly excited molecular radical cations [M]$^{\bullet+}$, which are formed initially, can energetically relax via extensive fragmentation processes. In typical EI, electrons with a kinetic energy of 70 eV are utilized because at this high energy we can ensure reproducibility of the mass spectra. The ion signals are most intense, there is fragmentation observable, and the first ionization potential of most organic molecules is below this value. A higher ionization potential is not affecting the total ion count significantly and small changes in electron energy do not affect fragmentation patterns. Furthermore, in most databases EI-MS spectra are measured at 70 eV and thus it is simpler to compare them.

In the evacuated and heated chamber of an EI ion source typical conditions are pressures of about $10^{-5} - 10^{-6}$ mbar and temperatures of around 400-500 K. The EI-MS technique is considered a harsh ionization method because of these relatively rough general conditions. Firstly, the analyte is heated for evaporation, which can induce thermal decomposition and induces vibrational excitation. Secondly, the analyte is further highly excited in the ionization process with the high energetic electrons which induces extensive fragmentation process.
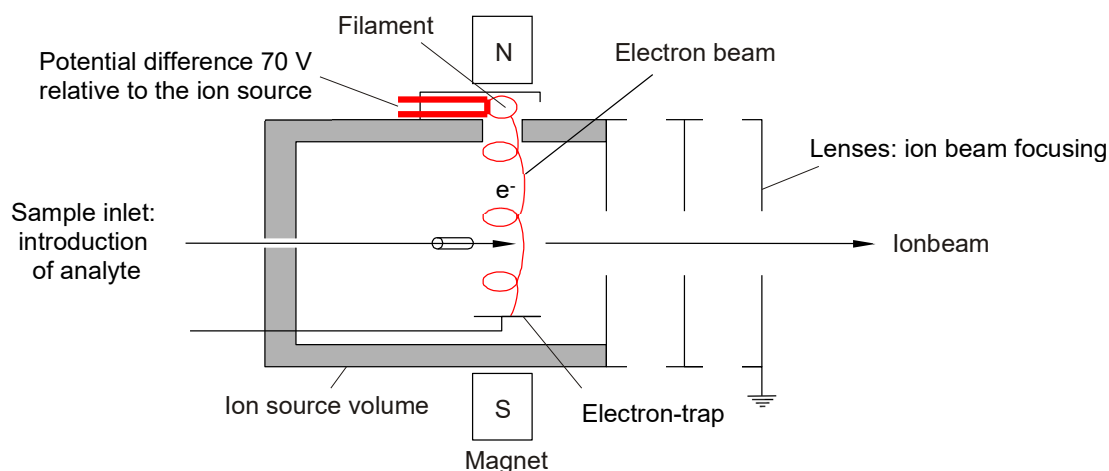
Figure 1
Scheme of the general assembly of a typical EI ion source.[29] Ions with 70 eV internal energy are generated at the filament and guided as a beam through the ion vacuum chamber. While colliding with these electrons, the neutral analyte from the sample inlet gets ionized as [M]$^{\bullet+}$. Lenses are then focusing the produces ions into an ion beam.
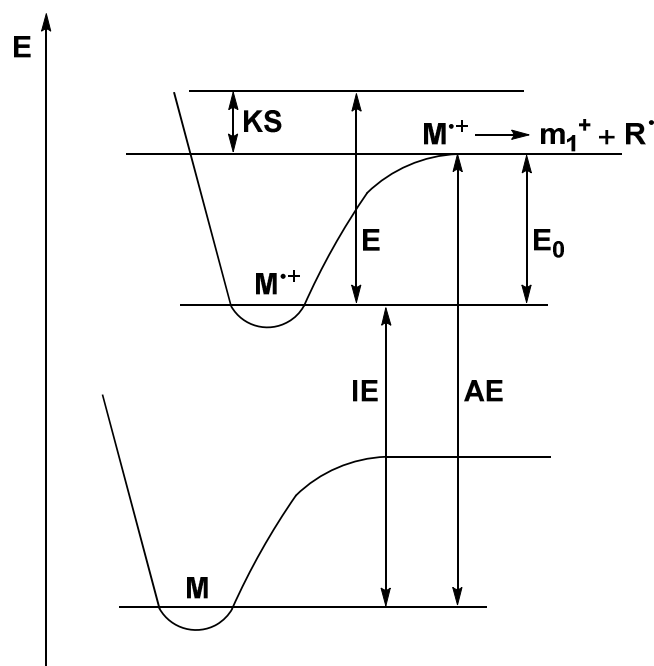
Figure 2
Schematic diagram of the relative internal energies of ions in the ionization process in an EI source. M is the intact non-ionized analyte, $[M]^{\cdot+}$ the respective molecular ion and m_1^+ and $R^{\cdot}$ are resulting fragments. IE = ionization energy, AE = appearance energy, KS = kinetic shift, E_0 = minimum energy needed for the respective fragmentation to occur.

For the electron ionization process we can assume a vertical transition according to the Born-Oppenheimer approximation (see also Chapter 1.4). Ions are formed relatively quickly and reside in the ion source for about a microsecond before accelerated effectively. This limits the time available for fragmentation reactions and product ion formation to roughly one microsecond.[15] Furthermore, molecular radical cations produced via EI exhibit a broad distribution of internal energy. Electron ionization with 70 eV electrons delivers molecular ions with an internal energy of mainly around 3 eV, but the distribution has a high energy tail with up to 20 eV.[30] Stable molecular radical cations have internal energies well below the critical energy of the lowest fragmentation channel, in order to allow detection as intact molecular ions. On the other hand, decomposing molecular ions have obtained sufficient internal energy for (fast) dissociation in the EI ion source at a residence time of around 10^{-6} s and with rate constants for intramolecular fragmentation reactions greater than $k \geq 10^6$ s^{-1}.[30] There is quite an amount of excess energy needed in order to actually observe this kinetically controlled fragmentation, the so-called kinetic shift (KS). This extra energy is required to sufficiently accelerate the respective fragmentation reactions and observe the fragmentation in the

experimental set-up within the residence time of the analyte in the EI ion source.[30, 31] If the minimum energy needed for the lowest fragmentation channel is defined to be E_0 and E is the energy at which we actually begin to observe the fragments at the detector, the kinetic shift is estimated to be $KS = E - E_0$. The total energy necessary to actually observe the fragmentation from the ground state analyte is called appearance energy (AE) of the respective fragment ion as depicted in Figure 2, which consist of the ionization energy (IE) plus the energy needed for the lowest fragmentation channel, and therefore roughly in EI-MS: $E_0 = AE - IE$.

1.2.3 ESI-MS and Tandem-MS

Electrospray ionization (ESI) is a newer technique developed by John. B. Fenn for which he was awarded with the Nobel Prize in chemistry in 2002. It is considered a soft ionization method because of its gentle conditions compared to EI discussed above. The general experimental setup of an ESI source, which is held at atmospheric pressure and room temperature, is shown in Figure 3. One big advantage of electrospray ionization is the fact that we can transfer polar analytes with immense molecular weights (e.g., intact proteins) as ions into the gas-phase, which was not possible several decades ago, or as John B. Fenn said around thirty years ago: it allows elephants to fly.[32]

The analyte is dissolved in a preferably volatile liquid and dispersed into the gas-phase as a fine aerosol via an electrospray. This process predominantly forms molecular ion species such as $[M+H]^+$, $[M+Na]^+$, $[M+K]^+$, $[M-H]^-$ or sometimes even radical cations $[M]^{\bullet+}$ as in electron ionization, depending on the polarity of the voltage applied to the capillary. A high voltage of usually around 3 kV between the tip of the capillary, containing the dissolved analyte, and the entrance funnel to the mass spectrometer induces a so called Taylor cone as shown in Figure 3.[33, 34] This is due to the charge separation in the liquid phase: the meniscus of a liquid becomes a semi-spherical shape if its affected by the electric field, which leads to liquid polarization.[35] If the voltage then exceeds a specific threshold, the meniscus of the liquid is drawn into the specific shape of the Taylor cone.[36] Further, the high charge density then forces the Taylor cone to emit a jet of small charged primary liquid droplets. The solvent quickly evaporates from the small, charged droplets until they become unstable due to the increasing high charge density. At some point they reach the Raleigh limit, where the electrostatic repulsion overcomes the surface tension. The droplet then bursts into many smaller charged nanodroplets. This

phenomenon is called Coulomb fission at the Raleigh limit.[33, 34] During all these processes the solvent evaporates more and more, ultimately yielding the naked ions finally, which are then guided into the mass spectrometer and to the detector. Nowadays, there are three ionization models for ESI used to describe this whole process of solvent evaporation, Coulomb fission, and ion formation. Namely they are: Charged residue model (CRM), ion evaporation model (IEM), and chain ejection model (CEM), which have been proofed by molecular dynamics (MD) simulations.[33] The latter (CEM) is the newest of these models and is applied to explain ESI of unfolded proteins or polymers.[37] IEM is relevant for small molecules and CRM for intact proteins and larger protein complexes (see Figure 4).
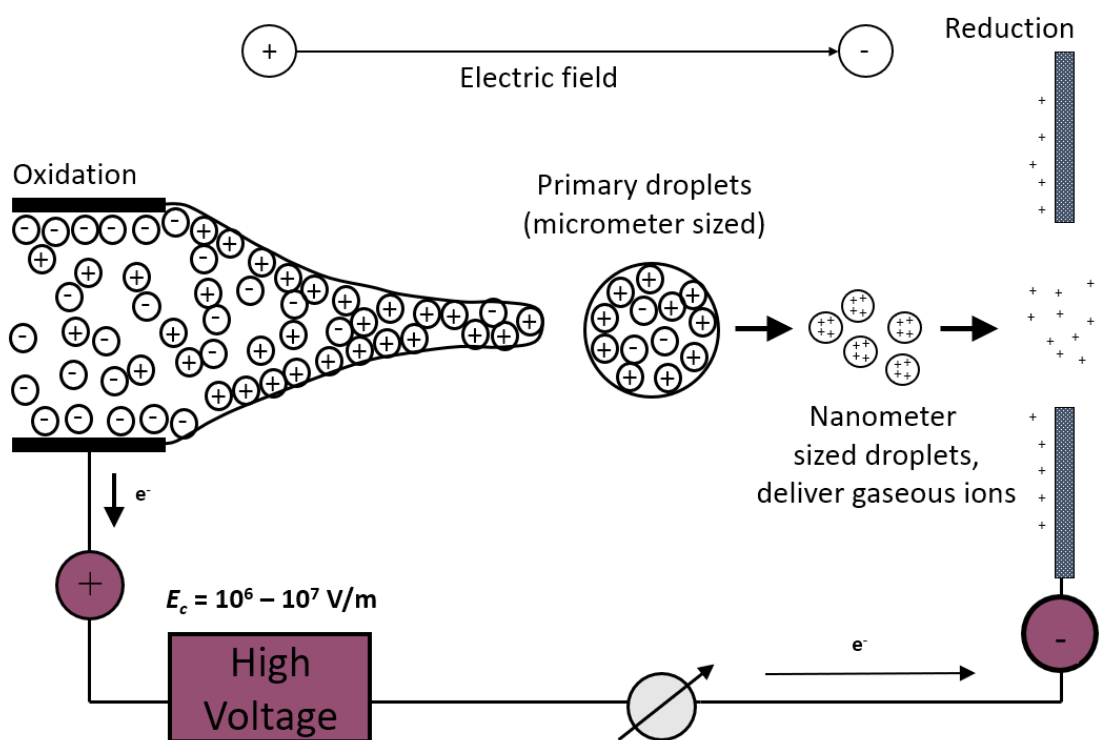
Figure 3
General assembly of an electrospray ionization (ESI) source used with positive polarity at the capillary delivering positively charged gaseous ions.[29]
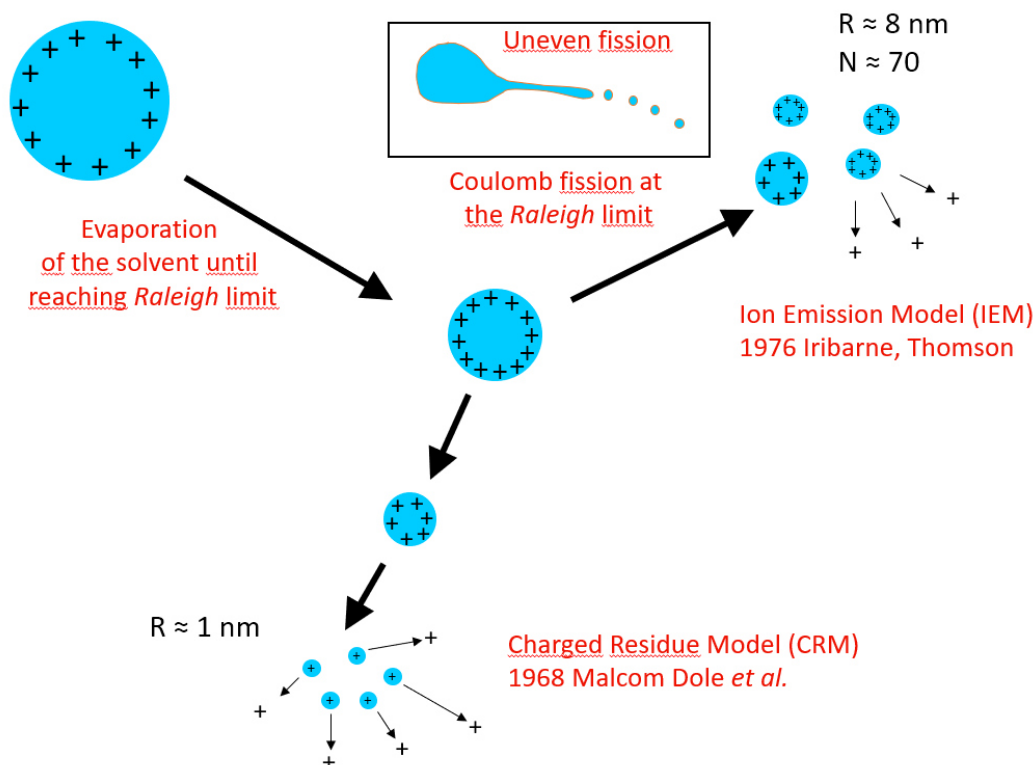
Figure 4
Two models for ion ejection. Charge residue model (CRM) on the bottom pathway, and ion emission model (IEM) on the top pathway. The box inlet shows the process of coulomb fission.[29]

The process of solvent evaporation also effectively cools the formed ions at room temperature und atmospheric pressure in the ESI ion source, explaining the absence of fragments. With the ions now softly ionized and evaporated into the gas-phase, we are going to have a closer look at so-called tandem mass spectrometry and collisional activation of ions. Because ESI produces mainly molecular ions, tandem MS techniques are used to trigger fragmentation reactions. One of these techniques, which is widely used and quite versatile, is the so-called collision-induced dissociation (CID).[17] The mass-selected ions are accelerated in an electric field to drastically increase their kinetic energy and then these ions are colliding with neutral and inert small molecules such as Helium, Nitrogen, or Argon.[38, 39] Due to the collision, part of the kinetic energy is transferred to internal ion energy, and this induces bond cleavage and thus fragmentation. One big advantage of this method is that we can continuously change the kinetic energy of the ions and therefore induce different fragmentation channels and the fragmentation behavior in general, which is yielding more information about the selected precursor ion. The resulting fragments can then easily be analyzed by tandem mass spectrometry.[40]

Tandem MS is an extremely helpful technique when it comes to analyzing complex samples but is helpful also for characterization of single analytes. To perform tandem MS, which is also called MS/MS or MS^2, in beam type instruments (e.g., triple quads), two or more mass analyzers are coupled together in one instrument, whereas in ion trap devices (e.g., orbitrap) only on mass analyzer is needed.[41] In the first mass analyzer the ions are selected according to their mass-to-charge (*m/z*) ratio (MS^1 stage). The ions selected with a specific *m/z* ratio can be activated via CID, which induces their decomposition, and the resulting fragments are then guided into the second mass analyzer, which again separates these fragments by their *m/z* ratio, and by which they are detected. This is helpful in that way that all fragments are yielded from only one specific precursor ion at a selected *m/z* ratio and are not originating from a complex ensemble of many different ions in the sample, making it easier assigning specific fragments to the precursor ion and its structural features.

1.3 Infrared Vibrational Ion Spectroscopy

Absorption spectroscopy relies on the interaction of radiation with a molecule.[42] The electric dipole vector of the radiation interacts with the dipole of the molecule, which may then be able to absorb the energy of the photon if the latter is in resonance with a vibrational transition of the molecule. This implies that without a dipole, we will observe no absorption. In ion spectroscopy, the investigated analyte always has a dipole because of its charge, thus enabling IR ion spectroscopy to characterize analytes without a dipole in their normal non-ionized state. These transitions are further assumed to be vertical according to the Born-Oppenheimer approximation (see Chapter 1.4), since the process of absorption is much faster than the movement of the nuclei.

Infrared spectra are in general very helpful when it comes to structural identification since they contain a lot of information about the measured molecule or in our case ion. For example, we can find the location of the charge, we can see specific functional groups by their characteristic band position in the IR spectrum, we can find information on secondary structures and also hydrogen bonding. The challenge, however, is that the density of ions in the gas-phase is extremely low compared to the liquid or solid phase and thus it is hard to measure via direct absorption as the concentration term in the Lambert-Beersche Law ($A = \varepsilon * d * c$) is close to zero, and therefore the whole equation and thus the absorption A becomes zero.[42]

This problem can be overcome with the approach of action spectroscopy, where we indirectly measure an IR spectrum, e.g., via photodissociation of trapped ions in a mass spectrometer as we will see below. In this chapter we are going to focus on two methods, which were utilized in our studies. Namely they are infrared multi-photon dissociation (IRMPD) ion spectroscopy and cryogenic messenger ion spectroscopy. Both of them use the concept of action spectroscopy, where mass-selected ions in an ion trap are irradiated with a powerful and tunable infrared laser, probing the ions over a specific wavenumber range. If the laser is in resonance with a vibrational degree of freedom mode, the ion can absorb one or several photons (depending on the method used as we will see below) and get excited above its dissociation threshold. The induced photo-dissociation leads to a decrease in the ion counts of the *m/z* ratio of the mass-selected precursor ions, which can then easily be detected by a coupled mass spectrometer and thus we can indirectly derive an IR spectrum from the different *m/z* intensities in the probed wavenumber range.

For our experiments we used the free electron laser (FEL) at the FEL user facility FELIX at the Radboud University, Nijmegen, Netherlands.[43, 44] Free electrons are bend in an undulator magnet as depicted in Figure 5. Due to this oscillation of electrons an incoherent dipole radiation with a specific wavelength is emitted, which is transferred into coherent radiation in an optical resonator and used as a tunable laser.
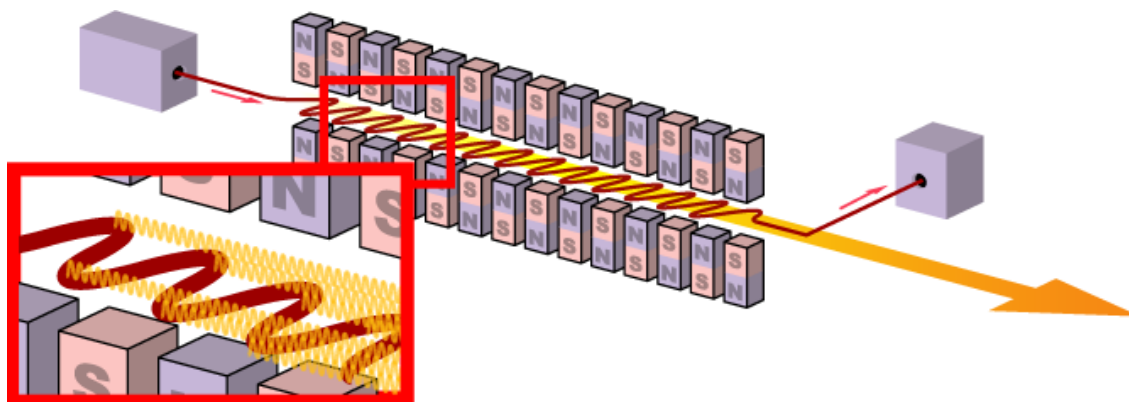
Figure 5
Scheme of a undulator magnet in a free electron laser source.[45] The constant change of direction (oscillation) of the electrons they are emitting incoherent radiation with a specific wavelength depending on the speed of the oscillation.

IRMPD.

In infrared multi-photon dissociation ion spectroscopy intramolecular dissociation is induced. As one photon does not possess enough energy to cause decomposition, multiple resonant photons are absorbed by the analyte, typically in the range of 10 to a hundred photons.[44] After one resonant photon is absorbed, the energy is quickly dispersed into all the vibrational degrees of freedom of the respective ion via the intramolecular vibrational redistribution (IVR), as shown in Figure 6, and another resonant photon can then be absorbed again to excite the same vibrational mode.[9, 46-48] This process is repeated until the dissociation threshold is reached or exceeded, which then leads to fragmentation of the analyte ion. IVR unfortunately induces broadened peaks (> 20 cm^{-1}) as well as a mostly red-redshift of a few percent.[5, 19, 21, 48-51] This sometimes can be a problem when comparing the experimental spectra with the calculated ones but usually is neglectable. Furthermore, the ions are heated due to the redistribution of the absorbed energy, which leads to peak broadening or can induce isomerization, which is usually not desired.

The IRMPD ion spectroscopy measurements in this work were carried out at room temperature with an ESI ion source at the Free Electron Laser for Infrared eXperiments (FELIX) Laboratory[43] at Radboud University, Nijmegen (The Netherlands), and conducted with a Bruker Amazon Speed ETD mass spectrometer coupled to the FEL, as described in detail elsewhere.[44]

Cryogenic messenger ion spectroscopy.

One way to overcome problems like that, is the use of another technique, which was in our case cryogenic messenger ion spectroscopy. Here, weakly bound rare-gas tags are used, for example Helium or Neon, to form complexes with the trapped ions such as [M·Ne]$^{•+}$ at cryogenic temperatures. The absorption of only a single resonant photon provides enough energy for dissociation, which is one huge advantage of this method.[4, 52-62] The trapped ions quickly thermalize under collisions with cold inert gas atoms present at relatively high pressures in the ion trap (10^{-3} mbar).[62, 63] At cryogenic temperatures of around 4-10 K these rare-gases begin to form complexes with the cold ions in the ion trap.[56] The messenger tags which are only weakly bound can then easily dissociate upon IR activation.[56, 62] This minimizes IVR and leads to narrowed absorption band widths and thereby close to the ones from experimental IR spectra, optimizing the correlation to gas-phase computations.[56, 64-66] It is even possible to resolve rotational features in these IR bands. However, the rare-gas tag is still able

to induce band shifts and peak broadening to some minimal extent.[67-70] Cryogenic messenger ion spectroscopy is well suited to investigate short-lived ion structures and intermediates in shallow potential wells of their potential energy surface (PES), with a minimal chance of isomerization or rearrangement reactions upon IVR prior to photo-dissociation at such low temperatures.[56]

The FELion instrument at FELIX was used for cryogenic messenger IR spectroscopy. The compounds were introduced as solid or liquid through an in-house build sample inlet, with the possible for heating, and subsequently ionized in an EI-MS ion source. The cryogenic 22-pole trap instrument FELion is described in detail elsewhere.[62]
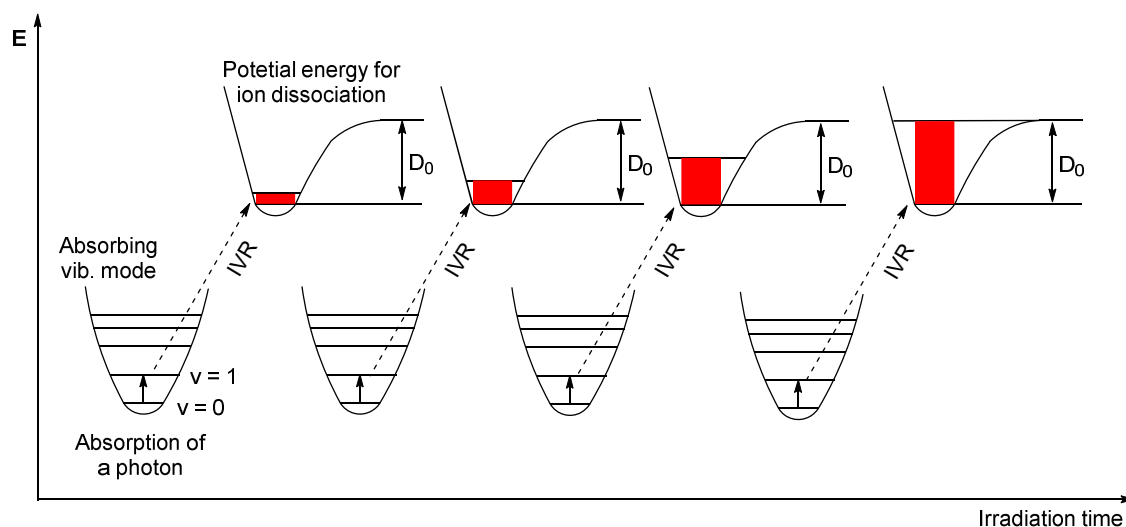
Figure 6
Schematic depiction of the IRMPD mechanism and the distribution of absorbed energy via intramolecular vibrational redistribution (IVR). The molecule absorbs a photon in resonance with a vibrational mode. The collected energy is then distributed via IVR over all vibrational degrees of freedom and the same vibration can get excited again. This process is repeated until the molecule reaches an internal energy which exceeds the dissociation threshold D_0.

1.4 Theoretical Chemistry

Schrödinger equation.

Quantum-mechanical computation has become a fundamental versatile tool in modern chemistry, which has evolved rapidly during the last decades due to the technical evolution and computer processing power, and it is hardly dispensable nowadays. However, there is a general

problem with quantum chemical calculations which is, that the complexity of a wave function of an observed system increases exponentially with the number of particles involved. This makes it literally impossible to solve the resulting Schrödinger equation for larger systems. This might, however, likely only be a problem until the final rise of usable and efficient quantum computers.[71, 72]

The Schrödinger equation was published by Erwin Schrödinger in 1926 and describes the correct properties of a quantum-mechanical system:[73, 74]

$$\hat{H}|\Psi\rangle = E|\Psi\rangle$$

It is a partial differential eigenvalue equation, where $\hat{H}$ is an observable, called the Hamiltonian, an operator which consists of the sum of the potential and kinetic energy of the system, E is the total energy of the same system and Ψ the wave function. This equation was setting the ground stone for modern quantum chemical calculations. Until up to today, it was solved only for one-electron systems like the H atom, harmonic oscillator, or the Morse potential. Paul M. Dirac commented on this equation, that the whole physics and chemistry are known due to that powerful equation, however, the problem is that it is much too complicated to be soluble for almost all systems. Therefore, it is desirable to develop approximations to overcome this problem.[71]

Max Born and J. Robert Oppenheimer proposed an approximation for the Schrödinger equation in 1927.[75] It assumes that the wave functions of the nuclei and the electrons of a system can be treated separately because nuclei are much heavier and thus slower than electrons. Therefore, the coordinated of the nuclei are set to be static whereas for the electrons they are dynamic, and therefore the kinetic energy of the nuclei is zero. This further means that we can separate the wave function of a system (e.g., an organic molecule) into the product of the electronic and the nuclear wave function:

$$\Psi_{total} = \Psi_{electronic}\Psi_{nuclear}$$

Which enables us to also separate the Hamiltonian into electronic and nuclear terms. This renders the calculations of the wavefunctions of a system much easier and feasible. For infrared spectroscopy this approximation then implies that the energy of a molecule consists of the sum of four separate independent terms, because we only have to consider the vertical transitions.

$$E_{total} = E_e + E_{vib} + E_{rot} + E_N$$

Meaning the sum of electronic, vibrational, rotational, and nuclear spin energy.

In general, the quantum-mechanical computations are divided into three fields: *ab initio* calculations, semi-empiric methods and the density functional theory.

Ab initio methods.

The main difference is that *ab initio* calculations are the only possibility to describe the microscopic properties of a many-particle system. In the other methods we use already know experimental parameters, and thus macroscopic properties, in other words, the calculations are executed without already know experimental results. The central model for these calculations is the Hartree-Fock (HF) equation:[76]

$$\hat{F}|\varphi_i\rangle = \varepsilon_i|\varphi_i\rangle$$

Where $\hat{F}$ is the Fock Operator, which is basically a single-electron Hamiltonian, and φ_i are a set of one-electron wave functions (Hartree-Fock molecular orbitals) and ε_i the respective orbital energies. These equations are solved iterative for each electron while the potential of the other electrons is kept as a constant average until the wave functions φ_i are not changing anymore which creates a so-called self-consistent field (SCF). This approach does consider that the electrons correlate in their probability density, which is not important as long as we are observing the ground state. There are post-HF approaches to take this into account, such as MP2 or MP3 (Møller-Plesset perturbation theory).[77]

Semi-empirical methods.

Semi-empirical calculations are based on the Hartree-Fock method, but there are many approximations made and empirical data is used. These calculations are much faster an allow for even larger molecules, mainly due to the use of the zero-differential overlap (ZDO) approximation, which usually ignores the two-electron repulsion integrals, which are the computational bottleneck.[78] This, however, results in an error which is compensated by using empirical parameters. Another approximation used is the complete neglect of differential overlap (CNDO), which includes ZDO and the Mataga-Nishimoto approximation, where p-

orbitals can be treated equally as s-orbitals. The intermediate neglect of differential overlap (INDO) approximation is similar, but integrals on the same atoms are parametrized. The last approximation to mention is the neglect of differential-diatomic overlap (NDDO), where INDO is expanded by including some of the two-electron repulsion integrals.[78]

Density functional theory.

If we want to calculate e.g., the potential energy surface (PES) of a system with N particles, we have to find the wave function in a $3N$ dimensional configuration, which lead to x^{3N} values we have to calculate, where x is the amount of grid points of the potential energy surface. This exponential increase of needed processing power makes exact calculations for larger systems basically impossible with the methods above, especially *ab initio* methods. Walter Kohn called this increase "exponential wall" in his Nobel price talk in 1998 for the development of the density functional theory (DFT), which is another method for quantum chemical calculations to further reduce the number of variables. The initial work of this theory is based on the Fermi theory,[79] which in essence represents the most rudimentary form of DFT and was developed with Pierre Hohenberg and Lu J. Sham.[80, 81] It basically replaces the many electron wavefunction with the electronic density distribution $n(r)$ of the ground state of a system. This is based the Hohenberg-Kohn theorem, which states that the properties of a system of electrons can be completely described by only the electron density $n(r)$. Therefore, the total energy E_{tot} of a system can be defined as:

$$E_{tot}[n(r)] = T_s[n(r)] + E_{ne}[n(r)] + E_{ee}[n(r)]$$

Meaning the sum of the kinetic energy T_s for non-correlating electrons, E_{ne} the nuclei-electron interaction and E_{ee} the electron-electron interaction. The latter can further be divided into an electrostatic repulsion $J[n(r)]$ term (Coulomb interaction) and an exchange correlation $E_{xc}[n(r)]$ term. $E_{xc}[n(r)]$ is necessary to compensate for exchange correlation energy between electrons because electrons with the spin are interacting with each other. The kinetic and the electron-electron functionals are not known in this equation. With the later introduced Kohn-Sham equation it was possible to calculate the kinetic energy in good approximation. This equation is basically the Schrödinger equation of a fictitious system of noninteracting electrons, which yield the same density as the system of interest and can be calculated iteratively by using one-electron wave functions in the Schrödinger equation and solve them separately. The major problem, however, is to find the exact functionals for the exchange correlation energy expect

for free electron gas. The simplest of these approximations is the local-density approximation (LDA), proposed by Kohn und Sham, where it is assumed that the functional only depends on the density where the functional is evaluated.[82] This approximation is refined in the local spin-density approximation, where the electron spin is further included. However, these approximations are often too erroneous, therefore the gradient of the density is considered in the generalized gradient approximation (GGA), where the non-homogeneity of the true electron density is taken into account.[83] This is further refined in the meta-GGA functionals, where the second derivative of the electron density (Laplacian), instead of the first, is included. However, even with these sophisticated approximations the exchange energy still can be difficult to express, which is why there are so-called hybrid functional, where the exact exchange energy is calculated from the HF theory. One of the most famous of these functionals is the B3LYP, in which the Becke's exchange functional (B)[84] is combined with the exact energy from the HF theory, named B3.[85] This is then combined with the correlation functional from Lee, Yang und Parr [86] to yield the hybrid B3LYP, functional which was used in the studies of this work. There is still a lot of research ongoing to refine functional and find new and better approximations.[83]

Basis sets.

Basis sets are necessary for most of the quantum chemical calculations and are describing the molecular orbitals. It is crucial to choose a specific basis set for a given system, because not all basis sets suit all problems or evaluated systems. These basis sets are describing molecular orbitals as Slater-type orbitals (STO), which are approximated with a linear combination of Gaussian-type functions (GTF). For example, in the most common minimal basis set STO-nG, each of the minimal Slater-type orbital (STO-) is represented by n GTFs (nG), e.g., STO-3G.[87, 88] These basis sets, however, do not consider molecular bonding or other interactions. To better describe the orbitals in such cases, we can expand the basis set and use more than one basis function to represent the core and valence orbitals, which are so-called valence double-, triple-, quadruple-zeta (ζ) basis sets. The split valence basis sets (or People basis sets)[89] are the simplest example, which are in general noted as X-YZg (e.g., 3-21G), where X represents the number of GTFs used for each core atomic orbital basis function, Y and Z are showing that each valence orbital is described by two basis functions, where the first one is comprised of Y GTFs and the second one by Z GTFs. The two numbers after the hyphen indicate, that this is a split valence double-zeta basis set.

The today most widely used basis sets are the correlation-consistent basis sets developed by Dunning and coworkers,[90] which were designed for valence-only correlation and post-HF calculations. They are note as cc-pVNZ, where cc-p stands for correlation-consistent polarized, V for valence only, and N for double- (D), triple- (T), quadruple-zeta (Q). These basis sets were used in the computations of this work.

Computations.

The in dept calculations in this work have been performed by Marcel Bast and Sven Thorwirth from the working group of Prof. Dr. Stephan Schlemmer in the Department of Physics at the University of Cologne and from Dr. Martin Breugst in the Department of Chemistry at the University of Cologne, which is gratefully acknowledged.

1.5 Phenol and Aniline in EI-MS

The molecular ions of phenol **1** as well as aniline **2** and their respective constitutional isomers in the gas-phase of EI-MS (see Scheme 1) have been investigated in many studies since decades.[28, 91-96] One reason is that phenol and aniline have relatively low first ionization energies: IE_{phenol} = 8.5 eV and $IE_{aniline}$ = 7.7 eV.[97] But more importantly, they form well stabilized aromatic molecular ions in EI-MS, which renders them long lived and thus they can be easily observed and studied.[1, 2, 91, 93-96, 98-101] One of the main questions of these studies was whether there are structural differences between the relative stable molecular ions and the decomposing species.

1	**3**	**5**	**4**	**2**
m/z 94	*m/z* 94	*m/z* 66	*m/z* 93	*m/z* 93
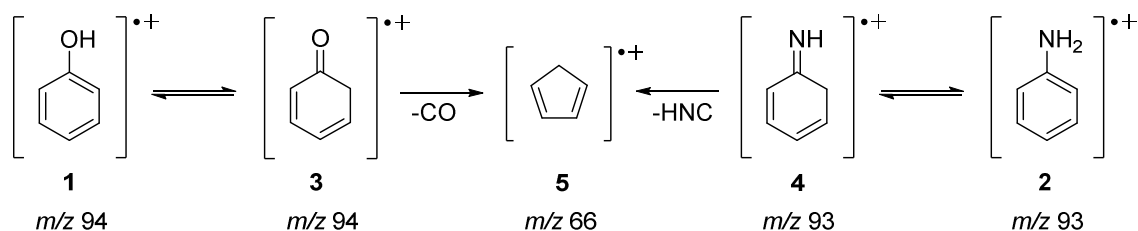
Scheme 1
Tautomeric equilibria of phenol and aniline molecular ions in EI-MS. Phenol enol-tautomer ions **1** perform a [1,3]-hydrogen shift to [2,4-cyclohexadien-1-one]$^{•+}$ keto-tautomer **3** to enable decarbonylation, whereas aniline molecular ions **2** are supposed to isomerize to the [2,4-cyclohexadien-1-imine]$^{•+}$ tautomer **4** prior to HNC loss and the ultimate formation of common cyclopentadiene radical cations [C_5H_6]$^{•+}$ **5**, at *m/z* 66.

For example, there is evidence shown in metastable ion kinetic energy (MIKE) experiments that activated phenol molecular ions tautomerize to [2,4-cyclohexadien-1-one]$^{•+}$ **3** before they decompose under decarbonylation to the product ion **5** at *m/z* 66, which is supposedly cyclopentadiene [C_5H_6]$^{•+}$.[91] The kinetic shift of the decarbonylation reaction of **1** was determined to be at least 0.8 eV according to MIKE measurements.[91] The energy needed for the keto-enol tautomerism is reported to be 2.4 eV, which is supported by experimental evidence as well as quantum chemical computations.[91, 93] Likewise, similar findings are reported for the activated molecular ions of aniline in EI-MS, which presumably form the short-lived imine isomer [2,4-cyclohexadien-1-imine]$^{•+}$ **4** before also finally decomposing to the common fragment **5** and the neutral loss of hydrogen isocyanide HNC.[2, 96, 98, 99, 102, 103] Therefore, the tautomers [2,4-cyclohexadien-1-one]$^{•+}$ **3** and [2,4-cyclohexadien-1-imine]$^{•+}$ **4** are supposedly the intermediates for the fragmentation pathways to the common fragment ion cyclopentadiene **5** at *m/z* 66. However, there is no clear evidence of the keto tautomer **3** from phenol, as it could not yet be directly detected in EI-MS with collision activation, ion cyclotron resonance mass spectrometry (ICR-MS) or MIKE experiments.[104-108] Similarly, the imine tautomer **4** could not yet be unambiguously detected in EI-MS. [2, 96, 98, 99]

1.6 Double- and Triple-Hydrogen Rearrangement in Mass Spectrometry

In mass spectrometric fragmentation processes, hydrogen rearrangement reactions are representing one of the most important elemental steps. A lot of the fragmentation reactions in which small neutral molecules such as water, arenes or hydrogen halogenides are eliminated, are caused by the transfer of a proton or a hydrogen atom.[10, 11, 109, 110] On the other hand, fragmentation reactions with hydride rearrangements are way less common and usually the hydride transfer occurs after C-C bond cleavage.[111]

The above-mentioned hydrogen transfer reactions in fragmentation processed may be reversible as well as irreversible,[112] stereoselective[16] and rate determining.[28, 113] They are often not obviously noticeable or measurable if the hydrogen species migrates within the part of the formed fragment ion or neutral loss.[114] Therefore, these hydrogen rearrangements and their analysis and clarification are very important for the fundamental mass spectrometric understanding.[28, 115-119]

There are hydrogen transfer reactions with more than one H atom, which are even more interesting and important for the understanding of MS fragmentation and other processes. This

is especially true if they occur unidirectional, meaning that the hydrogens migrate from one moiety to another, because this might be related to intramolecular redox processes and furthermore these specific rearrangements are not well understood nor studied. Double hydrogen (2H) rearrangements are relatively common[109, 110, 120-126] compared to the extremely rare triple hydrogen (3H) rearrangements.[120, 124, 125, 127-132]

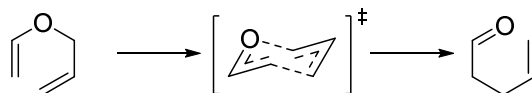## 1.7 The Claisen Rearrangement in the Gas-Phase

The Claisen rearrangement has been discovered over 100 years ago by Rainer Ludwig Claisen and has since been extensively studied.[133-141] It is an exothermic concerted carbon-carbon bond forming reaction, which makes it synthetically valuable. The kinetics of the rearrangement are of first order, and it is occurring intramolecular. It can be a solvent free reaction, occurring upon heating, but also occurs in solution as well. There were also solvent effects observed, for example polar solvents tend to accelerate the rearrangement substantially, e.g., Lewis acids.[133-135, 142] Further, it is also shown that the reaction is catalyzed by organometallics.[143, 144]

The general rearrangement in solution is illustrated with an allyl phenyl ether in Scheme 2. In the first step upon heating, the sidechain is cleaved in α-position where the σ-electrons and the two indicated π-bonds move in a concerted way of the transition state, which then finally forms a new carbon-carbon σ-bond in γ-position of the sidechain in a single step. The second step is a simple ionic proton transfer towards the oxygen driven by re-aromatization. The rearrangement generally follows the Woodward-Hoffmann rules in a suprafacial, stereospecific way and crossover experiments have shown that the reaction is indeed only intramolecular.[136] The reaction proceeds in a chair like transition state as shown in Scheme 3 for allyl vinyl ether. The residue prefers an equatorial position in the transition state. With such a formation, all the p-orbitals overlap in the correct and allowed way and the stereo information is retained.
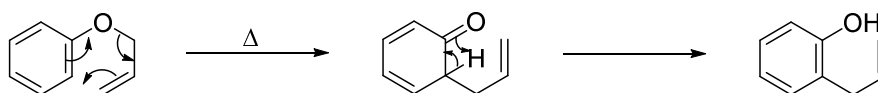
Scheme 2
Claisen rearrangement of allyl phenyl ether in the condensed phase upon heating.
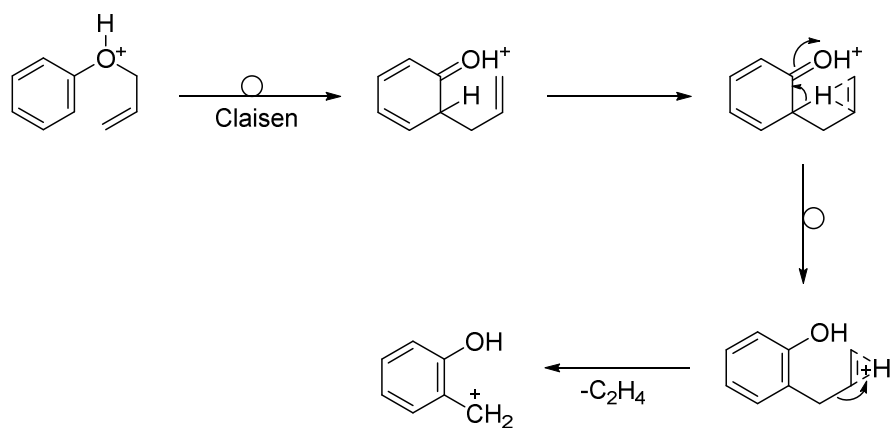
Scheme 3
Mechanism of the Claisen rearrangement according to common textbook literature.

These types of pericyclic reactions are called [3,3]-sigmatropic rearrangements, where a σ-bond is cleaved, and a new σ-bond is formed in the same process. The Claisen rearrangement is also observed in aliphatic compounds, which is however not relevant for this study, as we were only testing aryl allyl ethers and their aza-counterparts. The mechanism is analogous, except that in aliphatic compounds usually an unsaturated carbonyl is ultimately formed, as there is no re-aromatization possible.

This rearrangement is useful and has become very popular as it opens a route towards the synthesis of a variety of γ,δ-unsaturated carbonyl compounds and different alcohols, depending on the starting materials. The same rearrangement can also occur in aza-derivatives and several other functional groups, e.g., *N*-allyl aniline.[140, 145-147]

It is further reported Beynon *et al*. that the Claisen rearrangement occurs in the gas-phase in chemical ionization (CI) mass spectrometry.[148, 149] In CI-MS a reagent gas, mostly methane or ammonia, is ionized via EI-MS like processes and the ultimately formed reagent ions subsequently react with the analyte to form analyte ions via proton transfer.[150]

Scheme 4 shows the mechanism as proposed by Beynon *et al*., in which ionized protonated allyl phenyl ether undergoes the Claisen rearrangement in the first step, which is immediately followed by a concerted proton transfer from the *ortho*-position to the alkene sidechain double bond. In the next step ethene is then cleaved from the molecule to yield a benzylic ion as indicated in the scheme, which might rearrange further in, e.g., according to a Wagner-Meerwein or Demjanow type rearrangement.[151] According to the suggested mechanism, the proton necessary for the cleavage of the ethene group originates from the *ortho*-position, as it is usually also claimed in textbooks.[151]

Scheme 4
Gas-phase Claisen rearrangement in CI-MS followed by the loss of ethene as reported and proposed by Beynon *et al.*[148]

2 Statement of the Problem

2.1 Cryogenic Messenger-IR Ion Spectroscopy study of phenol & aniline molecular ions and of the common fragment ion [C₅H₆]⁺ formed by EI-MS

The molecular ions of phenol **1** as well as aniline **2** and their respective constitutional isomers present in the gas-phase upon EI-MS are well studied as highlighted in the introduction.[28, 91-96] Especially their keto- and enol-tautomers (see Scheme 1) have been in the focus of many studies. The respective equilibria of both are interesting as test systems for tautomerization processes and to study their intermediates. Most of the theoretical and experimental evidence indicates that the keto- and enol-tautomers **3** and **4** are the crucial intermediates in the fragmentation processes towards the common fragment ion **5** at *m/z* 66 (see Scheme 1). The [1,3]-hydrogen shifts in the tautomerization process are obviously necessary in both fragmentation pathways in order to ultimately eliminate the neutrals CO in the case of phenol and HNC in the case of aniline.[2, 91-96, 99, 100, 152]

As there is no direct and clear experimental proof and verification for the actual presence of the respective tautomers **3** and **4** as well as for the common product cyclopentadiene **5** as of the time this study was conducted, we wanted to elucidate the structures of the molecular ions **1**, **2**, **3** and **4** on the respective fragmentation pathway via IR ion spectroscopy. In this study we tried to investigate labile tautomeric ion structures of phenol and aniline molecular ions with cryogenic messenger ion spectroscopy to probe whether those isomers are detecable.[67-70] As we will see in the discussion chapter, the isomerization to **3** and **4** is the kinetic bottleneck of these reactions. Therefore, once isomerized, these ions possess enough energy to further decompose to the final product. It was our intend to "freeze out" these elusive isomers via cryogenic temperatures. Furthermore, we also investigated the important fragment ion **5** at *m/z* 66 and wanted to gather spectroscopic evidence for its definite structural identity.

2.2 Unidirectional Double and Triple Hydrogen Rearrangement Reactions Probed by Infrared Ion Spectroscopy

Several decades ago, Kuck and Filges discovered a unidirectional triple (3H) hydrogen rearrangements that occur upon the fragmentation of radical cations of electron-rich 3-arylpropanols $[M]^{\bullet+}$, as shown in Scheme 5.[3, 132, 153] Next to these 3H rearrangements, there was also a double hydrogen transfer (2H) observable, which made this older study even more interesting. Both processes were found to be most pronounced with long-lived, metastable molecular ions. The 3H rearrangement was observed with highest intensity in EI as well as in mass-analyzed ion kinetic energy (MIKE) experiments of *trans*-2-(4-*N,N*-dimethylaminobenzyl)-1-indanol.[3] In MIKE experiments, mass-selected metastable ion fragmentations are investigated by measuring the ratio of kinetic energy to charge of the product ions in an electric sector field analyzer, which enables to measure the kinetic energy release in the product ion formation.

Kuck and Filges proposed mechanisms for both rearrangement and fragmentation processes based on extensive deuterium labeling experiments, kinetic isotope effects, and rudimentary theoretical considerations. In their mechanism the final 3H rearrangement product ion is suggested to be *N*-protonated *N,N*-dimethylaminocyclohexa-2,5-diene. However, the authors clearly point out that the mechanistic details and the structural identity of the fragments and intermediate ions formed by both rearrangements remained speculative and need further proof and independent evidence. As the 2H and 3H rearrangements are very intriguing and important for the fundamental understanding of fragmentation and other processes in mass spectrometry, we decided to clarify these ion structures and mechanisms with infrared ion spectroscopy. IR ion spectroscopy has contributed a lot in specific ion structure elucidation studies,[154, 155] however, reasonable evidence for the structures of the ions formed by the 3H rearrangement has not been available up to date. In this study, we utilize IR ion spectroscopy, which is combined with DFT calculations, to effectively identify the structures of these fragment ions. That this can be done successfully with IR ion spectroscopy as was already shown in literature and was also discussed in Chapter 1.3.[21, 23, 48, 156-158]
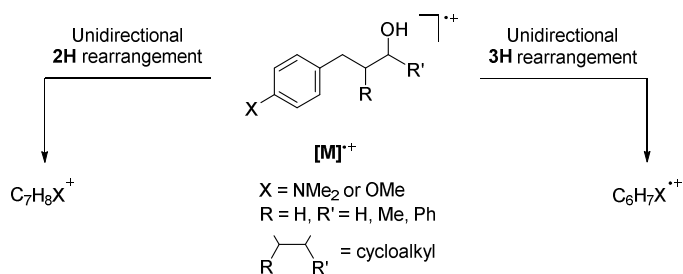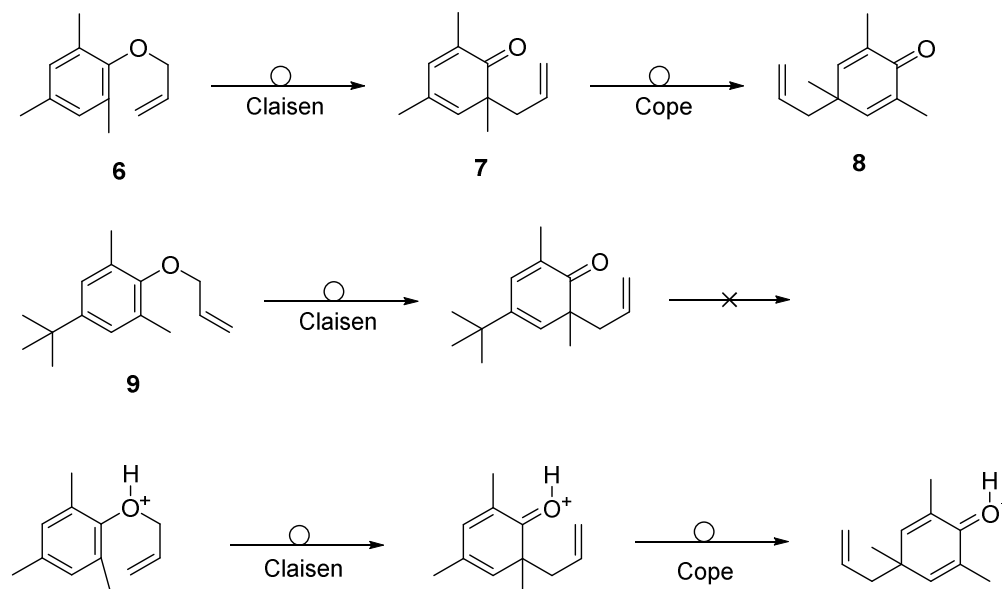
Scheme 5
General scheme depicting the unidirectional 2H and 3H rearrangement reactions in the molecular radical cations, $[M]^{\cdot+}$, of electron-rich *para*-substituted 3-aryl-1-alkanol derivatives.[22,23]

2.3 Investigation of the Claisen Rearrangement Reaction in protonated Allyl Phenyl Ether Derivatives

In case the *ortho*- and *para*-positions in allyl phenyl ethers are substituted as *e.g.* in allyl-2,4,6-trimethylphenylether **6**, the Claisen rearrangement should deliver either *ortho* (**7**) or *para* (**8**) doubly substituted cyclohexadienone ions (see Chapter 1.7) via a Claisen Cope tandem reaction as shown in Scheme 6,[142, 159-161] because there are no protons available in the *ortho*-positions for re-aromatization, i.e., to form the respective phenol derivative. Further, allyl-2,6-dimethyl-4-*tert*-butylphenylether **9** should suppress the Cope rearrangement to the *para*-product and should provide mainly the *ortho*-rearranged product, due to steric hindrance. Therefore, this approach might open an avenue to study cyclohexadienone derivatives in the gas-phase, which are interesting tautomers of phenol, and which could give access to reference spectra for the study of phenol and aniline tautomers in the gas-phase (see also Chapter 1.5 and 2.1). In the same way, the use of *N*-allyl aniline derivatives should give access to comparable imine tautomers of aniline for the same study.

Scheme 6
Claisen Cope tandem rearrangement in solution (reaction on top and middle) and in the gas-phase with protonated molecular ions [M+H]$^+$ in the bottom reaction. Allyl-2,4,6-trimethylphenylether **1** delivers a mixture of **2a** and **3a**, whereas the analogous reaction with allyl-2,6-dimethyl-4-*tert*-butylphenylether **2** should deliver exclusively the ortho-rearranged product due to steric hindrance.

Furthermore, there is evidence, that the Claisen rearrangement occurs in the gas-phase of a mass spectrometer as shown in the literature.[141, 148, 149, 162-164] This phenomenon is especially pronounced in CI-MS with the protonated species [M+H]$^+$.[148, 163] The loss of ethene is put forward to evidence the Claisen rearrangement in the gas-phase in CI-MS in the fragmentation patterns of protonated molecular ion precursors of allyl phenyl ether.[148] The mechanism proposed in a study by Beynon *et al.* is shown in Scheme 4 in Chapter 1.7. We found in our ESI-MS experiments that, i.e., analyte **6** is also showing the loss of ethene, although there are no protons in the *ortho*-positions after the Claisen rearrangement has occurred. Thus, we think the mechanism likely is based on different intermediates and/or reaction routes. This woke our interest and we therefore set a second goal for this study, which was to clarify or at least to get some insights into the reaction mechanism of the Claisen rearrangement in the gas-phase in ESI-MS. In order to achieve this goal, we were once more utilizing mass spectrometry as well as IR ion spectroscopy and computational chemistry.

3 Results and Discussion

3.1 Cryogenic Messenger-IR Ion Spectroscopy study of phenol & aniline molecular ions and of the common fragment ion [C₅H₆]•⁺ formed by EI-MS

3.1.1 EI-MS

Figure 7 and Figure 8 are showing the EI-MS spectra of phenol **1** and aniline **2** (left panels) recorded with the FELion instrument (see Chapter 1.3 and 6.4 for details). They are in accordance with the literature as shown in the right panels,[97] with both containing the common fragment at *m/z* 66 after the loss of CO and HCN, respectively. The signals at *m/z* 45 and *m/z* 46 are related to an ethanol contamination, which is not relevant for the study neither does it impede all the following results, because the respective analyte is always mass-selected in the spectrometer.

When examining the computed reaction trajectories of phenol and aniline molecular ions as shown in Figure 9 and Figure 10 (discussed in detail below), the tautomerization of phenol and aniline apparently is the kinetic bottleneck of the fragmentation processes towards the ultimate fragment ion $[C_5H_6]^{\bullet+}$ cyclopentadiene **5**. This means that the tautomerized ions cyclohexadienone **3** and imine **4** already possess enough excess energy after ionization and tautomerization to directly decompose to the fragment ion at *m/z* 66. It was our idea to trap the tautomeric molecular ions in their shallow potential wells behind the first energetic barrier after tautomerization when applying cryogenic temperatures of around 6-8 K. We therefore wanted to apply as mild ionization conditions as possible to yield molecular ions of minimal excess energy. In order to still have a decent number of molecular ions of **1** and **2** as well as fragmentation product ions at *m/z* 66 to be able to measure a meaningful IR spectrum, we had to apply the minimal electron energies of 17 eV for phenol and 20 eV for aniline. The appearance energies of the fragment ions were reported in the literature to range between 11 – 13 eV.[97] The fragment ion abundance of *m/z* 66 is thus drastically reduced under these special ionization conditions as shown in Figure 7 and Figure 8. Furthermore, a different relative ion intensity and the absence of fragments at lower *m/z* values document this.
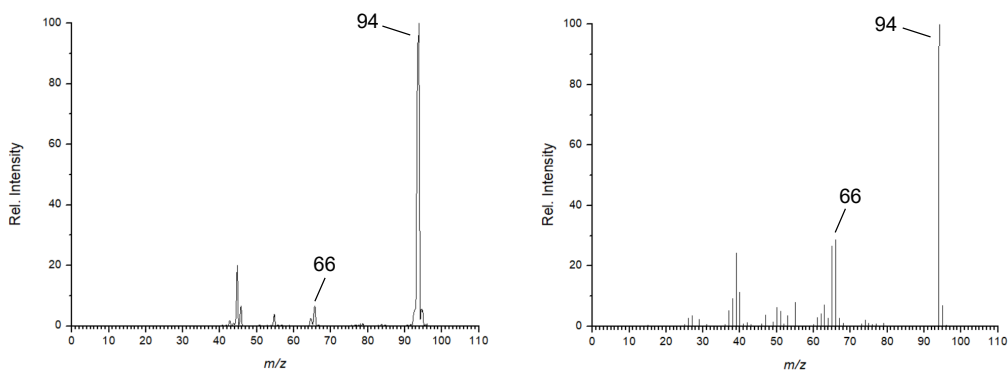
Figure 7
Left panel: Mass spectrum of phenol recorded with FELion via EI-MS (electron energy = 17 eV). The signals at *m/z* 45 and *m/z* 46 in the mass spectrum of phenol originate from an ethanol contamination. Right panel: Mass Spectrum of phenol from the NIST database[97] produced with EI-MS (electron energy = 70 eV).
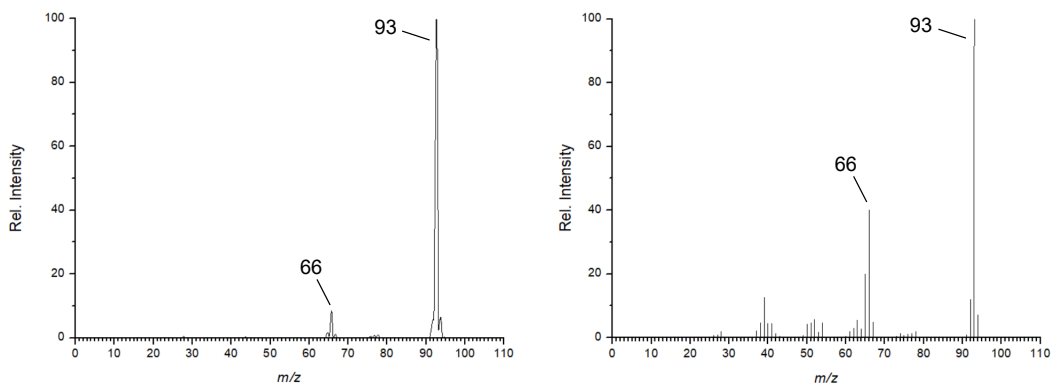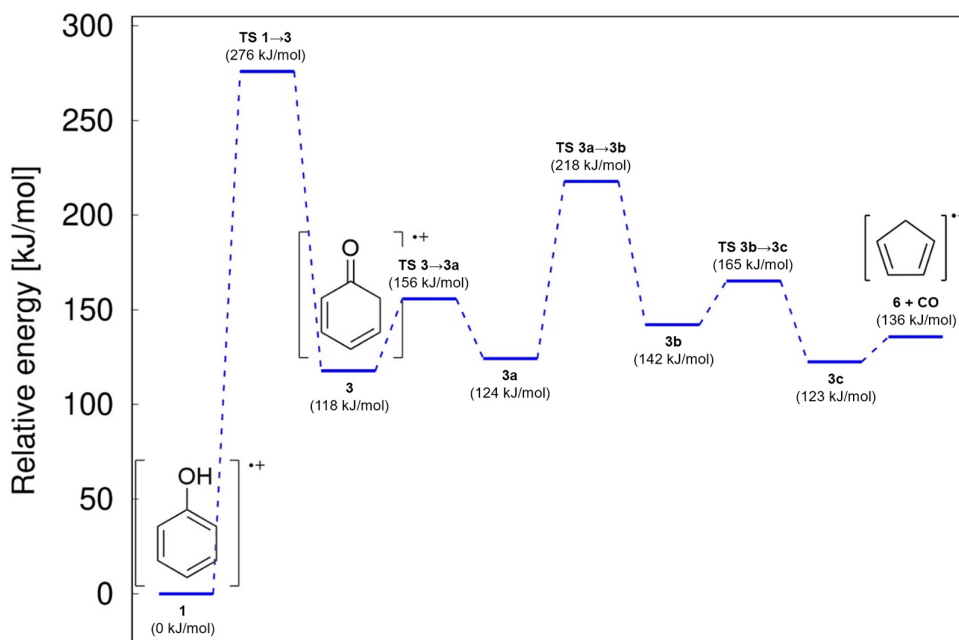

Figure 8
Left panel: Mass spectrum of aniline recorded with FELion via EI-MS (electron energy = 20 eV). Right panel: Mass Spectrum of aniline from the NIST database[97] produced with EI-MS (electron energy = 70 eV).

3.1.2 Computations

The following computations were executed by Marcel Bast and Sven Thorwirth from the Department of Physics at the University of Cologne.

Figure 9 and Figure 10 are showing the calculated potential energy surfaces (PES) of the fragmentation for phenol **1** and aniline **2** towards their common fragment at *m/z* 66, calculated with the DFT method using the (U)B3LYP functional and the cc-pVQZ basis set. According to the reported studies this ion is supposed to be cyclopentadiene. The energy given in the PES is relative to the energy of ionized phenol and aniline, respectively. Figure 11 illustrates the calculated structures of all ions in these PES. The calculations are based on already published results of Le *et al.*[95, 96] and are mainly consistent with those results except for a few small details: In our calculations the cyclohexadienone radical **3** is a non-planar ring structure, whereas in the literature it was calculated to be planar (see Figure 12). The methylene carbon 2 stands out of the ring plane , reflecting its sp^3 hybridization, which results in a different calculated IR spectrum compared to the planar isomer. Furthermore, structure **3c** also differs slightly from the literature and is found to be about 1 kJ/mol lower in relative energy than previously reported (see Figure 13).

Figure 9

Potential energy surface for the unimolecular decay of phenol radical cation **1**. The activation of $[C_6H_6O]^{+\bullet}$ at *m/z* 94 by electron impact leads to the formation of $[C_5H_6]^{+\bullet}$ **5** by the elimination of a neutral CO. The transition state TS**1**→**3** between the phenol ion structure **1** and its tautomer cyclohexadienone **3** is the rate limiting step on this PES.
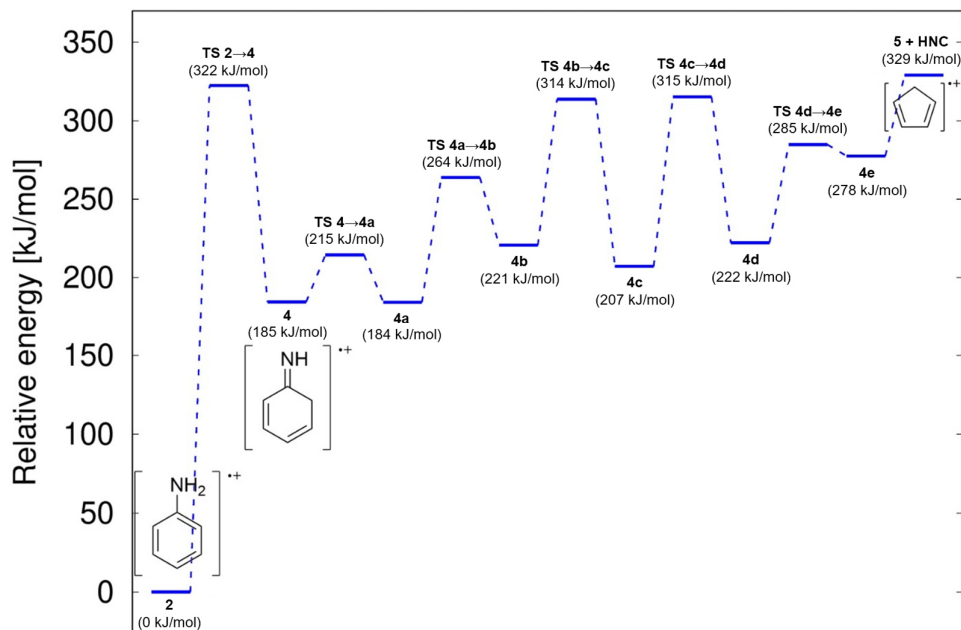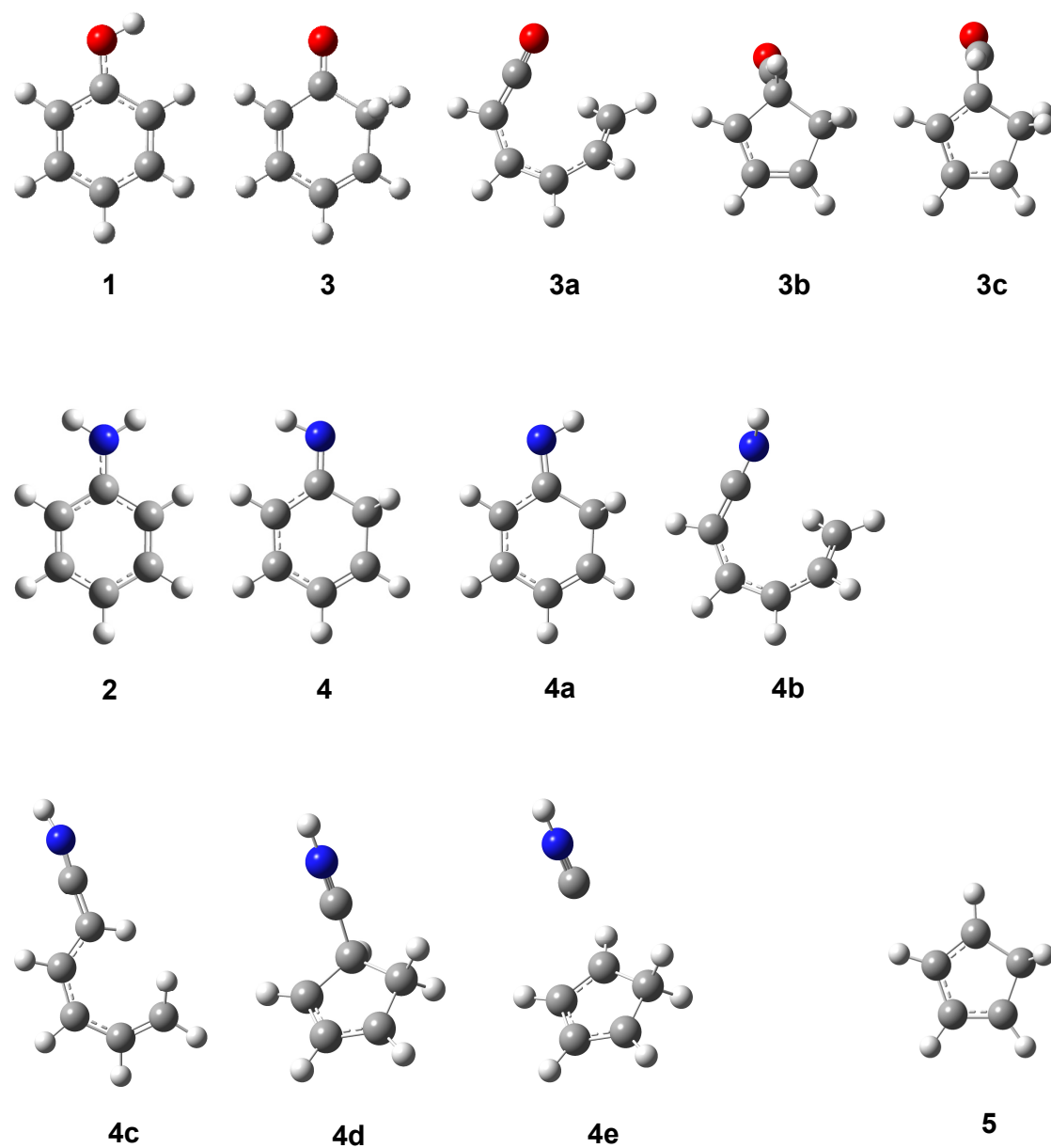
Figure 10

Potential energy surface for the unimolecular decay of the aniline radical cation **2**. The activation of $[C_6H_5NH_2]^{\bullet+}$ at *m/z* 93 by electron impact leads to the formation of $[C_5H_6]^{\bullet+}$ **5** with the elimination of a neutral HNC. Transition state TS**2**→**4** between the aniline ion **2** and its tautomeric imine structure **4** is the rate limiting step.

The transition state (TS) of the tautomerization of the radical cationic molecular ion of phenol to the respective cyclohexadienone ion **3** is calculated to be 276 kJ/mol higher than ionized phenol as we can see in Figure 9, with the ionization energy (IE) of phenol at 8.5 eV, this TS lies at about 11.5 eV, which is in the range for the appearance energy of the final fragmentation product cyclopentadiene **5** according to literature[97] (see Chapter 3.1.1). This is reasonable as we can see that the reaction trajectory lies completely below this energy level, meaning that tautomerized ions possess enough excess energy to immediately decompose to **5**. Ionized cyclohexadienone is calculated to be 118 kJ/mol higher in energy and the final product cyclopentadiene is 136 kJ/mol higher, both well below the first TS of the tautomerization. For Phenol there are three more structures on the reaction pathway to the final product cyclopentadiene **5**. Cyclohexadienone **3** has a small transition state (+38 kJ/mol barrier) towards the ring opening in structure **3a**. This ring opening is necessary to eliminate CO at the end. The next TS is the second highest energy level in the pathway (+94 kJ/mol barrier), because it closes the ring again, thus energy must be supplied for ring closure und strain, to yield the 5-ring system in structure **3b**. Finally, there is the last TS towards structure **3c**, which is only a 23 kJ/mol barrier, where the CO molecule finally leaves the ion in a direction out of

the ring plane (towards the back in Figure 11, and also shown in Figure 13) to ultimately yield cyclopentadiene **5** and carbon monoxide.

The TS for the tautomerization of aniline is even higher with 322 kJ/mol as shown in Figure 10. The ionization energy for aniline is reported to be 7.7 eV, and the TS at 11.2 eV also allows the formation of cyclopentadiene (see Chapter 3.1.1). The final products **5** and HNC are 329 kJ/mol higher in energy than ionized aniline, and thus this is the highest energy level in this reaction pathway. After the tautomerization to imine **4**, there are five more ion structures towards the final products. The first step has a low TS with only 30 kJ/mol above the tautomeric imine **4**, where the N-H bond must rotate to the other side towards the CH_2 group in α-position to yield ion **4a**. It is interesting, that structure **4a** is 1 kJ/mol lower in energy than the imine structure **4** as one would expect some spatial strain because the N-H bond is now pointing towards the methylene group. The next TS towards structure **4b** lies 80 kJ/mol higher than **4a**. This is as expected since we must break the C_1-C_2 bond to open the ring structure. The now open structure **4b** has a relative internal energy of 221 kJ/mol compared to ionized ground state aniline. This is followed by two transitions states which are almost equal in energy and need around 100 kJ/mol each to be overcome. From structure **4c** to **4d** the formation of the new 5-ring takes place and structure **4d** is slightly higher in energy (15 kJ/mol) due to ring strain. The final TS then leads to the break of the C_1-C_6 bond to ultimately eliminate HNC and form the common product **5**.

Figure 11
Calculated ion structures of phenol **1** – **3c** and aniline 2 – 5 as shown in Figure 9 and Figure 10, respectively.
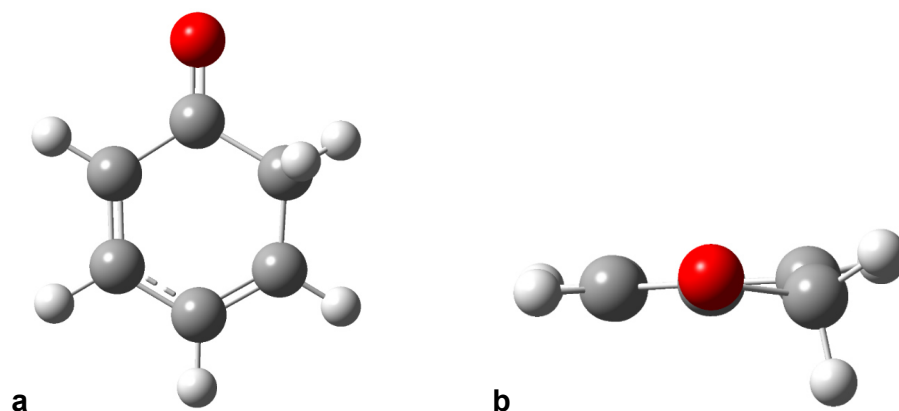
Figure 12
Energetically most favourable structure of the cyclohexadienone radical cation **3**. In a) and b) the asymmetric dihedral angle of the methylene group in structure **3** with respect to the 6-membered ring is highlighted. b) shows the non-planar structure of the carbon ring with a significant *out-of-plane* position of methylene carbon 2.
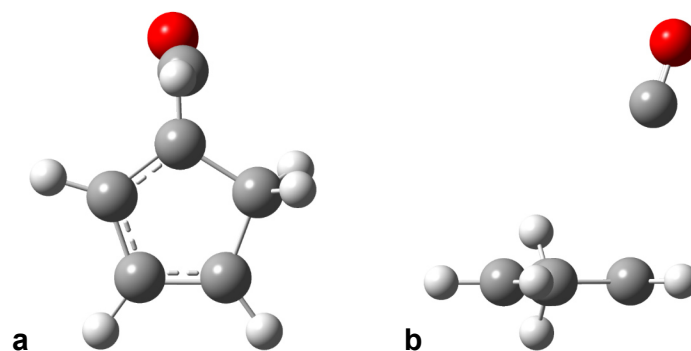
Figure 13
a) Energetically most favourable structure **3c**, which shows the elimination angle of the leaving CO molecule from different points of view a) and b). The CO leaves along the direction of its previous bond to the carbon atom and not along the ring plane.

3.1.3 Ion Spectroscopy

Phenol.

Figure 14a shows the experimental cryogenic messenger IR spectrum of the Ne-tagged phenol radical cation at *m/z* 114 $[C_6H_6O \cdot Ne]^{\bullet+}$ in black. It is compared to the calculated spectrum of ionized phenol **1** in green. The calculated IR spectrum is in convincing agreement. Characteristic modes of phenol, such as the N-O stretching mode at 1463 cm^{-1} or the O-H wagging mode at 599 cm^{-1} are matching the experimental spectrum quite well. This already indicates that the aromatic phenol tautomer is mainly present in the gas-phase. All bands can be assigned as shown in Table 1 and Table 2, except two strong bands at 1229 cm^{-1} and 1446 cm^{-1} respectively (marked with an asterisk). Several of the computationally predicted modes are red-shifted, but some others, e.g., the bands at 784 cm^{-1} or 927 cm^{-1}, are matching the observed values very good. Also, the anharmonic computations match the recorded IR spectrum of the phenol ground state structure **1** convincingly well and confirm the assignment, as shown in Figure 15. However, some bands in the experimental spectrum still cannot be assigned to basic vibrational modes and even do not match any overtones or combination bands predicted in these calculations, for example the bands at 1146 cm^{-1}, 1229 cm^{-1}, and 1446 cm^{-1} (marked with asterisks in Figure 14 and with question marks in Table 1).

Figure 14b also shows the experimental spectrum of Ne-tagged phenol in black, but this time compared to [2,4-cyclohexadien-1-one]$^{\bullet+}$ ion **3** in red. A few bands match quite well but a reasonable overall agreement is not visible. Especially the strong absorptions of **3** in the range between 600 cm^{-1} and 800 cm^{-1} are absent in the recorded spectrum of the molecular ion of phenol.

Furthermore, the saturation depletion scan (see Chapter 6.4 for details) in Figure 22 indicates the presence of only one isomer, which is apparently the aromatic phenol ion **1**. In a depletion scan, we irradiate the trapped ions at a wavelength, where only the isomer of interest absorbs and thus decomposes. If the ion count then extrapolates to zero with time, we can assume that only this isomer was present. At 1479 cm^{-1} only phenol tautomer ion structure **1** absorbs photons (v_{25}). The ion intensity with (blue) and without (orange) laser depletion is fitted as a function of the deposited energy. The fit indicates that only tautomer **1** is formed and present as the fit of the ion counts converges to 0. The increase of the counts in the off measurement (orange) for higher deposited energies is due to time-dependent changes of the source parameters during the different measurements.

This leads us to the conclusion that only one isomer is present, which is the aromatic ground state tautomer of phenol, or at least the percentage of the other tautomeric structure **3** is so low that it is not measurable in this case.
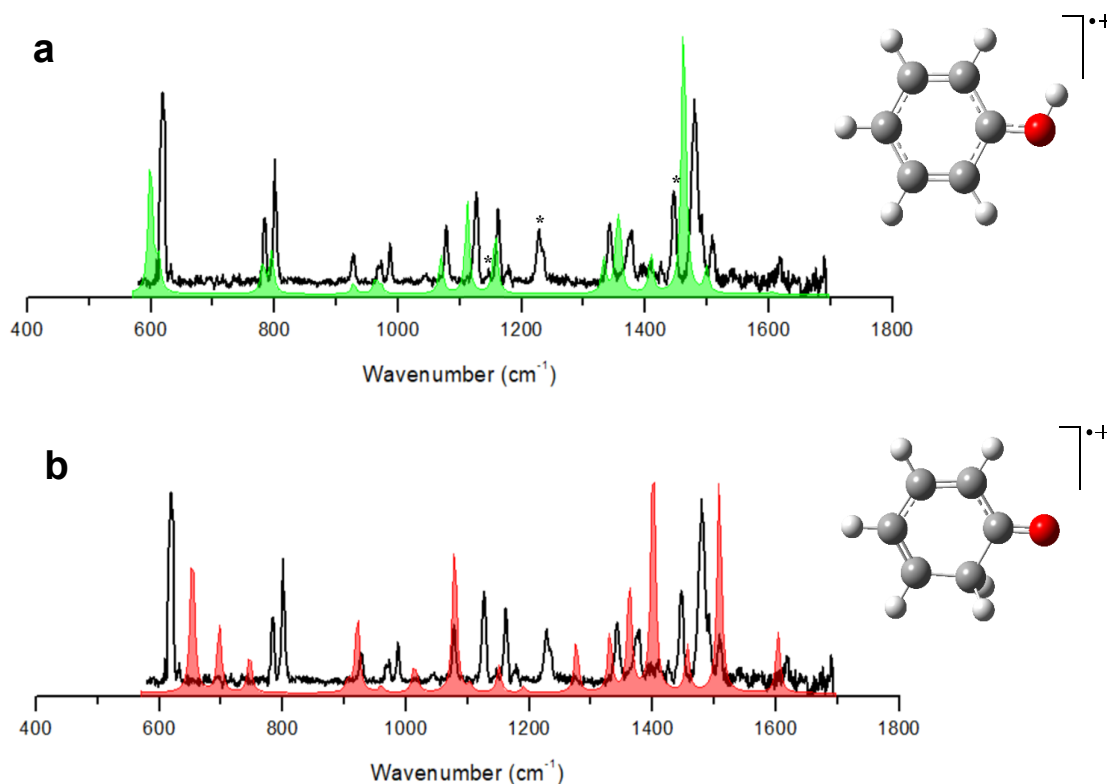
Figure 14
a) IR-PD spectrum (black) of the cooled, Ne-tagged phenol radical cation [C$_6$H$_6$O•Ne]$^{•+}$ at *m/z* 114 formed by EI-MS compared to the IR spectrum (green) calculated for the aromatic phenol ion **1** depicted in the inset. Signals marked with asterisks are not assigned to computed vibrational modes **b)** Measured IR-PD spectrum (black) of the cooled, Ne-tagged phenol radical cation [C$_6$H$_6$O•Ne]$^{•+}$ at *m/z* 114 formed by EI-MS compared to the IR spectrum (red) calculated for the cyclohexadienone tautomer of phenol **3** depicted in the inset.
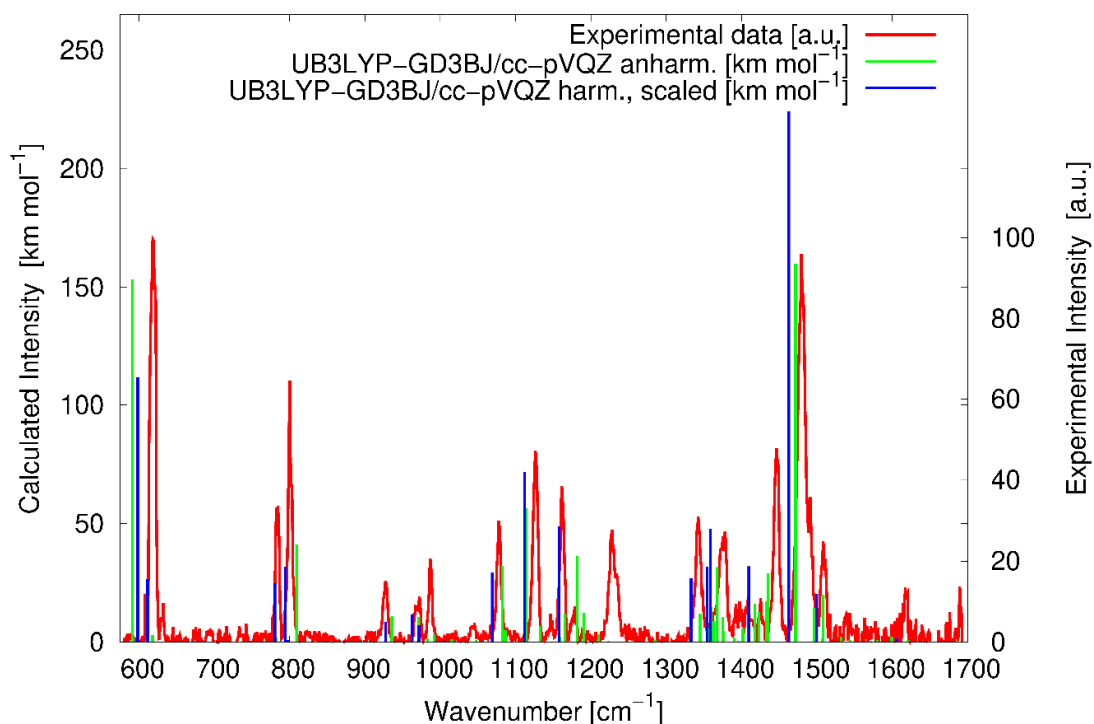
Figure 15
Experimental spectrum (red), harmonic (blue) and anharmonic (green) calculations of the phenol molecular ion **1**. The calculated intensities are given in km/mol. The experimental intensities were scaled arbitrarily according to the calculated ones.

Table 1
Assigned absorption bands found in the IR-PD spectrum of the phenol radical cation **1**. The relative experimental intensities are given with respect to the fitted area of the peaks and were normalized to the strongest transition. Band positions and intensities of overtones and combination bands are based on the anharmonic force field calculations. Possible superimposing modes are indicated by braces. Modes marked with question marks could not be identified.

Vibrational Mode #	Obs. ν_{vib} [cm^{-1}]	Int. [%] Vol.	Calc. ν_{vib} [cm^{-1}]	Int. [km/mol]
ν_7	619	74	599	112
ν_8	631	3	611	27
ν_9	784	19	781	25
ν_{10}	801	34	795	32
ν_{11}			798	0.9
ν_{12}	927	10	928	9
ν_{13}	970	7	963	12
ν_{14}	987	10	972	7
ν_{4+8}	1044	3	1048	0.9
ν_{17}	1078	19	1069	29
ν_{18}	1126	33	1112	72
?	1146	3		

ν₁₉	1161	21	1157	49
ν_{19}	1161	21	1157	49
ν_{20}	1177	4	1171	0.3
?	1229	29		
ν_{21}	1343	23	1333	27
ν_{22}			1354	32
ν_{23}	1374	}6	1359	48
ν_{24}	1426	4	1410	32
?	1446	39		
ν_{25}	1479	100	1463	224
ν_{26}	1508	17	1500	20
ν_{27}	1617	6	1606	2

Table 2

Mode descriptions of the calculated vibrational modes of the aromatic phenol[•+] **1** (first row of each vibrational mode ν_i) and the cyclohexadienone[•+] **3** (second row of each vibrational mode ν_i) structure.

Mode #	Mode description	calc. ν_{vib} [cm⁻¹]
ν_1	out of plane, ring and C-O twist.	179
	C-O wagg., H_2 rock., ring wagg. def.	110
ν_2	out-of-plane, ring and O-H twist.	354
	H_2 rock., ring bend.	245
ν_3	in-plane, C-O bend., ring bend.	404
	ring and C-H bend., C-O bend.	401
ν_4	out-of-plane, C-H and ring twist.	425
	C-O bend., C-H bend.	421
ν_5	in-plane, ring def. bend.	513
	ring bend., H_2 and C-H wagg.	438
ν_6	in-plane, ring. def. bend.	554
	ring bend., H_2 and C-H wagg.	517
ν_7	out-of-plane, O-H wagg., C-H wagg.	599
	ring bend., H_2 rock., C-H bend.	559
ν_8	out-of-plane, C-H wagg.	611
	C-H wagg., H_2 rock., ring stretch.	653
ν_9	out-of-plane, C-H twist.	781
	ring stretch. and bend., C-H wagg.	697
ν_{10}	out-of-plane, C-H wagg.	795
	C-H wagg., H_2 rock.	746
ν_{11}	in-plane, ring twist. and bend., C-O stretch.	798
	C-H twist., H_2 rock.	905
ν_{12}	out-of-plane, C-H twist., ring twist.	928
	ring bend., H_2 rock.	921
ν_{13}	in-plane, ring stretch. and bend.	963
	ring stretch., H_2 wagg., C-H twist.	942
ν_{14}	in-plane, ring bend., C-O stretch.	972

	ring stretch., H_2 twist., C-H twist.	960
ν_{15}	out-of-plane, C-O twist.	990
	ring stretch., H_2 wagg., C-H twist.	1013
ν_{16}	out-of-plane, C-O twist.	1006
	C-H twist., ring twist., H_2 twist.	1018
ν_{17}	in-plane, C-H and O-H bend., ring stretch.	1069
	H_2 wagg., C-H bend., ring stretch.	1079
ν_{18}	in-plane, C-H and O-H bend., ring stretch.	1112
	H_2 wagg., C-H bend., ring stretch.	1104
ν_{19}	in-plane, C-H and O-H bend., ring stretch.	1157
	C-H bend., ring stretch., H_2 wagg.	1151
ν_{20}	in-plane, C-H bend., ring bend.	1171
	C-H bend., ring stretch., H_2 wagg.	1191
ν_{21}	C-H and O-H bend., ring stretch.	1333
	H_2 bend., ring stretch., C-H bend.	1276
ν_{22}	in-plane, C-O stretch., ring stretch., C-H bend.	1354
	H_2 bend., ring stretch.	1331
ν_{23}	in-plane, asym. ring stretch., O-H bend., C-H bend.	1359
	ring stretch., H_2 bend., C-H bend.	1363
ν_{24}	in-plane, asym. ring stretch., O-H bend., C-H bend.	1410
	ring stretch., C-H bend.	1401
ν_{25}	in-plane, ring stretch., N-O stretch., C-H bend.	1463
	ring stretch., C-H bend.	1457
ν_{26}	in-plane, asym. ring stretch., C-H bend.	1500
	ring stretch., C-H bend., C-O stretch.	1509
ν_{27}	in-plane, sym. ring stretch., C-O stretch., C-H bend.	1606
	C-O stretch., ring stretch.	1604
ν_{28}	in-plane, C-H asym. stretch., ring bend.	3085
	one H of C-H_2 stretch.	2850
ν_{29}	in-plane, C-H asym. stretch., ring bend.	3099
	one H of C-H_2 stretch.	3002
ν_{30}	in-plane, C-H asym. stretch.	3107
	C-H stretch.	3079
ν_{31}	in-plane, C-H asym. stretch.	3112
	C-H stretch.	3084
ν_{32}	in-plane, C-H sym. stretch.	3117
	C-H stretch.	3104
ν_{33}	in-plane, O-H stretch.	3592
	sym. C-H stretch.	3107

Aniline.

Figure 16a shows the recorded cryogenic messenger IR spectrum of Ne-tagged aniline radical cation at *m/z* 113 $[C_6H_7N \bullet Ne]^{\bullet+}$ in black compared to the calculated IR spectrum of the aromatic aniline ion **2** in green. Characteristic modes are the N-H stretching band at 1624 cm^{-1}, N-H stretch N-H$_2$ bending combination mode at 1474 cm^{-1} or the C-H wagging mode at 625 cm^{-1} which are all visible in the experimental spectrum al well. Here again, the overall match is very satisfying, and all bands can be assigned as shown in Table 3 and Table 4. We can also see a red-shift of the calculated frequencies here as it was the case with phenol above. A few calculated features match the experimental modes very well, *e.g.,* the bands at 627 cm^{-1} and 916 cm^{-1}. The important inversion band (N-H$_2$ wagging) at 661 cm^{-1}, is obviously not predicted correctly by the computations, which was also reported before by Piest *et al.* [165] There are six bands that are not predicted by the harmonic calculations. Thus, we performed anharmonic calculations for aniline as well, which showed us that the five relatively weak features at 1072 cm^{-1}, 1237 cm^{-1}, 1285 cm^{-1}, 1449 cm^{-1}, 1463 cm^{-1} are combination bands as shown in Table 3 (and see also Figure 17). The band at 1330 cm^{-1} can be explained as an overtone of the mode at 661 cm^{-1}. These vibrational transitions were reported before,[165] although, the NH$_2$ wagging, and the C-H wagging bands are reversed in intensity compared to our approach. However, they used Argon tagged precursor ions and resonance-enhanced multiphoton ionization (REMPI) compared to our study. It has further to be noted that messenger pre-dissociation spectra are not reflecting the direct IR absorption probabilities – as is the case in the calculations – and thus the intensities might differ. This is also due to that specific vibrations are more effective in breaking the bond with the Ne-tag.[62] Other calculations we made with different basis sets and methods (e.g., MP2/cc-pVQZ) showed even more red shifted bands. This leads us further to the conclusion that the band at 661 cm^{-1} cannot be reasonably investigated via current quantum chemical calculations and might be a target for further studies.

Further, we also probed for the band positions of the N-H-stretching modes ν_{35} and ν_{36}, which were detected by using an OPO/OPA-laser (see Table 3, Figure 18 and Figure 19).[166-168] The Figures clearly show the N-H stretching modes as expected at 3390 cm^{-1} und 3484 cm^{-1}.

Figure 16b compares the recorded IR spectrum of Ne-tagged aniline radical cation in black to the calculated spectrum of the aniline tautomer **4**. It is clear, that the calculations do not match the experimental data at all, making it very unlikely that ion **4** was present in the gas-phase. Furthermore, the saturation depletion scan (see Chapter 6.4 for details) in Figure 23 shows again the presence of only one isomer. At 3390 cm^{-1} only aniline tautomer ion structure **2**

absorbs photons (ν_{35}). The ion intensity with (blue) and without (orange) laser depletion is fitted as a function of the deposited energy. The fit indicates that only tautomer **2** is formed, which is according to the IR data the aromatic aniline tautomer **2**. We also measured for the modes ν_{30}, ν_{31}, ν_{32}, ν_{33}, ν_{34} and ν_{35} of ion **4** (see Figure 20), and there are no bands visible as expected.

This brings us to the conclusion that in the case of aniline also only one isomer is present, which is the ground state molecular ion of aromatic aniline, or at least the amount of the other tautomeric structure **4** is too low to experimentally verify its presence.

These results are also in agreement with a newer study from a working group at the FELIX Laboratory.[169] They also did some extensive cryogenic messenger ion spectroscopy measurements and quantum chemical calculations on the aniline molecular ion and the fragmentation pathway, which basically match our results as well.
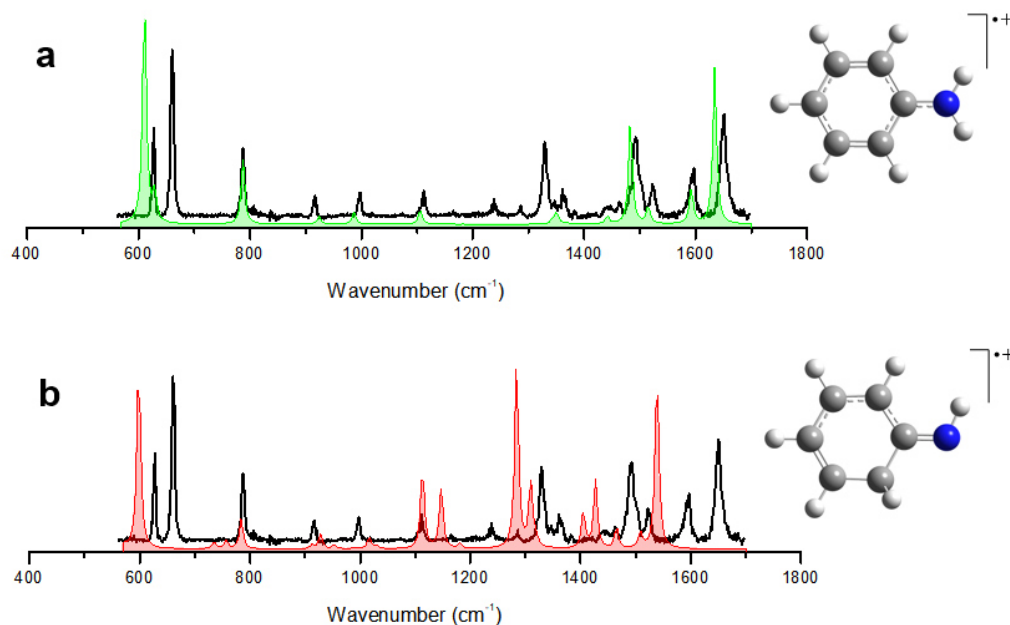
Figure 16

a) IR-PD spectrum (black) of the cooled, Ne-tagged aniline radical cation $[C_6H_7N \cdot Ne]^{\cdot +}$ at *m/z* 113 formed by EI-MS compared to the IR spectrum (green) calculated for the aromatic aniline molecular ion **2**, depicted in the inset. Signals marked with asterisks are not assigned to computed modes (see text: discussions part). **b)** Measured IR action spectrum (black) of the cooled, Ne-tagged aniline radical cation $[C_6H_7N \cdot Ne]^{\cdot +}$ at *m/z* 113 formed by EI-MS compared to the IR spectrum (red) calculated for the tautomeric imine structure of aniline **4**, depicted in the inset.
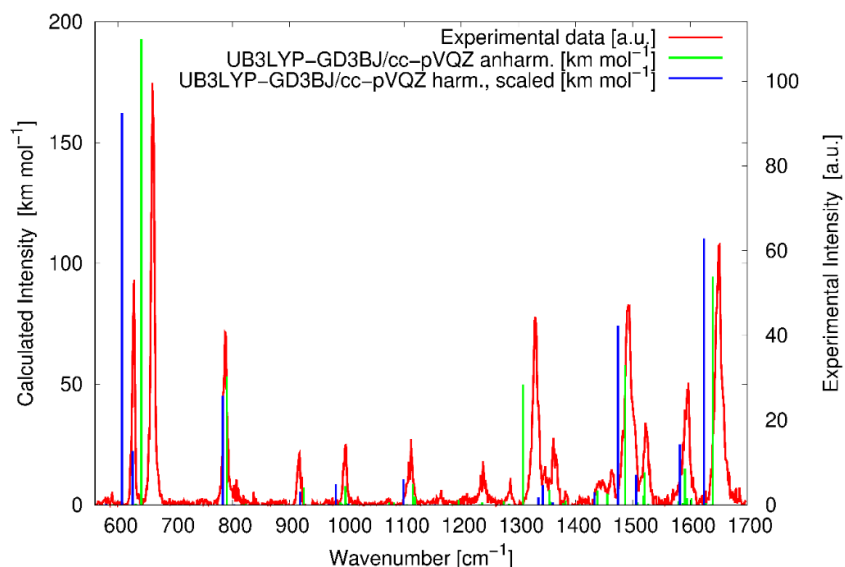
Figure 17
Experimental spectrum (red), harmonic (blue) and anharmonic (green) calculations of the molecular ion of aniline **2**. The calculated intensities are given in km/mol. The experimental intensities were scaled arbitrarily according to the calculated ones.

Table 3
Absorption band assignment of the observed vibrational frequencies of the radical cation of aniline **2**. The relative experimental intensities are given with respect to the fitted area of the peaks and were normalized to the strongest transition. Band positions and intensities of overtones and combination bands are based on the anharmonic force field calculations. Possible superimposing modes are indicated by braces. The signals at 1449 cm^{-1} and 1463 cm^{-1} cannot be clearly assigned to one specific combination band. Therefore, the corresponding assignments are parenthesized. *Due to experimental constraints, no relative experimental intensity can be determined for ν_{35} and ν_{36}. The appearance of the signal(s) presented in Figure 18 is perhaps related to rotational fine structure. This assumption is hampered by the insufficient quality of the recorded data.[166-168]

Vibrational Mode #	Obs. ν_{vib} [cm^{-1}]	Int. [%] Vol.	Calc. ν_{vib} [cm^{-1}]	Int. [km/mol]
ν_9	627	34	625	22
ν_8	661	90	607	162
ν_{10}	788	39	783	45
ν_{12}	806	4	804	0.2
ν_{13}	916	9	918	6
ν_{15}	997	12	981	9
ν_{4+9}	1072	1	1074	1
ν_{4+8}			1083	1
ν_{19}	1111	15	1099	11
ν_{20}	1164	1	1153	0.3
ν_{4+10}	1237	8	1232	0.3
ν_{4+11}			1237	1
ν_{9^2}	1285	4	1262	0.1
ν_{8+9}			1274	2

				1283	0.5
ν_{2+13}				1283	0.5
ν_{8^2}	1330	62		1308	50
ν_{22}	1346	10		1335	3
ν_{23}	1362	18		1343	8
ν_{24}	1383	1		1360	1
ν_{25}	1439	6		1433	5
(ν_{4+18})	1449	6		1438	6
(ν_{4+18})	1463	9			
ν_{26}	1493	94		1474	74
ν_{27}	1523	24		1506	13
ν_{28}	1593	41		1582	25
ν_{29}	1650	100		1624	110
$\nu_{35}{}^{*}$	3390	-		3424	252
$\nu_{36}{}^{*}$	3484	-		3533	92

Table 4

Mode descriptions of the calculated vibrational modes of the aromatic aniline$^{•+}$ **2** (first row of each vibrational mode ν_i) and the imine$^{•+}$ **4** (second row of each vibrational mode ν_i) structure.

Mode #	Mode description	calc. ν_{vib} [cm^{-1}]
ν_1	out-of-plane, N-H$_2$ wagg., ring wagg. def.	180
	out-of-plane, N-H wagg., H$_2$ rock., ring wagg. def.	109
ν_2	out-of-plane, H$_2$ twist., ring twist.	359
	out-of-plane, H$_2$ wagg., ring twist.	194
ν_3	in-plane, C-N rock.	379
	out-of-plane, ring twist., H$_2$ rock.	394
ν_4	out-of-plane, ring twist., N-H$_2$ twist.	441
	in-plane, N-H rock., ring twist.	405
ν_5	in-plane, ring bend. def.	518
	out-of-plane, H$_2$ rock., ring twist.	447
ν_6	out-of-plane, H$_2$ twist.	556
	in-plane, ring bend. def.	492
ν_7	in-plane, ring bend. def.	579
	in-plane, ring bend. def.	570
ν_8	out-of-plane, N-H$_2$ wagg., H and ring wagg.	607
	out-of-plane, N-H wagg., H$_2$ rock., H wagg.	595
ν_9	out-of-plane, C-H wagg.	625
	out-of-plane, N-H wagg., C-H wagg., H$_2$ twist.	731
ν_{10}	out-of-plane, C-H wagg., C-N wagg.	783
	in-plane, C-C sym. Stretch, ring bend. def.	753
ν_{11}	out-of-plane, C-H wagg.	792
	out-of-plane, H$_2$ rock., ring and H twist.	780
ν_{12}	in-plane, ring. sym. stretch., ring bend. def., C-N stretch.	804
	out-of-plane, H$_2$ rock., ring and H twist./wagg.	908
ν_{13}	out-of-plane, C-H twist./wagg.	918
	in-plane, ring sym. stretch., ring bend.	923

ν_{14}	in-plane, ring bend. def., ring sym. stretch., C-N stretch.	969
	in-plane, H_2 wagg., ring stretch.	948
ν_{15}	in-plane, ring sym. stretch., ring bend.	981
	out-of-plane, C-H rock., H_2 wagg.	986
ν_{16}	out-of-plane, C-H twist.	986
	in-plane, ring stretch., C-H bend., N-H bend.	1010
ν_{17}	in-plane, N-H_2 rock.	999
	out-of-plane, C-H twist., ring twist., N-H twist.	1024
ν_{18}	out-of-plane, C-H twist., ring twist.	1003
	in-plane, N-H rock., ring stretch., C-H bend.	1107
ν_{19}	in-plane, ring asym. stretch., C-H rock./twist.	1099
	out-of-plane, H_2 twist., ring and C-H twist.	1129
ν_{20}	in-plane, C-H bend., asym. ring stretch.	1153
	in-plane, C-H bend., N-H bend., H_2 wagg.	1140
ν_{21}	in-plane, C-H bend., ring stretch.	1176
	in-plane, C-H bend., N-H bend., H_2 wagg.	1174
ν_{22}	in-plane, asym. ring stretch., C-H rock.	1335
	in-plane, H_2 bend., ring stretch.	1276
ν_{23}	in-plane, asym. ring stretch., C-H bend., H_2 rock.	1343
	in-plane, H_2 wagg., ring stretch., N-H rock.	1301
ν_{24}	in-plane, C-N stretch., ring stretch., C-H rock., H_2 bend.	1360
	in-plane, N-H stretch., ring stretch., C-H and N-H rock.	1311
ν_{25}	in-plane, ring stretch., C-H rock., H_2 rock.	1433
	in-plane, ring stretch., C-H rock., N-H rock.	1397
ν_{26}	in-plane, ring stretch., C-N stretch., C-H bend., H_2 bend.	1474
	in-plane, ring stretch., C-N stretch., C-H rock.	1418
ν_{27}	in-plane, ring asym. stretch., C-H bend.	1506
	in-plane, ring stretch., C-N stretch., C-H rock.	1456
ν_{28}	in-plane, ring sym. stretch., H_2 bend., C-H bend.	1582
	in-plane, ring asym. stretch., C-H rock.	1499
ν_{29}	in-plane, H_2 bend., C-N stretch., ring stretch.	1624
	in-plane, ring stretch., C-H rock.	1529
ν_{30}	in-plane, C-H stretch.	3089
	in-plane, H_2 stretch.	2881
ν_{31}	in-plane, C-H stretch.	3090
	out-of-plane, H_2 rock.	2882
ν_{32}	in-plane, C-H stretch.	3100
	in-plane, C-H stretch.	3082
ν_{33}	in-plane, C-H stretch.	3110
	in-plane, C-H stretch.	3086
ν_{34}	in-plane, C-H stretch.	3115
	in-plane, C-H stretch.	3094
ν_{35}	in-plane, N-H_2 sym.-stretch.	3424
	in-plane, C-H stretch.	3108
ν_{36}	in-plane, N-H_2 asym.-stretch.	3533
	in-plane, N-H stretch, C-N rock.	3335
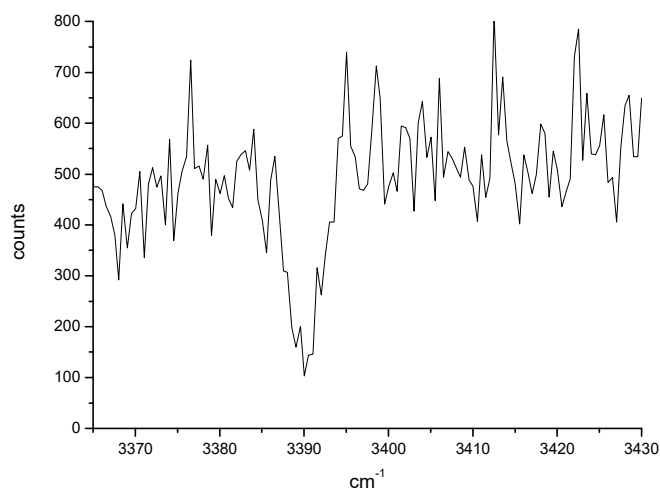
Figure 18
Cryogenic messenger IR spectra of the cooled, Ne-tagged aniline radical cation $[C_6H_7N \bullet Ne]^{\bullet+}$ at *m/z* 113. This spectral region was measured with an OPO/OPA tabletop system (Laservision) in the region of the vibrational transition ν_{35} of structure **2**.
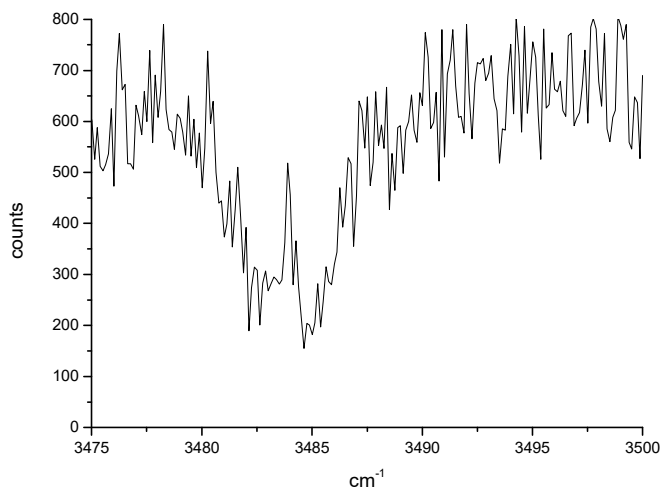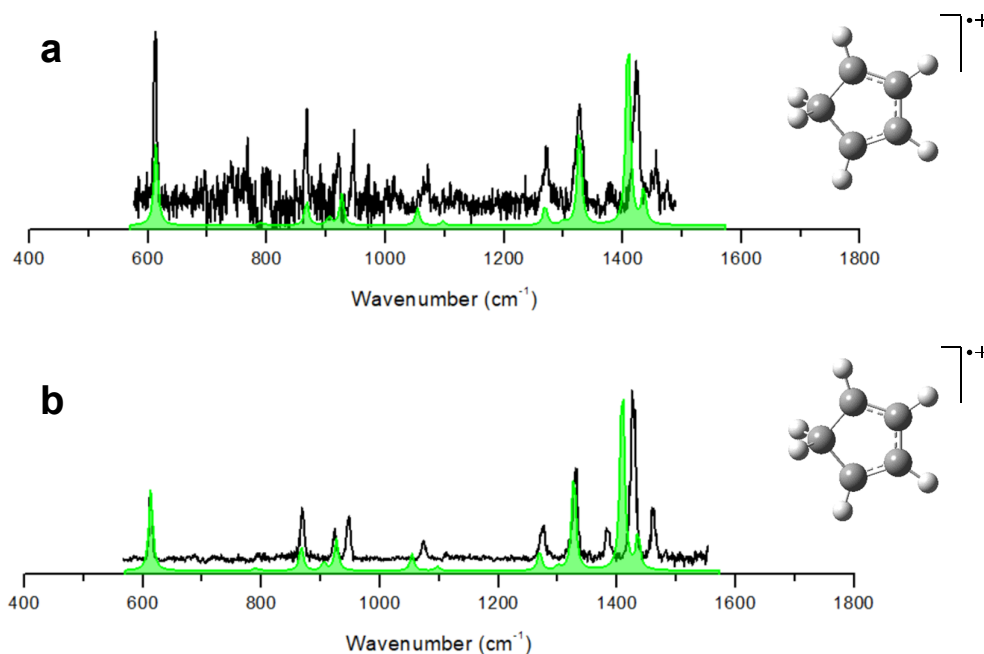

Figure 19
Cryogenic messenger IR spectra of the cooled, Ne-tagged aniline radical cation $[C_6H_7N \bullet Ne]^{\bullet+}$ at *m/z* 113. This spectral region was measured with an OPO/OPA tabletop system (Laservision) in the region of the vibrational transition ν_{36} of structure **2**.
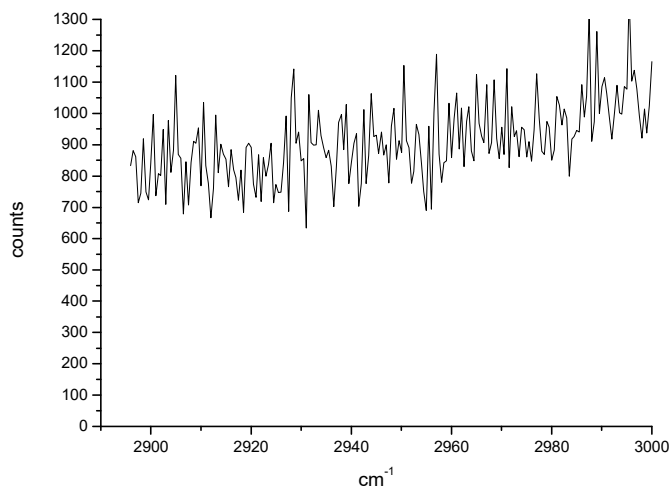
Figure 20
IR-PD spectra of the cooled, Ne-tagged aniline radical cation $[C_6H_7N \cdot Ne]^{\bullet+}$ at *m/z* 113. This spectral region was measured with an OPO/OPA tabletop system (Laservision) in the region of possible vibrational transitions v_{30}, v_{31}, v_{32}, v_{33}, v_{34} and v_{35} of structure **4**.

Cyclopentadiene.

Figure 21a and b are showing the experimental spectra of the Ne-tagged fragment ion at *m/z* 86 $[C_5H_6 \cdot Ne]^{\bullet+}$ found in the EI-MS mass spectra of molecular ions of phenol **1** and aniline **2**, respectively. These Ne-tagged ions refer to the product ion **5** at *m/z* 66, which is cyclopentadiene in the MS spectra of phenol and aniline, as shown with convincing agreement in the literature.[165, 170] Table 5 and

Table *6* are showing the assigned experimental vibrational modes as possible. There is a very good overall match of the calculated spectrum in both cases, clearly indicating the presence of the cyclopentadiene radical cation $[C_5H_6]^{\bullet+}$. Furthermore, the depletion saturation scan at 1427 cm^{-1} of Ne-tagged cyclopentadiene radical cation $[C_5H_6 \cdot Ne]^{\bullet+}$ at *m/z* 86 (see Figure 24) indicated the presence of only on isomer, which is ion structure **5**. The ion intensity with (blue) and without (orange) laser depletion is fitted as a function of the deposited energy.

Figure 21
a) IR-PD spectrum (black) of the cooled, Ne-tagged cation $[C_5H_6 \bullet Ne]^{\bullet +}$ at *m/z* 86 from phenol formed by EI-MS compared to the IR spectrum (green) calculated for the $[C_5H_6]^{\bullet +}$ ion, shown in the inset. **b)** IR-PD spectrum (black) of the cooled, Ne-tagged cation $[C_5H_6 \bullet Ne]^{\bullet +}$ at *m/z* 86 from aniline formed by EI-MS compared to the IR spectrum (green) calculated for the $[C_5H_6]^{\bullet +}$ ion.

Table 5
Absorption band assignment of the observed vibrational frequencies of the cyclopentadiene radical cation **5**. The relative experimental intensities are given with respect to the fitted area of the peaks and were normalized to the strongest transition. Possible superimposing modes are indicated by braces. The mode marked with a question mark could not be identified.

| Vibrational Mode #	Obs. ν_{vib} [cm^{-1}]	Int. [%] Vol.	Calc. ν_{vib} [cm^{-1}]	Int. [km/mol]
ν_3	613	24	613	54
ν_5	794	1	789	2
ν_6			798	0.6
ν_7	869	22	867	17
ν_8	924	13	905	6
ν_9	947	20	926	21
ν_{12}	1074	9	1054	12
ν_{14}	1112	2	1097	3
ν_{16}	1274	22	1269	14
ν_{18}	1329	55	1327	69
?	1384	17		
ν_{19}	1427	100	1409	136
ν_{21}	1461	26	1436	24

Table 6

Mode descriptions of the calculated vibrational modes, harmonic calculated and scaled harmonic calculated frequencies of the cyclopentadiene[•+] **6** structure.

Mode #	Mode description	calc. ν_{vib} [cm^{-1}]
ν_1	out-of-plane, H$_2$ rock., ring twist.	270
ν_2	out-of-plane, ring twist.	417
ν_3	out-of-plane, C-H wagg., H$_2$ rock.	613
ν_4	out-of-plane, H$_2$ twist., C-H twist.	781
ν_5	in-plane, ring bend.	789
ν_6	in-plane, ring bend.	798
ν_7	out-of-plane, H$_2$ rock., C-H wagg.	867
ν_8	in-plane, asym. ring stretch., H$_2$ wagg.	905
ν_9	in-plane, sym. ring stretch., C-H bend.	926
ν_{10}	out-of-plane, H$_2$ rock., ring twist.	969
ν_{11}	out-of-plane, C-H twist., ring twist., H$_2$ twist.	997
ν_{12}	in-plane, C-H bend./rock., ring stretch.	1054
ν_{13}	in-plane, ring stretch., C-H bend.	1077
ν_{14}	in-plane, C-H bend., ring stretch.	1097
ν_{15}	out-of-plane, C-H$_2$ twist.	1117
ν_{16}	in-plane, H$_2$ wagg., C-H bend., ring stretch.	1269
ν_{17}	in-plane, asym. ring stretch., H$_2$ wagg., C-H bend.	1300
ν_{18}	out-of-plane, H$_2$ bend., ring stretch.	1327
ν_{19}	in-plane, asym. ring stretch., C-H bend., H$_2$ wagg.	1409
ν_{20}	out-of-plane, sym. ring stretch., C-H bend., H$_2$ bend.	1413
ν_{21}	out-of-plane, sym. ring stretch., C-H bend., H$_2$ bend.	1436
ν_{22}	out-of-plane, sym. C-H$_2$ stretch.	2922
ν_{23}	out-of-plane, H$_2$ rock.	2938
ν_{24}	in-plane, C-H stretch.	3115
ν_{25}	in-plane, C-H stretch.	3120
ν_{26}	in-plane, C-H stretch.	3128
ν_{27}	in-plane, sym. C-H stretch.	3137
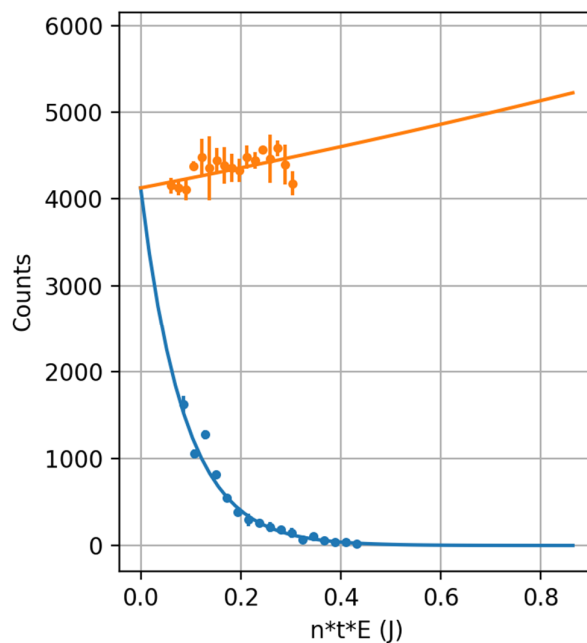
Figure 22

Depletion scan at 1479 cm^{-1} of Ne-tagged phenol radical cation **[C$_6$H$_6$O•Ne]$^{•+}$** at *m/z* 114. At 1479 cm^{-1} only phenol tautomer ion structure **1** absorbs photons (v_{25}). An EI electron energy of 20 eV was used to produce the ions. The ion intensity with (blue) and without (orange) laser depletion is fitted as a function of the deposited energy. The fit indicates that only tautomer **1** is formed and present as the fit of the ion counts converges to 0. The increase of the counts in the off measurement (orange) for higher deposited energies is due to time-dependent changes of the source parameters during the different measurements.
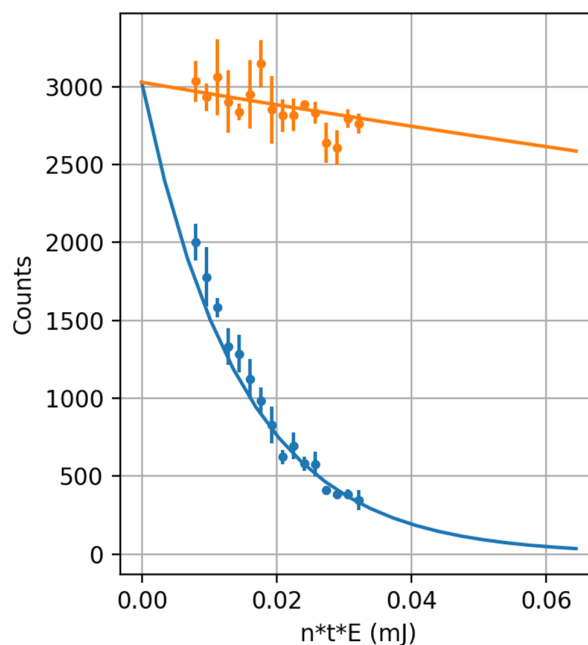
Figure 23

Depletion scan at 3390 cm^{-1} of Ne-tagged aniline radical cation **[C$_6$H$_7$N•Ne]$^{•+}$** at *m/z* 113. At 3390 cm^{-1} only aniline tautomer ion structure **2** absorbs photons (v_{35}). An EI electron energy of 10 eV was used to produce the ions. The ion intensity with (blue) and without (orange) laser depletion is fitted as a function of the deposited energy. The fit indicates that only tautomer **2** is formed.
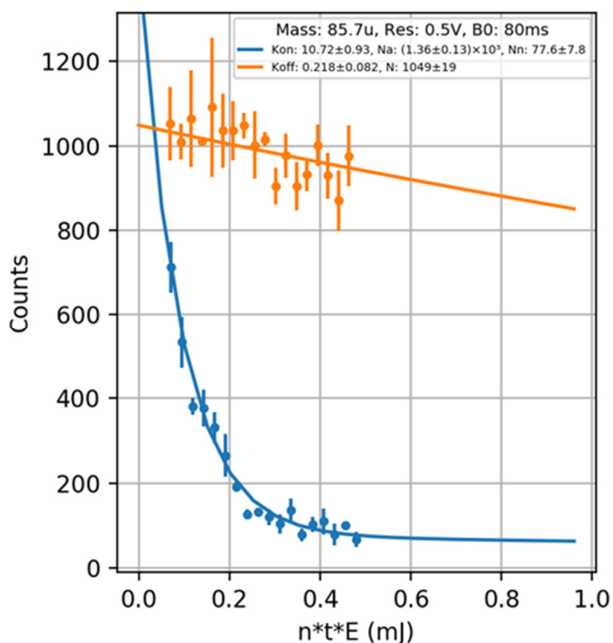
Figure 24

Depletion scan at 1427 cm^{-1} of Ne-tagged cyclopentadiene radical cation $[\mathbf{C_5H_6 \cdot Ne}]^{\bullet+}$ at *m/z* 86. At 1427 cm^{-1} ion structure **5** absorbs photons (ν_{19}). An EI electron energy of 20 eV was used to produce the ions. The ion intensity with (blue) and without (orange) laser depletion is fitted as a function of the deposited energy.

3.1.4 Conclusions on the Aniline and Phenol Study

We were able to record gas-phase IR spectra of the molecular radical cations of phenol as well as aniline, which completes the data set of these ions in the literature. In EI-MS phenol and aniline are forming stable molecular ions **1** and **3**. These were successfully identified in this study via modern cryogenic messenger ion spectroscopy with the FELion device. The tautomeric intermediates of both, which are ions **2** and **4**, have been reported in the literature to be important but reactive intermediates. Unfortunately, in our study we were not able to find evidence of the presence of those likely very short-lived intermediates on the pathway of the fragmentation towards the common fragment ion at *m/z* 66. This fact might reflect the reactivity of these intermediates, which means they decompose too quickly to be measured even at cryogenic temperatures. However, we were able to identify the common ion *m/z* 66 to be indeed the proposed structure cyclopentadiene **5** in both cases. The extensive theoretical calculations confirmed the unimolecular fragmentation pathway of the radical cations of phenol and aniline in EI-MS.

3.2 Unidirectional Double and Triple Hydrogen Rearrangement Reactions Probed by Infrared Ion Spectroscopy

3.2.1 EI- and ESI-MS Experiments

As discussed in Chapter 2.2, Kuck and Filges discovered a rare triple hydrogen rearrangement in EI-MS, as well as a double hydrogen rearrangement. These rearrangement reactions occurred upon fragmentation of the radical cations of electron-rich 3-arylpropanols [M]$^{\bullet+}$ in Scheme 5) and were especially pronounced in *trans*-2-(4-*N*,*N*-dimethylaminobenzyl)-1-indanol **12**, *trans*-2-(4-methoxybenzyl)-1-indanol **13**, two analytes also included in this study. They are shown in Scheme 7, alongside other derivatives we have tested in our newer study, which namely are 4-(4-*N*,*N*-dimethylaminophenyl)-2-butanol **14**, 3-(4-*N*,*N*-dimethylaminophenyl)-1-propanol **15** and 1-(4-*N*,*N*-dimethylaminophenyl)-5-(4-methoxyphenyl)-3-pentanol **16**.
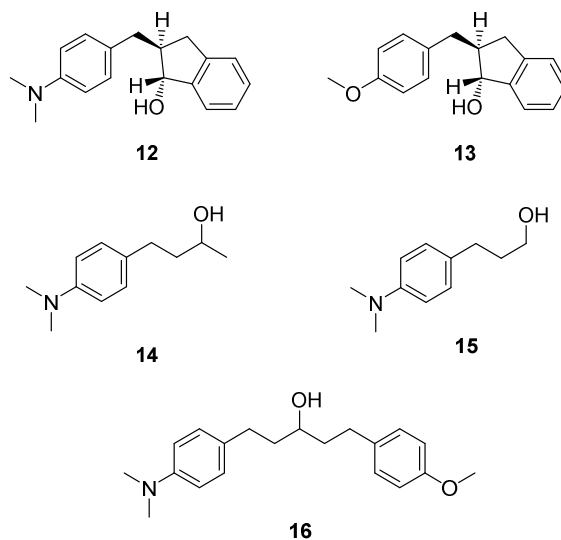
Scheme 7
Model compounds **12**–**16**. of this investigation: *trans*-2-(4-*N*,*N*-dimethylaminobenzyl)-1-indanol **12**, *trans*-2-(4-methoxybenzyl)-1-indanol **13**, 4-(4-*N*,*N*-dimethylaminophenyl)-2-butanol **14**, 3-(4-*N*,*N*-dimethylaminophenyl)-1-propanol **15** and 1-(4-*N*,*N*-dimethylaminophenyl)-5-(4-methoxyphenyl)-3-pentanol **16**.

Although Kuck and Filges based their proposed mechanism on experimental evidence and profound theoretical considerations, they also point out that the mechanism still needs further experimental and computational verification as already discussed in Chapter 2.2. This motivated us to clarify these intriguing reaction pathways with the help of modern quantum chemical DFT computations as well as IRMPD ion spectroscopy to characterize the structures involved and investigate the reaction mechanisms of both reactions.

First of all, we started with EI experiments in order to see if we can easily replicate the older results from Kuck *et al.*[3, 153] with the analytes **12** and **13**. We further tested the other new derivatives **14**, **15** and **16** (see Scheme 7). Figure 25 to Figure 31 are showing the resulting spectra on our regular EI and GC-MS systems (see Chapter 6.2 for technical details). In general, we were able to reproduce the results from the older study, Figure 25 and Figure 26 are showing the MS spectra for analyte **12**; in both, the EI and the GC-MS spectrum we observe the molecular ion at *m/z* 267 as well as the two fragments of interest at *m/z* 123 for the 3H rearrangement and at *m/z* 136 for the 2H rearrangement reactions. Additionally, we find a prominent fragment, the base peak in all spectra, at *m/z* 134, which is supposedly a specific product ion resulting from benzylic cleavage: p-Me$_2$NC$_6$H$_4$CH$_2^+$. Furthermore, analyte **13** exhibits similar behavior as shown in Figure 27 and Figure 28, where the intact molecular ion is found at *m/z* 254, as well as the 2H and 3H rearrangement fragments. In this case, those are found at *m/z* 123 and *m/z* 110, in accordance with the older results from Kuck *et al.*.[3]

The spectrum of 4-(4-*N*,*N*-dimethylaminophenyl)-2-butanol **14** (see Figure 27) also exhibits the intact molecular ion at *m/z* 193 as well as the 3H fragment at *m/z* 123, although the latter is much lower in relative intensity compared to analytes **12** and **13**. The 2H rearrangement product ion is not clearly observable here. This also was the case in the MIKE spectra in the older study.[3]

Interestingly, the 2H and 3H rearrangement products are completely absent in the spectrum of analyte **15** (see Figure 30) and in the spectrum of **16.** In both spectra only a peak of the 3H rearrangement product is visible, albeit, in low abundance (see Figure 31).
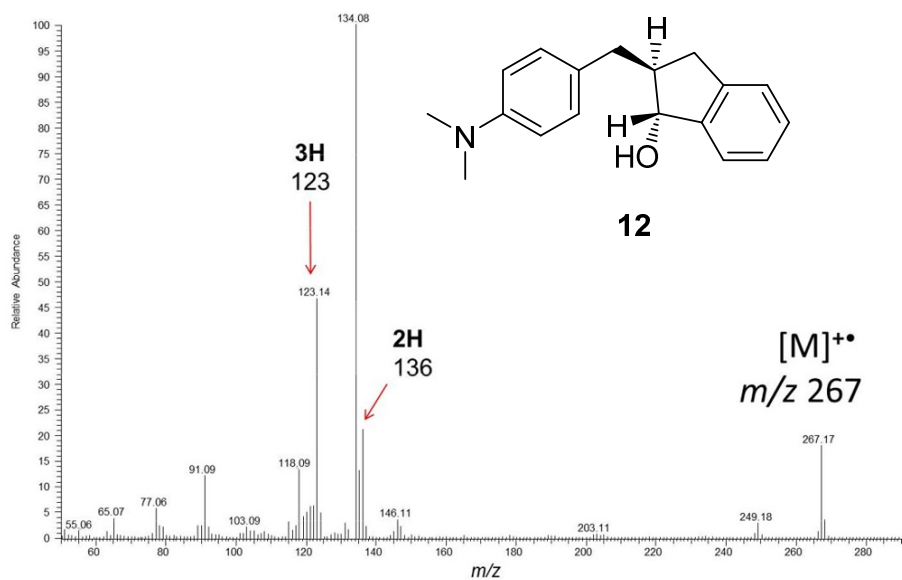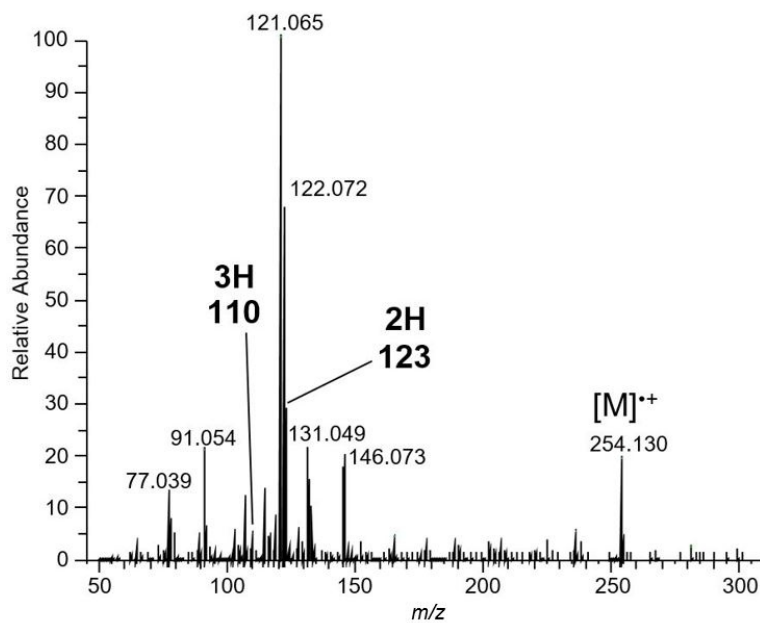
Figure 25
EI mass spectrum of analyte **12** introduced via a heated direct inlet probe (DIP, spectrum acquired at ca. 150 °C) under conventional EI-MS conditions (Thermo Fisher ISQ, ion source conditions: electron energy 70 eV, source temperature 250 °C, source pressure ~ 70 mTorr).
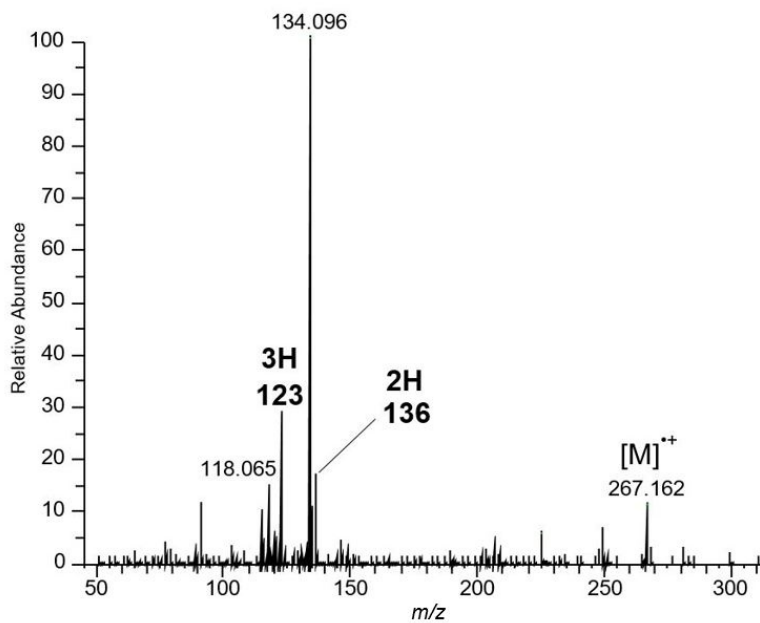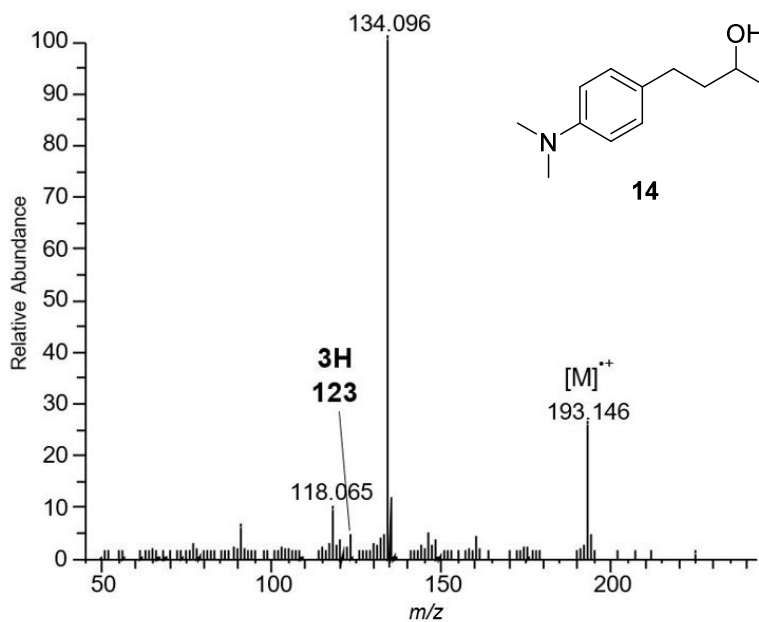

Figure 26
GC-EI mass spectrum of analyte **12** (GC Exactive Orbitrap, ion source conditions: electron energy 70 eV, source temperature 50–270 °C).
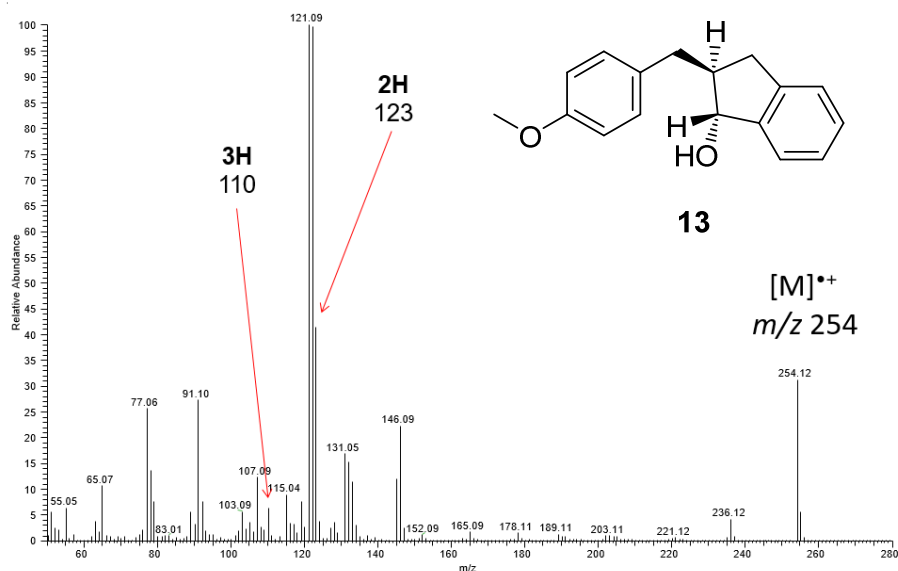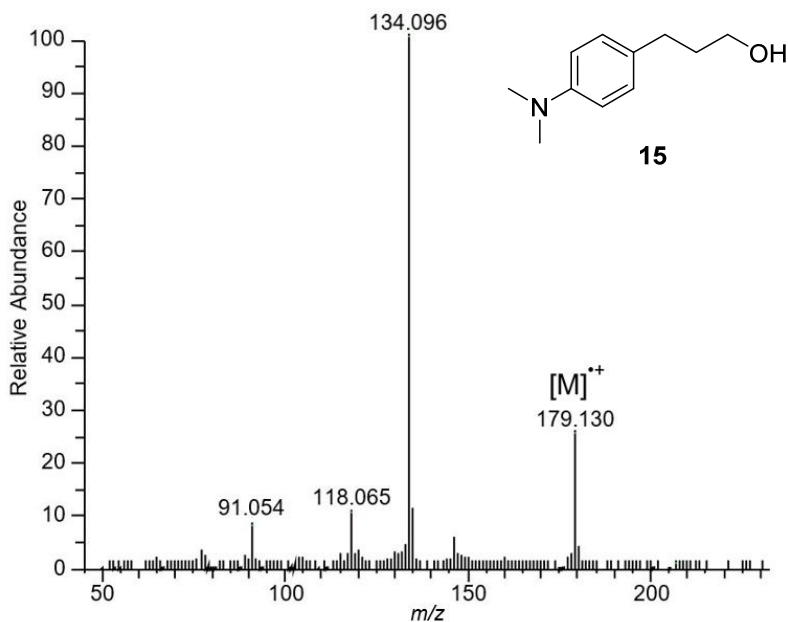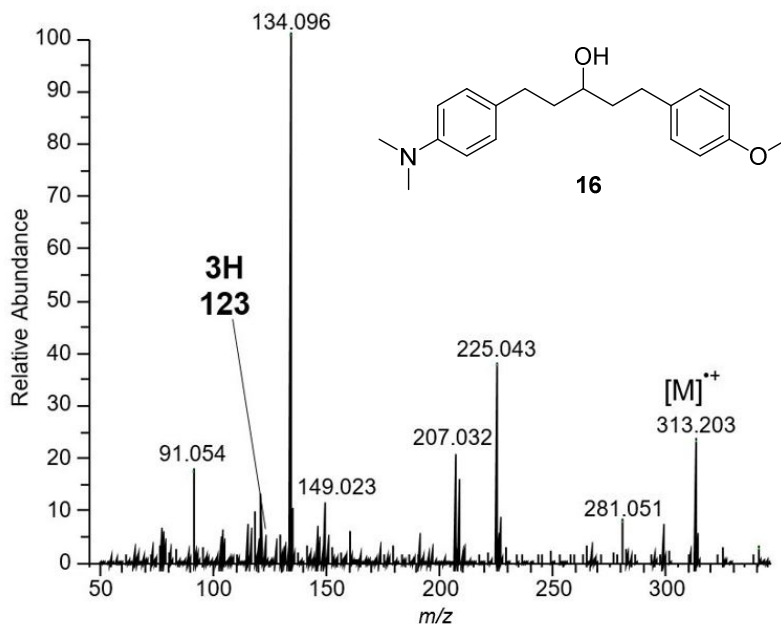
Figure 27
EI mass spectrum of analyte **13** introduced via a heated direct inlet probe (DIP, spectrum acquired at ca. 150 °C) under conventional EI-MS conditions (Thermo Fisher ISQ, ion source conditions: electron energy 70 eV, source temperature 250 °C, source pressure ~ 70 mTorr).

Figure 28
GC-EI mass spectrum of analyte **13** (GC Exactive Orbitrap, ion source conditions: electron energy 70 eV, source temperature 50–270 °C).

Figure 29
GC-EI mass spectrum of analyte **14** (GC Exactive Orbitrap, ion source conditions: electron energy 70 eV, source temperature 50–270 °C).

Figure 30
GC-EI mass spectrum of analyte **15** (GC Exactive Orbitrap, on source conditions: electron energy 70 eV, source temperature 50–270 °C).

Figure 31
GC-EI mass spectrum of analyte **16** (GC Exactive Orbitrap, ion source conditions: electron energy 70 eV, source temperature 50–270 °C).

The main problem with the low volatility compounds **14**, **15** and especially **12**, **13** and **16** were the measurements at the FELIX Laboratory with the FELion cryogenic ion trap device. It was not possible to vaporize the analytes in sufficient amount for enough ion counts in order to measure a reasonable cryogenic messenger IR spectrum. We therefore tried to investigate the compounds on an ESI-MS device, based on the fact that tertiary aromatic amines are able form molecular radical cations from anhydrous aprotic solutions, such dry acetonitrile.[158] This is due to the fact that the ESI source can be seen as an electrolytic cell, where redox processes can occur, especially at high voltages.[171] To form open shell radical cationic molecular ions via ESI oxidation, a high positive voltage is needed and the oxidation potential of the analyte needs to be low enough. Furthermore, it is advantageous if the analyte possesses the ability to stabilize unpaired electrons and if the solvent can further stabilize such species.

We found in our experiments that some of the analytes indeed form radical cations in ESI-MS in sufficient abundance, namely analyte **12**, **14**, and **16**, reflecting the importance of the tertial amines in the formation of radical cationic molecular ions in ESI-MS with dry acetonitrile. The respective spectra are shown in Figure 32 to Figure 36.

The ESI mass spectrum of **12** (Figure 32) exhibits the molecular ion **12**$^{•+}$ at *m/z* 267 as the base peak next to the **[12+H]**$^+$ species at *m/z* 268. The CID activated MS^2 spectrum of analyte **12**

(see Figure 34) shows the molecular ion $\mathbf{12}^{\bullet+}$ at m/z 267 also as base peak. We can observe the 3H and 2H rearrangement product ions in 40 % and 20 % relative abundance at m/z 123 and m/z 136, respectively. The benzylic cleavage product at m/z 134 is strongly suppressed and lower in abundance than the 2H and 3H rearrangement fragments compared to the EI-MS results. We further can observe that the loss of a water neutral molecule at m/z 249 is much more pronounced compared to EI ionization.

The ESI mass spectrum of $\mathbf{14}$ (Figure 33) also exhibits the molecular ion $\mathbf{14}^{\bullet+}$ at m/z 193 as the base peak next to the $[\mathbf{12+H}]^+$ species at m/z 194. Interestingly, in the CID activated MS^2 spectrum of analyte $\mathbf{14}$ the benzylic cleavage product m/z 134 is the base peak, and we can even see the 2H rearrangement in very low abundance here as well as the 3H product ions with about 35% abundance. The loss of water is also visible in this case at m/z 175.

Finally, we tested analyte $\mathbf{16}$ in ESI-MS^2 experiments upon CID (see Figure 36). We find similar results as for analyte $\mathbf{14}$, both, the 2H and 3H fragments are visible in good abundance, the benzylic cleavage fragment is the base peak, and we can also observe the loss of water here. There is no peak at m/z 110 and furthermore the product ion at m/z 123 is exclusively due to the 3H product ion $C_8H_{13}N^{\bullet+}$ (found: m/z 123.1042, calculated: m/z 123.1043, $\Delta m = 0.4$ ppm), whereas the isobaric 2H product ion $C_8H_{11}O^+$ from the other moiety (calculated m/z 123.0804) is completely absent. The dominance of the 1-N,N-dimethylanilino-3-alkanol moiety in the intramolecular competition with the 1-methoxyphenyl-3-alkanol moiety can be attributed to the preferred localization of the positive charge in the electron rich aniline ring.

Since the fragmentation patterns are the same as in EI-MS and the accurate ion mass determinations in Table 7 are showing the correct masses for the product ion molecular formulas, $C_8H_{13}N^{\bullet+}$ (m/z 123), $C_9H_{12}N^+$ (m/z 134) and $C_9H_{14}N^+$ (m/z 136), derived from analyte $\mathbf{12}$ and $\mathbf{14}$, respectively. we can assume that we are observing the same rearrangement reactions as in the EI-MS experiments reported above. The accurate ion mass determinations of the molecular ions are given in Table 8 and Table 9.

These results enabled us to not only rely on cryogenic messenger ion spectroscopy on the FELion device with EI-MS, but also utilize a more established regular user station at the FELIX Laboratory with an Amazon Bruker ESI-MS device coupled with IRMPD ion spectroscopy.
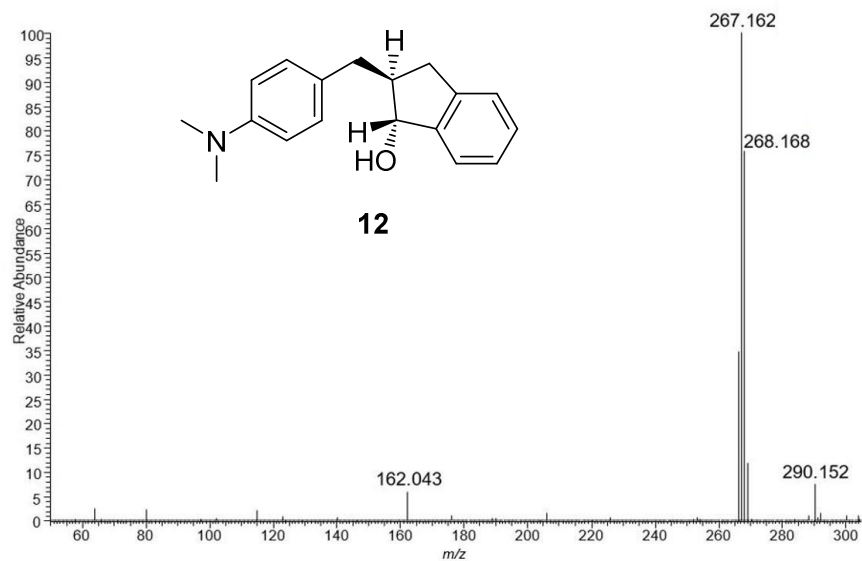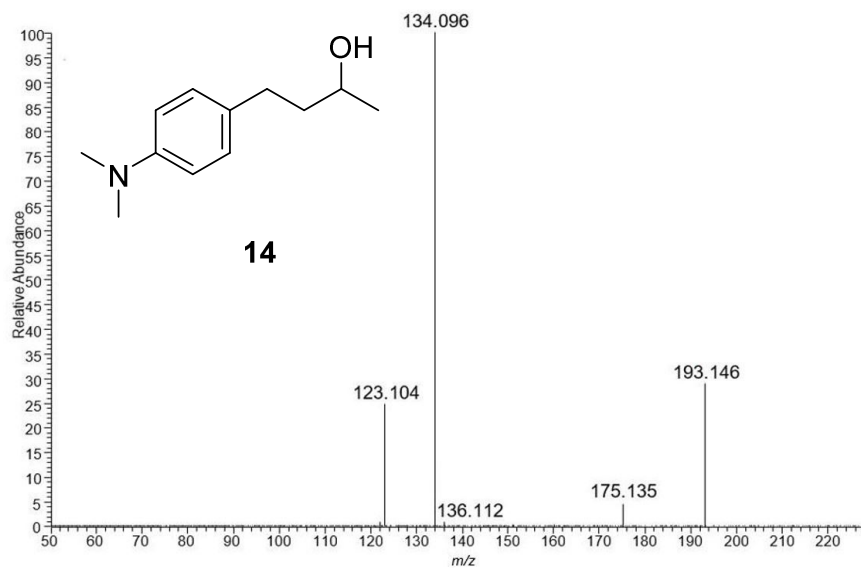
Figure 32
ESI mass spectrum of *trans*-2-(4-*N*,*N*-dimethylaminobenzyl)-1-indanol **12** from anhydrous acetonitrile. The molecular radical cation **12**·⁺ appears at *m/z* 267, the sodium adduct [**12**+Na]⁺ is observed at *m/z* 290, and part of the signal at *m/z* 268 is due to the protonated species [**12**+H]⁺.
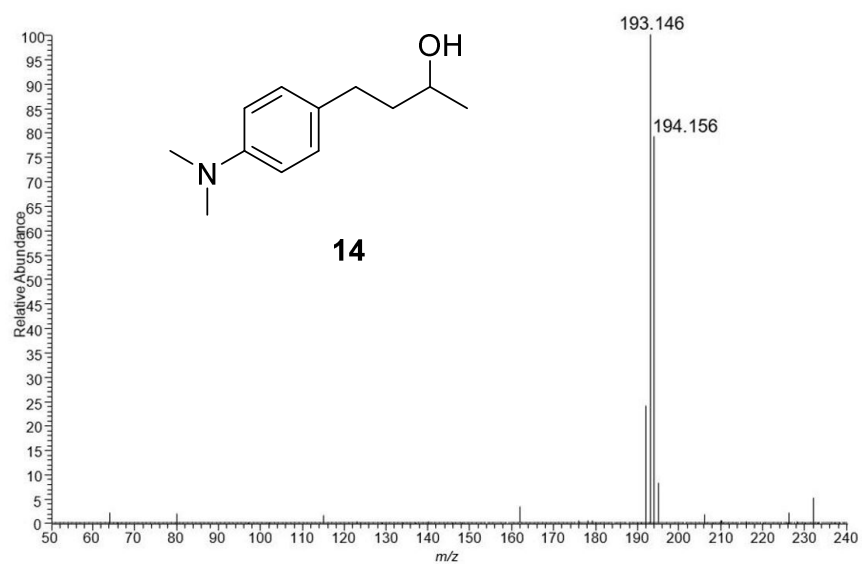
Figure 33
ESI mass spectrum of 4-(4-*N*,*N*-dimethylaminophenyl)-2-butanol **14** from anhydrous acetonitrile. The molecular radical cation **14**·⁺ appears at *m/z* 193 and part of the signal at *m/z* 194 is due to the protonated species [**14**+H]⁺.
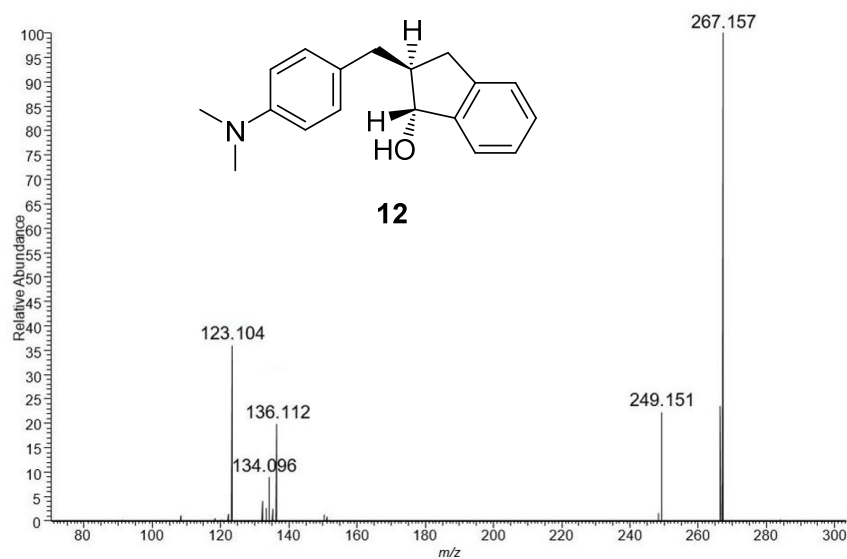
Figure 34
ESI-MS^2 CID spectrum of the molecular ion **12**$^{•+}$ (*m/z* 267). The peaks at *m/z* 123 and *m/z* 136, respectively, indicate the formation of the 2H and 3H rearrangement product ions. The peak at *m/z* 249 is due to the loss of water.

Figure 35
ESI-MS^2 CID spectrum of the molecular ion **14**$^{•+}$ (*m/z* 193). The peaks at *m/z* 123 and *m/z* 136, respectively, indicate the formation of the 2H and 3H rearrangement product ions. The peak at *m/z* 175 is due to the loss of water.
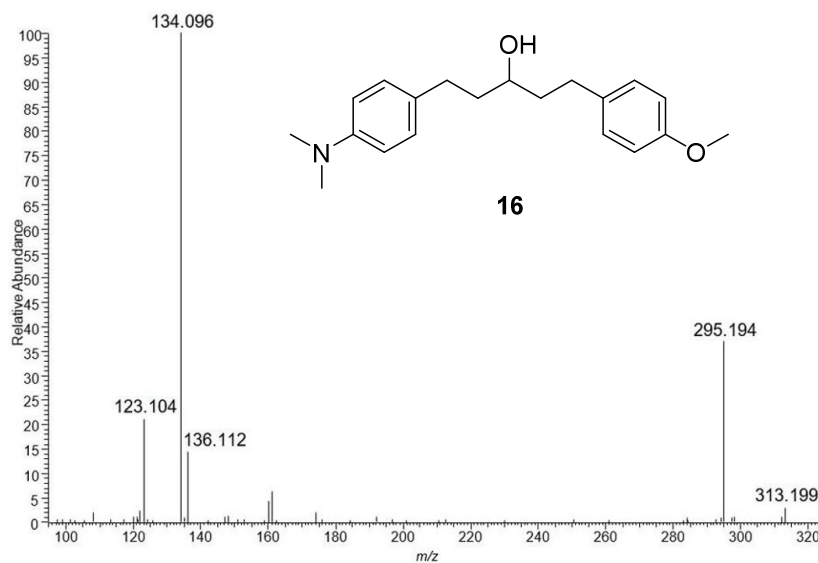
Figure 36
ESI-MS^2 CID spectrum of the molecular ion **16**$^{•+}$ (*m/z* 313). The peaks at *m/z* 123 and *m/z* 136, respectively, indicate the formation of the 2H and 3H rearrangement product ions originating exclusively from the (dimethylanilino)propanol moiety. The peak at *m/z* 295 is due to the loss of water.

Table 7
Accurate ion mass determination of the ESI-MS^2 product ions measured on the LTQ Orbitrap XL instrument. R: 30000 FWHM.

Product ion *m/z*	Calculated fragment ion mass [u]	Observed mass [u]	Error Δ [ppm]
123 (from **1**, $C_8H_{13}N^+$)	123.1043	123.1044	3.25
123 (from **3**, $C_8H_{13}N^+$)	123.1043	123.1043	4.06
136 (from **1**, $C_9H_{14}N^+$)	136.1126	136.1122	2.94
136 (from **3**, $C_9H_{14}N^+$)	136.1126	136.1123	2.20
134 (from **1**, $C_9H_{12}N^+$)	134.0964	134.0961	2.24
134 (from **3**, $C_9H_{12}N^+$)	134.0964	134.0963	0.75

Table 8
Accurate ion mass determination of the analytes on the GC-Exactive Orbitrap Instrument.

Analyte	Calculated ion mass [u]	Observed ion mass [u]	Error Δ [ppm]
1 ($C_{18}H_{21}NO$)	267.1623	267.1621	0.75
2 ($C_{17}H_{18}O_2$)	254.1307	254.1303	1.57
3 ($C_{12}H_{19}NO$)	193.1467	193.1462	2.38
4 ($C_{11}H_{17}NO$)	179.1310	179.1304	3.41
5 ($C_{20}H_{27}NO_2$)	313.2042	313.2033	2.81

Table 9
ESI-MS accurate ion mass determination of the molecular ions of the analytes **1**−**5** measured on the LTQ Orbitrap XL. R: 100000 FWHM.

| Analyte	Calculated ion mass [u]	Observed ion mass [u]	Error Δ [ppm]
1 ($C_{18}H_{21}NO$)	267.1623	267.1621	0.75
2 ($C_{17}H_{18}O_2$)	254.1307	254.1302	1.97
3 ($C_{12}H_{19}NO$)	193.1467	193.1464	1.35
4 ($C_{11}H_{17}NO$)	179.1310	179.1309	0.61
5 ($C_{20}H_{27}NO_2$)	313.2042	313.2038	1.21

3.2.2 Computations and Ion Spectroscopy

The following computations were executed by Marcel Bast and Sven Thorwirth from the Department of Physics at the University of Cologne.

Computations.

In the earlier work of Kuck *et al.* it was proposed that the 3H rearrangement product ion is supposed to be the distonic *N*-protonated *para*-isomer **a**, $C_8H_{13}N^{\bullet+}$ (see Scheme 8), based on theoretical considerations. One of the reasons was that its analogue, the distonic methyleneammonium radical cation ($^{\bullet}CH_2\text{-}NH_3^+$) is more stable than $CH_3\text{-}NH_2^{\bullet+}$.[172-175] In our new study we also included the other distonic ion structures **b** and **c**, which are resonance

stabilized in the ring system, as well as the conventional fully π-conjugated radical cations **d** and **e**, which are also shown in Scheme 8.
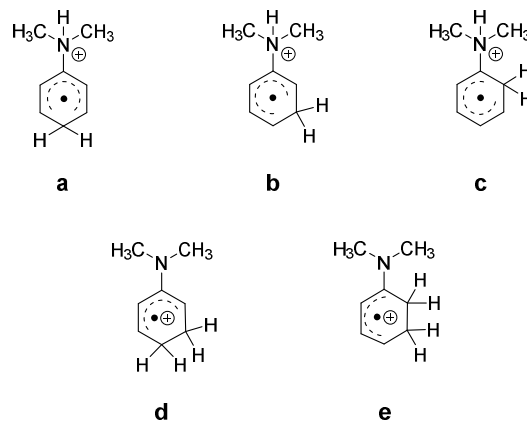
Scheme 8

Computationally investigated structures **a**–**e** considered as candidates for the product ions $C_8H_{13}N^{•+}$ (*m/z* 123) formed by unidirectional 3H rearrangement. Note that ions **a**-**c** are distonic ions, while ions **d** and **e** represent conventional radical cations.

In order to elucidate the ion structures of these isomers by theoretical calculations, we started with planar structures (C1-symmetry) and regular bond lengths and angles for the preoptimization with smaller basis sets such as cc-pVDZ. Relevant dihedral angles were scanned using Hartree-Fock (HF) as well as DFT methods in combination with the UB3LYP functional and cc-pVDZ/cc-pVTZ basis sets. Then, the most favorable structures were finally optimized using UB3LYP/cc-pVTZ level of theory. These structures are shown along with their relative energies in Figure 37. It is worth mentioning, that all five structures yielded the same symmetry group as well as orientations of the methyl groups with UHF/cc-pVDZ and UB3LYP calculations with the three basis sets cc-pVDZ, cc-pVTZ and cc-pVQZ. The most important result was that the originally proposed structure **a** was by far not the most stable on in this ion series. It lies almost 66 kJ/mol higher in energy than the lowest isomer **e**, the radical cation of 1-dimethylamino-1,3-cyclohexadiene. This is most likely due to the more effective delocalization of the charge and the unpaired electron in the conjugated part of the molecule. Another interesting finding is that isomer **d** lies energetically directly in between **a** and **e**, and is the second lowest in this series, which reflects the low ionization energies of enamines.[172, 176-178]
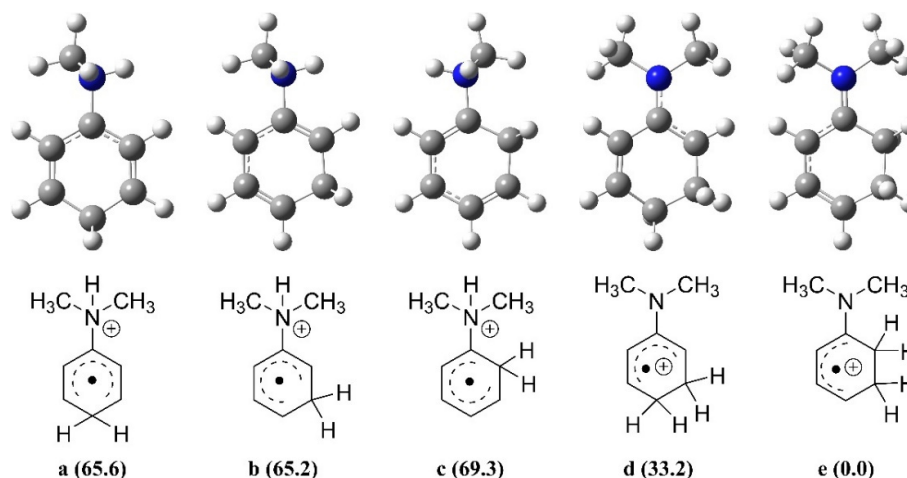
Figure 37

Minimum-energy ion structures for the 3H rearrangement product ions **a–e** ($C_8H_{13}N^{•+}$ *m/z* 123) and their relative energies (kJ/mol) with respect to structure **e**, determined by theoretical calculations (UB3LYP/cc-pVQZ). Note that ions **a-c** are distonic ions, while ions **d** and **e** represent conventional radical cations.

We also performed theoretical calculations and IRMPD spectroscopic measurements to elucidate the structure of the 2H rearrangement product ion $C_9H_{14}N^+$ (*m/z* 136). We used the same procedures and levels of theory for the theoretical calculations as we did for the 3H product ion above. The main difference here is that 2H rearrangement product ions represent closed-shell singlet cationic species compared to the open-shell radical cations from the 3H rearrangement. Next to the ring-protonated *para*-toluidinium ions **f-h**, we also considered the *N*-protonated equivalent **i**. Furthermore, we took a closer look at the ring-protonated *meta*- and *ortho*-toluidinium ions **j-m** and **o-p** as well es their respective *N*-protonated equivalents **n** and **r**. These structures are shown in Figure 38 along with their calculated relative energies. In the case of the 2H product ion it is obvious that the *N*-protonated aromatic isomers are the more stable ones (compared to the 3H product ions, where the ring-protonated isomers were most stable), namely isomer **i**, **n** and **r**. The isomer with the lowest energy is ion **i** (0 kJ/mol), closely followed by **n** (0.3 kJ/mol) and r (2.9 kJ/mol), with neglectable higher energies and **r** slightly higher due to steric clash of the adjacent methyl group. In general, the relative energies of all calculated structures reflect their electronic stabilization as well as steric destabilization. Another important result is that the most unfavorable ion structure are the ones with *meta*-protonation, ions **h** and **m**, due to the lack of resonance stabilization by the dimethylamino group. Further, the relative energies of the ion structures **f**, **g** and **h** are consistent with the local proton affinities of such substituted benzenium ions and the additivity rule for substituent effects.[179-181]
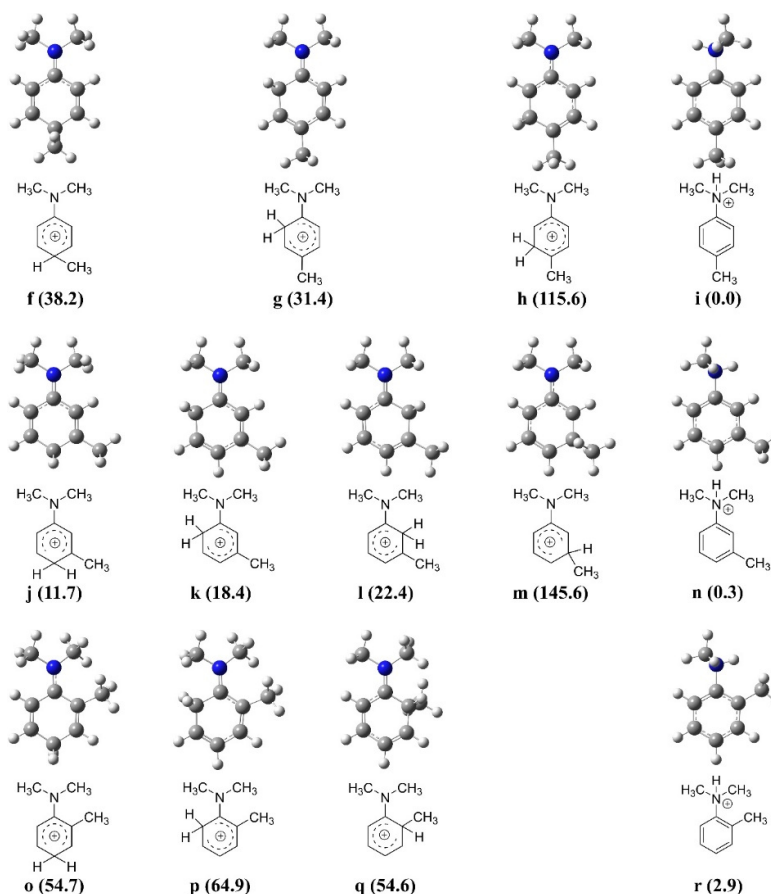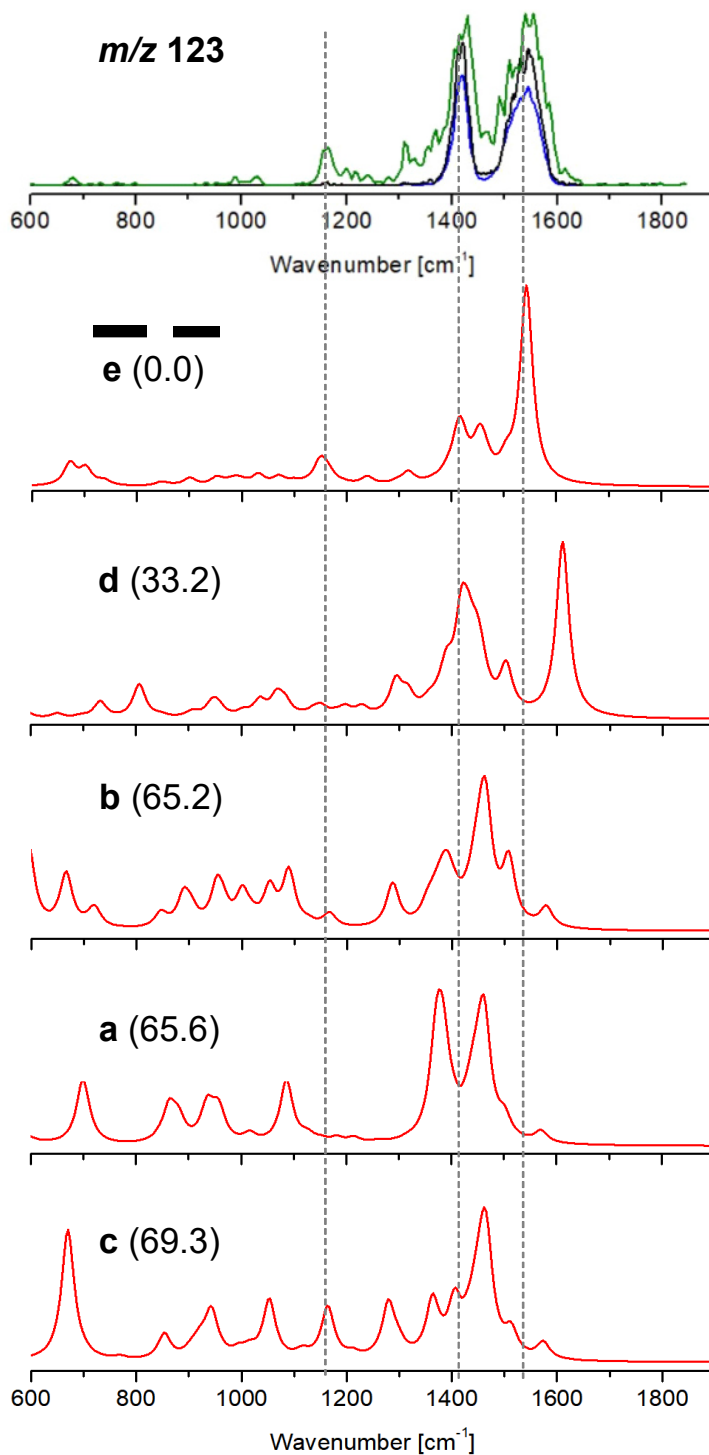
Figure 38
Minimum-energy ion structures for the 2H rearrangement product ions **f–r** ($C_9H_{14}N^+$, *m/z* 136) and their relative energies (kJ/mol) with respect to structure **i**, determined by theoretical calculations (B3LYP/cc-pVQZ).

Ion Spectroscopy.

For all ions discussed above we also calculated the linear IR spectra, which we then compared with the experimental ones. The experimental spectra were recorded via IRMPD ion spectroscopy on a Bruker Amazon Speed ETD mass spectrometer coupled with the FEL laser at the FELIX Laboratory (see Chapter 1.3 and 6.4 for more details). Figure 39 shows the experimental IR spectra of the 3H rearrangement product ion (*m/z* 123) in the top panel, derived respectively from the three different analytes **12** (black), **14** (blue) and **16** (green) as ESI-MS^2 [M]$^{\bullet+}$ precursors. There are two main strong bands visible at 1380-1480 cm^{-1} and at 1500-1600 cm^{-1}, alongside several smaller bands between 1180 cm^{-1} and 1305 cm^{-1}. The panels below depict the calculated spectra for all 5 isomers **a-e** discussed above. By comparison and band matching we can assign isomer **e** to be by far the best match, which is *N,N*-dimethyl-

2,3,dihydroaniline. The assignment of all calculated bands to the calculated vibrational modes is shown in Table 10. Since isomer **e** is by far the most stable one, these findings are reasonable. Calculations predict a N-H stretching mode of the ion structures **a–c** to appear at wavenumbers of 3334, 3337 and 3331 cm^{-1}. We therefore also probed for these modes with EI-MS and the FELion device via cryogenic messenger ion spectroscopy and an OPO tabletop laser (see Chapter 6.4 for details) in order to rule out an N-H bond in this fragment ion. Figure 40 is showing the results and as we can seem there is no band visible as expected, thus there is also no N-H bond in our ion, underlining the results from the IRMPD measurements, and making the assignment of isomer **e** even more likely, as we can assume due to all our results so far that the ions at *m/z* 123 formed by EI mass spectrometry and ESI-MS[2] are the same species und identical. The absence of an N-H stretching mode also excludes the ion structures **a-c**. Therefore, we postulate that the ion formed by the 3H rearrangement reaction at *m/z* 123 is indeed *N,N*-dimethyl-2,3-dihydroaniline (isomer **e**).

Figure 39

Top: IR spectra of the 3H rearrangement ions $C_8H_{13}N^{\bullet+}$ (*m/z* 123) generated by ESI-MS^2 from the molecular ions **11$^{\bullet+}$** (black trace), **13$^{\bullet+}$** (blue), and **15$^{\bullet+}$** (green). Below: Computed linear IR spectra of the isomeric ions **a–e** (see Figure 6), ordered by increasing energy (DFT, UB3LYP, cc-pVQZ; scaling 0.969). Values in brackets represent relative energies in kJ/mol.
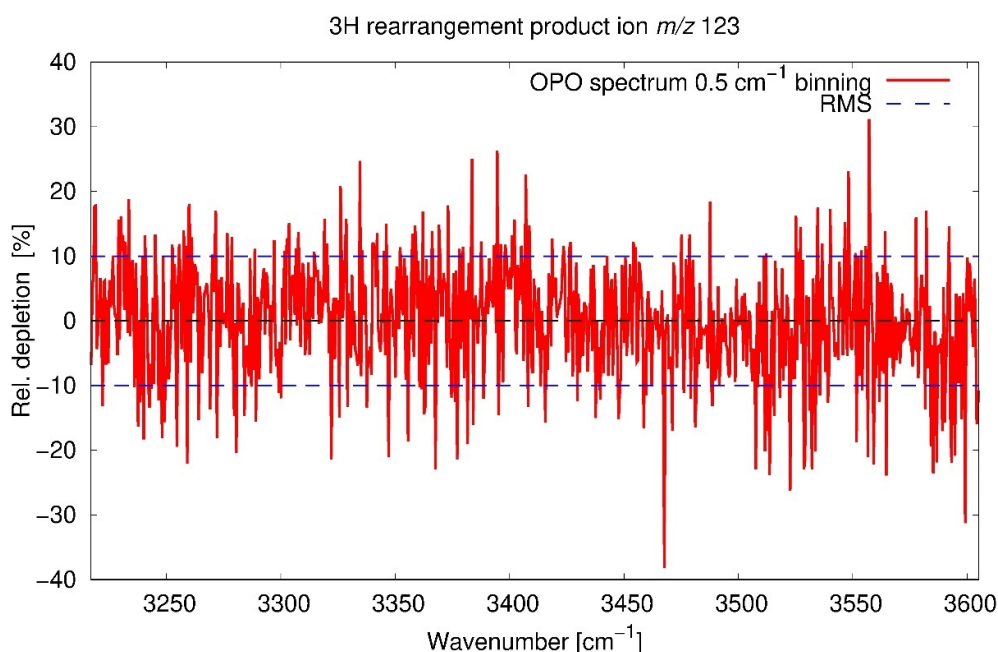
Figure 40

Cryogenic messenger IR spectrum based on the depletion of Ne-tagged precursor ions [$C_8H_{13}N \cdot Ne$]$^{\bullet+}$ (m/z 143) generated from analyte **12**. Binning 0.5 cm^{-1}. To achieve a baseline of 0% depletion (gray) in the depicted range, an additional baseline correction of the experimental data by a depletion offset of 4.18% was performed. The RMS of the ion signal for the used binning of 0.5 cm^{-1} is about 10%.

Table 10

Experimentally observed IR absorption bands of the 3H rearrangement product ion $C_8H_{13}N^{\bullet+}$ (m/z 123) (see Figure 8) and scaled harmonic vibrational bands calculated for isomer **e**. Only transitions with an experimental intensity of >5% of the strongest observed transition are listed. See SI Table S10 for further information.

Mode #	Observed ν_{vib} [cm^{-1}]	Calculated ν_{vib} [cm^{-1}]	Mode description
14	680	673	C-H wagg., ring breath., N-CH$_3$ stretch.
22	985	990	C-H$_2$ rock., C-H wagg.
24	1027	1032	N-CH$_3$ asym. stretch.
28	1159	1147	H-C-C-H bend., C-H$_2$ twist., C-C & N-CH$_3$ asym. stretch.
29		1155	C-N stretch., C-H$_2$ twist., CH$_3$ rock.
30		1167	H-C-C-H bend., C-H$_2$ twist., C-N stretch.
32	1237	1240	C-H$_2$ twist., ring stretch.
34	1311	1318	C-H$_2$ & C-H wagg., ring stretch.
36		1391	asym. ring stretch., C-H wagg., CH$_3$ umbrella
37		1409	C-H$_3$ umbrella, C-H$_2$ bend., C-N stretch.
38	1416	1410	C-H$_3$ umbrella, C-N stretch., C-H$_2$ bend.
39		1416	C-H$_2$ bend., C-H$_3$ umbrella, C-N stretch.
40		1423	C-H$_2$ bend., C-H wagg.
41		1437	C-H$_3$ bend., ring stretch., C-H wagg.

42		1450	C-H$_3$ bend., ring stretch.
43		1452	C-H$_3$ bend., ring stretch.
44		1459	C-H$_3$ bend., ring stretch.
45		1468	C-H$_3$ bend.
46	1542	1504	C-C stretch., C-H wagg., C-N stretch.
47		1543	C-N stretch.

The results from the IRMPD measurements and the calculations of the IR spectra for the isomer in case of the 2H rearrangement reaction are shown in Figure 41. The top panels depict all the same experimental IRMPD spectrum, for the fragment at *m/z* 136 from the precursor ion **12**$^{\bullet+}$. There are two bands visible, a strong composite band at 1500-1600 cm^{-1} and a smaller band at around 1410 cm^{-1}. The lower panels depict all the calculated ion structures **f-r** discussed above, sorted by relative energy. By comparing the calculated spectra with the experimental one, and by assigning each of the bands, we find that isomer **g** matches the data best, especially the two strong calculated bands at 1521 cm^{-1} and 1563 cm^{-1} match the main composite band at 1500-1600 cm^{-1} very good. Further, the observed bands at 1413 cm^{-1} and 1325 cm^{-1} are matching with calculated bands quite well. It is further obvious that the calculated band at around 1650 cm^{-1}, which originates from C=C double bond ring stretching and C=N double bond stretching, must be absent or very weak according to the experimental data. This band is most pronounced in isomers **j**, **f**, and **o**, where the C2-C3 and C5-C6 and C-N bonds have the most double bond character (see Figure 38). It is weaker in isomers **k**, **l**, **p**, and **q**, and almost absent in **g**. In these ions the C2-C3 and C4-C5 bonds have most double bond character, and the N-C double bond character is weaker. And finally, this band is completely absent in isomers **h**, **i**, **m**, **n**, and **r**, which are either aromatic or the C-N bond has most single bond character. We therefore can exclude the ions **f**, **j**, **k**, **l**, **o**, **p** and **q**, because they show this band in strong to middle intensity. Furthermore, all of the low energy isomers **i**, **n**, **r** and **j** can be safely excluded as candidates, because they do not match the experimental data at all. In addition, isomers **p**, **h** and **m** can be ruled out because they are too high in energy and are not matching the experimental data well. We thus conclude that isomer **g** is formed in the 2H rearrangement process at *m/z* 136, although it is about 31 kJ/mol higher in energy than the lowest isomer **i**. Table 11 shows the assigned calculated vibrational modes for the assigned isomer **g**.
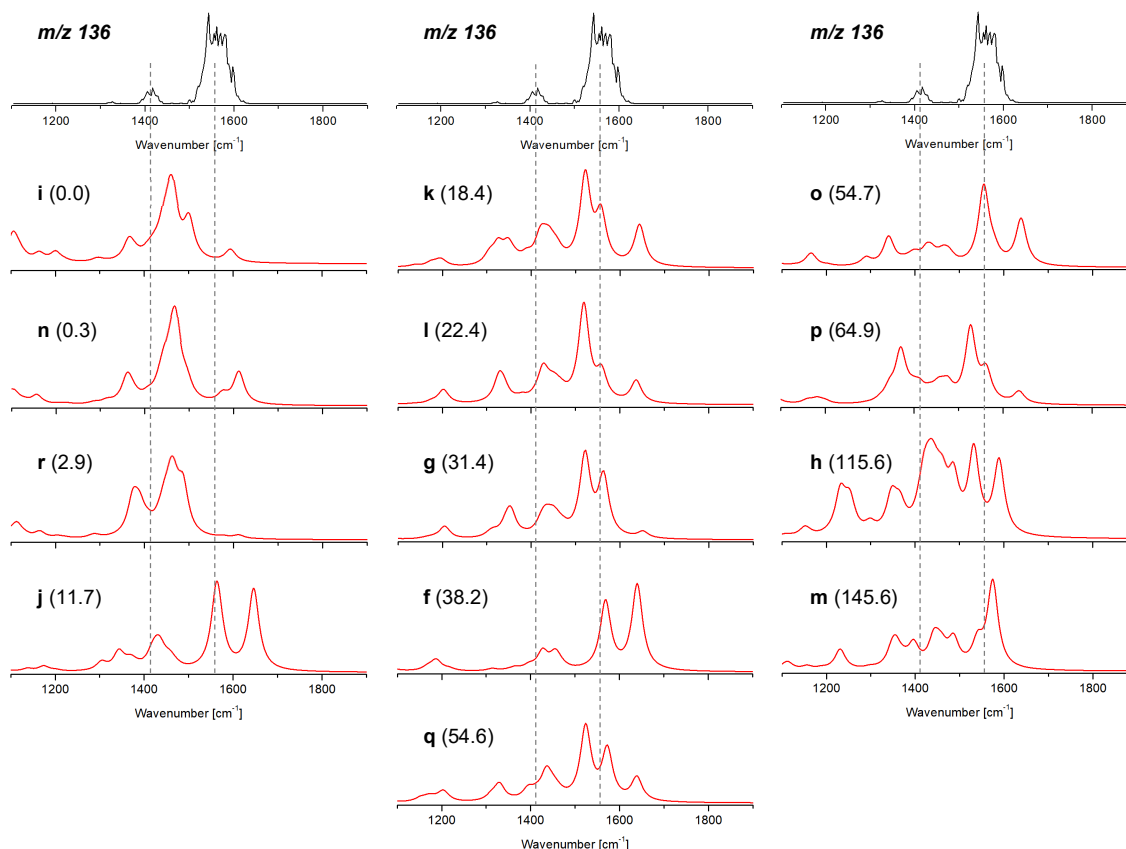
Figure 41

Top: IR spectrum of the 2H rearrangement ions $C_9H_{14}N^+$ (*m/z* 136) generated by ESI-MS^2 from the molecular ion **12•+**. Below: Computed linear IR spectra of the isomeric ions **f–r** (see Figure 7), ordered by increasing energy (DFT, B3LYP/cc-pVQZ; scaling 0.969). Values in brackets represent relative energies in kJ/mol.

Table 11

Experimentally observed IR absorption bands of the 2H rearrangement product ion $C_9H_{14}N^+$ (*m/z* 136) (see Figure 9) and scaled harmonic vibrational bands calculated for isomer **g**. See Table S12 for further information.

Mode #	Observed ν_{vib} [cm^{-1}]	Calculated ν_{vib} [cm^{-1}]	Mode description
32	1194	1167	in-plane, C-CH$_3$ stretch., N-CH$_3$ stretch., ring bend.
36		1307	in-plane, C-H wagg., ring stretch., N-CH$_3$ stretch.
37		1315	in-plane, C-H$_2$ wagg., ring stretch., C-N stretch.
38	1325	1343	out-of-plane, C-H$_2$ bend.
39		1354	in-plane, C-H wagg., ring stretch., N-CH$_3$ stretch.
41		1411	in-plane, C-H$_3$ asym. wagg.
42	1413	1424	in-plane, C-H$_3$ wagg., C-N stretch., ring stretch.
43		1434	in-plane, C-H$_3$ bend., C-H bend., ring stretch.
50	1543	1521	in-plane, C-N stretch., ring stretch., C-H$_3$ bend.
51	1569	1563	in-plane, C-N stretch., ring stretch., C-H$_3$ bend.

3.2.3 Mechanistic Discussion

Based on our calculations and IR ion spectroscopy results discussed above, we propose a new mechanism for the 3H rearrangement which is depicted in Scheme 9. Due to the older results from Kuck *et al.* and our new insights, we initially assume that the three migrating hydrogen atoms of the butanol **14** are including the carbinol-H, the hydroxyl-H, and one of the methylene-H atoms at C-3. The carbinol-H migrates in the first step, in which the *ipso*-position acts as the acceptor site. There are two possible pathways shown, with the same initial step, which is a 1,4-H shift (blue) where the first proton migrates to the *para*-position of the dimethylamino group. Such 1,4-H shifts to the *ipso*-position are known to compete with the more frequent 1,5-H transfer.[182, 183] The electron donating dimethylamino groups apparently governs the regioselectivity of the first hydrogen transfer step and thus giving rise to the distonic ion **14$_i$$^{•+}$** rather than tautomer **14$_o$$^{•+}$** as proposed earlier by Kuck *et al.*.

In the first und upper pathway, this is followed by another 1,4-H shift (green) in which the second hydrogen migrates to the *meta*-position of the ring. In the final step the last 1,7-H-shift (red) takes place to form the final product ion *m/z* 123 and induces the cleavage of the weak bisallylic C-C bond to the neutral loss methyl vinyl ketone. In the second pathway the first step (green) is followed by the 1,7-H shift (red) in which the *ortho*-position is protonated first. In the next step (green) the last hydrogen migrates to the *meta*-position. Finally, the C-C bond is cleaved in a homolytic manner, to form the same products as above, the fragment *m/z* 123 and the neutral loss. The formation of the ion-neutral complex **I-N$_{(3H)}$$^{•+}$** is not necessary in this new and revised mechanism, but it is still a possibility which cannot be excluded.

Furthermore, we also propose a new mechanism for the formation of 2H product ion at *m/z* 136 as well as the *para*-dimethylaminobenzyl cation yielded from the benzylic cleavage (*m/z* 134), which is shown in Scheme 10. The 2H rearrangement reaction in ion **14$^{•+}$** (*m/z* 193) is proposed to start with the benzylic cleavage yielding the fragment at *m/z* 134. In the next step, some of these ions might form an ion-neutral complex **I-N$_{(2H)1}$$^{•+}$** with the also present 2-hydroxy-1-propyl radicals and via an intracomplex hydride transfer the complex **I-N$_{(2H)2}$$^{•+}$** is formed, which then undergoes intracomplex rotation followed by a proton transfer to produce the final fragment ion $C_9H_{14}N^+$ at *m/z* 136, the *ortho*-protonated *para*-toluidinium ion **g**, as we have assigned above by IR spectroscopy, and an acetonyl radical.

Scheme 9

Possible mechanisms leading to the dihydroaniline structure **e** of ions $C_8H_{13}N^{\bullet+}$ (*m/z* 123) from the molecular ions **14**$^{\bullet+}$ by unidirectional 3H rearrangement. The 1,4-H migration step **14**$^{\bullet+}$ → **14**$_i$$^{\bullet+}$ is assumed to be the key step of the process for thermochemical reasons, which disfavors the 1,5-H transfer **14**$^{\bullet+}$ → **14**$_o$$^{\bullet+}$. Two possible sequences of the overall 3H rearrangement are depicted. Possible involvement of ion-neutral complexes, such as **I-N$_{(3H)}$**$^{\bullet+}$ (with alternative localization of charge and radical) is included tentatively (see text).
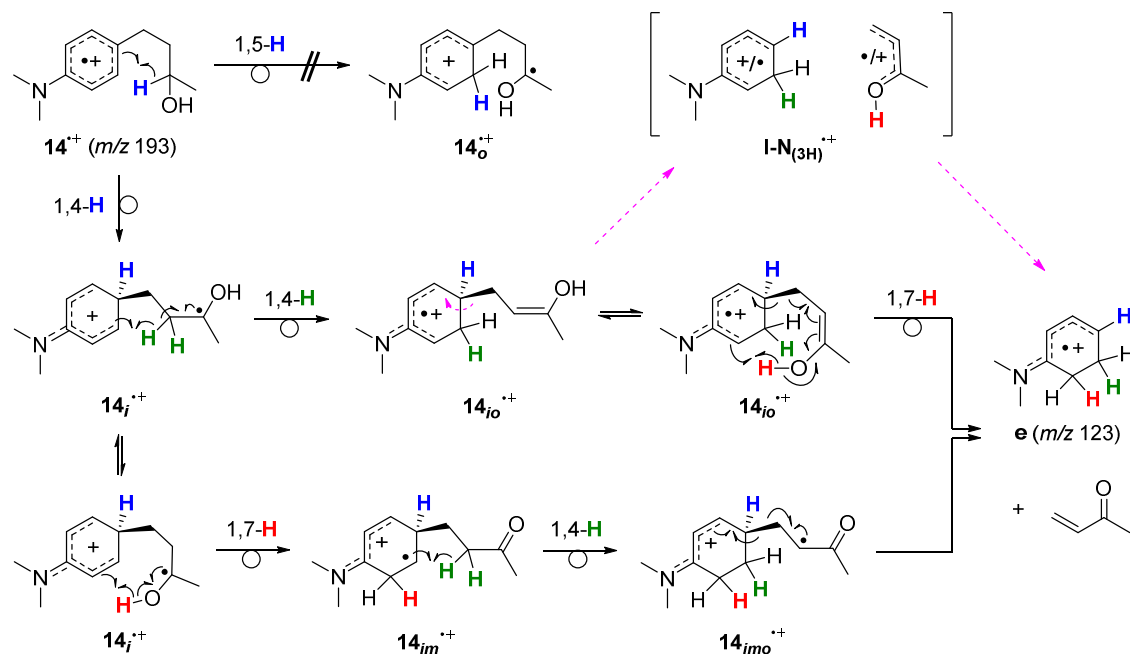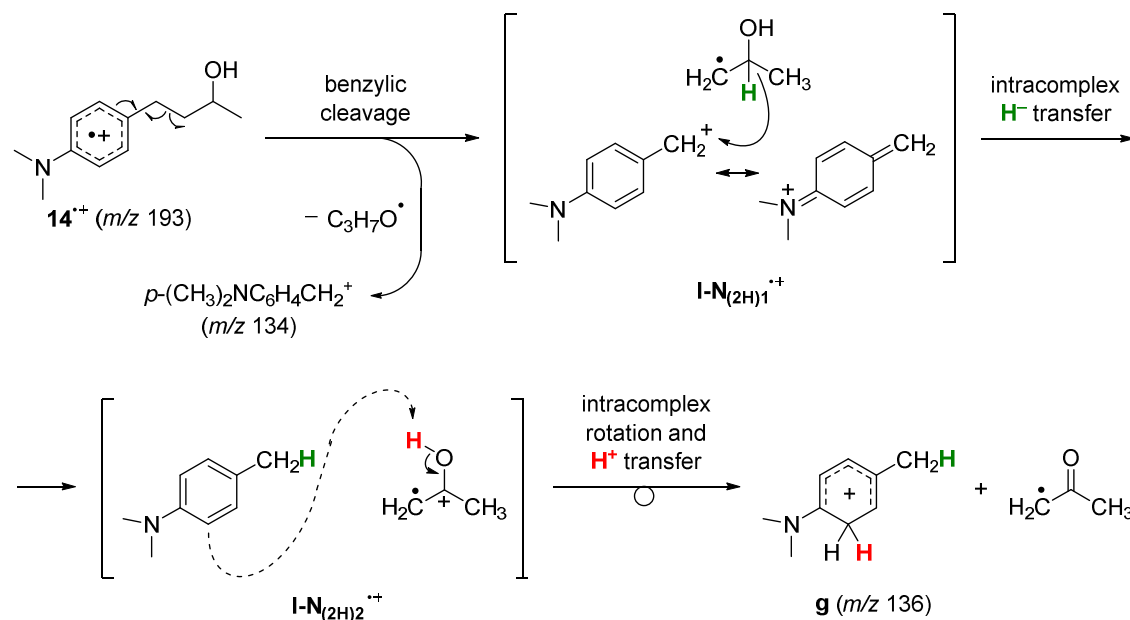
Scheme 10

Possible mechanism leading to the *ortho*-toluidinium structure **g** of ions $C_9H_{14}N^+$ (*m/z* 136) from the molecular ions **14**$^{\bullet+}$ by unidirectional 2H rearrangement. Besides the direct cleavage generating the free benzylic ion $C_9H_{12}N^+$ (*m/z* 134), this ion can undergo hydride abstraction from the neutral fragment within the ion-neutral complex **I-N$_{(2H)1}$**. Subsequent proton transfer within the complex **I-N$_{(2H)2}$** leads to the fragmentation products.

3.2.4 Conclusions on the 2H and 3H Rearrangement Study

We have investigated the unidirectional 2H and 3H rearrangement reaction in the molecular radical cations of several electron rich aryl alkanols in EI- and ESI-MS with IRMPD and theoretical calculations. These rare gas-phase redox processes have found to be main fragmentation pathways of benzyl indanols in EI-MS.

In this work we showed that we can generate the radical cations of some precursor ions of aryl alkanols in ESI-MS and then initiate the 2H and 3H rearrangements via CID activation and observe the respective fragment ions, which was not done before. The respective fragment ions at m/z 136 ($C_9H_{14}N^+$) for the 2H and m/z 123 ($C_8H_{13}N^{\bullet+}$) for the 3H rearrangement were successfully characterized via IRMPD spectroscopy. The ion structure of $C_9H_{14}N^+$ was confirmed to be protonated *N,N*-dimethyl-*para*-toluidine, as suggested already in the older study by Kuck *et at.*.[3] However, we showed that the extra proton is located in the *ortho* position and not in the postulated *para* position, which was an interesting finding, because the *N*-protonated species are supposedly the more stable ones. As for the 3H rearrangement the suggested ion by Kuck *et al.* had to be revised in this study as we identified the actual ion structure of this radical cation to be *N,N*-dimethyl-2,3-dihydroaniline. Our calculations further showed that this isomer also is the most stable one in the ion series we tested.

In addition, this study offers revised mechanisms for the 2H and 3H rearrangement reactions based on our new findings and evidence from computational chemistry and IRMPD ion spectroscopy experiments. In essence, the 3H rearrangement reaction pathway is likely a sequence of 1,4-H and 1,7-H transfer steps, yielding an intriguing novel intramolecular 1,2-hydrogenation of an electron-rich arene. The 2H rearrangement mechanism is suggested to be quite similar as proposed in the earlier study by Kuck *et al.*.

3.3 Investigation of the Claisen Rearrangement Reaction in protonated Allyl Phenyl Ether Derivatives

3.3.1 MS-Experiments

As reported by Beynon *et al*. for protonated allyl phenyl ether in CI-MS (see also Chapter 1.7 and 2.3),[148] the loss of ethene is put forward to evidence the gas-phase Claisen rearrangement in the fragmentation patterns of protonated molecular ion precursors as shown in Scheme 4. In the case of allyl-2,4,6-trimethylphenylether **6** (see Scheme 12) there are no protons in the *ortho*-positions, which are necessary for the ethene loss to follow the reported mechanism. However, in the ESI-MS/MS experiments of [**6+H**]$^+$ a loss of ethene leads to the most prominent fragment ion at *m/z* 149, as shown in Figure 42. Thus, it is assumed that the ionizing proton, very likely positioned initially at the ether oxygen of allyl-2,4,6-trimethylphenylether **6** is involved in the rearrangement process and the loss of ethene, as Scheme 11 illustrates. This assumption is further supported by experiments with deuterated solvents as we can see in Figure 43. Here, the loss of ethene as well as mono-deuterated ethene (C_2H_3D) is visible, indicating that the deuterium from protonation is indeed involved in the fragmentation process.

With allyl-2,4,6-trimethylphenylether **6** and the Claisen rearrangement to the ortho position, several ionic cyclohexadienone derivatives could be formed as indicated in Scheme 11. Firstly, the product ion at *m/z* 135 generated by loss of propene; secondly, slight collision activation of the [**6+H**]$^+$ ion at *m/z* 177 could trigger the Claisen rearrangement and might be a possibility to examine the isomerized molecular ion [**7+H**]$^+$ at *m/z* 177. And finally, the already discussed CID product ion of the C_2H_4-loss at *m/z* 149 **15a** could likely be formed. The resulting cyclohexadiene structures are also interesting, because they could give us access to reference spectra for the study of phenol and aniline tautomer study in the gas-phase. This was our original intend and goal of this project.
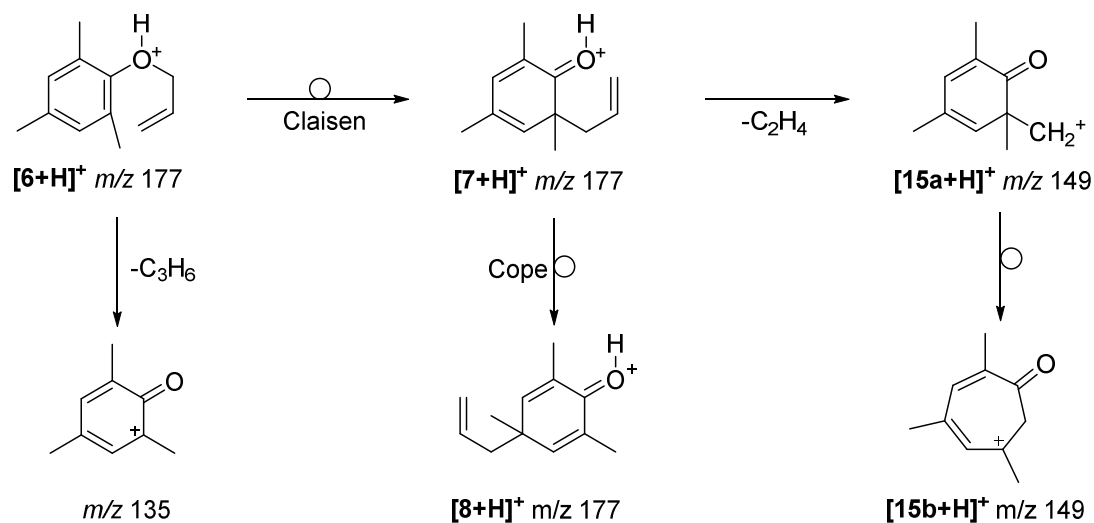
Scheme 11
Possible Structures of protonated analyte **6** *m/z* 177 and fragmentation product *m/z* 149 in ESI-MS.

In order to investigate this mechanism in more detail, several derivates were synthesized and are shown in Scheme 12. Allyl-2,6-dimethyl-4-*tert*-butylphenylether **9** also shows the loss of ethene upon collision without deuterated solvents, see Figure 44. Another important fragment is *m/z* 163, which corresponds to the loss of a *tert*-butyl radical. This is reasonable due to the stability of such tertiary radicals. Interestingly, **9** does not show the loss of ethene with deuterated solvents (see Figure 45). The only fragment which can be assigned here is the loss of a ·CH3 radical (*m/z* 205). One possible reason might be, that the positive charge is transferred to the *tert*-butyl residue upon fragmentation and this ion is not visible in the spectra, as the *m/z* value of 57 is below the scan range in this CID collision mode.

6
m/z 176,12012

9
m/z 218,1671
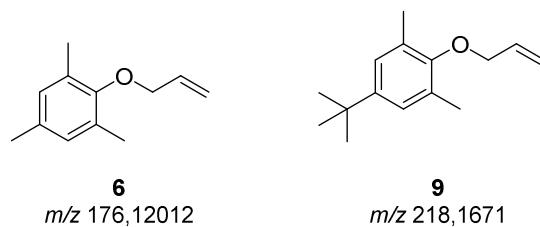
Scheme 12
The synthesized analytes allyl-2,4,6-trimethylphenylether **6** and Allyl-2,6-dimethyl-4-*tert*-butylphenylether **9** for this study.
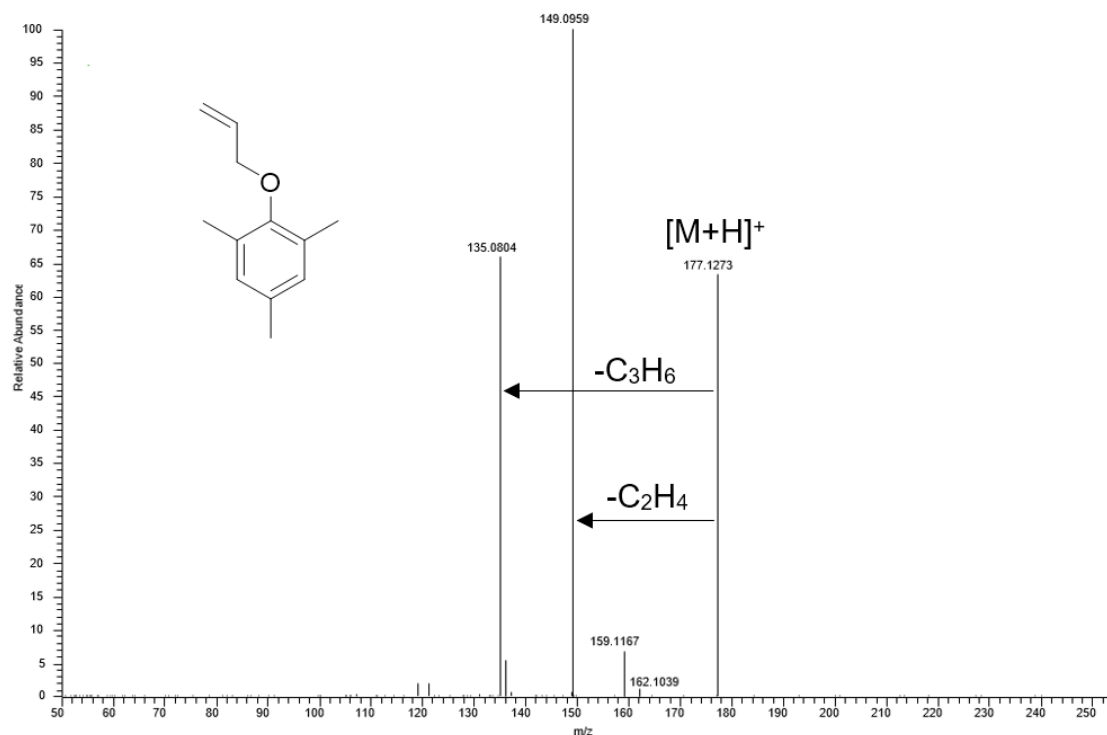
Figure 42
ESI-MS/MS spectrum of allyl-2,4,6-trimethylphenylether **6** in MeOH with ~0,1% formic acid.
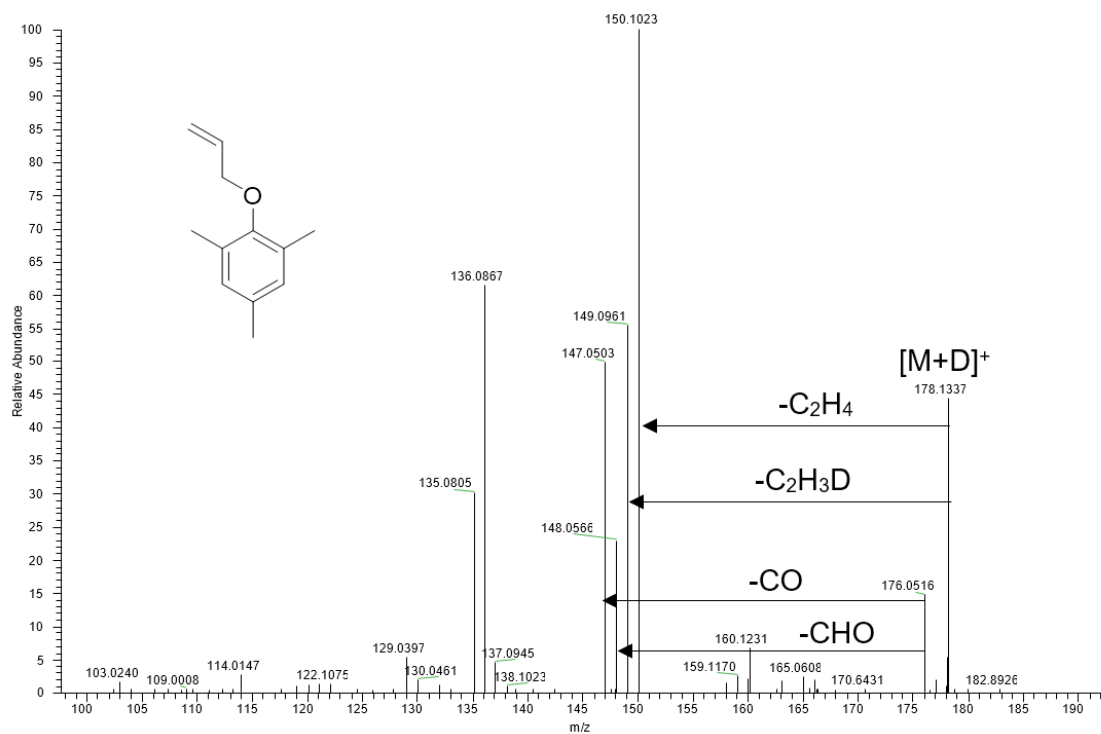
Figure 43
ESI-MS/MS spectrum of allyl-2,4,6-trimethylphenylether **6** in MeOD with ~0,1% deuterated formic acid.
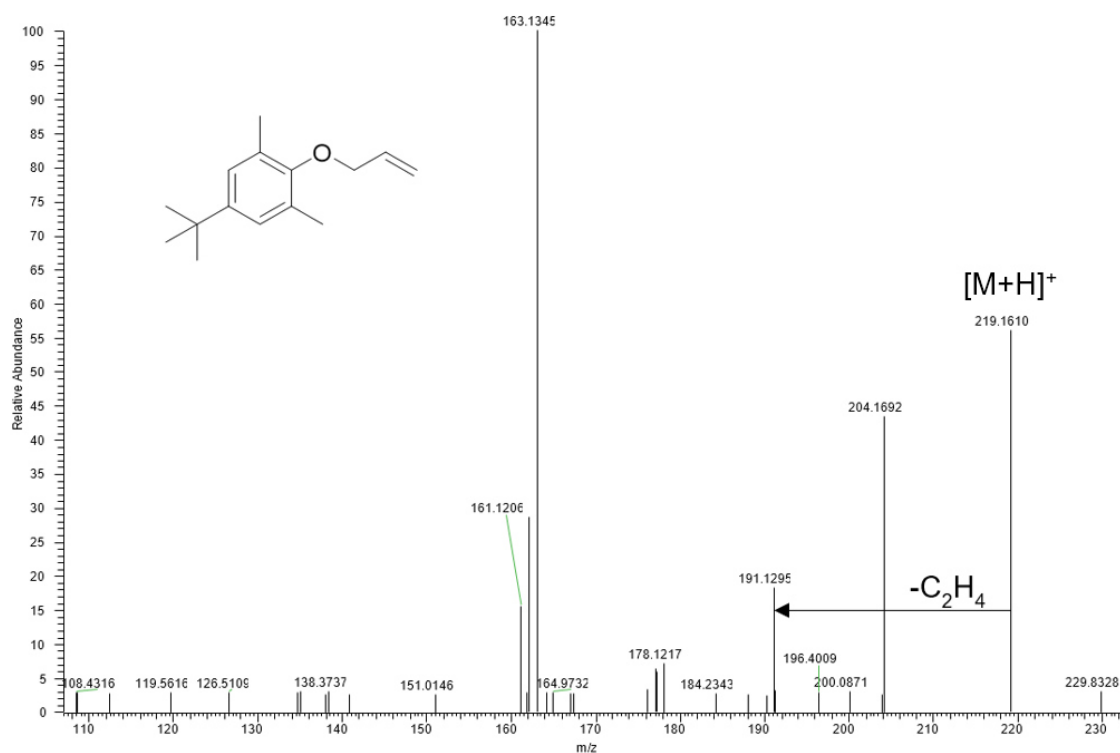
Figure 44
ESI-MS/MS spectrum of allyl-2,4-dimethyl-6-*tert*-butylphenylether **9** in MeOH without formic acid.
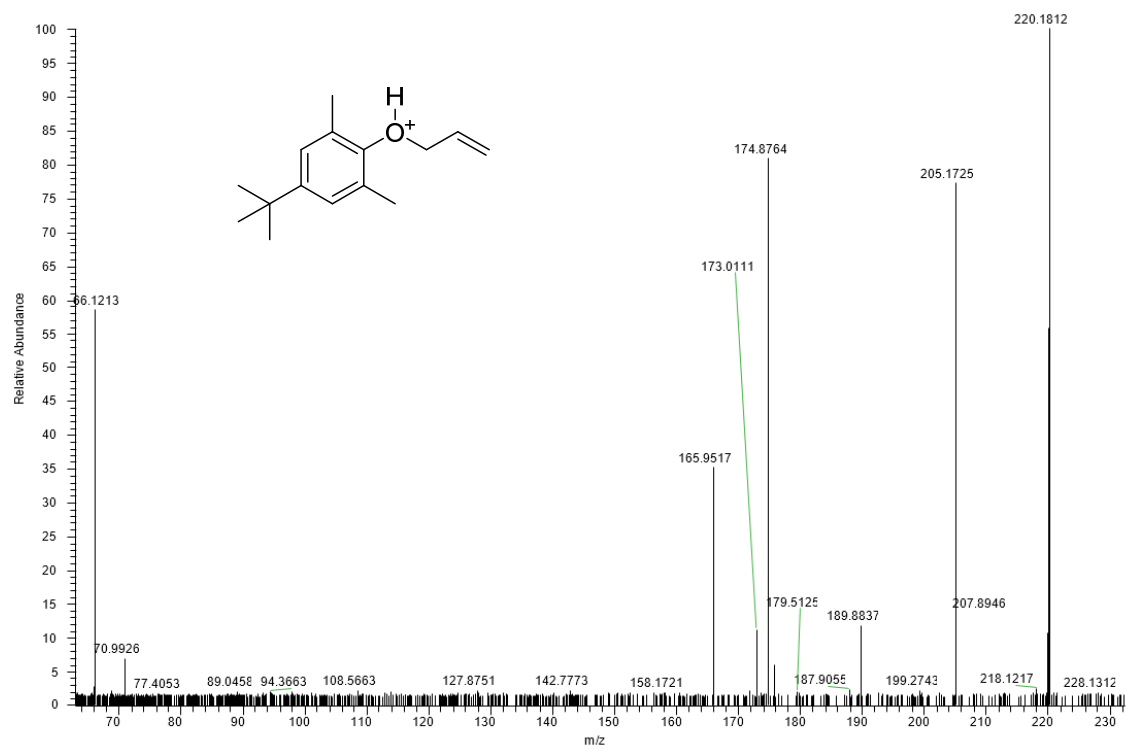
Figure 45
ESI-MS/MS spectrum of allyl-2,4-dimethyl-6-*tert*-butylphenylether **9** in MeOD without formic acid.

3.3.2 IR-Ion Spectroscopy and Computations

The following computations were executed by Martin Breugst from the Department of Chemistry at the University of Cologne.

Energetic considerations.

We also utilized ion spectroscopy as an alternative analytical method to get more insights into the mechanism and the present structures of the ions. Scheme 13 gives an overview of the considered structures and references to the related IR spectra below. The **6**-series are merely isomers with different protonation sites, ions **7** and **8** are the Claisen and Cope rearrangement products, respectively. The **10**-series gives possible isomers after the loss of ethene C_2H_4.

Table 12 shows the calculated relative energies of the different isomers **6-6e** as well as **7** and **8**. Interestingly, the most stable isomer is **6b**, which refers to protonation in position 2 of the aromatic ring. This is an important information, as the proton from protonation is not available in a manner as reported by Beynon *et al*. (see Scheme 4) and indicated in Scheme 11. A H-shift from this position to the allyl residue seems rather difficult and energetically unfavored. However, the protonation at the oxygen atom yields an ion **6** which is only 5 kJ/mol higher in energy, which is a relatively small. Isomers **6b** and **6c** have their protonation sites in position 3 and 4 of the aromatic ring and are on the same relative energy level (0 kJ/mol) as **6** and thus should be considered as possible candidates as well, although the H-shift from these positions to the allylic residue after the Claisen rearrangement seems rather unfavored. Ion **6a** loses some energy due to the loss of conjugation (+28 kJ/mol). Further, structure **6e** is even higher in energy (+83 kJ/mol) as expected due to the lack of stabilization of the positive charge. Therefore, these two structures are ruled out as candidates for the examined mechanism.

The isomers **7** and **8** are lower in energy (50 kJ/mol and 61 kJ/mol, respectively) as expected after the Claisen and Cope rearrangement, as this is part of the driving force of these rearrangement reactions. **8** is even more stable than **7** by 11 kJ/mol due to steric benefits, which is also the reason why the Claisen reaction often is followed in a cascade reaction by the Cope rearrangement (see Scheme 6).

The ion series **10** shows possible ion structures after the loss of ethene as discussed above. The two aromatic structures **10c** and **10d** are by far the most stable ones as shown in Table 13 (-46 kJ/mol and -41 kJ/mol compared to **6**, respectively), indicating that the re-aromatization might be an important step in the mechanism. Therefore, these two ions are the most promising candidates for comparison. Structure **10a** is not even stable and decomposes immediately in

the computational approaches and is thus ruled out as well as ion **10e** due the high energy of +119 kJ/mol. The other ions **10b** (+29 kJ/mol), **11a** (+31 kJ/mol) and **11b** (+49 kJ/mol) might be still possible candidates.
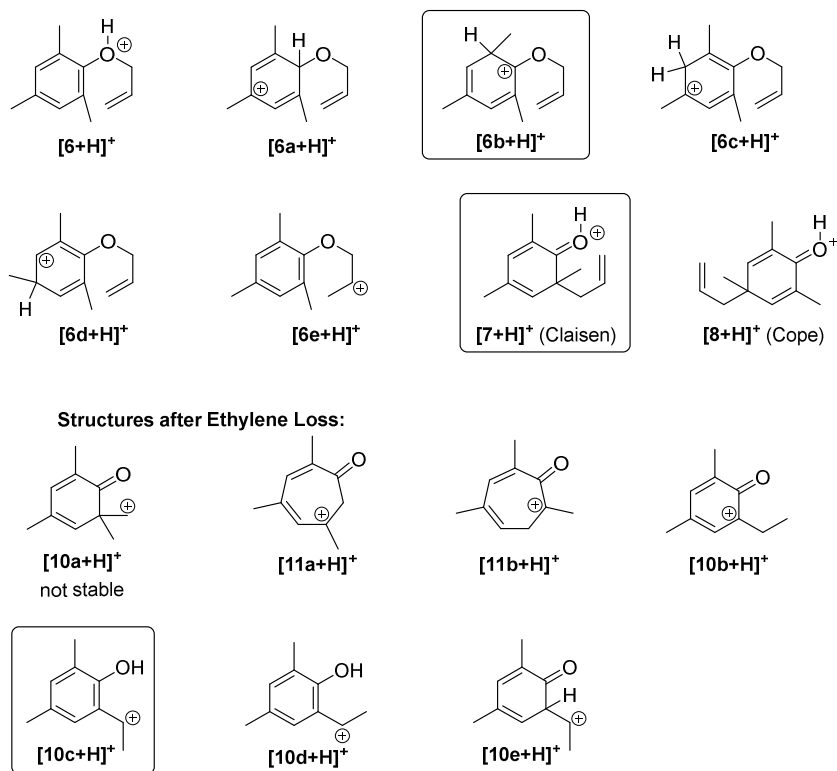
Scheme 13
Overview of the investigated ion structures in the Claisen rearrangement study.

Table 12
Relative Energies of structures **6-6e**, **7a**, and **8a**.

Structure	6	6a	6b	6c	6d	6e	7	8
$\Delta\Delta G$ [kJ mol^{-1}]	0	+28	-5	0	0	+83	-50	-61

Table 13
Relative Energies (rel. to **6**) of structures **10b-g**.

Structure	11a	11b	10b	10c	10d	10e
$\Delta\Delta G$ [kJ mol^{-1}]	+31	+49	+29	-46	-41	+119

IR ion spectroscopy.

We examined the protonated molecular ions of analyte **6** (*m/z* 177) in an unactivated and a "softly" collision-activated state, without inducing any fragmentation yet to hopefully force the ion to undergo the Claisen rearrangement without decomposing (losing ethene). We then also measured IR ion spectra of the product ions after the loss of ethene (*m/z* 149), to clarify the final ion structure as well, as the structure shown in the mechanism of Beynon *et al.* seems rather instable with the positive charge at the primary carbon position.

Ions before loss of ethene (m/z 177).

Figure 46 shows the experimental IR ion spectra of collision-activated **[6+H]**⁺ (grey line) and unactivated (black line) **[6+H]**⁺ (*m/z* 177). There are five obvious bands in the range of 1000-1400 cm⁻¹, which are less pronounced upon collision-activation, the others are still visible as without activation. Also, one band at around 1650 cm⁻¹ is observed after activating the molecular ion **[6+H]**⁺ with collision activation. These findings indicate a change in the ion structure.

In the following we will compare the activated and the unactivated precursor ion **[6+H]**⁺ experimental IR ion spectra with the calculated spectra of the ions structures above (red lines; see Figure 47 to Figure 68). It is obvious – without even comparing the bands individually – that some ion structures do not match the calculated spectra at all and therefore can be safely ruled out as probable ion structures.

For ions series **6** (*m/z* 177) we will compare to the non-activated experimental spectrum (black line), because we expect that this ion should be the main representative ion in ESI-MS of non-rearranged analyte. Ion structure **6** (Figure 47), for example, exhibits several intense bands at the lower end of the spectrum around 500-1100 cm⁻¹ which are mainly arising from the aromatic ring vibration modes. These bands are not visible in the measured spectrum; hence, this ion is ruled out as possible candidate as the match is not convincing at all. Ion structure **6a** (Figure 49) matches the experimental spectra much better, however the band at 1600 cm⁻¹ is too intense compared to the calculations. This band originates mainly from C=C ring stretching modes, which are according to our data always more intense if the π-system in the ring is not conjugated (double bonds opposite at position C2=C3 and C5=C6), a phenomenon which we will also see in the Aza-Claisen rearrangement study below. Therefore, this ion is partly ruled out as well, although the relative position of the bands match quite well. Ion structure **6b** (Figure 51) matches the calculations very well, it is even the best match in this ion series, and it is also the lowest in relative energy as shown in Table 12 (-5 kJ/mol), thus this ion is the most

promising candidate. Only the bands between 800 – 1000 cm^{-1} are quite weak in the experimental spectrum. These bands are arising mainly from sidechain vibrations. This is remarkable, as in literature usually the oxygen is used as protonation site – whereas here we find the aromatic ring protonated even with the loss of aromatization. The literature reports that, e.g., diethyl ether has a proton affinity of 828 kJ/mol, dimethyl ether 792 kJ/mol, benzene 750 kJ/mol, isopropyl benzene 791 kJ/mol, 1,3,5-trimethyl benzene (mesitylene) 836 kJ/mol, hexafluoro benzene 648 kJ/mol and anisole 840 kJ/mol.[184] Thus, in general, ethers possess higher proton affinities than the aromatic ring, however, substituted benzenes are ranging in the same category, if the substituents are electron donating. The three methyl groups in the case of allyl-2,4,6-trimethylphenylether **6** therefore enable the aromatic ring to be in competition with the ether oxygen for protonation, as the high proton affinity of mesitylene proofs.

Ion structure **6c** (Figure 53) also matches quite well in high wavenumber range, however, here again the band at 1600 cm^{-1} (C=C ring stretching and) is too intense when compared with the calculations. Furthermore, the calculated bands below 1400 cm^{-1} do not match very well. These bands are originating from several ring stretching, C-H ring wagging and especially C-H$_2$ wagging and bending modes, therefore, we can assume that the isomer present exhibits no C-H$_2$ group in the ring. Hence, **6c** is ruled out as probable candidate. For ion structure **6d** (Figure 55) the intense band at 1300 cm^{-1} does not fit the experimental data at all. Finally, ion structure **6e** (Figure 57) can be ruled out due to the high relative energy and the obvious bad matching in the IR spectrum especially in the aromatic ring vibration modes at lower wavenumbers. Based on these considerations and the lowest relative energy level, we postulate that ion **6b** is the most probably structure in this study and the bands are assigned to the respective calculated modes in Table 14.

To compare the collision-activated, but not fragmented experimental spectrum, we also calculated IR spectra of the Claisen as well as the Cope product ions. These are shown in Figure 59 to Figure 62. Especially ion **7** matches the experimental data very good as we can see in Figure 60. There is a second band in the calculated spectrum at 1652 cm^{-1} originating from mode ν_{66} (C=C ring stretching and C-H ring bending) which is also becoming visible in the experimental spectra upon activation as discussed above. Further, the much less intense band at 1386 cm^{-1} from a C-O stretching mode is also predicted with less intensity in the calculations. This is also true for the calculated bands below 1400 cm^{-1} and is expected for these bands as was discussed above. Ion **8** on the other hand does not match as well. The collision-activated spectrum is compared to the calculated one in Figure 62. The intensity of the calculated vibration mode ν_{66} is too intense. Which it the same for several bands below 1400 cm^{-1}, i.e.,

1169 cm^{-1} and 1270 cm^{-1}. This leads us to the conclusion that **7** is the most likely ion present after collision-activation.

The above discussed criteria and factors lead us to the general conclusion, that energetically as well as in accordance with the IR spectra, ion structure **6b** is the best candidate for non-activated analyte and **7** the best match for collision-activated analyte. Table 14, Table 15, and Table *16* are giving an overview to the observed and calculated vibration modes and their description for **6b**, **7**, and **8**.

Next we must clarify which vibrations are responsible for the less intense bands as well as the newly observed band in the experimental spectrum upon collision-activation. In Figure 46 we can see that the two observed signals at 948 cm^{-1} and 984 cm^{-1} are not visible anymore upon activation. These bands are originating mainly from sidechain vibrations as well as an O-C$_{sidechain}$ stretching mode (see Table 14and Table 15). As the O-C$_{sidechain}$ bond is cleaved in the Claisen rearrangement, these bands should not be visible anymore upon collision-activation, which is the case. The next band which loses intensity upon activation is around 1120 cm^{-1} and originates from ring stretching as well as several ring wagging and bending vibration modes. Important here is, that isomer **7** shows an O-H rocking vibration mode in this wavenumber range, which is presumably why this band is still visible after collision-activation, however less intense because the original ring wagging and bending modes at this position are shifted. The next two bands which are less intense after collision activation are the ones at 1228 cm^{-1} and 1317 cm^{-1}, mainly originating from ring stretching and side chain vibration modes but also from the C$_{ring}$-O stretching at 1228 cm^{-1} for **6b**. In case of ion **7** there are no side chain vibration signals in this range, only O-H rocking as well as ring stretching and rocking. The most obvious changing band upon collision-activation is the one at 1385 cm^{-1}, which comes mainly from ring stretching and bending. For **7** also partly from a C-O stretching and for **6** partly from sidechain bending. It is predicted to be much less intense for **7**, which probably is the main reason for the change in intensity of this band. Finally, there is a new signal visible after CID-activation at 1652 cm^{-1}. This is as expected since ion structure **7** exhibits two bands in this range as shown in Table 15, one of which is originating from a O-H bending.

Ions after loss of ethene (m/z 149).

Ion series **10** in Scheme 13 gives an overview over the possible and calculated ion structures after ethylene loss (*m/z* 149), which was according to Beynon *et. al.* an indication for the Claisen rearrangement to occur.[148] As discussed above, ion **10a** is not stable at all and decomposes in the computational approach. The most stable ion structures are **10c** and **10d** (-

46 kJ/mol and -41 kJ/mol compared to **6**, respectively). The experimental IR spectrum of *m/z* 149 is compared with the calculated IR spectra in Figure 63 to Figure 68. Ion **10e** can already safely ruled out because of the bad accordance of the IR spectrum. For ions **10b**, **11a** and **11b** the two bands at the highest wavenumbers (between 1500 cm^{-1} and 1800 cm^{-1}) are too far apart and they are not matching the calculations very well. Furthermore, for the ions with a carbonyl function in their structure, e.g., **11a**, **11b** and **10b** with the C=O stretching at around 1750 cm^{-1} is absent in the experimental spectrum. Additionally, the intense band for isomers **11a**, **11b** and **10b** at around 1500 cm^{-1} arising from C=C ring stretching modes are not visible as well. We can therefore rule these ions out. This is not the case for ions **10c** and **10d**, where these two bands are close together and thus might be measured as only one band. A look in

Table *17* shows us that the two modes from the calculation are origination from the same vibration and are only 46 cm^{-1} apart, thus increasing the likelihood of the two bands to be measured as only one. As in the calculated spectrum of **10c** the bands below 1400 cm^{-1} are lower in intensity than for **10d**, and it furthermore is the most stable ion in this series with -46 kJ/mol. The bands at lower wavenumbers could likely be below the measurable threshold and thus they are not visible in the experimental data. We can therefore assign ion **10c** as the most likely present structure here, however this assignment cannot be made unambiguously based on our data.
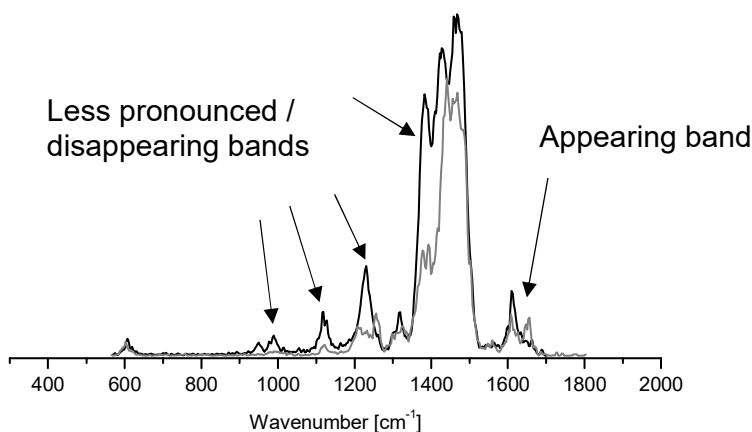
Figure 46
Experimental IRMPD ion spectra of both collision-activated (grey) and unactivated (black) **[6+H]⁺** *m/z* 177.
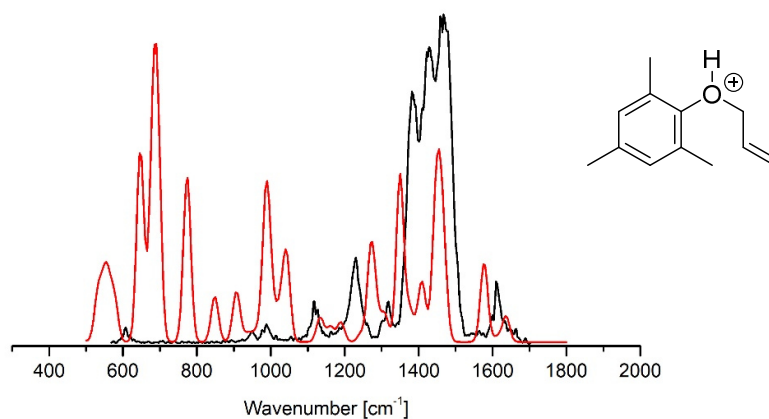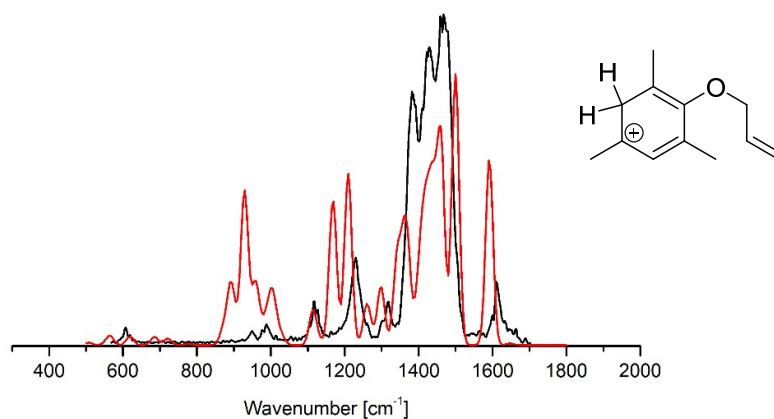
Figure 47
Experimental IRMPD ion spectrum of unactivated (black) **[6+H]⁺** *m/z* 177, and the calculated spectra of structure **6** in red.
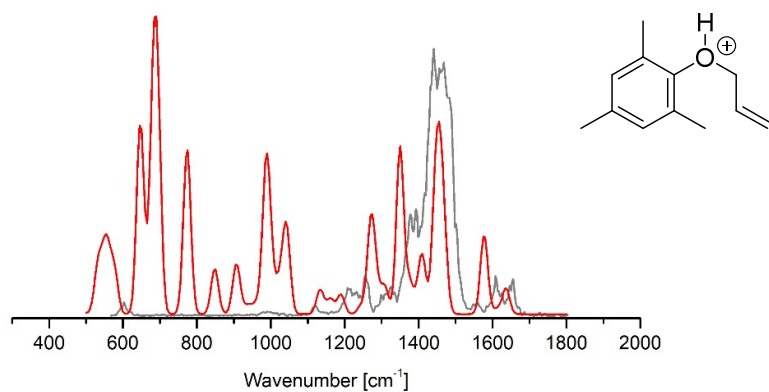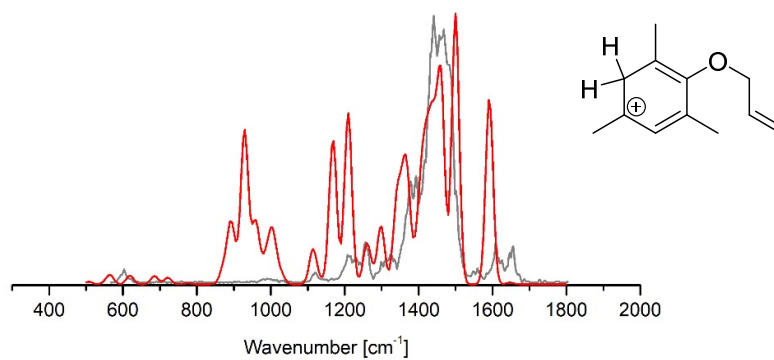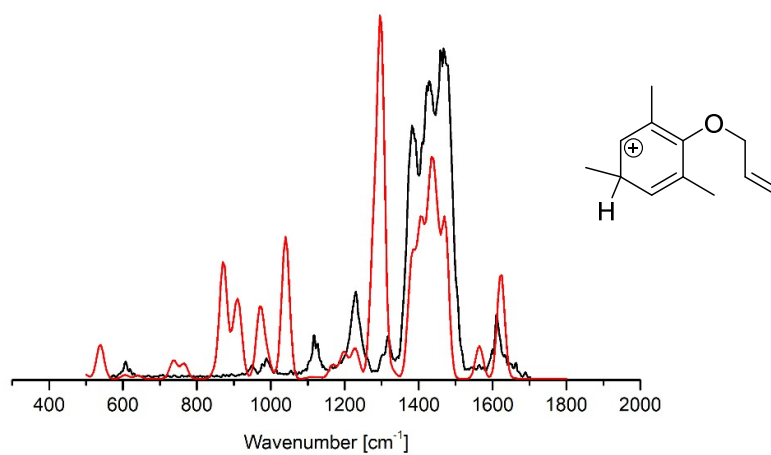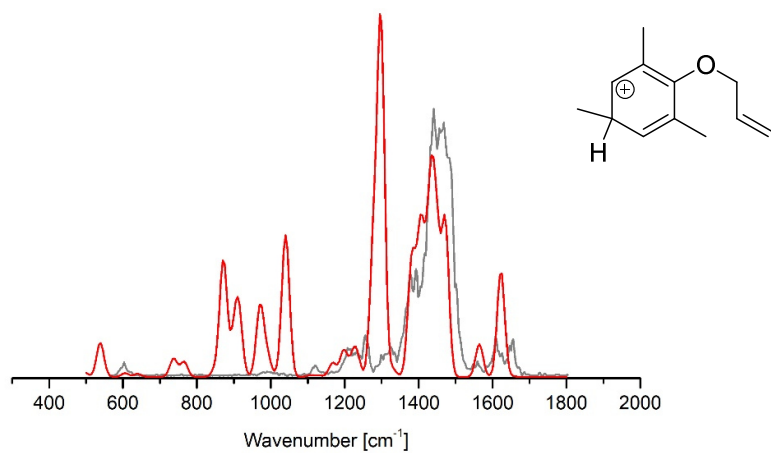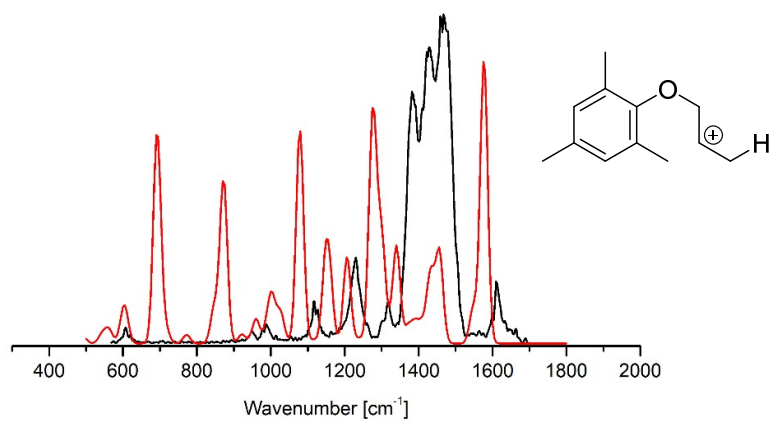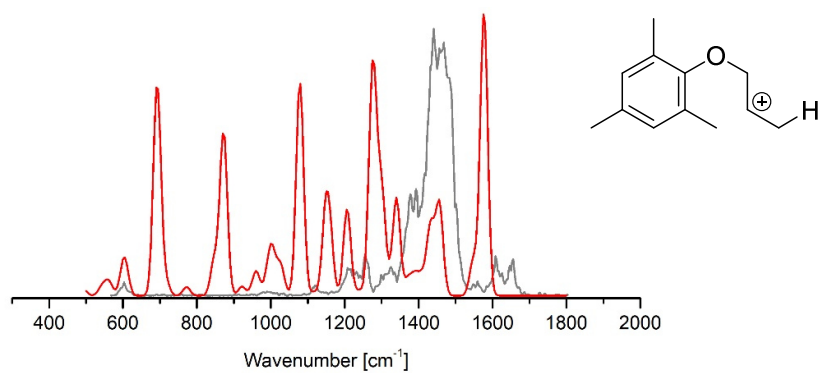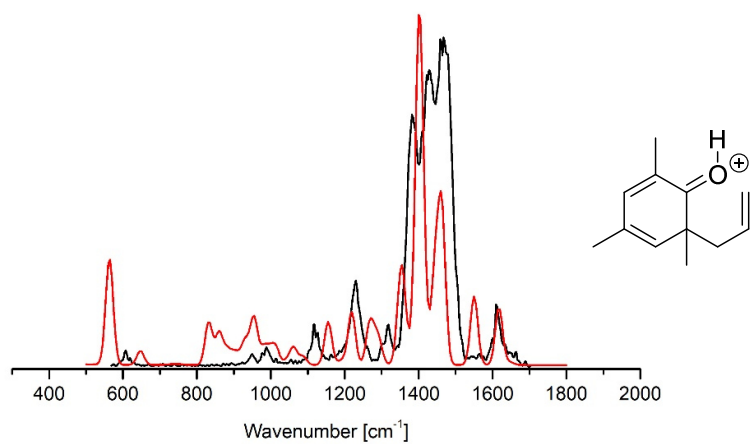

Figure 48
Experimental IRMPD ion spectrum of collision-activated (grey) **[6+H]⁺** *m/z* 177, and the calculated spectra of structure **6** in red.
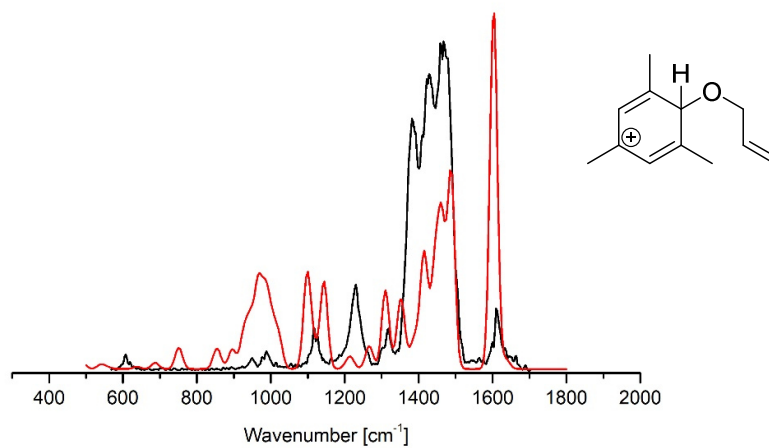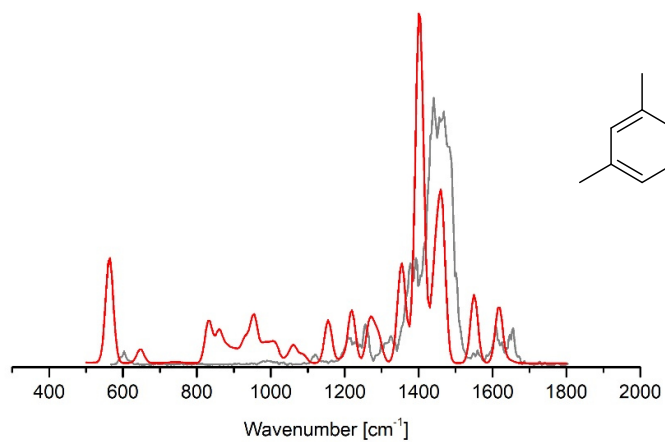
Figure 49
Experimental IRMPD ion spectrum of unactivated (black) **[6+H]**$^+$ *m/z* 177, and the calculated spectra of structure **6a** in red.
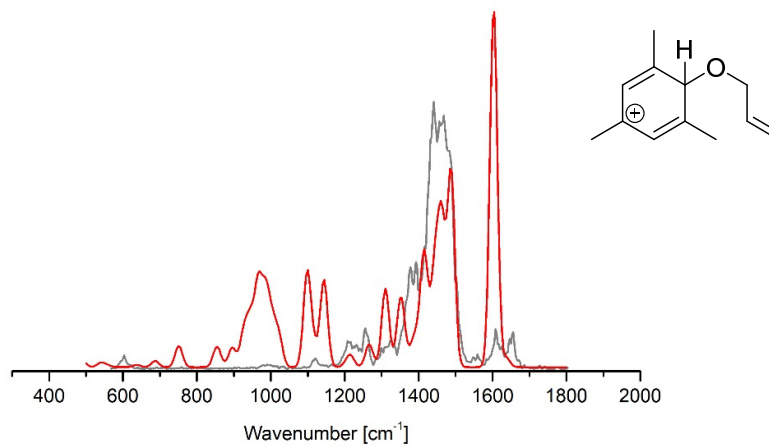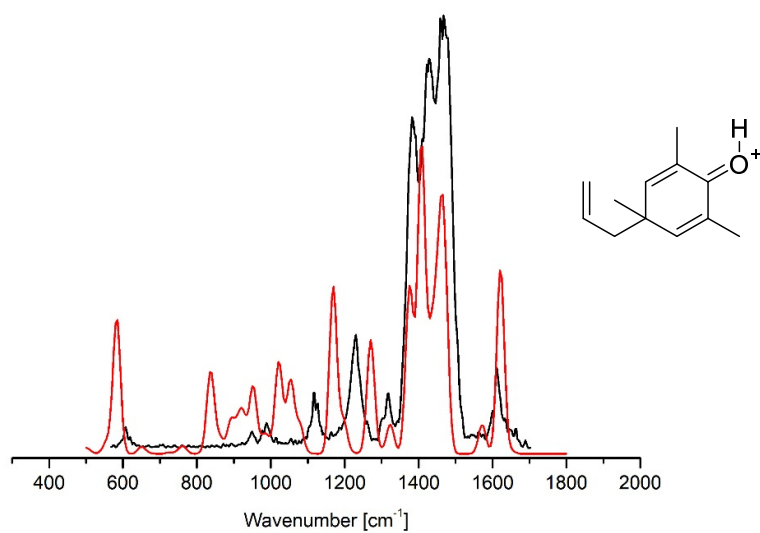

Figure 50
Experimental IRMPD ion spectrum of collision-activated (grey) **[6+H]**$^+$ *m/z* 177, and the calculated spectra of structure **6a** in red.
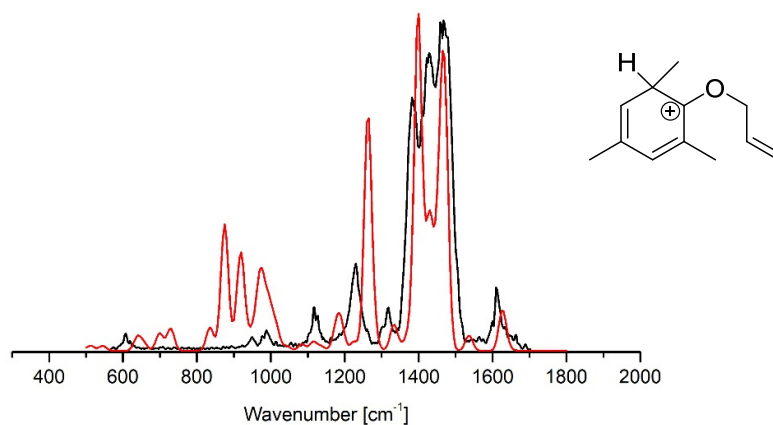
Figure 51
Experimental IRMPD ion spectrum of unactivated (black) **[6+H]⁺** *m/z* 177, and the calculated spectra of structure **6b** in red.
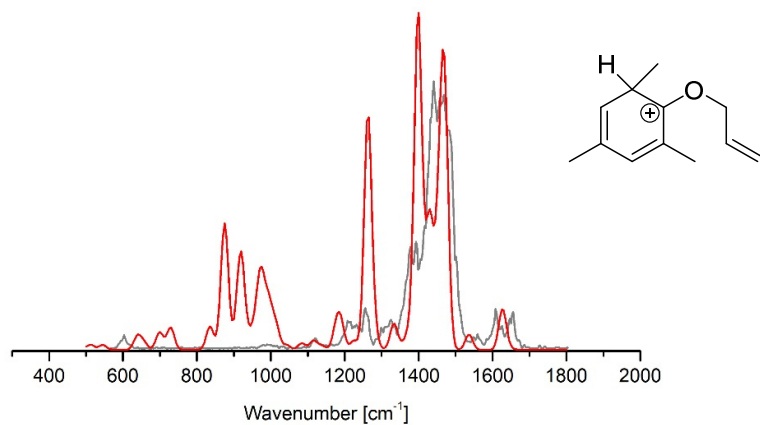
Figure 52
Experimental IRMPD ion spectrum of collision-activated (grey) **[6+H]⁺** *m/z* 177, and the calculated spectra of structure **6b** in red.
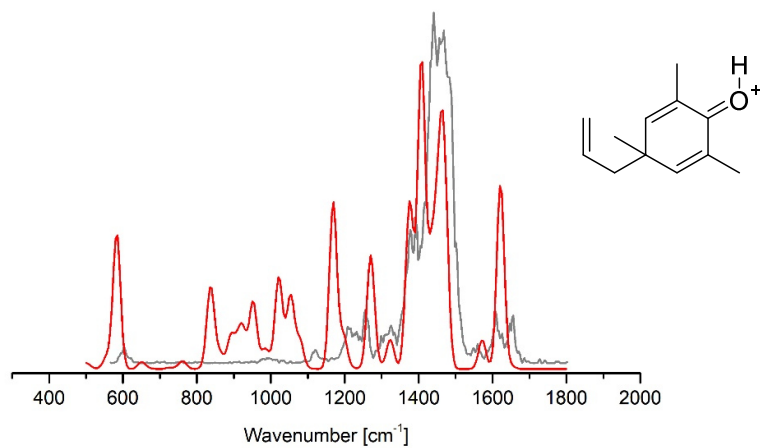
Figure 53
Experimental IRMPD ion spectrum of unactivated (black) **[6+H]**⁺ *m/z* 177, and the calculated spectra of structure **6c** in red.
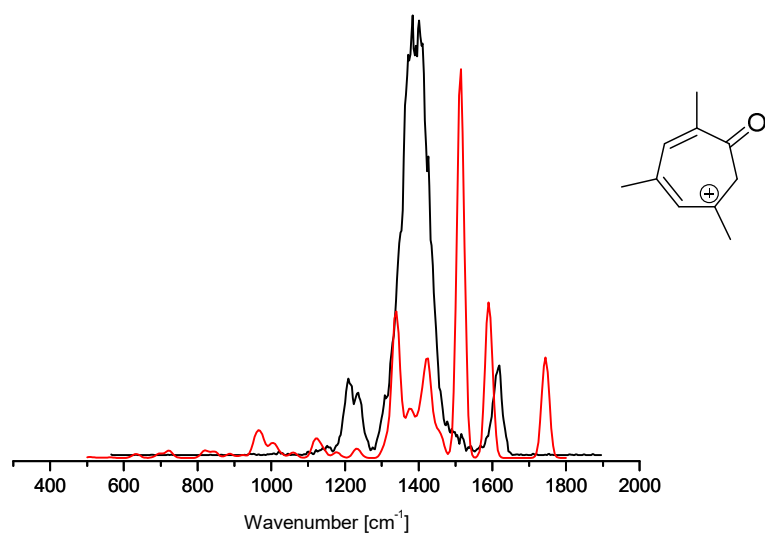

Figure 54
Experimental IRMPD ion spectrum of collision-activated (grey) **[6+H]**⁺ *m/z* 177, and the calculated spectra of structure **6c** in red.

Figure 55
Experimental IRMPD ion spectrum of unactivated (black) **[6+H]**[+] *m/z* 177, and the calculated spectra of structure **6d** in red.

Figure 56
Experimental IRMPD ion spectrum of collision-activated (grey) **[6+H]**[+] *m/z* 177, and the calculated spectra of structure **6d** in red.
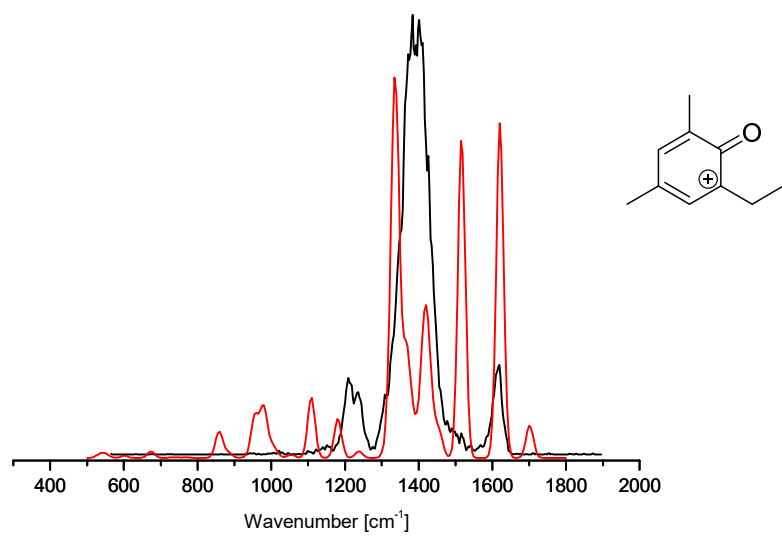
Figure 57
Experimental IRMPD ion spectrum of unactivated (black) **[6+H]**[+] *m/z* 177, and the calculated spectra of structure **6e** in red.

Figure 58
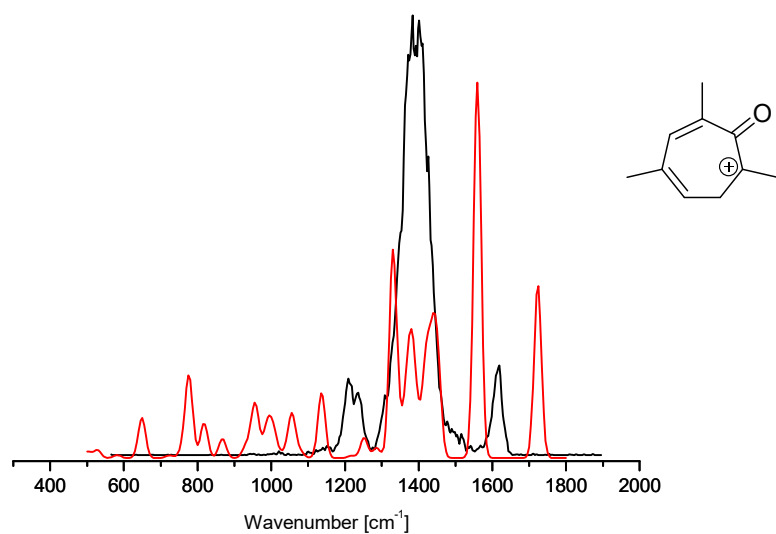Experimental IRMPD ion spectrum of collision-activated (grey) **[6+H]**[+] *m/z* 177, and the calculated spectra of structure **6e** in red.

Figure 59
Experimental IRMPD ion spectrum of unactivated (black) **[6+H]**[+] *m/z* 177, and the calculated spectra of structure **7** in red.

Figure 60
Experimental IRMPD ion spectrum of collision-activated (grey) **[6+H]**[+] *m/z* 177, and the calculated spectra of structure **7** in red.

Figure 61
Experimental IRMPD ion spectrum of unactivated (black) **[6+H]**[+] *m/z* 177, and the calculated spectra of structure **8** in red.

Figure 62
Experimental IRMPD ion spectrum of collision-activated (grey) **[6+H]**[+] *m/z* 177, and the calculated spectra of structure **8** in red.

Figure 63
Experimental IRMPD ion spectrum of the fragment ion at *m/z* 149 in black and the calculated spectra of structure **11a** in red.
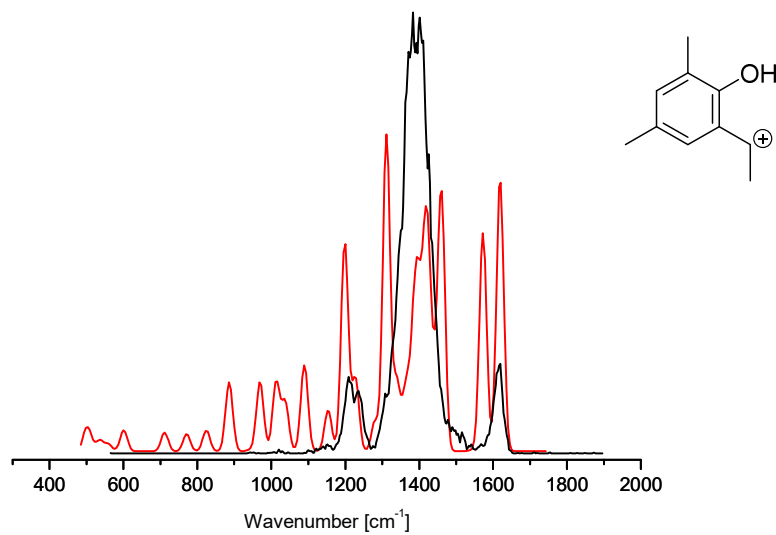

Figure 64
Experimental IRMPD ion spectrum of the fragment ion at *m/z* 149 in black and the calculated spectra of structure **10b** in red.
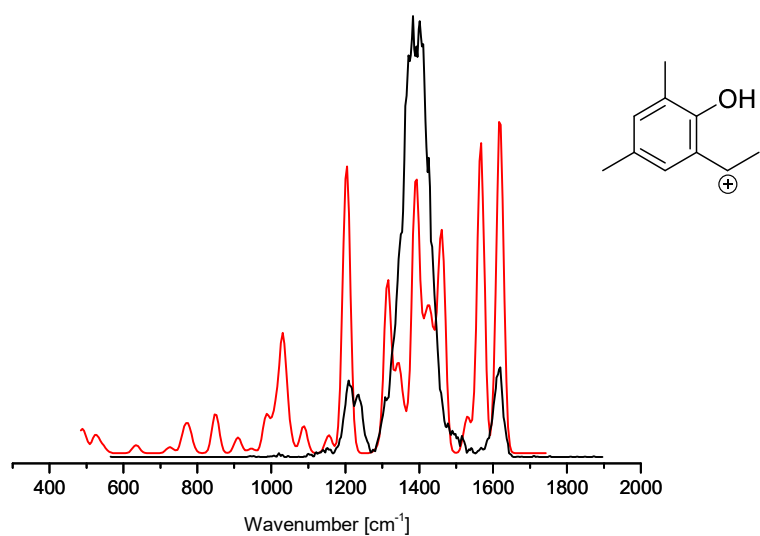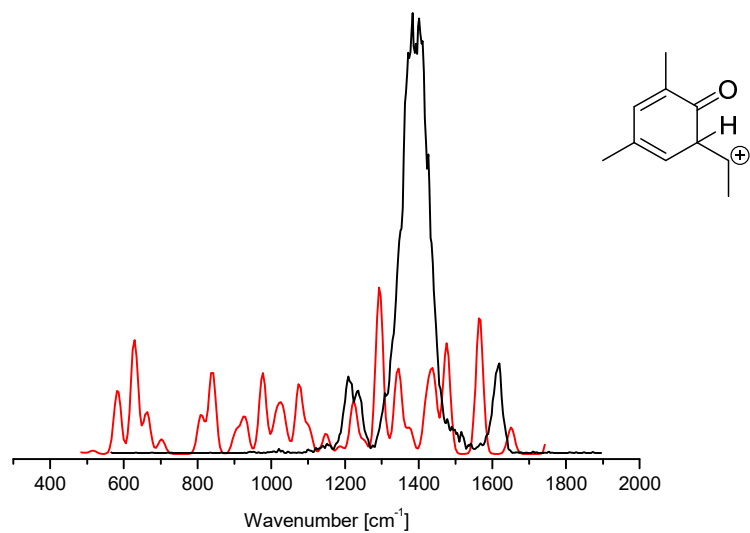
Figure 65
Experimental IRMPD ion spectrum of the fragment ion at *m/z* 149 in black and the calculated spectra of structure **11b** in red.

Figure 66
Experimental IRMPD ion spectrum of the fragment ion at *m/z* 149 in black and the calculated spectra of structure **10c** in red.

Figure 67
Experimental IRMPD ion spectrum of the fragment ion at *m/z* 149 in black and the calculated spectra of structure **10d** in red.

Figure 68
Experimental IRMPD ion spectrum of the fragment ion at *m/z* 149 in black and the calculated spectra of structure **10e** in red.

Table 14
Experimentally observed IR absorption bands of analyte **[6+H]⁺** (*m/z* 177) with and without collision-activation, and scaled harmonic vibrational modes calculated for ion structure **6b**.

Mode #	Obs. ν_{vib} [cm⁻¹]	Obs. (CID) ν_{vib} [cm⁻¹]	Calc. ν_{vib} [cm⁻¹]	Mode description
22	607	603	639	sidechain rock./twist.
23			656	C6 ring stretch., side-chain rock./twist.
30	948		921	ring breath., side-chain rock., O-C$_{side}$ stretch.
34	984		970	sidechain CH$_2$ wagg.
37			995	sidechain CH$_2$ twist./CH wagg.
44	1121	1120	1177	C6-H wagg., C5-H/C3-H rock., ring stretch.
45			1189	H-C6-CH$_3$ bend., C5-H/C3-H rock., ring stretch.
47	1228	mean 1231, peak 1254	1263	sidechain C-H$_2$ wagg./CH rock., C-O stretch., C3-H/C6-H rock.
50	1317	mean 1316, peak 1325	1332	ring stretch./breath., C5-H rock.
51			1338	ring stretch., C6-H rock., sidechain C-H$_2$ wagg.
55	1385	1386	1398	C1-C2-C3 ring stretch., C2-CH$_3$ bend./wagg., sidechain =C-H$_2$ bend.
57	1427	1441	1428	C-O stretch., sidechain C-H$_2$ bend., C6-CH$_3$ bend.
63	1468	1462	1459	C2-CH$_3$ wagg./bend., ring stretch
64			1471	C1-O stretch., sidechain C-H2 bend., C6-CH$_3$ bend.
66	1610	1608, 1652	1627	C=C ring stretch, C3-H/C5-H bend.

Table 15
Experimentally observed IR absorption bands of analyte **[6+H]⁺** (*m/z* 177) with and without collision-activation, and scaled harmonic vibrational modes calculated for ion structure **7**.

Mode #	Obs. ν_{vib} [cm⁻¹]	Obs. (CID) ν_{vib} [cm⁻¹]	Calc. ν_{vib} [cm⁻¹]	Mode description
22			563	O-H bend./rock.
24	607	603	647	sidechain rock./twist.
33	948		954	sidechain =CH$_2$ wagg.
44	1121	1120	1155	ring stretch., C3-H/C5-H rock., O-H rock, C4-CH$_3$ stretch.
46	1228	mean1231, peak 1254	1219	O-H rock., C3-H C5-H rock., C6-CH$_3$ stretch
47	1317	mean 1316, peak 1325	1267	O-H rock., C3-H rock., C2-CH$_3$ stretch.

51	1385	1386	1348	C3-H rock., ring stretch., C4C-H$_3$ bend., C2C-H$_3$ bend./wagg.
52			1356	C2C-H$_3$ bend./wagg., C-O stretch., C6C-H$_3$ bend./wagg.
55	1427	1441	1399	ring stretch., C-O stretch., sidechain bend.
56			1407	sidechain bend., ring stretch.
64	1468	1462	1464	C6C-H$_3$ bend./wagg., C2C-H$_3$ bend./wagg.,
65	1610	1608	1550	C=C ring. Stretch., C3-H bend., O-H bend.
66		1652	1617	C=C ring. stretch., C3-H bend. C5-H bend.

Table 16

Experimentally observed IR absorption bands of analyte **[6+H]**[+] (*m/z* 177) with and without collision-activation, and scaled harmonic vibrational modes calculated for ion structure **8**.

| Mode #	Obs. ν_{vib} [cm^{-1}]	Obs. (CID) ν_{vib} [cm^{-1}]	Calc. ν_{vib} [cm^{-1}]	Mode description
23			585	O-H bend./rock.
34	948		951	sidechain =C-H$_2$ wagg.
44	1121	1120	1169	O-H bend./rock., C3-H bend., C5-H bend., ring stretch
47	1228	mean 1231, peak 1254	1270	C5-H bend., C3-H bend., O-H bend./rock., ring stretch.
48			1271	C3-H bend., C5-H bend., O-H bend./rock., ring stretch.
51	1317	mean 1316, peak 1325	1325	C5-H bend./rock., C3-H bend./rock., ring stretch.
53	1385	1386	1375	C2C-H$_3$ bend./wagg.
54			1381	C6C-H$_3$ bend./wagg.
55	1427	1441	1407	sidechain bend.
56			1408	C-O stretch., ring stretch., C2C-H$_3$ bend., C6C-H$_3$ bend.
63	1468	1462	1460	C2C-H$_3$ bend./wagg., C6C-H$_3$ bend./wagg.
64			1471	C6C-H$_3$ bend./wagg., ring stretch., O-H bend./rock.
65	1610	1608	1572	ring stretch., C5=C6 stretch., O-H bend., C3-H bend., C5-H bend.
66		1652	1622	C2=C3 stretch., C5=C6 stretch., C3-H bend., C5-H bend.

Table 17

Experimentally observed IR absorption bands of analyte **[6+H]$^+$** after fragmentation to induce loss of ethene (*m/z* 149), and scaled harmonic vibrational modes calculated for ion structure **10c**.

Mode #	Obs. ν_{vib} [cm^{-1}]	Calc. ν_{vib} [cm^{-1}]	Mode description
34	1152	1154	O-H bend., C3-H/C5-H bend.
35	1209	1198	O-H bend., ring breath., C5-H bend., C2-CH$_3$/C4-CH$_3$ stretch.
36	1235	1228	C5-H bend., ring breath.
38		1312	C-O stretch., O-H bend., C-H$_{sidechain}$ bend., ring breath.
43	1393	1393	C-H$_3$ umbrella., ring breath.
46		1421	C-H$_{3,sidechain}$ umbrella
50		1460	C2-H$_3$ bend./umbrella, ring breath.
52		1573	C1-C$_{sidechain}$ stretch., C=C$_{ring}$ stretch., O-H bend., ring breath.
53	1618	1619	C1-C$_{sidechain}$ stretch., O-H bend., ring breath., C3-H bend.

3.3.3 Mechanistic Investigation

As we now have decided about the most likely ion structures present at the three different stages (unactivated, collision-activated and ethene loss product ions), we can have a closer look at the mechanism. Scheme 14 shows a new suggested mechanism of the Claisen rearrangement in accordance with the most probable ion structures discussed above.

The first step is the migration of the side chain from the oxygen to position 2 of the ring in ion **1b**, where four electron pairs are relocated concertedly as indicated. In the second step a 1,3-H shift takes place in which the oxygen is protonated and thus takes over the positive charge. This stabilizes the charge in the conjugated structure **7**. These two steps could also possibly occur in one step and leads to our actual Claisen rearrangement product, which then loses ethene upon fragmentation in the third step as indicated, where the vinylic bond is cleaved and the proton on the oxygen migrates to the side chain in order to eliminate ethene to yield the ion at *m/z* 149. In the next step the methyl group in position 2 is migrating to the positively charged residue of the sidechain under re-aromatization of the ring, which likely is the main driving force in this part of the mechanism. In the resulting intermediate, a hydride-shift to the now positively charged oxygen occurs to yield our final ion structure **10c**, which is further stabilized by mesomeric effects.
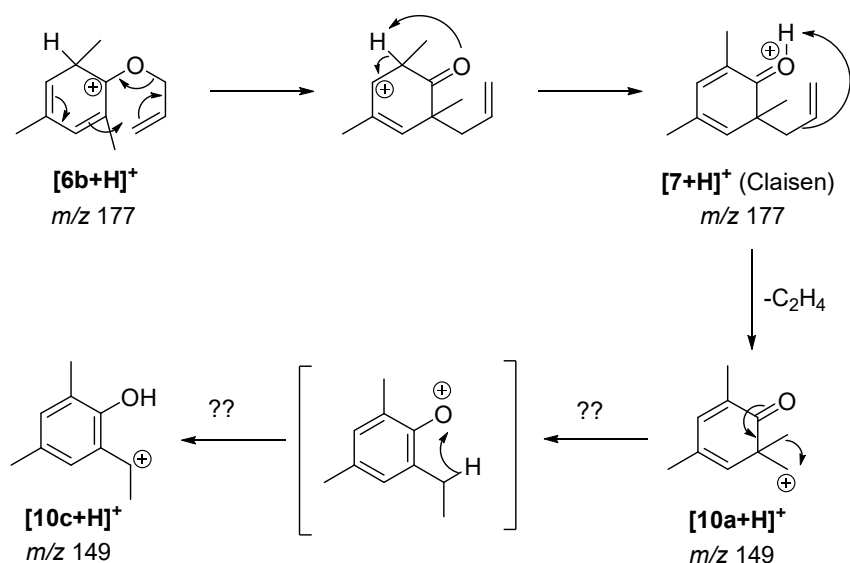
Scheme 14
Suggested mechanism of the Claisen rearrangement in the gas-phase in ESI-MS according to the most probable ion structures.

3.3.4 Claisen Rearrangement Reaction in Aza Derivatives - the Aza-Claisen Rearrangement

Beynon *et al.* also investigated Aza-derivates in the Claisen rearrangement in the gas-phase.[149] They were examining N-allyl-aniline in CI-MS and MIKE experiments, in which they are showing evidence for the acid-catalyzed Aza-Claisen rearrangement to also occur in the gas-phase. As it was the case in the regular Claisen reaction above, here also the loss of ethene is visible, next to the competing loss of ammonia.

We therefore wanted to probe this rearrangement in our study as well with *N*-allyl-aniline derivatives. The reaction path is shown for *N*-allyl-2,4,6-trimethylphenylamine **17** in Scheme 16. We further studied several other derivatives **17** – **20**, which are shown in Scheme 15.

The ESI-MS/MS experiments of protonated molecular ions of the aza-model compounds are shown in Figure 69 to Figure 74. Interestingly, the aza-*tert*-butyl derivatives **19** and **20** do not show the loss of ethene. In the spectrum of **19** with deuterated solvents, only the loss of a $^{\bullet}CH_3$ radical is visible at *m/z* 204. In the case of the other aza-derivatives **17** and **18**, the loss of ethene is visible, however, much less pronounced than it is in **6**. It is also worth to mention, that the deuterated compound **17** does not lose the C_2H_3D fragment if the deuterated molecular ion is isolated and fragmented. The main fragmentation channel in this case is the loss of the allyl-residue compared to the loss of the $^{\bullet}CH_3$ radical in **19**, which is already an interesting observation. The loss of the CH_3 radical might be favored if it is cleaved from the tert-butyl group, however this is not the case for compound **20**.

We also investigated analyte **17** via IRMPD ion spectroscopy. Figure 75 is showing the CID-activated (in gray) as well as the unactivated (in black) experimental spectrum of the ion **[17+H]**$^+$ at *m/z* 176. It is obvious that both spectra are almost the same, thus also likely originating from the same species. The position of the bands is the same in both spectra, just the intensities are slightly different, which might be likely due to a small change in the experimental conditions in the two experiments, but not due to the ions from which the spectra are yielded.

Figure 76 and Figure 77 are showing the experimental IR spectrum of **[17+H]**$^+$ (*m/z* 176) compared to calculated spectra of the isomer **17a** and **17b** respectively. The latter does not match the experiment well and can be safely ruled out. The first isomer matches quite good, however, the strong band at 1650 cm^{-1} is absent in the calculated spectrum and furthermore the band at 600 cm^{-1} is too low in intensity. In isomer **21**, the strong band at 1650 cm^{-1} results from N-H$_2$ bending and N=C double bond stretching combination mode in isomer 21 (see Figure 78

and Table 18). This N-H2 bending mode is shifted to lower wavenumbers in isomers 17**a** and 17**b** which is another criterion why we can rule them out. The strong band at 600 cm^{-1} is supposed to be a N-H_2 wagging mode as we can see for isomer 21, therefore we can again rule out ion **17b**. Also, for isomer **21** the modes ν_{23}, ν_{56}, ν_{65}, and ν_{66} (see Table 18) are matching convincingly well. If we compare isomer **21** to the experimental spectrum the match is most more convincing and therefore we postulate that in the case of analyte **17** in the aza-Claisen rearrangement the isomerization channel is easier to be overcome than it was the case for analyte **6**, and we already see only the rearrangement product without putting more energy into the ions via CID activation. All bands visible are assigned to the computed spectrum in Table 18.

Interestingly, in the case of the aza-derivates, the computations predict the protonation at the Nitrogen the be more stable than ring-protonation as Table 19 shows. The ring-protonated isomer **17b** is 43 kJ/mol higher in energy than the *N*-protonated isomer **17a**. This stands in contrast to the result in the normal Oxy-Claisen study above, where ring-protonation was energetically favored, which reflects the much higher proton affinity of the Nitrogen atom. Furthermore, the rearranged isomer **21** is 25 kJ/mol higher in energy than isomer **17a**, which is not expected as we observed the Aza-Claisen to occur even without activation.

Figure 79 finally is showing the comparison of the experimental spectrum of the fragment after the loss of ethene at *m/z* 148. The spectrum is compared with the calculation of isomer **23a**. There match is not convincing. The intense calculated bands at 1300 cm^{-1} and 1570 cm^{-1} as well as several bands below 1000 cm^{-1} are completely absent in the experimental data. We therefore cannot assign this structure unambiguously and this isomer might be a target for further computational studies.

17
m/z 175,1361

18
m/z 215,1674

19
m/z 217,1831

20
m/z 217,1831
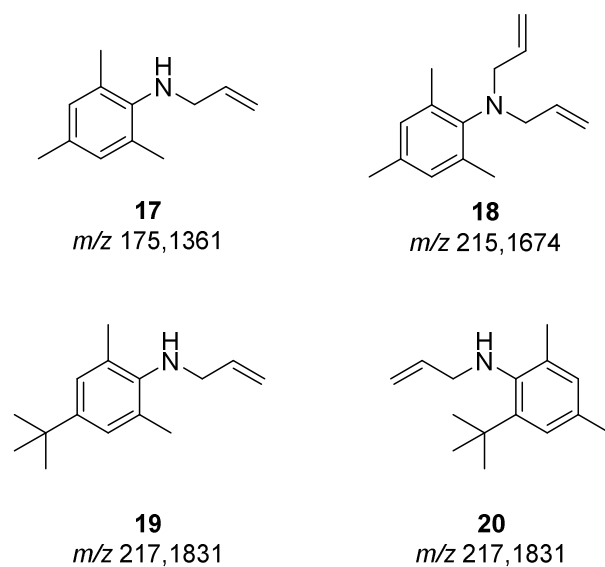
Scheme 15
Synthesized analytes **17**, **18**, **19** and **20** for the Aza-Claisen Study.

[17+H]⁺
m/z 176

Claisen

[21+H]⁺
m/z 176

-C_2H_4

[23a+H]⁺
m/z 148

Cope

[22+H]⁺
m/z 176

[23b+H]⁺
m/z 148
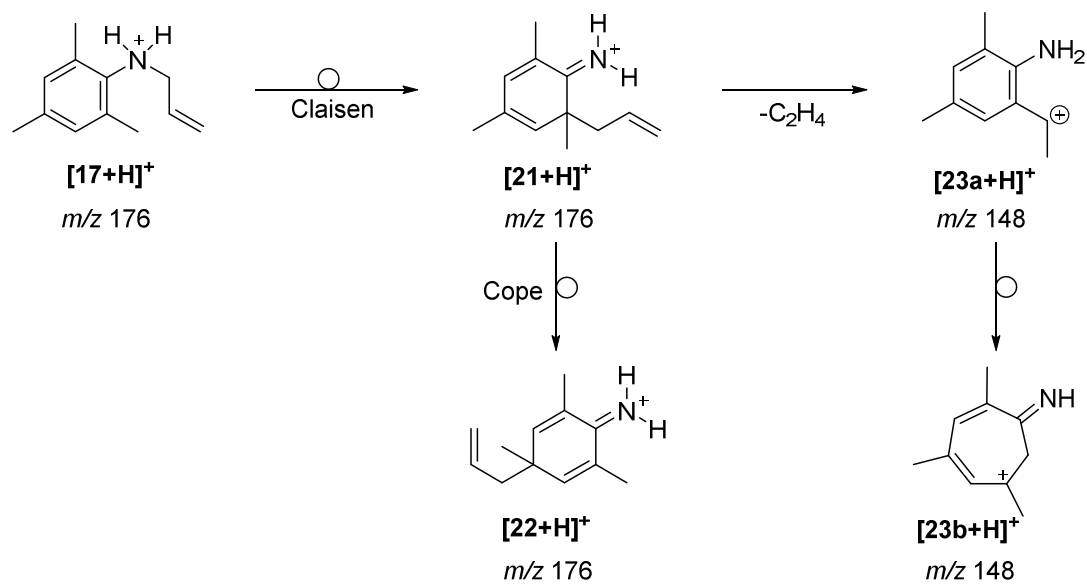
Scheme 16
Possible Structures before and after Claisen and Cope rearrangement of protonated analyte **17** (*m/z* 176) and fragmentation product *m/z* 148 in ESI-MS.

Table 18

Experimentally observed IR absorption bands of analyte **[17+H]$^+$** (*m/z* 176) without CID-activation, and scaled harmonic vibrational modes calculated for ion structure **21**.

Mode #	Obs. ν_{vib} [cm^{-1}]	Calc. ν_{vib} [cm^{-1}]	Mode description
20	599	530	NH$_2$ wagg., ring-C-H wagg., sidechain rock,/wagg.
23		562	NH$_2$ wagg.
29	858	859	ring-C3-H wagg.
34	977	954	ring-C5-H wagg.
38	1009	1003	sidechain wagg./twist.
46	1209	1180	sidechain rock., NH$_2$ rock., ring stretch.
47		1195	ring-C-H rock.
49	1306	1279	sidechain rock./wagg., ring-C-H-rock.
56	1375	1411	ring stretch., C6-CH$_3$ wagg./twist., NH$_2$ rock.
65	1461	1477	C1-N stretch., C1/C6-CH$_3$ wagg./twist.
66	1573	1553	ring stretch, NH$_2$ bend.
67	1648	1629	NH$_2$ bend., C1-N stretch., ring stretch.
68		1653	NH$_2$ bend., C1-N stretch., ring stretch.

Table 19

Relative energies of the Aza-Claisen structures **17a**, **17b**, and **21**.

Structure	17a	17b	21
$\Delta\Delta G$ [kJ mol^{-1}]	0	+43	+25
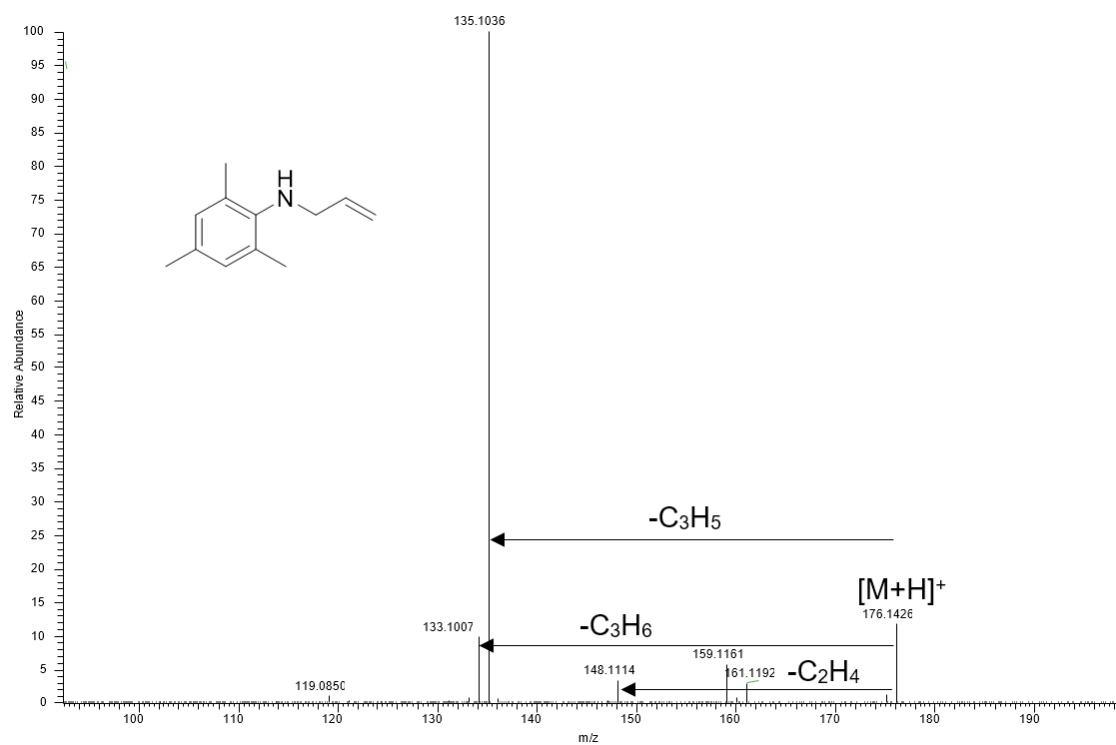
Figure 69
ESI-MS/MS spectrum of *N*-allyl-2,4,6-trimethylphenylamin **17** in MeOH without formic acid.
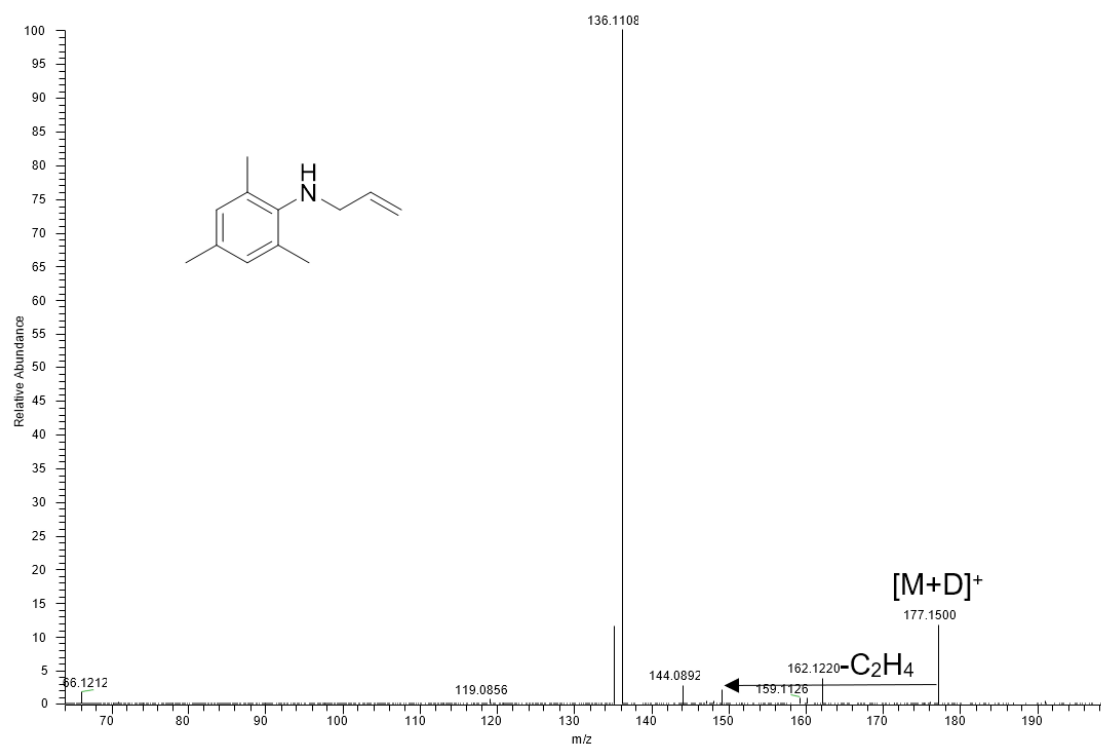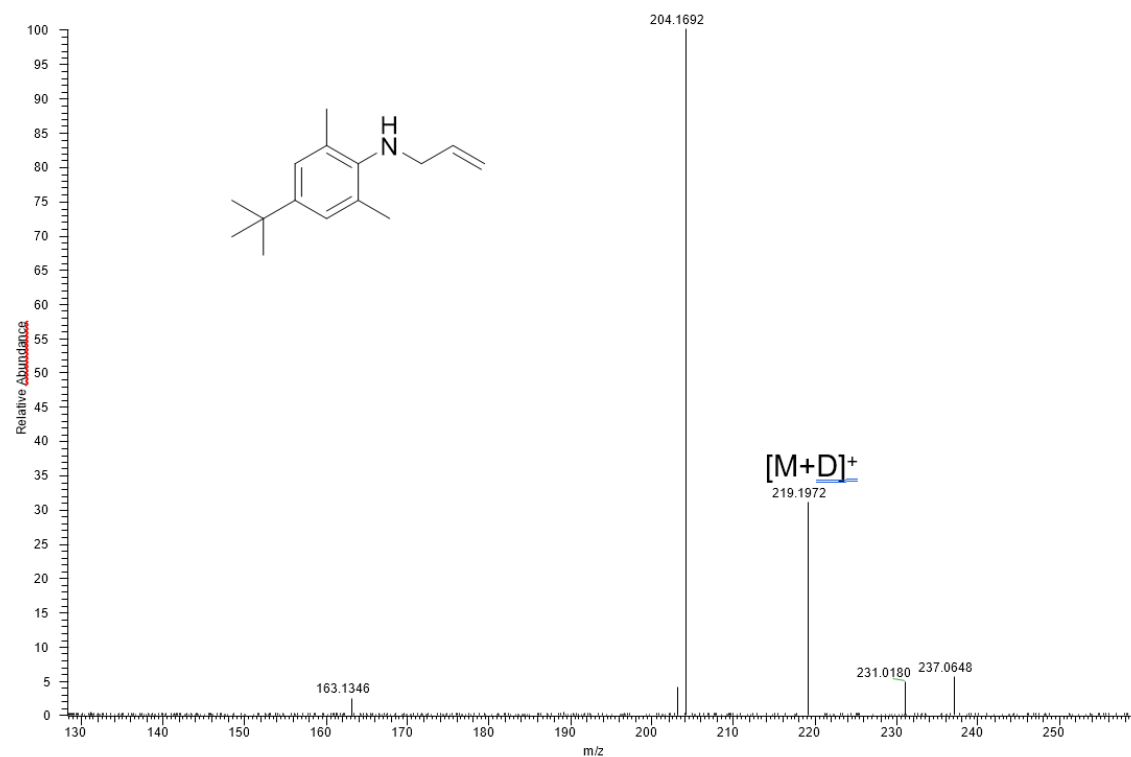

Figure 70
ESI-MS/MS spectrum of *N*-allyl-2,4,6-trimethylphenylamin **17** in MeOD without formic acid.
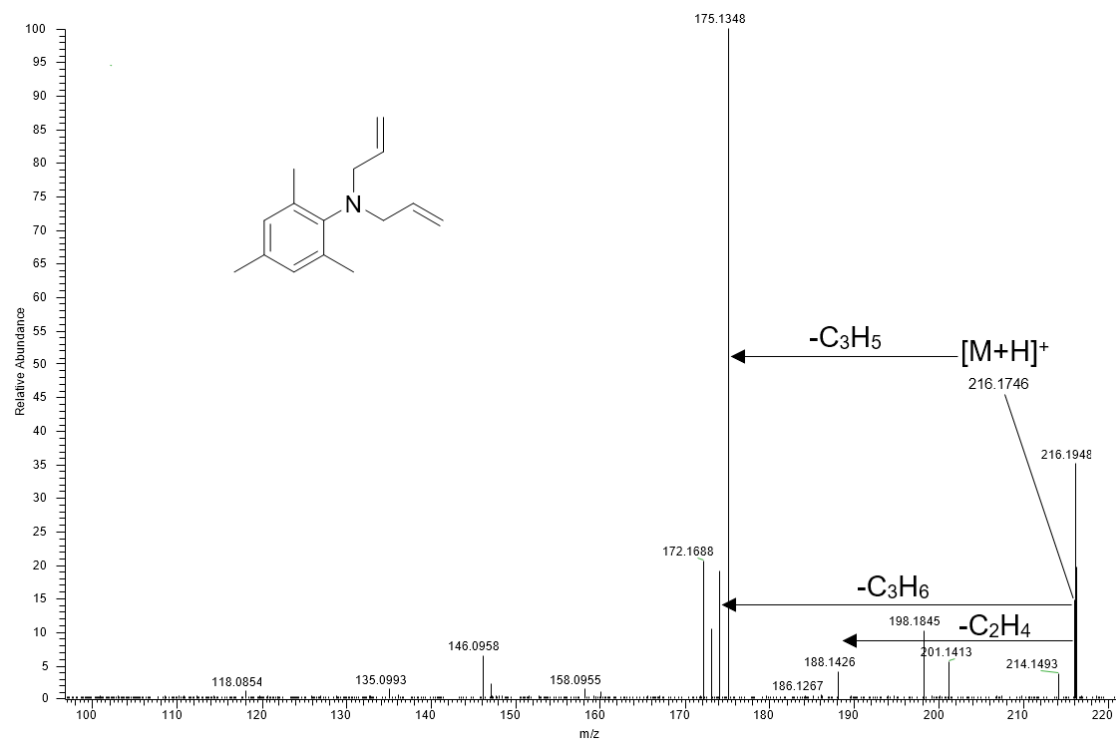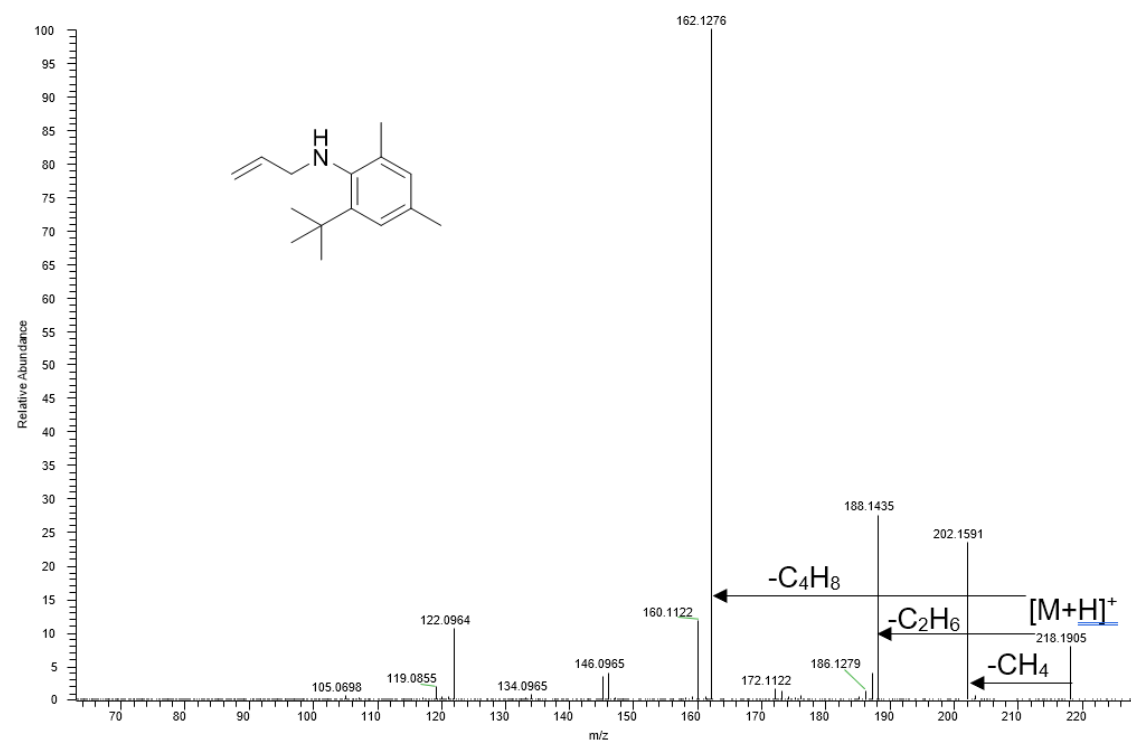
Figure 71
ESI-MS/MS spectrum of *N,N*-diallyl-2,4,6-trimethylphenylamin **18** in MeOH without formic acid.
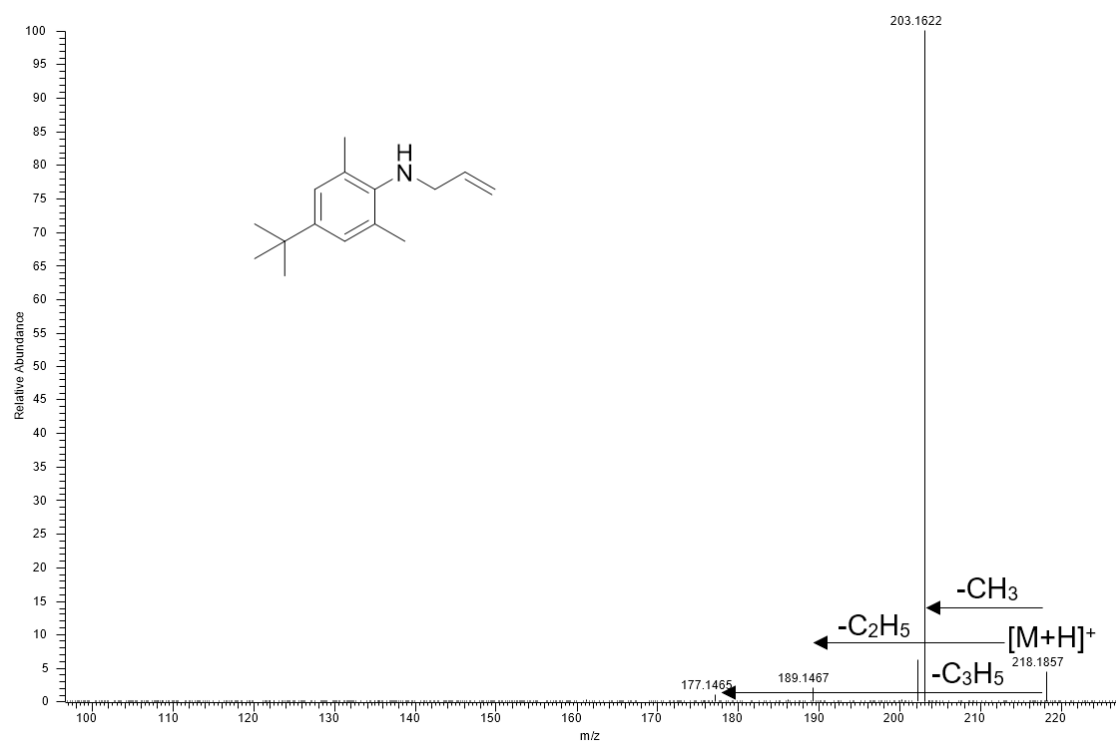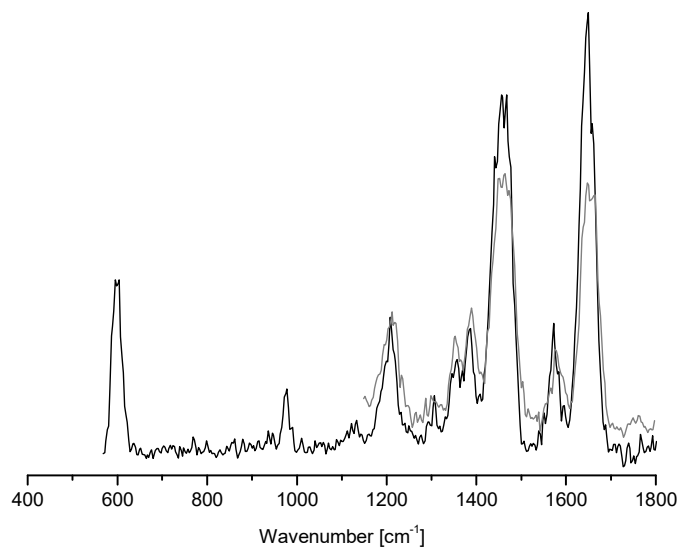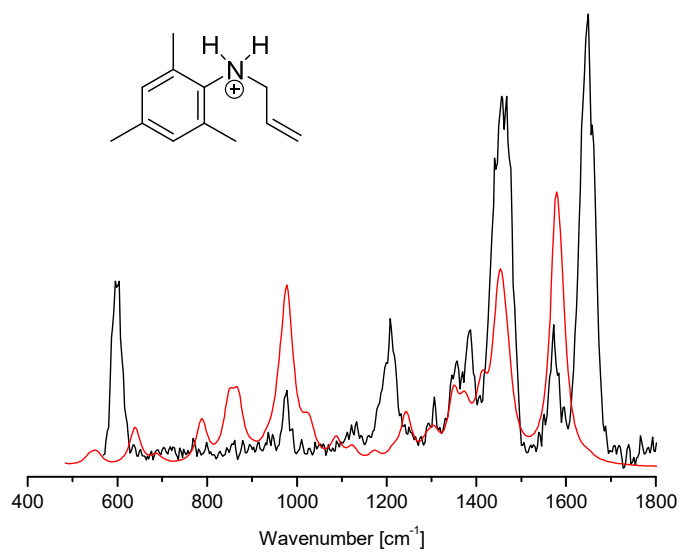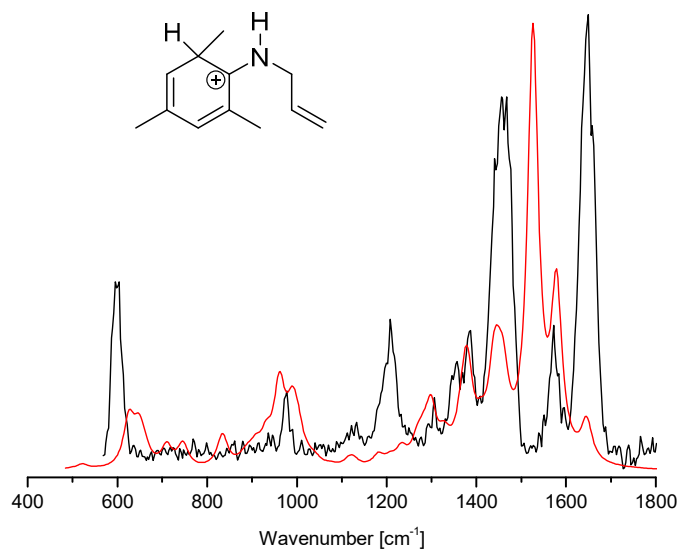

Figure 72
ESI-MS/MS spectrum of *N*-allyl-2,6-dimethyl-4-*tert*-butylphenylamin **19** in MeOH without formic acid.

Figure 73
ESI-MS/MS spectrum of *N*-allyl-2,6-dimethyl-4-*tert*-butylphenylamin **19** in MeOD without formic acid.

Figure 74
ESI-MS/MS spectrum of *N*-allyl-4,6-dimethyl-2-*tert*-butylphenylamin **20** in MeOH without formic acid.

Figure 75
Experimental IRMPD ion spectra of both CID-activated (grey) and unactivated (black) **[17+H]**[+] (*m/z* 176).
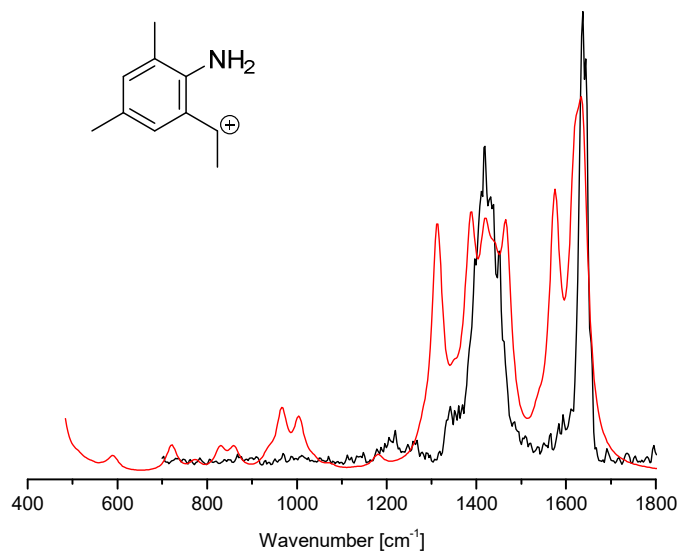

Figure 76
Experimental IRMPD ion spectrum of the **[17+H]**[+] ion at *m/z* 176 in black and the calculated spectrum of structure **17a** in red.

Figure 77
Experimental IRMPD ion spectrum of the **[17+H]+** ion at *m/z* 176 in black and the calculated spectrum of structure **17b** in red.
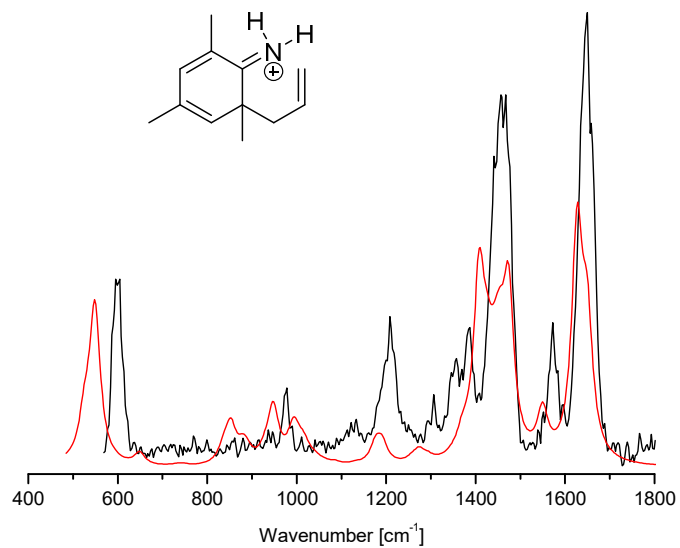
Figure 78
Experimental IRMPD ion spectrum of the **[17+H]**[+] ion at *m/z* 176 in black and the calculated spectrum of structure **21** in red.

Figure 79
Experimental IRMPD ion spectrum of the fragment ion at *m/z* 148 in black and the calculated spectrum of structure
23a in red.

3.3.5 Conclusions on the Claisen Rearrangement Study

In this study we aimed to probe the mechanism of the Claisen and Aza-Claisen rearrangement in the gas-phase, unperturbed from solvent effects, and collected spectroscopic data via IRMPD ion spectroscopy and theoretical calculations on the different possible isomers.

Our data indicates for the test-case of allyl-2,4,6-trimethylphenylether, that before the Claisen rearrangement occurs, the ion is protonated in *ortho*-position to the ether-group, and therefore annulling the aromatization. This is an interesting finding and different from most common textbook literature, in which such ethers are usually described to be protonated at the ether-oxygen.

Further we find that after collision-activation when the Claisen rearrangement occurred, the sidechain has migrated to the ortho position and is not transferred further to the *para*-position as the Claisen-Cope-Tandem reaction would suggest.

In case of the Aza-Claisen our data suggests that the rearrangement already occurred without any activation, reflecting the lower energy needed for the Aza-Claisen reaction to be triggered. However, we were not able to unambiguously assign a structure for the ion after the loss of ethene.

We further proposed a new mechanism for the Claisen rearrangement in the gas-phase.

4 General Summary and Conclusion

In this thesis three main studies were successfully finished and acquired a lot of new IR data as well as extensive theoretical computations, where the latter were contributed from collaborators.

The first study was the investigation of the unimolecular fragmentation pathways of phenol and aniline radical cations in EI-MS and the characterization of the molecular ions as well as possible tautomeric structures via cryogenic messenger ion spectroscopy. Furthermore, we aimed to identify the common product ion at m/z 66. Our new data set suggest that the molecular radical cations **1** and **3** are the exclusive present ion isomers in EI-MS. In case their reactive tautomers **2** and **4** are formed too, they are too short-lived to be measured with our technique of cryogenic messenger ion spectroscopy. The PES of their reaction trajectories also indicate, that once they isomerized, they possess more than enough energy to decompose. We further showed in our study that the common fragment yielded from both, phenol as well as aniline, at m/z 66, is indeed the cyclopentadiene radical cation as proposed earlier in the literature. Additionally, this study complements the gas-phase ion chemistry of the open shell molecular ions investigated in the cryogenic messenger-IR ion spec study of tautomeric structures of $[C_6H_6O]^{\bullet+}$ and $[C_6H_7N]^{\bullet+}$ ions formed by EI-MS. Furthermore, our results are in accordance with already published results in the literature.[2, 24, 95, 96, 169]

The second study aimed to identify the ion structure of the product fragment of intriguing 2H and 3H rearrangement reactions in several electron rich aryl alkanols in EI- and ESI MS via IRMPD ion spectroscopy. We showed that product ion from the 2H rearrangement m/z 136 ($C_9H_{14}N^+$) is indeed protonated *N,N*-dimethyl-*para*-toluidine, as was already suggested by Kuck et al..[3] However, the position of the extra proton is confirmed to be in the *ortho*-position according to our data and not in *para*-position as proposed earlier. Furthermore, our data shows that the product ion yielded from the 3H rearrangement at m/z 123 ($C_8H_{13}N^{\bullet+}$) is the radical cation of *N,N*-dimethyl-2,3-dihydroaniline. This new finding necessitates a correction of the older results. Our calculations further showed that this isomer also is the most stable one in the ion series examined in this work. In addition, this study offers a revised mechanisms for the 2H and 3H rearrangement reactions based on our new findings and evidence from computational chemistry and IRMPD ion spectroscopy.

In the third study we engaged to investigate the classic and well know Claisen and Aza-Claisen rearrangement reaction in the gas-phase in ESI-MS and ESI-MS^2 via IRMPD ion spectroscopy and computational chemistry. Our data shows that before the Claisen rearrangement occurs, the ion is protonated in *ortho*-position to the ether-group, and not at the oxygen as expected, which is likely due to the trimethyl substituents enabling the aromatic ring to be in competition for protonation with the oxygen. Further we show that upon collision-activation the sidechain migrates to the *ortho*-position according to the Claisen rearrangement and is not transferred further to the *para*-position as the Claisen-Cope-Tandem reaction would suggest. In case of the Aza-Claisen reaction our data suggests that the rearrangement reaction already occurred without any activation, reflecting the lower energy needed for the Aza-Claisen reaction to be triggered. However, we were not able to unambiguously assign a structure for the ion after the loss of ethene. Additionally, we also proposed a new mechanism for the Claisen rearrangement in the gas-phase.

All these results further demonstrate that IR ion spectroscopy of gaseous ions is a powerful tool in combination with computational chemistry to elucidate the structural identity of fragment ions and elusive intermediates for which precedent information from independent and regular mass spectrometric methods is not available.

5 Outlook

In an independent approach, one could aim to generate [2,4-cyclohexadien-1-one]$^{\bullet+}$ ions **3** by a *retro*-Diels-Alder reaction from the bicyclo[2.2.2]oct-2-ene-5,7-dione molecular ion upon ketene loss (see Scheme 17) in EI-MS as a promising alternative route to access the phenol tautomer **3** for IR ion spectroscopic analysis and reference data.
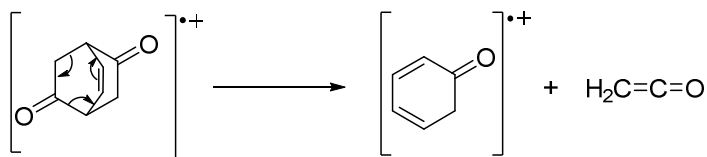
Scheme 17
The molecular ion of bicyclo[2.2.2]oct-2-ene-5,7-dione delivers [2,4-cyclohexadien-1-one]$^{\bullet+}$ ion in a *retro*-Diels-Alder ketene loss reaction.[94]

The vibrational inversion mode (N-H$_2$ wagging) at 661 cm^{-1} was not predicted correctly with current quantum chemical calculations in our study and in the literature. Therefore, this band might be a target for further computational studies as a model for vibrational modes which are difficult to predict via computational chemistry.

The energetic and mechanistic details of the unusual 3H rearrangement intramolecular redox process and of those associated with the dihydrogen transfer occurring in the 2H rearrangement reaction await further computational investigation. Computing the PES and transitions states in more detail might help clarify these mechanisms in more detail. This research may also include the role of ion-neutral complexes.

We were not able to unambiguously assign the ion structure after the loss of ethene for the isomer at *m/z* 148 in the Aza-Claisen rearrangement. Therefore, this uncharacterized ion might be a target for further computational studies.

6 Experimental Section

6.1 General

Chemicals

Commercially available chemicals were bought from *Merck*, *Acros*, *Alfa Aesar*, *TCI* or *Sigma Aldrich* and were used without further purification.

Solvents

All solvents were purified by a distillation column before usage. Dry solvents were used after distillation with the addition of a specific drying-agent under argon atmosphere.

Inert Gas

BIP© Argon (O_2 < 10 ppb, H_2O < 20 ppb, $CO + CO_2$ < 100 ppb) was used as inert gas. The gas was purchased from AirProducts and was further dried over silica gel blue and phosphor pentoxide. Oxygen was removed from the argon by a BTS-catalysator from *BASF*.

Reactions under exclusion of water and air

Reactions that were done under argon were executed with dry solvents. The set up was dried and flushed with argon before the addition of any compounds.

Thin Layer Chromatography (TLC)

60 F254 aluminum plates with a layer of silica were used for TLC. A fluorescence directors provided by *Merck KGaA* was used to analyze the TLC samples with UV-light. Compounds were detected by UV-light ($\lambda = 254$ nm) or by colorization with $KMnO_4$.

Flash Chromatography

The solvent mixtures are stated in volumetric ratios. *Macherey-Nagel* silica gel (0.040 – 0.060 mm / 230 – 400 mesh) was used for flash chromatography. The length and width of the column were determined individually depending on the reaction. For increasing the flowing rate pressure was used.

Mass Spectrometry (GC-MS)

GC-MS spectra were recorded by a *Hewlett-Packard HP 6890* Series Plus gas chromatograph with injector, auto sampler, and HP 5973 mass selective detector. The carrier gas was Hydrogen. The used column was a *Hewlett Packard HP-5 MS*, 30 m x 0.25 mm ID with 2.5 μm film thickness.

Nuclear Magnetic Resonance Spectroscopy (NMR)

A *Bruker* DPX300 NMR-spectrometer was used to determine the structure of the compounds. All NMR-spectra were recorded at RT. Parts per million (ppm) was used as the unit of the chemical shift δ. The 1H-NMR spectra were calibrated to TMS (0.00 ppm), and the 13C-spectra were calibrated to CDCl3 (77.2 ppm). The scalar coupling was specified in Hertz (Hz). To determine the multiplicity of a signal "s" for singlet, "d" for doublet, "t" for triplet and "m" for multiplet were used.

Fourier-Transform Infrared Spectroscopy (FT-IR)

The IR-spectra recording was executed with an UART-spectrometer with ATR technique from the company *Perkin-Elmer*. The relative frequency is specified in wave number $\tilde{v}[cm^{-1}]$. The relative intensity is specified with (br) broad, (w) weak, (m) medium and (s) strong.

Melting Point

To identify the melting point of solid compounds a *Büchi 535* was used. Melting point analysis was executed in open glass capillary.

6.2 EI-MS

For EI-MS experiments we used an ISQ GC-MS instrument (Thermo Fisher) and an Exactive GC-MS Orbitrap instrument (Thermo Fisher). For EI-MS on the ISQ instrument, samples of the analytes were dissolved in methanol ($\sim 10^{-3}$ mol/L) and introduced via a heated direct inlet probe (DIP). The DIP-EI-MS measurements were performed under programmed DIP heating from 50 °C to 280 °C in steps with a temperature gradient of 60 °C/min, electron energy of 70 eV and source pressure of ~70 mTorr. The EI mass spectra were acquired at a source temperature of 250 °C. For GC-EI-MS (70 eV) on the Exactive GC-MS Orbitrap instrument,

the samples were dissolved in anhydrous acetonitrile (~10 µg/mL) and injected automatically. The temperature program for the GC fractionation was set from 50 °C to 270 °C in steps of 10 °C every minute. Helium gas was used as a carrier gas and the spectra were acquired at a resolution of 60,000 in the Orbitrap analyzer. We used a TG-5SILMS GC column (Thermo Fisher) with a length of 30 m and a diameter of 0.15 mm.

6.3 ESI-MS

All ESI-MS experiments were performed on an LTQ Orbitrap XL instrument (ThermoFisher, Bremen). The samples were dissolved in anhydrous acetonitrile (~10 µg/mL) and injected via a direct injection syringe with a flow rate of 3-5 µL/min. All solvents used were HPLC grade and acquired from Acros or Fisher Chemicals. The samples were ionized in an ESI source with a spray voltage of 3.2 kV and a vaporizer temperature of 53 °C. The capillary temperature was set to 250 °C and the tube lens was set to 130 V. The LTQ vacuum was $2 \cdot 10^{-5}$ torr and the Orbitrap vacuum was $0.25 \cdot 10^{-10}$ torr. The energy used for the product ion spectra was set between 20% and 26% normalized collision energy. The ESI-MS data were acquired at a resolution of 100,000 for MS^1 (exp error ≤ 2 ppm) and 30,000 for MS^2.

6.4 IR Ion Spectroscopy

IR-PD and IRMPD.
The FELion instrument at FELIX was used for cryogenic messenger IR spectroscopy. The compounds were introduced as solid or liquid through an in-house build sample inlet, with the possible for heating, and subsequently ionized in an EI-MS ion source. The cryogenic 22-pole trap instrument FELion is described in detail elsewhere.[62]
The ESI-MS, ESI-MS^2 and IR ion spectroscopy measurements were carried out at room temperature at the Free Electron Laser for Infrared eXperiments (FELIX) Laboratory[43] at Radboud University, Nijmegen (The Netherlands), and conducted with a Bruker Amazon Speed ETD mass spectrometer coupled to the FEL, as described in detail elsewhere.[44] The ions were irradiated with 4 laser pulses of FELIX (90-120 mJ per pulse, bandwidth 0.4% of the IR wavelength)   and   the   IRMPD   intensity   defined   as   −ln [precursor / (precursor +

sum_fragments)] was linearly corrected to account for the frequency-dependent variations in laser pulse energy.

A commercial cw IR optical parametric oscillator (Aculight Argos Model 2400) was used for the OPO measurements. These lasers can usually operate in the region of roughly around 2,000–5000 cm^{-1} and at a power level of several hundred mW up to a few Watts. They essentially consist of an optical resonator and an optical nonlinear crystal (e.g., beta barium borate, BBO). The big advantage is that they are small and easy to handle and can be basically mounted anywhere.

Saturation depletion scans.

To determine the ratio of a tautomer with respect to the total stored ion number, a saturation depletion measurement was performed. Here, the depletion of the ion signal intensity as a function of the number of laser pulses and hence the deposited energy is investigated. Based on the quantum-chemical calculations described in detail the main part of the publication, a laser frequency is chosen for which a vibrational transition for only one of the two possible tautomers is expected. Therefore, only one of the two tautomers is able to absorb photons and the other one is basically transparent. By using a laser on-off measurement, ion signal losses that do not result from excitation of the ion by the laser, but from variable storage times in the ion trap, can be taken into account. Extrapolating the measured curves accordingly, the maximal possible depletion of the ion signal due to the laser pulses at this specific energy can be determined. In several independent measurements for different excitation frequencies, it was found for both aniline$^{\bullet+}$ and phenol$^{\bullet+}$ that in each case only one tautomer could be stored in the ion trap.

6.5 Computations

Quantum chemical calculations were performed to determine the structures of the ions. All calculations in the studies of this work were performed with the Gaussian16 software,[185] by the Density Functional Theory (DFT) method using the (U)B3LYP functional (opt = tight, int = ultrafine) and the basis sets cc-pVDZ, cc-pVTZ or cc-pVQZ.[90] As is common practise, the calculated harmonic vibrational frequencies were scaled by a factor of 0.969,[90] similar to the one used earlier.[19, 21-23] To take dispersion interactions into account, Grimme's D3 correction with Becke–Johnson damping (GD3BJ) was used.[186] The perturbation caused by the weakly

bound tagged Ne-atom in cryogenic ion spectroscopy experiments is expected to be small.[62, 187, 188] It is assumed to be negligible compared to the accuracy of the frequency calculations as well as the measured vibrational band width. Thus, all calculations were performed omitting the neon tags. Scaled harmonic frequencies have been used to assign vibrational fundamentals in the spectra. Additionally, anharmonic force field calculations - also performed at the (U)B3LYP and cc-pVQZ level of theory - have been used in the assignment of assumed combination modes and overtones. Based on these calculations, zero-point vibrational energy (ZPVE) corrections were also made where necessary.

All ion structures were verified as stationary minima on the PES having no imaginary frequencies. Based on these calculations, zero-point vibrational energy (ZPVE) corrections were made.

6.6 Synthesis of the Analytes

Synthesis of allyl-2,4,6-trimethylphenylether 6
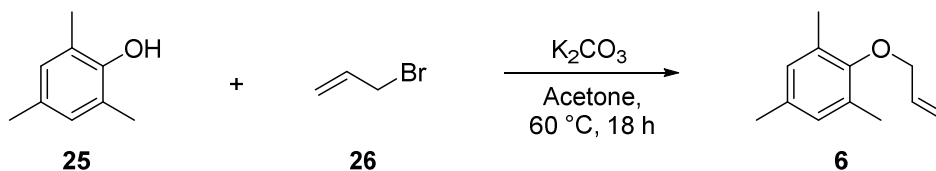
Mesitol **25** (2.00 g, 14.7 mmol) was dissolved in acetone (20 mL). Potassium carbonate (2.44 g, 17.6 mmol) and allyl bromide **26** (2.67 g, 22.0 mmol) were added subsequently, and the suspension was heated to 60 °C for 18 h. The suspension was filtered, and the filtrate was concentrated under reduced pressure. The residue was dissolved dichloromethane (30 mL) and the solution was washed with aqueous sodium hydroxide solution (40 mL, 2 M) and the combined organic layers were dried over MgSO$_4$. After the solvent was removed under reduced pressure and the crude product was purified by flash chromatography (EtOAc/*c*-Hex, 1:10), the product **6** was gained as colorless liquid with a yield of 78 % (2.01 g, 11.4 mmol).

6   C$_{12}$H$_{16}$O (176.26 g/mol).

Yield   2.01 g (11.4 mmol, 78 %, Lit.[189]: 44 %).

Habitus   Colorless liquid.

TLC R_f = 0.45 (EtOAc/*c*-Hex 1:10).

GC-MS   *m/z* (%) = 176 (35), 135 (100), 105 (9), 91 (29), 79 (10).

¹H NMR   (500 MHz, Chloroform-*d*) δ = 6.82 (s, H-2, 2H), 6.16 – 6.06 (m, H-5, 1H), 5.46
                   - 5.39 (m, H-6′, 1H), 5.25 (dd, *J*=10.4, 1.3, H-6, 1H), 4.28 (dt, *J*=5.5, 1.2, H-4,
                   2H), 2.24 (s, H-3, 6H), 2.24 (s, H-1, 3H) ppm.

¹³C-NMR   (126 MHz, Chloroform-*d*) δ = 153.82, 134.40, 133.23,130.76, 129.47, 117.19,
                   73.32, 20.81, 16.43 ppm.

IR   (ATR): $\tilde{\nu}$ = 3082 (w), 2919 (w), 2860 (w), 2731 (w), 1728 (w), 1647 (w), 1483
                   (m), 1421 (w), 1407 (w), 1374 (w), 1353 (w), 1308 (w), 1212 (s), 1146 (m),
                   1006 (m), 990 (s), 922 (m), 852 (s), 792 (w), 758 (w), 734 (w), 622 (w), 585
                   (m), 555 (w) cm⁻¹.
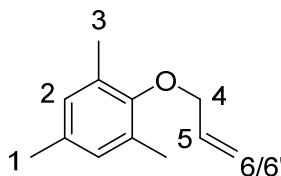
Synthesis of 4-*tert*-butyl-2,6-phenol 29
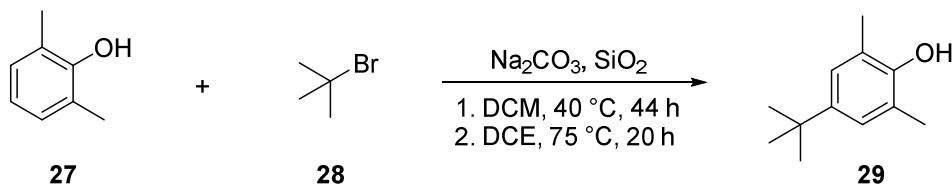
2,6-Dimethylphenol **27** (2.00 g, 11.2 mmol), Na₂CO₃ (3.57 g, 33.7 mmol) and SiO₂ (11.3 g,
187 mmol) were suspended in DCM (30 mL). The suspension was treated with *tert*-butyl-
bromide **28** (2.50 mL, 11.0 mmol) and refluxed at 40 °C for 44 h. The mixture was diluted with
DCE (20 mL) and another portion of *tert*-butyl-bromide (2.5 mL, 11 mmol) was added. The

solution was refluxed for 20 h at 75 °C and cooled to room temperature and filtered. The residue was washed with diethyl ether (100 mL) and the solvent was evaporated under reduced pressure. After the crude product was recrystallized from *n*-pentane the desired alcohol **29** was gained as colorless solid with a yield of 41 % (0.811 g, 4.55 mmol).

29 $C_{12}H_{18}O$ (178.27 g/mol).

Yield   0.811 g (4.55 mmol, 41 %, Lit.[190]: 85 %).

Habitus   Colorless solid.

M.P.   80 – 82 °C (Lit.[191]: 81.6 – 82.2 °C).

GC-MS   *m/z* (%) = 178 (29), 163 (100), 135 (17).

¹H NMR   (300 MHz, Chloroform-*d*) δ = 6.99 (s, H-2, 2H), 4.47 (s, H-O, 1H), 2.24 (s, H-3, 6H), 1.28 (s, H-1, 9H) ppm.

¹³C-NMR   (75 MHz, Chloroform-*d*) δ = 149.89, 142.90, 125.52, 122.34, 33.92, 31.62, 16.20 ppm.

IR   (ATR): $\tilde{\nu}$ = 3340 (br), 3051 (w), 2959 (w), 2731 (m), 2903 (m), 2865 (w), 2051 (w), 1742 (w), 1605 (w), 1504 (m), 1487 (s), 1460 (m), 1212 (s), 1414 (w), 1391 (w), 1361 (m), 1335 (m), 1307 (m), 1274 (w), 1236 (m), 1195 (s), 1122 (s), 1026 (w), 994 (w), 949 (w), 867 (s), 817 (m), 731 (m), 635 (m), 533 (br) cm⁻¹.
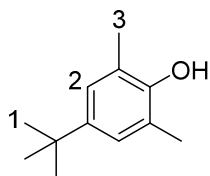
Synthesis of allyl-2,6-dimethyl-4-*tert*-butylphenylether 9
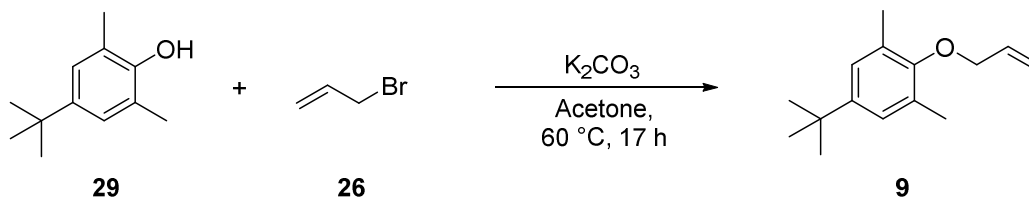
The alcohol **29** (0.77 g, 4.31 mmol) and K_2CO_3 (0.72 g, 5.17 mmol) were suspended in acetone (10 mL). The suspension was treated with allyl bromide **26** (0.56 mL, 6.47 mmol) and the reaction mixture was refluxed at 60 °C for 17 h. The suspension was cooled to room temperature, and it was filtered and washed with acetone (20 mL). The solvent was evaporated and the reside was treated DCM (20 mL) and washed with NaOH (2 M, 30 mL). The organic layer was dried over $MgSO_4$, and the solvent was removed under reduced pressure. After the residue was purified by column chromatography (*c*-Hex/EtOAc 10:1) the desired ether **9** was gained as a colorless liquid with a yield of 67 % (0.63 g, 2.88 mmol).

9 $C_{15}H_{22}O$ (218.34 g/mol).

Yield   0.63 g (2.88 mmol, 67 %).

Habitus   Colorless liquid.

TLC R_f = 0.79 (*c*-Hex/EtOAc 10:1).

GC-MS   *m/z* (%) = 218 (15), 208 (20), 207 (100), 191 (10), 177 (33), 163 (16), 137 (13),
                   119 (11).

^{1}H NMR   (500 MHz, Chloroform-*d*) δ = 7.00 (s, H-2, 2H), 6.15 – 6.07 (m, H-5, 1H), 5.43
                   (dq, *J*=17.2, 1.7, H-6, 1H), 5.25 (dq, *J*=10.4, 1.4, H-6′, 1H), 4.29 (dt, *J*=5.5, 1.5,
                   H-4, 2H), 2.27 (s, H-3, 6H), 1.28 (s, H-1, 9H) ppm.

^{13}C-NMR   (126 MHz, Chloroform-*d*) δ = 153.65, 146.35, 134.38, 130.06, 125.66, 116.92,
                   73.06, 34.10, 31.52, 16.65 ppm.

IR   (ATR): $\tilde{v}$ = 3017 (w), 2962 (m), 2866 (m), 2730 (w), 1745 (w), 1647 (w), 1595 (w), 1486 (s), 1461 (m), 1420 (m), 1394 (w), 1374 (w), 1362 (m), 1310 (m), 1197 (s), 1123 (s), 1009 (m), 989 (s), 921 (s), 870 (s), 820 (m), 768 (m), 735 (w), 646 (m), 556 (w), 530 (w), 516 (w) cm^{-1}.
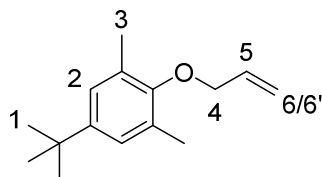
**Synthesis of *N*-allyl-2,4,6-trimethylaniline 17 and Synthesis of *N*,*N*-diallyl-2,4,6-trimethylaniline 18**
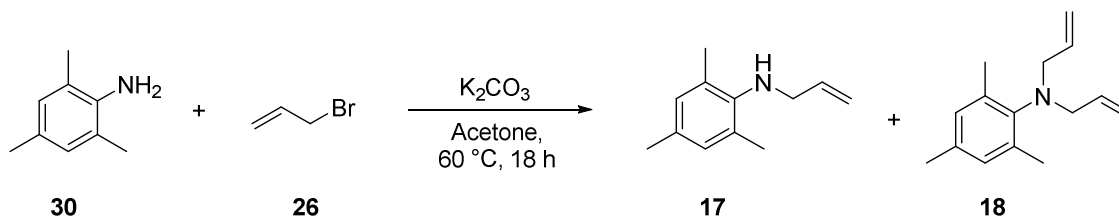
K$_2$CO$_3$ (6.13 g, 44.4 mmol) was suspended in acetone (15 mL) and the suspension was treated with allyl bromide **26** (2.56 mL, 29.6 mmol) and 2,4,6-trimethylaniline **30** (2.10 mL, 14.8 mmol). The reaction mixture was refluxed at 60 °C for 18 h and then cooled to room temperature. It was filtered and the residue was washed with acetone (25 mL). The solvent was evaporated, and the residue was treated with DCM (40 ml) and washed with NaOH (2 M, 60 mL). The organic layer was dried over MgSO$_4$, and the solvent was removed under reduced pressure. After the residue was purified by column chromatography (*c*-Hex/EtOAc 9:1) the desired monosubstituted amine **17** was gained as a red liquid with a yield of 37 % (0.96 g, 5.50 mmol). The disubstituted amine **18** was gained as a yellow liquid with a yield of 60 % (1.93 g, 8.94 mmol).

17   C$_{12}$H$_{17}$N (175.28 g/mol).

Yield   0.96 g (5.50 mmol, 37 %, Lit.[145]: 32 %).

Habitus   Red liquid.

TLC R_f = 0.51 (*c*-Hex/EtOAc 9:1).

ESI-MS   Calc. for $C_{12}H_{17}NH$ $[M+H]^+$: 176.1439 found: 176.1429; Δ = 5.7 ppm.

¹H NMR   (500 MHz, Chloroform-*d*) δ = 6.82 (s, H-2, 2H), 6.03 – 5.95 (m, H-5, 1H), 5.26 (dq, *J*=17.1, 1.2, H-6, 1H), 5.13 – 5.08 (m, H-6′, 1H), 3.54 (dq, *J*=6.1, 1.1, H-4, 2H), 2.77 (s, br, H-N, 1H), 2.25 (s, H-3, 6H), 2.22 (s, H-1, 3H) ppm.

¹³C-NMR   (126 MHz, Chloroform-*d*) δ = 143.22, 136.82, 131.41, 129.79, 129.40, 115.89, 51.52, 20.59, 18.35 ppm.

IR   (ATR): $\tilde{\nu}$ = 3373 (br), 3078 (w), 2971 (w), 2915 (m), 2858 (w), 2731 (w), 1729 (w), 1643 (w), 1594 (w), 1484 (s), 1443 (m), 1417 (m), 1373 (w), 1351 (w), 1328 (w), 1304 (m), 1224 (s), 1155 (m), 1136 (w), 1064 (w), 1028 (m), 1011 (m), 994 (m), 953 (w), 917 (s), 852 (s), 734 (m), 698 (m), 580 (m), 562 (m) cm⁻¹.
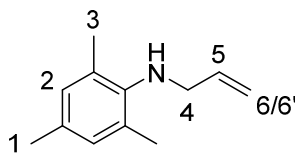
18 $C_{15}H_{21}N$ (215.34 g/mol).

Yield   1.93 g (8.94 mmol, 60 %, Lit.[145]: 61 %).

Habitus   Yellow liquid.

TLC R_f = 0.84 (*c*-Hex/EtOAc 9:1).

ESI-MS   Calc. for $C_{15}H_{21}NH$ $[M+H]^+$: 216.1708 found: 216.1741; Δ = 15 ppm.

¹H NMR   (300 MHz, Chloroform-*d*) δ = 6.80 (s, H-2, 2H), 5.82 (ddt, *J*=16.6, 10.0, 6.5, H-5, 2H), 5.10 (dt, *J*=17.1, 1.4, H-6 2H), 5.03 – 4.97 (m, H-6′, 2H), 3.60 (d, *J*=6.5, H-4, 4H), 2.26 (s, H-3, 6H), 2.23 (s, H-1, 3H) ppm.

¹³C-NMR   (75 MHz, Chloroform-*d*) δ = 145.53, 137.25, 137.03, 134.39, 129.38, 115.86, 56.09, 20.74, 19.57 ppm.

IR   (ATR): $\tilde{v}$ = 3077 (w), 3006 (w), 2978 (w), 2918 (m), 2859 (w), 2816 (w), 1839 (w), 1725 (w), 1639 (w), 1609 (w), 1573 (w), 1482 (m), 1435 (m), 1416 (m), 1371 (m), 1343 (w), 1303 (w), 1271 (w), 1218 (m), 1163 (m), 1128 (m), 1033 (w), 990 (s), 915 (s), 851 (s), 755 (w), 733 (w), 659 (m), 580 (m), 508 (w) cm⁻¹.
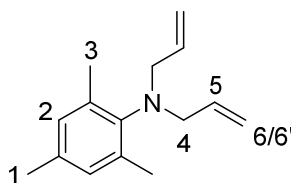
Synthesis of 5-*tert*-butyl-1,3-dimethyl-2-nitrobenzene 33
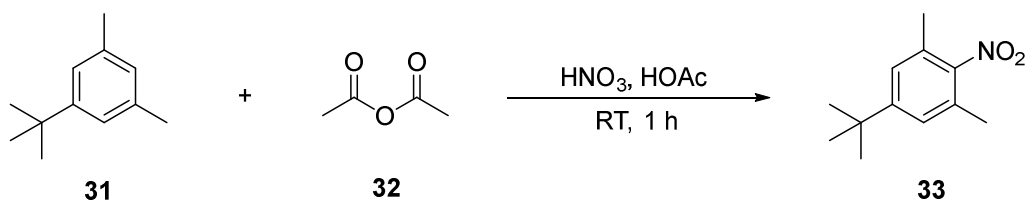
1-*tert*-butyl-3,5-dimethylbenzene **31** (3.80 mL, 20.0 mmol) was treated with acetic anhydride **32** (3.3 mL, 35.2 mmol) and the solution was cooled to 0 °C. The solution was then slowly treated with a solution of HNO_3 (1.30 mL, 30.0 mmol), acetic acid (1.10 mL, 20.0 mmol) and acetic anhydride **32** (1.2 mL, 17.8 mmol) so that a temperature of 25 °C was not exceeded. The solution was stirred at room temperature for 1 h and then transferred into ice water (200 mL). The solution was extracted with diethyl ether (3 × 100 mL) and the combined organic layers were washed with NaOH (10 %, 100 mL) and then dried over $MgSO_4$. After the solvent was

removed under reduced pressure, the desired product **33** was gained as a light brown solid with a yield of 49 % (2.04 g, 9.84 mmol).

33 $C_{12}H_{17}NO_2$ (207.27 g/mol).

Yield   2.04 g (9.84 mmol, 49 %).

Habitus   Light brown solid.

**TLC**   79 – 80 °C (Lit.[192]: 85 – 86 °C).

GC-MS   *m/z* (%) = 207 (22), 192 (100), 162 (16), 134 (14), 91 (10).

**¹H NMR**   (300 MHz, Chloroform-*d*) δ = 7.10 (s, H-2, 2H), 2.31 (s, H-3, 6H), 1.30 (s, H-1, 9H) ppm.

¹³C-NMR   (75 MHz, Chloroform-*d*) δ = 153.39, 137.35, 129.24, 125.94, 123.13, 31.12, 17.87 ppm.

IR   (ATR): ṽ = 3340 (br), 2965 (m), 2871 (w), 1594 (m), 1517 (s), 1479 (m), 1462 (w), 1442 (m), 1409 (w), 1363 (s), 1308 (w), 1234 (m), 1158 (m), 1123 (w), 1047 (w), 1038 (w), 1007 (w), 956 (w), 927 (m), 874 (s), 837 (s), 817 (w), 791 (m), 763 (w), 730 (w), 716 (m), 650 (w), 636 (w), 614 (w), 589 (m), 548 (w), 535 (w), 509 (w) cm⁻¹.
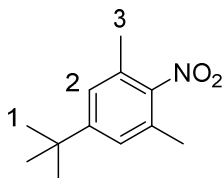
Synthesis of 4-*tert*-butyl-2,6-dimethylaniline 34
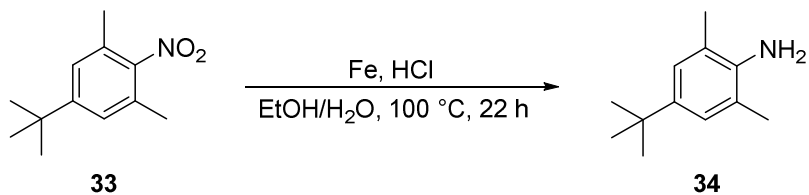
Compound **33** (2.00 g, 9.70 mmol) was dissolved in ethanol (3 mL) and water (20 mL) and the solution was treated with HCl (1 mL, 37 %) and iron (1.9 g, 34 mmol). The reaction mixture was refluxed for 22 h. The mixture was then cooled to room temperature and the suspension was filtered. The residue was washed with diethyl ether (100 mL) and the layers were separated. The aqueous layer was extracted with diethyl ether (3 × 70 ml) and the combined organic layers were dried over $MgSO_4$. The solvent was evaporated, and the crude product was purified by column chromatography (*c*-Hex/EtOAc 5:1). The desired product **34** was gained as a colorless liquid with a yield of 36 % (0.62 g, 3.51 mmol).

34 $C_{12}H_{19}N$ (177.29 g/mol).

Yield   0.62 g (3.51 mmol, 36 %, Lit.[193]: 56 %).

Habitus   Colorless liquid.

TLC R_f = 0.51 (*c*-Hex/EtOAc 4:1).

ESI-MS   Calc. for $C_{11}H_{13}NONa$ $[M+H]^+$: 178.1591 found: 178.1578; Δ = 7.3 ppm.

¹H NMR   (300 MHz, Chloroform-*d*) δ = 6.97 (s, H-2, 2H), 3.46 (s, H-N, 2H), 2.19 (s, H-3, 6H), 1.28 (s, H-1, 9H) ppm.

¹³C-NMR   (75 MHz, Chloroform-*d*) δ = 140.81, 140.24, 125.15, 121.37, 33.76, 31.64, 17.95 ppm.

IR   (ATR): $\tilde{v}$ = 3471 (br), 3385 (br), 2961 (s), 2901 (m), 2864 (m), 2732 (w), 1747 (w), 1623 (s), 1603 (m), 1490 (s), 1460 (m), 1443 (m), 1392 (w), 1376 (w), 1361 (m), 1306 (s), 1270 (w), 1214 (s), 1127 (w), 1029 (w), 997 (m), 935 (w), 870 (s), 816 (w), 735 (m), 656 (br), 624 (m), 563 (m), 535 (m) $\tilde{v}$.
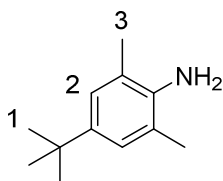
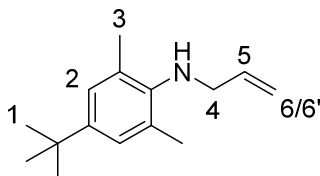**Synthesis of *N*-allyl-2,6-dimethyl-4-*tert*-butylaniline 19**
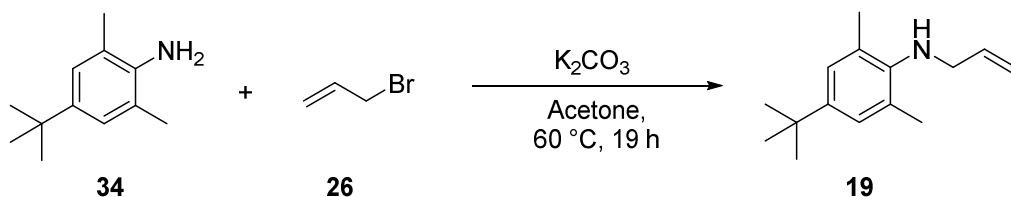
K$_2$CO$_3$ (1.31 g, 9.45 mmol) was suspended in acetone (10 mL) and the suspension was treated with allyl bromide **26** (0.54 mL, 6.30 mmol) and the amin **34** (0.56 g, 3.15 mmol). The reaction mixture was refluxed at 60 °C for 19 h. After the suspension was cooled to room temperature, it was filtered, and the residue was washed with acetone (25 mL). The solvent was evaporated, and the residue was treated DCM (20 mL) and the organic phase was washed with NaOH (2 M, 30 mL). The organic layer was dried over MgSO$_4$, and the solvent was removed under reduced pressure. After the residue was purified by column chromatography (*c*-Hex/EtOAc 10:1) the desired monosubstituted amin **19** was gained as a red liquid with a yield of 39 % (0.27 g, 1.24 mmol).

19   C$_{15}$H$_{23}$N (217.36 g/mol).

Yield   0.27 g (1.24 mmol, 39 %).

Habitus   Red liquid.

TLC R_f = 0.53 (*c*-Hex/EtOAc 10:1).

ESI-MS   Calc. for $C_{15}H_{23}NH$ $[M + H]^+$: 218.1903 found: 218.1906; Δ = 1.4 ppm.

¹H NMR   (500 MHz, Chloroform-*d*) δ = 7.00 (s, H-2, 2H), 6.07 – 5.93 (m, H-5, 1H), 5.27 (dq, *J*=17.1, 1.6, H-6, 1H), 5.11 (dq, *J*=10.2, 1.3, H-6′, 1H), 3.56 (dt, *J*=6.0, 1.4, H-4, 2H), 2.91 (s, br, H-N, 1H), 2.28 (s, H-3, 6H), 1.28 (s, H-1, 9H) ppm.

¹³C-NMR   (126 MHz, Chloroform-*d*) δ = 144.63, 143.31, 136.94, 129.11, 125.68, 115.80, 51.41, 33.95, 31.51, 18.75 ppm.

IR   (ATR): $\tilde{\nu}$ = 3375 (w), 2962 (s), 2905 (m), 2866 (m), 1747 (w), 1642 (m), 1592 (w), 1486 (s), 1460 (m), 1417 (m), 1393 (w), 1373 (w), 1361 (m), 1341 (m), 1327 (w), 1306 (m), 1266 (w), 1247 (w), 1210 (s), 1128 (m), 1065 (m), 1027 (m), 994 (s), 918 (s), 867 (s), 821 (w), 737 (s), 665 (m), 641 (m), 626 (w), 567 (m), 535 (m) cm⁻¹.

Synthesis of *N*-allyl-4,6-dimethyl-2-*tert*-butylaniline 20
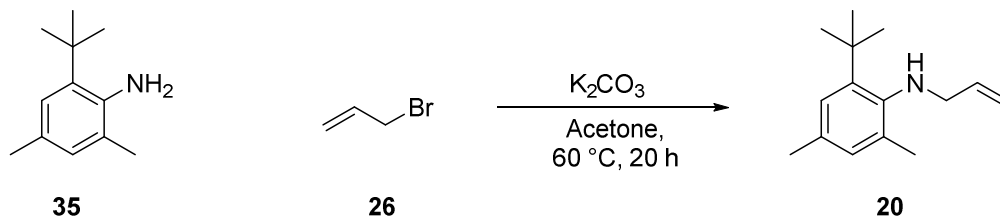
K$_2$CO$_3$ (0.82 g, 5.94 mmol) was suspended in acetone (10 mL) and the suspension was treated with allyl bromide **26** (0.48 mL, 3.96 mmol) and **35** (0.24 g, 1.98 mmol). The reaction mixture was refluxed at 60 °C for 20 h. After the suspension was cooled to room temperature, it was filtered, and the residue was washed with acetone (25 mL). The solvent was evaporated, and the residue was treated DCM (20 mL) and washed with NaOH (2 M, 30 mL). The organic layer was dried over MgSO$_4$, and the solvent was removed under reduced pressure. After the residue was purified by column chromatography (*c*-Hex/EtOAc 10:1) the desired monosubstituted amine **20** was gained as a brown liquid with a yield of 24 % (101 mg, 0.47 mmol).

|	
20	C$_{15}$H$_{23}$N (217.36 g/mol).
Yield	0.82 g (4.56 mmol, 24 %).
Habitus	Brown liquid.
TLC	R$_f$ = 0.81 (*c*-Hex/EtOAc 10:1).
ESI-MS	Calc. for C$_{15}$H$_{23}$NH [M + H]$^+$: 218.1904 found: 218.1909; Δ = 2.3 ppm.
^{1}H NMR	(300 MHz, Chloroform-*d*) δ = 6.98 (s, H-2, 1H), 6.89 (s, H-3, 1H), 6.15 – 6.00 (m, H-7, 1H), 5.35 (dq, *J*=17.2, 1.7, H-8, 1H), 5.17 (dq, *J*=10.3, H-8′, 1.4, 1H), 3.52 (dt, *J*=5.5, 1.6, H-6, 2H), 3.23 (s, H-N, 1H), 2.29 (s, H-4, 3H), 2.25 (s, H-1, 3H), 1.41 (s, H-5, 9H) ppm.
^{13}C-NMR	(75 MHz, Chloroform-*d*) δ = 144.09, 141.48, 136.55, 132.70, 131.10, 130.41, 125.03, 115.56, 51.71, 34.71, 31.52, 20.99, 18.96 ppm.

IR   (ATR): $\tilde{\nu}$ = 3438 (w), 3081 (w), 2957 (s), 2915 (m), 2872 (m), 1736 (w), 1643 (m), 1606 (w), 1531 (m), 1477 (s), 1432 (s), 1418 (s), 1397 (m), 1367 (m), 1327 (w), 1294 (w), 1261 (m), 1223 (s), 1201 (m), 1146 (m), 1062 (w), 1018 (m), 994 (s), 918 (s), 856 (s), 837 (w), 789 (w), 756 (w), 706 (br), 592 (m), 578 (m), 563 (m), 518 (w) cm⁻¹.
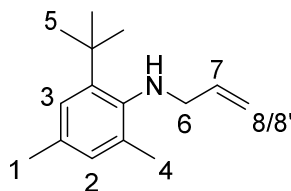
Synthesis of *trans*-2-(4-*N,N*-dimethylaminobenzyl)-1-indanol 12 and *trans*-2-(4-methoxybenzyl)-1-indanol 13

Compounds **12** and **13** were kindly contributed and send to us by D. Kuck from the University of Bielefeld. The compounds can be synthesized according to the literature.[3, 132]

Synthesis of (E)-4-(4-(dimethylamino)phenyl)but-3-en-2-one 38
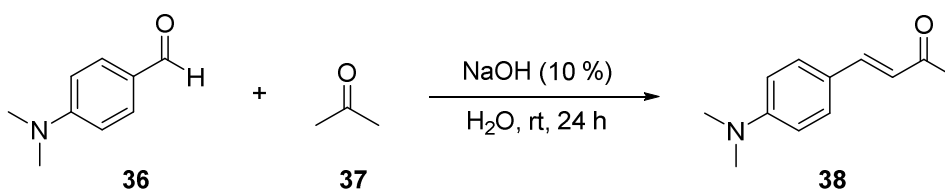
4-*N,N*-Dimethylaminobenzaldehyde **36** (1.20 g, 8.0 mmol) was suspended in water (80 mL). Acetone **37** (5.11 g, 88.0 mmol) and aqueous sodium hydroxide (10%, 10 mL) were then added. The solution was stirred for 24 h at room temperature. Benzylideneacetone **38** was isolated as a yellow solid (1.45 g, 95%).

38 $C_{12}H_{15}NO$ (189.26 g/mol)

Yield   1.45 g (7.66 mmol, 95 %)

Habitus   Yellow Solid.

M.P.   135–136 °C (Lit.[194]: 135–137 °C)

ESI-MS   Calc. for $C_{12}H_{15}NONa$ [M+Na]$^+$: 212.1051; found: 212.1061; Δ = 4.7 ppm.

^{1}H NMR   (300 MHz, Chloroform-*d*) δ = 7.48 and 6.70 (AA'BB', H-2/H-3, 4H), 7.45 (d, ^3J = 16.2 Hz, H-4, 1H), 6.56 (d, ^3J = 16.2 Hz, H-5, 1H), 3.05 (s, H-1, 6H), 2.36 (s, H-6, 3H) ppm.

^{13}C-NMR   (75 MHz, Chloroform-*d*) δ = 198.5, 152.0, 144.4, 130.1, 122.4, 122.0, 111.9, 40.1, 27.2 ppm.

IR   (ATR): $\tilde{\nu}$ = 3336 (w), 3147 (w), 3005 (w), 2904 (w), 2822 (w), 2735 (w), 2490 (w), 2085 (w), 1897 (w), 1835 (w), 1672 (m), 1653 (w), 1617 (w), 1575 (s), 1545 (m), 1521 (m), 1447 (m), 1554 (s), 1329 (m), 1294 (m), 1254 (m), 1235 (m), 1181 (m), 1166 (s), 1067 (w), 992 (m), 966 (m), 945 (m), 917 (m), 841 (w), 803 (s), 808 (s), 722 (w), 637 (w), 597 (m), 545 (w), 530 (m), 517 (m) cm^{-1}.
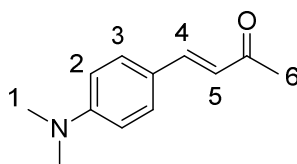
Synthesis of 4-(4-(dimethylamino)phenyl)butan-2-one 39
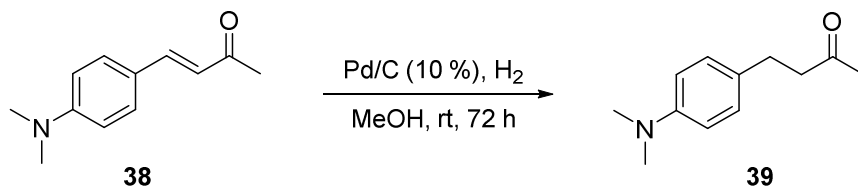
Benzylideneacetone **38** (3.30 g, 17.4 mmol) was dissolved in methanol (70 mL) and Pd/C (10%) (400 mg) was added. The mixture was saturated with hydrogen and stirred for three days under hydrogen atmosphere at room temperature. The crude product was purified by flash chromatography (EtOAc/cyclohexane 1:4) to give ketone **39** as a colorless solid (2.37 g, 71%).

39 $C_{12}H_{17}NO$ (191,13 g/mol)

Yield   2.37 g (12.40 mmol, 71 %)

Habitus   Colorless Solid.

M.P.   50 °C (Lit.[195]: 48-51 °C)

ESI-MS   Calc. for $C_{12}H_{17}NNaO$ [M+Na]$^+$: 214.1208 found: 214.1196; Δ = 5.6 ppm.

^{1}H NMR   (300 MHz, Chloroform-*d*) δ = 7.06 and 6.68 (AA'BB', H-2/H-3, 4H), 2.91 (s, H-1, 6H), 2.83–2.78 (t, ^3J = 4.9 Hz, H-5, 2H), 2.73–2.69 (t, ^3J = 4.9 Hz, H-4, 2H), 2.13 (s, H-6, 3H) ppm.

^{13}C-NMR   (75 MHz, Chloroform-*d*) δ = 208.6, 149.2, 129.0, 128.9, 113.0, 45.7, 40.8, 30.1, 28.9 ppm.
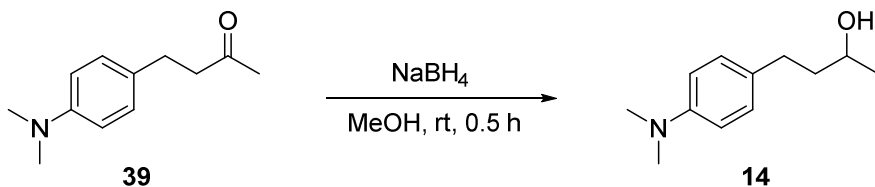
IR   (ATR): $\tilde{\nu}$ = 3393 (w), 3071 (w), 2993 (w), 2940 (w), 2929 (w), 2906 (w), 2892 (w), 2862 (w), 2806 (w), 2324 (w), 2051 (w), 1876 (w), 1701 (s), 1612 (m), 1565 (w), 1520 (s), 1483 (m), 1443 (m), 1404 (w), 1346 (s), 1330 (m), 1271 (w),

1232 (m), 1196 (w), 1160 (m), 1127 (m), 1070 (m), 1042 (w), 949 (m), 807 (s), 734 (w), 717 (w), 702 (w), 663 (w), 588 (w), 533 (m), 518 (m) cm^{-1}.
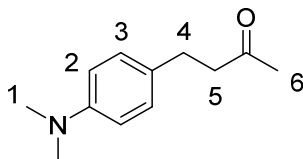
Synthesis of 4-(4-*N,N*-dimethylaminophenyl)-2-butanol 14

Ketone **39** (1.22 g, 6.41 mmol) was dissolved in methanol (60 mL) and sodium borohydride (270 mg, 7.11 mmol) was added at 0 °C. The solution was stirred at room temperature for 30 min. It was then diluted with acetone and neutralized with hydrochloric acid (1 M), followed by water (100 mL) and brine (30 mL). The aqueous layer was extracted repeatedly with ethyl acetate. The combined organic layers were dried, and the solvent was removed under reduced pressure. Alcohol **14** was obtained as a brown oil in quantitative yield.

14 $C_{12}H_{19}NO$ (193,15 g/mol)

**Yield**   1.23 g (quant.) (6.40 mmol, 99 %)

Habitus   Brown Oil.

ESI-MS   Calc. for $C_{12}H_{19}NONa$ [M+Na]$^+$: 216.1364 found: 216.1360; Δ = 1.9 ppm.

   Calc. for $C_{12}H_{19}NOH$ [M+H]$^+$: 194.1545 found 194.1540; Δ = 2.6 ppm.

¹H NMR   (300 MHz, Chloroform-d) δ = 7.07 and 6.69 (AA'BB', H-2/H-3, 4H), 4.31–4.25 (m, H-6, 1H), 3.81 (s, H-O, 1H), 2.90 (s, H-1, 6H), 2.67–2.50 (m, H-4, 2H), 1.81–1.63 (m, H-5, 2H), 1.22–1.16 (d, H-7, 3H) ppm.

¹³C-NMR   (75 MHz, Chloroform-d) δ = 149.0, 129.1, 129.0, 113.3, 67.9, 41.1, 40.5, 31.1, 23.6 ppm.

IR   IR (ATR): $\tilde{\nu}$ = 3368 (br), 3096 (w), 2966 (m), 2926 (m), 2854 (w), 2798 (w), 1867 (w), 1615 (m), 1567 (w), 1519 (s), 1478 (w), 1444 (m), 1394 (m), 1372 (m), 1328 (s), 1222 (m), 1190 (m), 1162 (m), 1130 (s), 1059 (m), 1023 (w), 947 (m), 890 (w), 859 (w), 807 (s), 701 (w), 667 (m), 641 (w), 551 (m), 520 (m) cm^{-1}.
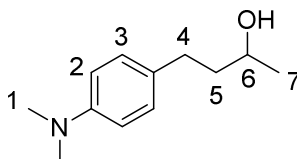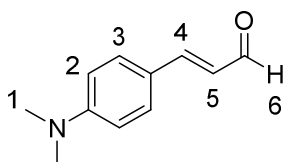

Synthesis of (E)-3-(4-(dimethylamino)phenyl)acrylaldehyde 41
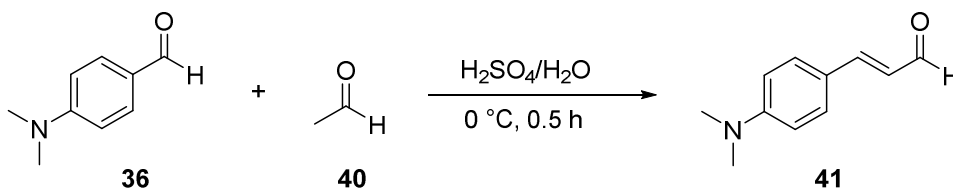

4-N,N-Dimethylaminobenzaldehyde **36** (1.19 g, 8.0 mmol) was dissolved in 97% H_2SO_4 (10 mL). Water (1.0 mL) was then added carefully, the solution was cooled to −17 °C and acetaldehyde **40** (1.4 mL, 25 mmol) was added under argon. The solution was stirred for 30 min at 0 °C and then poured into ice water (200 mL). The mixture was neutralized with aqueous sodium hydroxide (10%) and the precipitate was collected by filtration. Recrystallization of the solid from ethanol gave aldehyde **41** as an orange solid (170 mg, 12%).

41 $C_{11}H_{13}NO$ (175.23 g/mol)

Yield   170 mg (0.97 mmol, 12 %)

Habitus   Orange solid.

M.P.   128–130 °C (Lit.[196]: 129–129.5 °C)

ESI-MS   Calc. for $C_{11}H_{13}NONa$ [M+Na]$^+$: 198.0895 found: 198.08804; Δ = 7.4 ppm.

^{1}H NMR   (300 MHz, Chloroform-*d*) δ = 9.59 (d, ^3J = 7.9 Hz, H-6, 1H), 7.45 and 6.69 (AA'BB', H-2/H-3, 4H), 7.38 (d, ^3J = 15.6 Hz, H-4, 1H), 6.54 (dd, ^3J = 15.6 Hz, ^3J = 7.9 Hz, H-5, 1H), 3.05 (s, H-1, 6H) ppm.

^{13}C-NMR   (75 MHz, Chloroform-*d*) δ = 193.8, 154.0, 152.4, 130.5, 123.8, 121.7, 111.8, 40.1 ppm.

IR   (ATR): $\tilde{\nu}$ = 455 (w), 3300 (w), 3035 (w), 2903 (w), 2802 (w), 2738 (w), 2706 (w), 2654 (w), 2533 (w), 2248 (w), 2092 (w), 1896 (w), 1733 (w), 1654 (s), 1586 (m), 1548 (w), 1522 (m), 1484 (w), 1437 (w), 1419 (m), 1390 (w), 1365 (m), 1328 (m), 1262 (w), 1233 (m), 1212 (m), 1188 (w), 1167 (w), 1134 (m), 1118 (m), 1068 (m), 1007 (m), 972 (s), 939 (m), 853 (w), 808 (s), 722 (m), 663 (w), 640 (w), 621 (w), 582 (m), 549 (m), 523 (s) cm^{-1}.

Synthesis of 3-(4-*N,N*-dimethylaminophenyl)-1-propanol 15
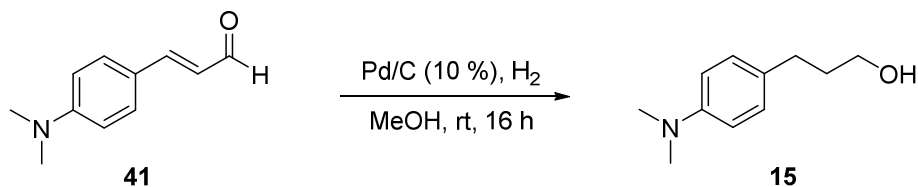
Aldehyde **41** (2.34 g, 9.43 mmol) was dissolved in methanol (70 mL) and Pd/C (10%) (330 mg) was added. The solution was stirred under hydrogen for 16 h at ambient temperature and pressure. The suspension was filtered, and the catalyst was washed with methanol. The solvent was removed under reduced pressure and the crude product was purified by flash chromatography (EtOAc/cyclohexane 1:10, gradient). The desired alcohol **15** was obtained as yellow oil (820 mg, 34%). The spectroscopic data (NMR, IR) agree with those given in the literature.[197]

15 $C_{11}H_{17}NO$ (179.26 g/mol)

Yield   820 mg (4.57 mmol, 34 %)

Habitus   Yellow Oil.

TLC R_f = 0.54 (EtOAc/C-Hex 1:1).

GC-MS   Calc. for $C_{11}H_{17}NO$ [M]$^{+}$: 179.12989 found: 179.1310; Δ = 6.2 ppm.

^{1}H NMR   (300 MHz, Chloroform-*d*) δ = 7.08 and 6.70 (AA'BB', H-2/H-3, 4H), 3.67 (t, ^3J = 6.4 Hz, H-4, 2H), 2.95 (s, H-O, 1H), 2.91 (s, H-1, 6H), 2.62 (t, ^3J = 6.9 Hz, H-6, 2H), 1.86 (quint, ^3J = 7.9 Hz, H-5, 2H) ppm.

^{13}C-NMR   (75 MHz, Chloroform-*d*) δ = 149.1, 130.7, 129.0, 113.1, 62.5, 40.9, 34.6, 31.0 ppm.

IR   (ATR): $\tilde{v} = 3338$ (br), 3096 (w), 3008 (w), 2936 (m), 2858 (m), 2799 (w), 1872 (w), 1736 (w), 1615 (m), 1567 (w), 1520 (s), 1478 (m), 1444 (m), 1341 (m), 1224 (m), 1191 (m), 1162 (m), 1142 (m), 1057 (m), 946 (m), 911 (w), 824 (m), 801 (s), 698 (w), 676 (w), 640 (w), 556 (m), 517 (m) cm^{-1}.
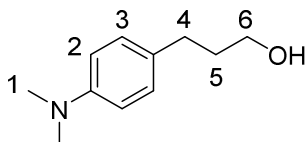
Synthesis   of N-(4-((*trans*-1-hydroxyindan-2-yl)methyl)phenyl)-*N,N,N*-trimethylammonium iodide 12a
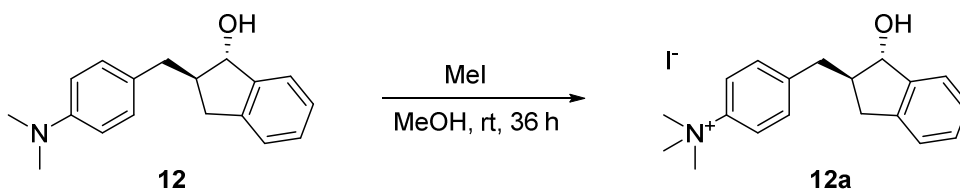
Benzylindanol **12** (70.0 mg, 300 µmol) was dissolved in methanol (1.0 mL). The mixture was stirred while methyl iodide (40 µL, 600 µmol) was added very slowly. After about 18 h, another portion of methyl iodide (30 µL, 500 µmol) was added and the mixture was stirred for another 18 h. The solvent was evaporated in an open vessel. The residue was redissolved in methanol and placed into a closed vessel that contained cyclohexane to exchange the solvent. After two days the solvent was again evaporated in an open vessel and the crystals were analyzed by X-ray diffraction. The resonance of 2-H is missing and probably hidden under the broad DMSO-d$_5$ singlet.

12a   C$_{19}$H$_{24}$INO (409.09 g/mol)
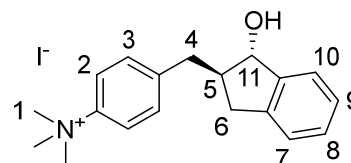

Yield   Quantitative.

Habitus   Colorless solid.
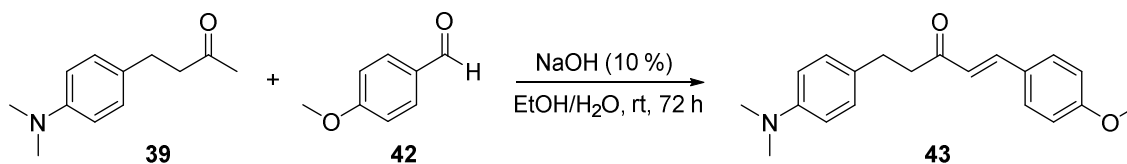
M.P.   123–124 °C.

¹H NMR   (300 MHz, Chloroform-*d*) δ = 7.90 and 7.52 (AA'BB', H-2/H-3, 4H), 7.30 (m,
H-10, 1H), 7.17 (m, H-7/H-8/H-9, 3H), 4.74 (m, H-11 1H), 3.61 (s, H-1 9H),
3.16 (d, ³J = 5.8 Hz, H-O, 1H), 2.80 (m, H-4, 2H), 2.35 (m, H-6, 2H) ppm.

Crystal Structure: See chapter 6.7 below.

Synthesis of 1-(4-*N*,*N*-dimethylaminophenyl)-5-(4-methoxyphenyl)-3-pentanol 15

A mixture of water (40 mL), ethanol (40 mL), anisaldehyde **42** (1.27 mL, 10.5 mmol) and the
ketone **39** (2.00 g, 10.5 mmol) was stirred while aqueous NaOH (10%, 13 mL) was added.
After continued stirring at room temperature for 72 h, the reaction mixture was diluted with
ethyl acetate (100 mL) and the layers were separated. The aqueous layer was extracted with
ethyl acetate (2 × 100 mL) and the combined organic layers were dried over MgSO₄. The
solvent was evaporated, and the residue was purified by column chromatography
(cyclohexane/EtOAc 5:1). The desired product **43** was isolated as a pale-yellow solid (3.02 g,
93%).

43   C₂₀H₂₃NO₂ (309.41 g/mol)

Yield   3,02 g (9.76 mmol, 93 %)

Habitus   Pale-yellow solid.

TLC   R$_f$ = 0.23 (*c*-Hex/EtOAc 5:1).

M.P.   86.5–87.5 °C.

GC-MS   *m/z* (%) = 309 (25), 134 (100).

¹H NMR   (300 MHz, Chloroform-*d*) δ = 7.59 (d, ^3J =16.2, H-6, 1H), 7.47 and 6.90 (AA'BB', H-8/H-9, 4H^{anisole}), 7.11 and 6.70 (AA'BB', H-2/H-3 4H^{aniline}), 6.61 (d, ^3J = 16.2, H-7, 1H) 3.83 (s, H-10, 3H), 2.93–2.91 (m, H-1/H-4/H-5, 10H) ppm.

¹³C-NMR   (75 MHz, Chloroform-*d*) δ = 199.9, 161.6, 149.3, 142.5, 130.1, 129.5, 129.1, 127.3, 124.3, 114.5, 113.2, 55.5, 43.0, 41.0, 29.5 ppm.

IR   (ATR): $\tilde{\nu}$ cm⁻¹ = 3011 (w), 2959 (w), 2909 (w), 2855 (w), 2802 (w), 2556 (w), 2051 (w), 1873 (w), 1678 (w), 1643 (m), 1626 (m), 1612 (m), 1600 (s), 1573 (m), 1521 (s), 1510 (s), 1482 (w), 1465 (w), 1441 (m), 1421 (m), 1340 (m), 1309 (m), 1293 (m), 1245 (s), 1194 (m), 1173 (s), 1126 (m), 1113 (m), 1094 (w), 1060 (w), 1032 (s), 985 (s), 961 (m), 945 (m), 865 (w), 831 (m), 817 (s), 768 (w), 728 (w), 656 (w), 616 (w), 590 (w), 558 (m), 518 (s) cm⁻¹.
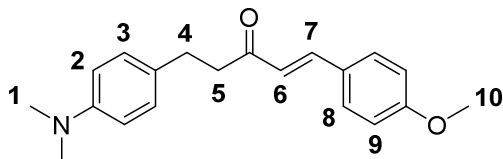
Synthesis of 1-(4-*N*,*N*-dimethylaminophenyl)-5-(4-methoxyphenyl)-3-pentanol 16
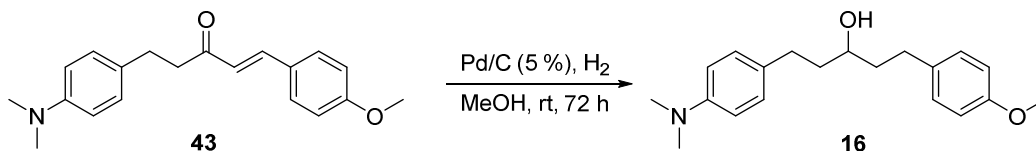
Benzylideneacetone **43** (2.00 g, 6.45 mmol) was dissolved in methanol (200 mL) and Pd/C (5%) (300 mg) was added. The mixture was saturated with hydrogen and stirred for three days under hydrogen atmosphere at room temperature. The suspension was filtered, the residue was washed with methanol (30 mL) and the solvent was evaporated under reduced pressure. The crude product was purified by column chromatography (cyclohexane/EtOAc 4:1) to give the desired alcohol **16** as a colorless solid (0.66 g, 33%).

16 $C_{20}H_{27}NO_2$ (313.44 g/mol)

Yield   0.66 g (2.10 mmol, 33 %)

Habitus   Colorless Solid.

TLC R_f = 0.18 (*c*-Hex/EtOAc 4:1).

M.P.   61–62 °C (Lit.[198]: 60 °C).

**GC-MS**   *m/z* (%) = 313 (24), 207 (21), 134 (100) 121 (17).

ESI-MS   Calc. for $C_{15}H_{23}NH$ [M]$^+$: 313.2042 found: 313.1994; *Δ* = 15.3 ppm.

¹H NMR   (300 MHz, Chloroform-*d*) δ = 7.10 and 6.82 (AA'BB', H-9/H10, 4H^{anisole}), 7.06 and 6.69 (AA'BB', H-2/H-3, 4H^{aniline}), 3.78 (s, H-11, 3H), 3.67–3.63 (quint, H-6, 1H), 2.90 (s, H-1, 6H), 2.77–2.65 (m, H-4, 2H), 2.63–2.55 (m, H-8, 2H), 1.82–1.69 (m, H-5/H-7, 4H), 1.46 (s, H-O, 1H) ppm.

¹³C-NMR   (75 MHz, Chloroform-*d*) δ = 157.9, 149.2, 134.3, 130.2, 129.4, 129.1, 114.0, 113.2, 71.1, 55.4, 41.0, 39.6, 39.6, 31.3, 31.1 ppm.

IR   (ATR): $\tilde{\nu}$ = 3407 (br), 3098 (w), 3070 (w), 3029 (w), 3003 (w), 2957 (w), 2938 (w), 2927 (w), 2874 (w), 2858 (w), 2831 (w), 2789 (w), 2325 (w), 2064 (w), 1992 (w), 1873 (w), 1717 (w), 1613 (m), 1583 (w), 1569 (w), 1520 (s), 1509 (s), 1485 (m), 1455 (m), 1440 (m), 1418 (m), 1334 (m), 1300 (m), 1285 (w), 1270 (w), 1241 (s), 1198 (w), 1177 (m), 1162 (m), 1126 (m), 1111 (w), 1080 (s), 1037 (s), 991 (w), 942 (m), 891 (m), 845 (w), 819 (s), 806 (s), 771 (w), 749 (m), 730 (w), 714 (w), 702 (w), 644 (w), 626 (w), 555 (s), 521 (m), 506 (w) cm⁻¹.
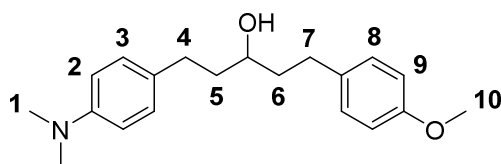
6.7 X-ray crystallography

In order to prove independently the *trans*-configuration of indanol **12**, we tried to obtain a crystal structure of this compound but without success. Therefore, we performed an *N*-methylation using methyl iodide and prepared the corresponding salt, i.e., *N*-(4-((*trans*-1-hydroxyindan-2-yl)methyl)phenyl)-*N,N,N*-trimethylammonium iodide **12a**. Crystals suitable for X-ray crystallography were obtained by slowly evaporation of the solvent at room temperature after purification (see above). A suitable crystal was selected and measured on a DESY Petra III P24 Beamline diffractometer. The crystal was kept at 100 K during data collection. Using Olex2, the structure was solved with the ShelXT structure solution program using Intrinsic Phasing and refined with the ShelXL refinement package using Least Squares minimization. The crystallographic data of compound **12a** is deposited at CCDC under the deposition number 2115718 and can be accessed free of charge by the joint Cambridge Crystallographic Data Centre and Fachinformationszentrum Karlsruhe Access Structures service. Figure 80 shows the crystal structure of compound **12a**, confirming the *trans*-configuration of the alcohol functionality and the benzylic residue. One water molecule is present and coordinated close to the iodide counterion and the OH group. Figure 81 shows a top-down view onto both aromatic rings and the compound.
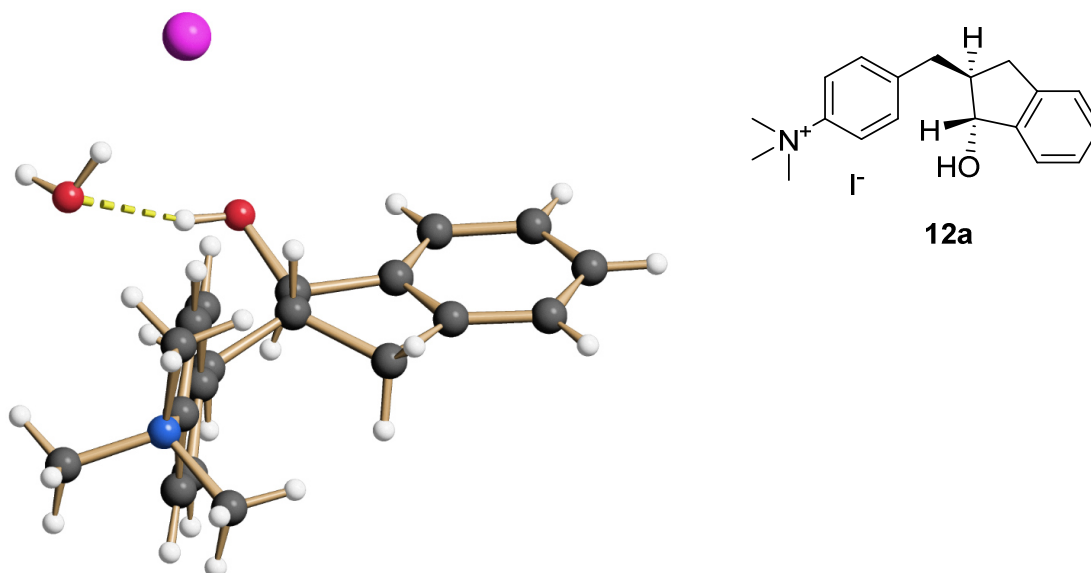
Figure 80
Crystal structure of *N*-(4-((*trans*-1-hydroxyindan-2-yl)methyl)phenyl)-*N,N,N*-trimethylammonium iodide (**12a**). The view along the C2-C1 bond highlights the *trans*-configuration of the indanol **12**.
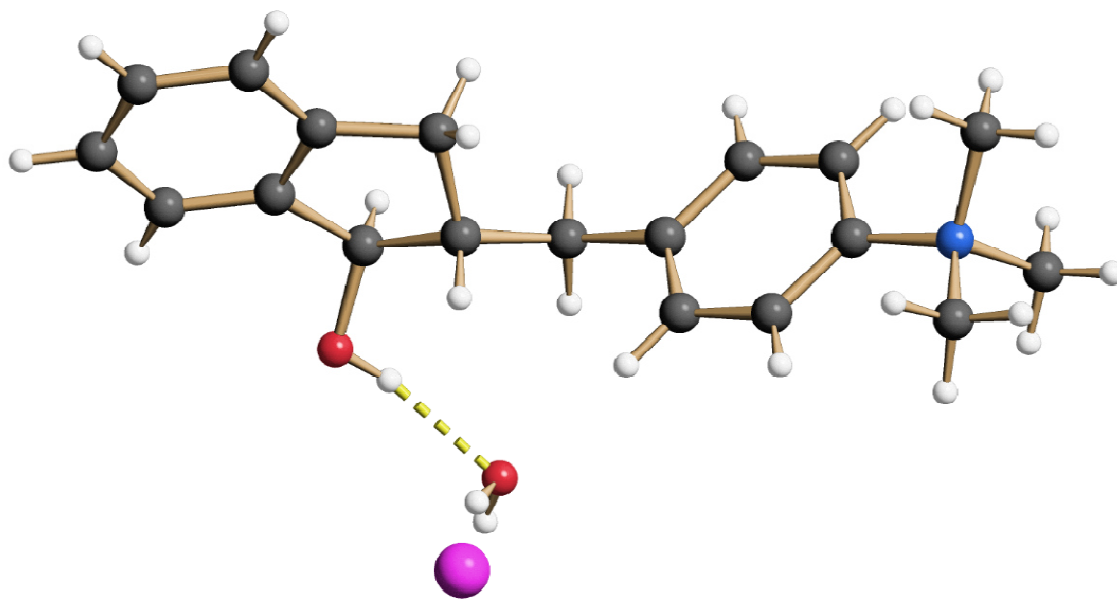
Figure 81
Crystal structure of *N*-(4-(((*trans*-1-hydroxyindan-2-yl)methyl)phenyl)-*N,N,N*-trimethylammonium iodide (**12a**).
The view onto the two aromatic rings also displays the coordination of a water molecule between the hydroxyl
group and the iodide counterion.

Summary of the crystal data and structure refinement for *N*-(4-((t*rans*-1-hydroxyindan-2-yl)methyl)phenyl)-*N,N,N*-trimethylammonium iodide (**12a**).

Identification code	k208_run3_001
Empirical formula	$C_{19}H_{25.40}INO_{1.70}$
Moiety formula	$C_{19}H_{24}NO$, I, 0.7 (H_2O)
Formula weight	421.90
Temperature	100.00 K
Wavelength	0.56076 Å
Crystal system	Monoclinic
Space group	P 1 21/c 1
Unit cell dimensions	a = 5.76330(10) Å α= 90°
	b = 18.2024(4) Å β= 90.984(2)°
	c = 17.5480(4) Å γ = 90°
Volume	1840.62(7) $Å^3$
Z	4
Density (calculated)	1.522 Mg/m^3
Absorption coefficient	0.918 mm^{-1}
F(000)	852
Crystal size	0.1 x 0.1 x 0.05 mm^3
Theta range for data collection	1.765 to 27.572°.
Index ranges	-8<=h<=8, -29<=k<=29, -27<=l<=27
Reflections collected	26093
Independent reflections	6769 [R(int) = 0.0553]
Completeness to theta = 19.661°	99.9 %
Absorption correction	Semi-empirical from equivalents
Max. and min. transmission	1.00000 and 0.88424
Refinement method	Full-matrix least-squares on F^2
Data / restraints / parameters	6769 / 0 / 215
Goodness-of-fit on F^2	1.091
Final R indices [I>2sigma(I)]	R1 = 0.0365, wR2 = 0.0905
R indices (all data)	R1 = 0.0483, wR2 = 0.0943
Extinction coefficient	n/a
Largest diff. peak and hole	1.159 and -1.412 e.$Å^{-3}$

7 Literature

1. Scheer, A. M.; Mukarakate, C.; Robichaud, D. J.; Nimlos, M. R.; Carstensen, H. H.; Ellison, G. B., *J. Chem. Phys.* **2012,** *136* (4), 044309.
2. Choe, J. C., *Bulletin of the Korean Chemical Society* **2013,** *34* (11), 3249-3252.
3. Kuck, D.; Filges, U., *Org. Mass Spectrom.* **1988,** *23* (9), 643-653.
4. Gerlich, D., *J. Chin. Chem. Soc.* **2018,** *65* (6), 637-653.
5. Jasikova, L.; Roithova, J., *Chemistry* **2018,** *24* (14), 3374-3390.
6. Neese, F., *Angew. Chem. Int. Ed. Engl.* **2017,** *56* (37), 11003-11010.
7. Iacobucci, C.; Reale, S.; De Angelis, F., *Angew. Chem. Int. Ed. Engl.* **2016,** *55* (9), 2980-93.
8. Demarque, D. P.; Crotti, A. E.; Vessecchi, R.; Lopes, J. L.; Lopes, N. P., *Nat. Prod. Rep.* **2016,** *33* (3), 432-55.
9. Polfer, N. C., *Chem. Soc. Rev.* **2011,** *40* (5), 2211-21.
10. Kuck, D., *Mass Spectrom. Rev.* **1990,** *9* (2), 187-233.
11. Kuck, D., *Mass Spectrom. Rev.* **1990,** *9* (6), 583-630.
12. DePuy, C. H.; *J. Am. Chem. Soc.y* **1990,** *112* (24), 8650-8655.
13. Hammerum, S., *Mass Spectrom. Rev.* **1988,** *7* (2), 123-202.
14. Atkinson, R., *Chem. Rev.* **1986,** *86* (1), 69-201.
15. Holmes, J. L., *Org. Mass Spectrom.* **1985,** *20* (3), 169-183.
16. Mandelbaum, A., *Mass Spectrom. Rev.* **1983,** *2* (2), 223-284.
17. Levsen, K.; Schwarz, H., *Mass Spectrom. Rev.* **1983,** *2* (1), 77-148.
18. Bonrath W.; Medlock J.; Müller M.-A.; J., S., *Catalysis for Fine Chemicals, Gas-phase reactions*, Walter de Gruyter GmbH, Berlin/Munich/Boston. **2021**.
19. Paul, M.; Peckelsen, K.; Thomulka, T.; Neudorfl, J.; Martens, J.; Berden, G.; Oomens, J.; Berkessel, A.; Meijer, A.; Schäfer, M., *Phys. Chem. Chem. Phys.* **2019,** *21* (30), 16591-16600.
20. Paul, M.; Detmar, E.; Schlangen, M.; Breugst, M.; Neudorfl, J. M.; Schwarz, H.; Berkessel, A.; Schäfer, M., *Chemistry* **2019,** *25* (10), 2511-2518.
21. Schäfer, M.; Peckelsen, K.; Paul, M.; Martens, J.; Oomens, J.; Berden, G.; Berkessel, A.; Meijer, A., *J. Am. Chem. Soc.* **2017,** *139* (16), 5779-5786.
22. Peckelsen, K.; Martens, J.; Czympiel, L.; Oomens, J.; Berden, G.; Grundemann, D.; Meijer, A.; Schäfer, M., *Phys. Chem. Chem. Phys.* **2017,** *19* (34), 23362-23372.
23. Peckelsen, K.; Martens, J.; Berden, G.; Oomens, J.; Dunbar, R. C.; Meijer, A. J. H. M.; Schäfer, M., *J. Mol. Spec.* **2017,** *332*, 38-44.
24. Walker, S. W. C.; Mark, A.; Verbuyst, B.; Bogdanov, B.; Campbell, J. L.; Hopkins, W. S., *J. Phys. Chem. A* **2018,** *122* (15), 3858-3865.
25. Glish, G. L.; Vachet, R. W., *Nat. Rev. Drug. Discov.***2003,** *2* (2), 140-50.
26. Griffiths, J., *Anal. Chem.* **2008,** *80* (15), 5678-83.
27. Gross, J. H., *Mass Spectrometry - A Textbook.* Springer Verlag **2011,** (2nd Edition).
28. *The Encyclopedia of Mass Spectrometry,* Ed.: Michael L. Gross, Richard Caprioli, Elsevier, 2003.

29.   *Personal Communication*, Schäfer, M., Universität zu Köln, Institut für Organische Chemie, Greinstraße 4, 50939 Köln, Germany, **2022**.

30.   Vékey, K., *J. Mass Spectrom.* **1996,** *31* (5), 445-463.

31.   *Fundamental aspects of mass spectrometry,* K. Levsen, Ed.: H Budzikiewicz, Progress in Mass Spectrometry, Vol, 4, Verlag Chemie, **1987**.

32.   Fenn, J. B.; Mann, M.; Meng, C. K.; Wong, S. F.; Whitehouse, C. M., *Science* **1989,** *246* (4926), 64-71.

33.   Konermann, L.; Ahadi, E.; Rodriguez, A. D.; Vahidi, S., *Anal. Chem.* **2013,** *85*, 2-9.

34.   Banerjee, S.; Mazumdar, S., *Int. J. Anal. Chem.* **2012,** *2012*, 282574.

35.   Loeb, L. B.; Kip, A. F.; Hudson, G. G.; Bennett, W. H., *Phys. Rev.* **1941,** *60* (10), 714-722.

36.   Taylor, G., *Proceedings of the Royal Society of London. Series A. Mathematical and Physical Sciences* **1964,** *280* (1382), 383-397.

37.   Metwally, H.; Duez, Q.; Konermann, L., *Anal. Chem.* **2018,** *90* (16), 10069-10077.

38.   Cody, R. B.; Burnier, R. C.; Freiser, B. S., *Anal. Chem.* **1982,** *54* (1), 96-101.

39.   Sleno, L.; Volmer, D. A., *J. Mass Spectrom.* **2004,** *39* (10), 1091-112.

40.   Cody, R. B.; Freiser, B. S., *Int. J. Mass Spectrom. Ion Phys.* **1982,** *41* (3), 199-204.

41.   Louris, J. N.; Wright, L. G.; Cooks, R. G.; Schoen, A. E., *Anal. Chem.* **2002,** *57* (14), 2918-2924.

42.   Atkins, P.; Paula, J.; *Physical Chemistry.* 8th ed., Oxford University Press, **2006**.

43.   Oepts, D.; van der Meer, A. F. G.; van Amersfoort, P. W., *Infrared Phys. Tech.* **1995,** *36* (1), 297-308.

44.   Martens, J.; Berden, G.; Gebhardt, C. R.; Oomens, J., *Rev. Sci. Instrum.* **2016,** *87* (10), 103108.

45.   https://en.wikipedia.org/wiki/Free-electron_laser (accessed on 05.09.2022).

46.   Grant, E. R.; Schulz, P. A.; Sudbo, A. S.; Shen, Y. R.; Lee, Y. T *Phys. Rev. Lett.* **1978,** *40* (2), 115-118.

47.   Fung, Y. M.; Kjeldsen, F.; Silivra, O. A.; Chan, T. W.; Zubarev, R. A., *Angew. Chem. Int. Ed. Engl.* **2005,** *44* (39), 6399-403.

48.   Roithova, J., *Chemi. Soc. Rev.* **2012,** *41* (2), 547-59.

49.   Oomens, J.; Rijs, A., *Top. Curr. Chem.* **2015,** *364*, 1-42.

50.   Martens, J.; Grzetic, J.; Berden, G.; Oomens, J., *Nature Comm.* **2016,** *7*, 11754.

51.   Oomens, J.; Sartakov, B. G.; Meijer, G.; von Helden, G., *Int. J. Mass Spectrom.* **2006,** *254* (1-2), 1-19.

52.   Asmis, K. R.; Brümmer, M.; Kaposta, C.; Santambrogio, G.; von Helden, G.; Meijer, G.; Rademann, K.; Wöste, L., *Phys. Chem. Chem. Phys.* **2002,** *4* (7), 1101-1104.

53.   Asmis, K. R.; Sauer, J., *Mass Spectrom. Rev.* **2007,** *26* (4), 542-62.

54.   Asmis, K. R.; Neumark, D. M., *Acc. Chem. Res.* **2012,** *45* (1), 43-52.

55.   Bush, M. F.; Saykally, R. J.; Williams, E. R., *J. Am. Chem. Soc.* **2007,** *129*, 2220.

56.   Wolk, A. B.; Leavitt, C. M.; Garand, E.; Johnson, M. A., *Acc. Chem. Res.* **2014,** *47* (1), 202-10.

57.   Roithova, J.; Gray, A.; Andris, E.; Jasik, J.; Gerlich, D., *Acc. Chem. Res.* **2016,** *49* (2), 223-30.

58.   Garand, E., *J. Phys. Chem. A* **2018,** *122* (32), 6479-6490.

59.	Asvany, O.; Brünken, S.; Kluge, L.; Schlemmer, S., *App. Phys. B* **2014,** *114*, 203-211.

60.	Gerlich, D., *Ad. Chem. Phys.* **1992,** *82*, 1–176.

61.	Gerlich, D.; Horning, S., *Chem. Rev.* **1992,** *92* (7), 1509-1539.

62.	Jusko, P.; Brünken, S.; Asvany, O.; Thorwirth, S.; van der Meer, L.; Berden, G.; Redlich, B.; Oomens, J.; Schlemmer, S., *Farad. Discuss.* **2019,** *217*, 172-202.

63.	Brümmer, M.; Kaposta, C.; Santambrogio, G.; Asmis, K. R., *J. Chem. Phys.* **2003,** *119* (24), 12700-12703.

64.	Cismesia, A. P.; Tesler, L. F.; Bell, M. R.; Bailey, L. S.; Polfer, N. C., *J. Mass Spectrom.* **2017,** *52* (11), 720-727.

65.	Cismesia, A. P.; Bell, M. R.; Tesler, L. F.; Alves, M.; Polfer, N. C., *Analyst* **2018,** *143* (7), 1615-1623.

66.	Schwarz, H.; Asmis, K. R., *Chemistry* **2019,** *25* (9), 2112-2126.

67.	Miyazaki, M.; Sakata, Y.; Schutz, M.; Dopfer, O.; Fujii, M., *Phys. Chem. Chem. Phys.* **2016,** *18* (35), 24746-54.

68.	Dopfer, O.; Fujii, M., *Chem. Rev.* **2016,** *116* (9), 5432-63.

69.	Fujii, M.; Dopfer, O., *Int. Rev. Phys. Chem.* **2012,** *31* (1), 131-173.

70.	Dopfer, O., *Z. Phys. Chem.* **2005,** *219* (2), 125-168.

71.	Dirac, P., *Proc. R. Soc. A* **1929,** *123*, 714.

72.	Feynman, R. P., *Int. J. Theor. Phys.* **1982,** *21* (6-7), 467-488.

73.	Schrödinger, E., *Annalen der Physik* **1926,** *384* (4), 361-376.

74.	Schrödinger, E., *Phys. Rev.* **1926,** *28* (6), 1049-1070.

75.	Born, M.; Oppenheimer, R., *Annalen der Physik* **1927,** *389* (20), 457-484.

76.	Hartree, D. R., *Math- Proc. Cam. Phil. Soc.* **1928,** *24* (1), 89-110.

77.	Møller, C.; Plesset, M. S., *Phys. Rev.* **1934,** *46* (7), 618-622.

78.	Christensen, A. S.; Kubar, T.; Cui, Q.; Elstner, M., *Chem. Rev.* **2016,** *116*, 5301-37.

79.	Fermi, E., *Z. Phys.* **1934,** *88*, 161-177.

80.	Hohenberg, P.; Kohn, W., *Phys. Rev.* **1964,** *136* (3B), B864-B871.

81.	Kohn, W.; Sham, L. J., *Phys. Rev.* **1965,** *140* (4A), A1133-A1138.

82.	Baseden, K. A.; Tye, J. W., *J. Chem. Ed.* **2014,** *91* (12), 2116-2123.

83.	Becke, A. D., *J. Chem. Phys.* **2014,** *140* (18), 18A301.

84.	Becke, A. D., *Phys. Rev. A Gen. Phys.* **1988,** *38* (6), 3098-3100.

85.	Becke, A. D., *J. Chem. Phys.* **1993,** *98* (7), 5648-5652.

86.	Lee, C.; Yang, W.; Parr, R. G., *Phys. Rev. B Condens. Mat.* **1988,** *37* (2), 785-789.

87.	Stewart, R. F., *J. Chem. Phys.* **1970,** *52* (1), 431-438.

88.	Hehre, W. J.; Stewart, R. F.; Pople, J. A., *J. Chem, Phys.* **1969,** *51*, 2657-2664.

89.	Ditchfield, R.; Hehre, W. J.; Pople, J. A., *J. Chem. Phys.* **1971,** *54*, 724-728.

90.	Dunning, T. H., *J. Chem. Phys.* **1989,** *90* (2), 1007-1023.

91.	Russell, D. H.; Gross, M. L.; Nibbering, N. M. M., *J. Am. Chem. Soc.* **1978,** *100* (19), 6133-6137.

92.	Turecek, F.; Drinkwater, D. E.; Maquestiau, A.; McLafferty, F. W., *Org. Mass Spectrom.* **1989,** *24* (8), 669-672.

93.	Muntean, F.; Armentrout, P. B., *J. Phys. Chem. B* **2002,** *106* (33), 8117-8124.

94.	Van Velzen, P. N. T.; Van der Hart, W. J.; Van der Greef, J.; Nibbering, N. M. M.; Gross, M. L., *J. Am. Chem. Soc.* **1982,** *104* (5), 1208-1212.

95.   Le, H. T.; Flammang, R.; Gerbaux, P.; Bouchoux, G.; Nguyen, M. T., *J. Phys. Chem. A* **2001,** *105* (51), 11582-11592.

96.   Le, H. T.; Flammang, R.; Barbieux-Flammang, M.; Gerbaux, P.; Nguyen, M. T., *Int. J. Mass Spectrom.* **2002,** *217* (1-3), 45-54.

97.   Shen, V. K.; Siderius, D. W.; Krekelberg, W. P.; Hatch, H. W., Eds., NIST Standard Reference Simulation Website, NIST Standard Reference Database Number 173, National Institute of Standards and Technology, Gaithersburg, (retrieved 13.02.2020).

98.   Bouchoux, G., *Int. J. Mass Spectrom. Ion Phys.* **1978,** *26* (4), 379-394.

99.   *The Chemistry of Anilines*, Ed.: Rappoport, Z., John Wiley & Sons, Ltd., Hoboken, NJ, **2007**.

100.   *The Chemistry of Phenols*, Ed.: Rappoport, Z., John Wiley & Sons, Ltd., Hoboken, NJ, **2003**.

101.   Fraser-Monteiro, M. L.; Fraser-Monteiro, L.; De Wit, J.; Baer, T., *J. Phys. Chem.* **1984,** *88* (16), 3622-3627.

102.   Burgers, P. C.; Holmes, J. L.; Mommers, A. A.; Terlouw, J. K., *Chem. Phys. Lett.* **1983,** *102* (1), 1-3.

103.   Lifshitz, C.; Gotchiguian, P.; Roller, R., *Chem. Phys. Lett.* **1983,** *95*, 106-108.

104.   Hoffman, M. K.; Friesen, M. D.; Richmond, G., *Org. Mass Spectrom.* **1977,** *12* (3), 150-152.

105.   Maquestiau, A.; Van Haverbeke, Y.; Flammang, R.; De Meyer, C.; Das, K. G.; Reddy, G. S., *Org. Mass Spectrom.* **1977,** *12* (10), 631-635.

106.   Nibbering, N. M. M., *Tetrahedron* **1973,** *29* (2), 385-390.

107.   B. Tomer, K. B.; Hammerum, S.; Djerassi, C., *Tetrahedron Lett.* **1973,** *12* (12), 915-917.

108.   Borchers, F.; Levsen, K.; Theissling, C. B.; Nibbering, N. M. M., *Org. Mass Spectrom.* **1977,** *12* (12), 746-750.

109.   Kingston, D. G. I.; Bursey, J. T.; Bursey, M. M., *Chem. Rev.* **1974,** *74* (2), 215-242.

110.   McLafferty, F. W.; Turecek, F., *Interpretation of Mass Spectra*, 4th Ed., Ch. 8, University Science Books, Mill Valley. **1993**.

111.   Kuck, D., *Eur. J. Mass Spectrom.* **2012,** *18*, 161–181.

112.   Kuck, D., *Int. J. Mass Spectrom.* **2002,** *213* (2-3), 101-144.

113.   Mandelbaum, A., *The Effect of Stereochemistry on Mass Spectral Fragmentations. In Encyclopedia of Mass Spectrometry;* Nibbering, N. M. M. (Ed.); Elsevier, Amsterdam, **2005**, Vol. 4, pp 410−417.

114.   Dass, C., *Kinetic Isotope Effects, in Encyclopedia of Mass Spectrometry*; Nibbering, N. M. M. (Ed.); Elsevier, Amsterdam. **2005**, Vol. 4, 39–49.

115.   Schwarz, H., *Top. Curr. Chem.* **1981,** *97*, 1–31.

116.   Trikoupis, M. A. T., J. K., *Hidden Hydrogen Rearrangements. In Encyclopedia of Mass Spectrometry;* Nibbering, N. M. M. (Ed.); Elsevier, Amsterdam, **2005**, Vol. 4, pp 403−410.

117.   van Setten, D. C.; Jan ten Hove, G.; Wiertz, E. J. H. J.; Kamerling, J. P.; van de Werken, G., *Anal. Chem.* **1998,** *70*, 4401-4409.

118.   Grossert, J. S.; Cook, M. C.; White, R. L., *Rapid Commun. Mass Spectrom.* **2006,** *20*, 1511-1516.

119.   Lu, Y.; Hong, S.; Yang, R.; Uddin, J.; Gotlinger, K. H.; Petasis, N.; A.; Serhan, C. N., *Rapid Commun. Mass Spectrom.* **2007,** *21*, 7−22.

120.   Wesdemiotis, C.; Solak, N.; Polce, M. J.; Dabney, D. E.; Chaicharoen, K.; Katzenmeyer, B. C., *Mass Spectrom. Rev.* **2011,** *30*, 523-559.

121.   Tsugawa, H.; Kind, T.; Nakabayashi, R.; Yukihira, D.; Tanaka; W.; Cajka, T.; Saito, K.; Fiehn, O.; Arita, M., *Anal. Chem.* **2016,** *88*, 7946-7958.

122.   S. Meyerson; I. Puskas; Fields, E. K., *Chem. Ind. (London)* **1968**, 1845-1846.

123.   S. Meyerson; I. Puskas; Fields, E. K., *Adv. Mass Spectrom.* **1974,** *6*, 17-23.

124.   M. A. Winnik; Kwong, P. T. Y., *Org. Mass Spectrom.* **1975,** *10*, 339-346.

125.   Winnik, M. A.; Lee, C. K.; Kwong, P. T. Y., *J. Am. Chem. Soc.* **1974,** *96*, 2901-2907.

126.   F. M. Benoit; Harrison, A. G., *Org. Mass Spectrom.* **1976,** *11*, 1056-1062.

127.   F. M. Benoit; A. G. Harrison; Losing, F. P., *Org. Mass Spectrom.* **1977,** *12*, 78-82.

128.   Longevialle, P.; Botter, R., *J. Chem. Soc. Chem. Comm.* **1980,** (17).

129.   P. Longevialle; Botter, R., *Org. Mass Spectrom.* **1983,** *18*, 1-8.

130.   Longevialle, P., *Org. Mass Spectrom.* **1985,** *20*, 644−645.

131.   Katoh, M.; Djerassi, C., *J. Am. Chem. Soc.* **1970,** *92* (3), 731-732.

132.   Kuck, D., *Adv. Mass Spectrom.* **1986,** (10), 773-774.

133.   Claisen, L., *Berichte der deutschen chemischen Gesellschaft* **1912,** *45* (3), 3157-3166.

134.   Claisen, L.; Tietze, E., *Berichte der deutschen chemischen Gesellschaft (A and B Series)* **1925,** *58* (2), 275-281.

135.   Claisen, L.; Tietze, E., *Berichte der deutschen chemischen Gesellschaft (A and B Series)* **1926,** *59* (9), 2344-2351.

136.   Hurd, C. D.; Schmerling, L., *J. Am. Chem. Soc.* **1937,** *59* (1), 107-109.

137.   Tarbell, D. S., *Chem. Rev.* **1940,** *27* (3), 495-546.

138.   Rhoads, S. J.; Raulins, N. R., *Org. React.* **1975,** *22*, 1-252.

139.   Ziegler, F. E., *Chem. Rev.* **1988,** *88* (8), 1423-1452.

140.   Martin Castro, A. M., *Chem Rev* **2004,** *104* (6), 2939-3002.

141.   Davidson, M. M.; Hillier, I. H.; Vincent, M. A., *Chem. Phys. Lett.* **1995,** *246*, 536-540.

142.   Claisen, L.; Eisleb, O., *Justus Liebig's Annalen der Chemie* **1913,** *401* (1), 21-119.

143.   Goering, H. L.; Jacobson, R. R., *J. Am. Chem. Soc.* **2002,** *80* (13), 3277-3285.

144.   White, W. N.; Wolfarth, E. F., *J. Org. Chem.* **1970,** *35* (7), 2196-2199.

145.   Barmettler, P.; Hansen, H.-J., *Hel. Chim. Acta* **1990,** *73* (6), 1515-1573.

146.   Majumdar, K.; Bhattacharyya, T.; Chattopadhyay, B.; Sinha, B., *Synthesis* **2009,** *2009* (13), 2117-2142.

147.   Wang, H. Y.; Xu, C.; Zhu, W.; Liu, G. S.; Guo, Y. L., *J. Am. Soc. Mass. Spectrom.* **2012,** *23* (12), 2149-57.

148.   Kingston, E. E.; Beynon, J. H.; Liehr, J. G.; Meyrant, P.; Flammang, R.; Maquestiau, A., *Org. Mass Spectrom.* **1985,** *20* (5), 351-359.

149.   Kingston, E. E.; Beynon, J. H.; Flammang, R.; Maquestiau, A., *Org. Mass Spectrom.* **1988,** *23* (6), 437-442.

150.   Harrison, A. G., *Chemical Ionization Mass Spectrometry*. CRC-Press: **1983**.

151.   Clayden, J., Greeves, N., & Warren, S. G., *Organic chemistry*. Oxford, Oxford University Press, **2012**.

152.   Choe, J. C.; Cheong, N. R.; Park, S. M., *Int. J. Mass Spectrom.* **2009,** *279* (1), 25-31.

153. Kuck, D.; Salameh, L. C.; Onwuka, K. I.; Letzel, M. C., *Eur. J. Mass. Spectrom.* **2014,** (20), 51-61.

154. Solcà, N.; Dopfer, O., *Angew. Chem. Int. Ed.* **2002,** *41*, 3628-3631.

155. Dopfer, O.; Lemaire, J.; Maître, P.; Chiavarino, B.; Crestoni, M. E.; Fornarini, S., *Int. J. Mass Spectrom.* **2006**, 149−154.

156. Thevis, M.; Beuck, S.; Hoppner, S.; Thomas, A.; Held, J.; Schäfer, M.; Oomens, J.; Schanzer, W., *J. Am. Soc. Mass. Spectrom.* **2012,** *23* (3), 537-46.

157. Massah, A. R.; Dreiocker, F.; Jackson, R. F.; Pickup, B. T.; Oomens, J.; Meijer, A. J.; Schäfer, M., *Phys. Chem. Chem. Phys.* **2011,** *13* (29), 13255-67.

158. Schäfer, M.; Drayß, M.; Springer, A.; Zacharias, P.; Meerholz, K., *Eur. J. Org. Chem.* **2007,** *2007* (31), 5162-5174.

159. Ryan, J. P.; O'Connor, P. R., *J. Am. Chem. Soc.* **1952,** *74* (23), 5866-5869.

160. Gozzo, F. C.; Fernandes, S. A.; Rodrigues, D. C.; Eberlin, M. N.; Marsaioli, A. J., *J Org. Chem.* **2003,** *68* (14), 5493-9.

161. Kürti, L.; Czakó, B., *Strategic Applications Of Named Reactions In Organic Synthesis: Background And Detailed Mechanics: 250 Named Reactions*; Elsevier Science, Academic Press, **2005**.

162. Ramana, D. V.; Sudha, M. S., *Org. Mass Spectrom.* **1992,** *27* (10), 1121-1126.

163. Crotti, S.; Stella, L.; Munari, I.; Massaccesi, F.; Cotarca, L.; Forcato, M.; Traldi, P., *J. Mass Spectrom.* **2007,** *42* (12), 1562-8.

164. Vandezonneville, A.; Flammang, R.; Maquestiau, A.; Kingston, E.; Beynon, J. H., *Org. Mass Spectrom.* **1986,** *21* (6), 351-355.

165. Piest, H.; von Helden, G.; Meijer, G., *J. Chem. Phys.* **1999,** *110* (4), 2010-2015.

166. Mukherjee, M.; Bandyopadhyay, B.; Biswas, P.; Chakraborty, T., *Ind. J. Phys.* **2012,** *86* (3), 201-208.

167. Honda, M.; Fujii, A.; Fujimaki, E.; Ebata, T.; Mikami, N., *J. Phys. Chem. A* **2003,** *107* (19), 3678-3686.

168. Piracha, N. K.; Nakanaga, T., *J. Mol. Struc.* **2002,** *611* (1-3), 179-183.

169. Rap, D. B.; van Boxtel, T.; Redlich, B.; Brunken, S., *J. Phys. Chem. A* **2022,** *126* (19), 2989-2997.

170. Chalyavi, N.; Sanelli, J. A.; Dryza, V.; Bieske, E. J., *J. Phys. Chem. A* **2013,** *117* (44), 11276-81.

171. Van Berkel, G. J.; Zhou, F., *Anal. Chem.* **1995,** *67* (17), 2916-2923.

172. Lias, S. G.; Bartmess, J. E.; Liebman, J. F.; Holmes, J. L.; Levin, R. D.; Mallard, W. G., *J. Phys. Chem. Ref. Data* **1988**, 17 (1).

173. Sana, M.; Leroy, G.; Hilali, M.; Nguyen, M. T.; Vanquickenborne, L. G., *Chem. Phys. Lett.* **1992,** *190*, 551-556.

174. Mayer, P. M.; Glukhovtsev, M. N.; Gauld, J. W.; Radom, L., *J. Am. Chem. Soc.* **1997,** *119*, 12889−12895.

175. Holmes, J. L.; Aubry, C.; Mayer, P. M., *Assigning Structures to Ions in Mass Spectrometry*; CRC Press, **2007**; Chapter 3, pp 130−131.

176. Tureč k, F.; Pancír, J.; Stahl, D.; Gäumann, T., *Org. Mass Spectrom.* **1987,** *22*, 145−153.

177. Brown, R. S., *Can. J. Chem.* **1976,** *54*, 1521−1527.

178.   Müller, K.; Previdoli, F.; Desilvestro, H., *Helv. Chim. Acta* **1981,** *64*, 2497−2507.

179.   Devlin, J. L.; Wolf, J. F.; Taft, R. W.; Hehre, W. J., *J. Am. Chem. Soc.* **1976,** *98*, 1990−1992.

180.   Eckert-Maksić, M.; Knězević, A.; Maksić, Z. B., *J. Phys. Org. Chem.* **1998,** *11*, 663−669.

181.   Kuck, D., *Protonated Aromatics and Arenium Ions. In Encyclopedia of Mass Spectrometry*; Nibbering, N. M. M. (Ed.); Elsevier, Amsterdam, **2005**, Vol. 4, pp 229−242.

182.   Grützmacher, H.-F.; Kuck, D., *Int. J. Mass Spectrom.* **2017,** *413*, 106-116.

183.   Kuck, D., *Org. Mass Spectrom.* **1989,** *24*.

184.   Hunter, E. P. L.; Lias, S. G., *J. Phys. Chem. Ref. Data* **1998,** *27*, 413.

185.   Frisch, M. J.; Trucks, G. W.; Schlegel, H. B.; Scuseria, G. E.; Robb, M. A.; Cheeseman, J. R.; Scalmani, G.; Barone, V.; Petersson, G. A.; Nakatsuji, H.; Li, X.; Caricato, M.; Marenich, A. V.; Bloino, J.; Janesko, B. G.; Gomperts, R.; Mennucci, B.; Hratchian, H. P.; Ortiz, J. V.; Izmaylov, A. F.; Sonnenberg, J. L.; Williams; Ding, F.; Lipparini, F.; Egidi, F.; Goings, J.; Peng, B.; Petrone, A.; Henderson, T.; Ranasinghe, D.; Zakrzewski, V. G.; Gao, J.; Rega, N.; Zheng, G. Liang, W.; Hada, M.; Ehara, M.; Toyota, K.; Fukuda, R.; Hasegawa, J.; Ishida, M.; Nakajima, T.; Honda, Y.; Kitao, O.; Nakai, H.; Vreven, T.; Throssell, K.; Montgomery Jr., J. A.; Peralta, J. E.; Ogliaro, F.; Bearpark, M. J.; Heyd, J. J.; Brothers, E. N.; Kudin, K. N.; Staroverov, V. N.; Keith, T. A.; Kobayashi, R.; Normand, J.; Raghavachari, K.; Rendell, A. P.; Burant, J. C.; Iyengar, S. S.; Tomasi, J.; Cossi, M.; Millam, J. M.; Klene, M.; Adamo, C.; Cammi, R.; Ochterski, J. W.; Martin, R. L.; Morokuma, K.; Farkas, O.; Foresman, J. B.; Fox, D. J. *Gaussian 16 Rev. C.01*, Wallingford, CT, 2016.

186.   Grimme, S.; Ehrlich, S.; Goerigk, L., *J. Comput. Chem.* **2011,** *32*, 1456-1465.

187.   Thorwirth, S.; Harding, M. E.; Asvany, O.; Brünken, S.; Jusko, P.; Lee, K. L. K.; Salomon, T.; McCarthy, M. C.; Schlemmer, S., *Mol. Phys.* **2020,** *118* (19-20).

188.   Brünken, S.; Lipparini, F.; Stoffels, A.; Jusko, P.; Redlich, B.; Gauss, J.; Schlemmer, S., *J. Phys. Chem. A* **2019,** *123* (37), 8053-8062.

189.   D. S. Hemming; E. P. Talbot; Steel, P. G., *Tetrahedron Lett.* **2017**, *58*, 17–20.

190.   Kamitori, Y.; Hojo, M.; Masuda, R.; Izumi, T.; Tsukamoto, S., *J. Org. Chem.* **1984,** *49* (22), 4161-4165.

191.   M. Reitti; R. Gurubrahamam; M. Walther; E. Lindstedt; Olofsson, B., *Org. Lett.* **2018**, 1785–1788.

192.   Yamato, T.; Arimura, T.; Tashiro, M., *J. Chem. Soc., Perkin Trans. 1* **1987,** (0), 1-7.

193.   I. Malina; V. Kampars; B. Turovska; Belyakov, S., *Dye. Pigment.* **2017,** *139*, 820–830.

194.   Unoh, Y.; Hirano, K.; Satoh, T.; Miura, M., *J. Org. Chem.* **2013,** *78* (10), 5096-102.

195.   Koltunov, K. Y.; Repinskaya, I. B.; Borodkin, G. I., *Rus. J. Org. Chem.* **2001,** *37* (11), 1534-1541.

196.   Haraguchi, R.; Tanazawa, S. G.; Tokunaga, N.; Fukuzawa, S. I., *Eur. J. Org. Chem.* **2018,** *2018* (15), 1761-1764.

197.   Wendling, T.; Risto, E.; Krause, T.; Goossen, L. J., *Chemistry* **2018,** *24* (23), 6019-6024.

198.   Copp, F. C., *J. Chem. Soc.* **1953**, 3116-3118.

8. Appendix

8.1 List of Abbreviations

2H	double hydrogen
3H	triple hydrogen
AE	appearance energy
CEM	chain ejection model
CID	collision induced dissociation
CNDO	complete neglect of differential overlap
CRM	charged residue model
DFT	density functional theory
EI	electron ionization
ESI	electrospray ionization
ETD	electron transfer dissociation
eV	electron volt
FEL	free electron laser
FTICR	Fourier-transform ion cyclotron resonance
G3DBJ	Grimme's D3 correction with Becke–Johnson damping
GGA	generalized gradient approximation
GTF	Gaussian-type function
GTO	Gaussian-type orbital
HF	Hartree-Fock
ICR	ion cyclotron resonance
IE	ionization energy
IEM	ion evaporation model
INDO	intermediate neglect of differential overlap
IR	infrared
IRPD	infrared photodissociation spectroscopy
IRMPD	infrared multiphoton dissociation spectroscopy
IVR	intramolecular vibrational redistribution
KS	kinetic shift
LDA	local-density approximation
m/z	mass-to-charge ratio

MD	molecular dynamics
MIKE	mass-analyzed ion kinetic energy (experiments)
MS	mass spectrometry
NDDO	neglect of differential-diatomic overlap
OPO	optical parametric oscillator
PES	potential energy surface
SCF	self-consistent field
STO	Slater-type orbital
TOF	time-of-flight
TS	transition state
ZDO	zero-differential overlap
ZPVE	zero-point vibrational energy

8.2 NMR Spectra
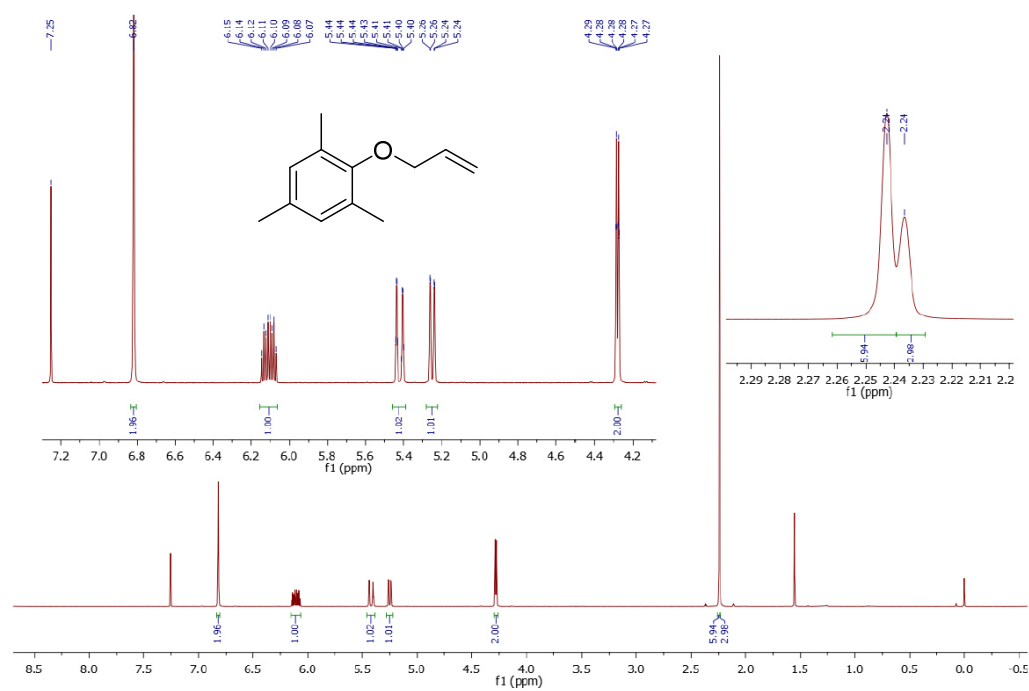
Figure 82

^{1}H-NMR spectrum (500 MHz) of allyl-2,4,6-trimethylphenylether **6** in CDCl$_3$.
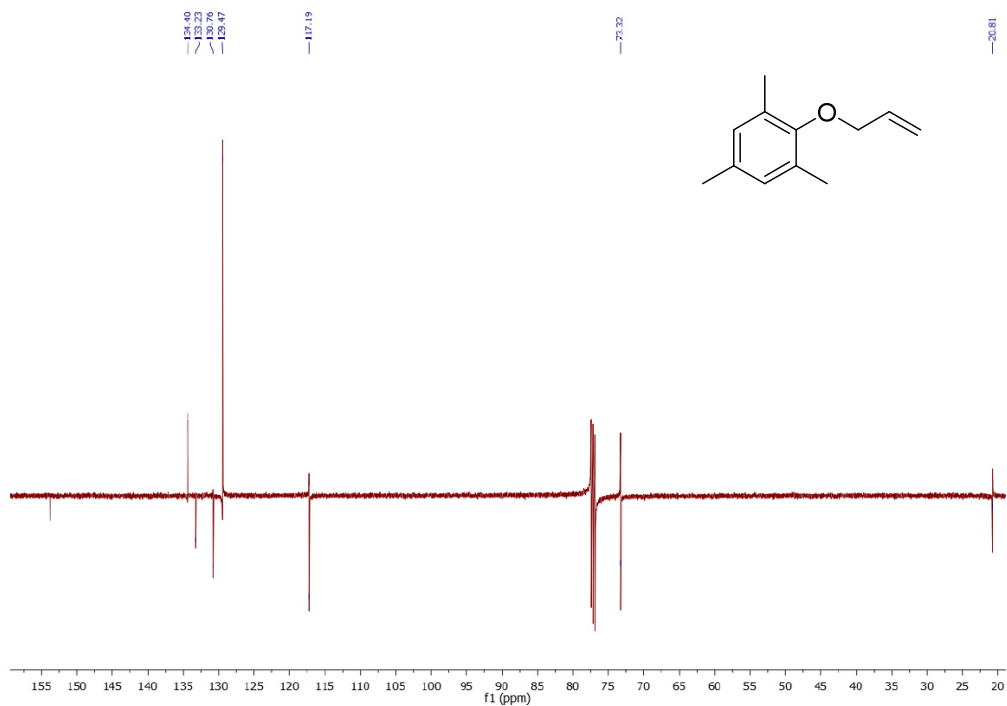
Figure 83

^{13}C-NMR spectrum (126 MHz) of allyl-2,4,6-trimethylphenylether **6** in CDCl$_3$.
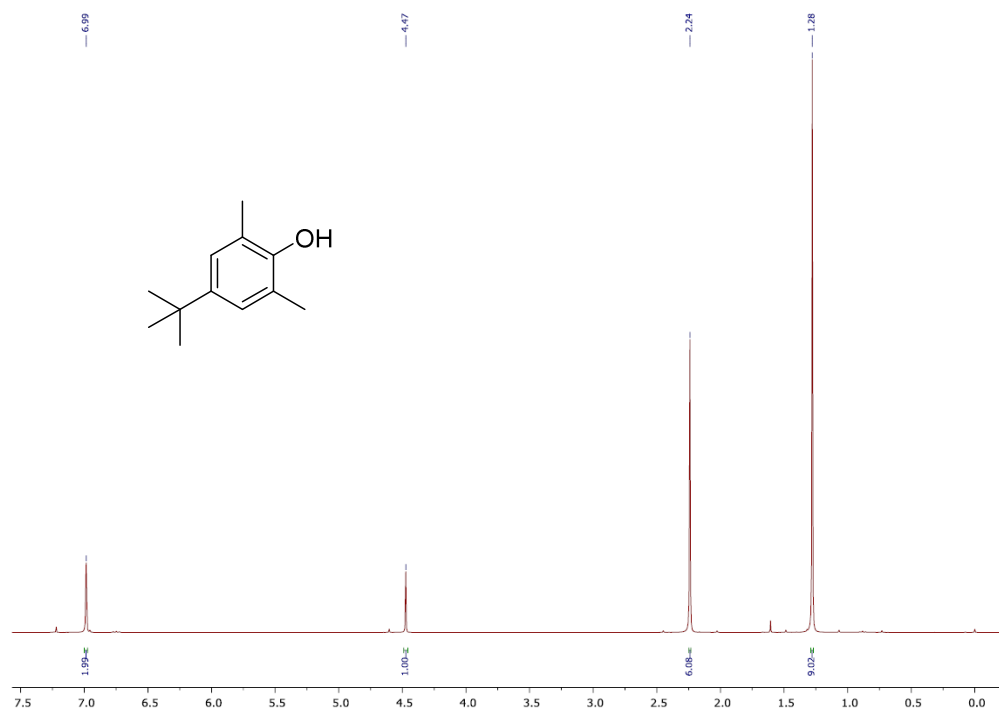
Figure 84
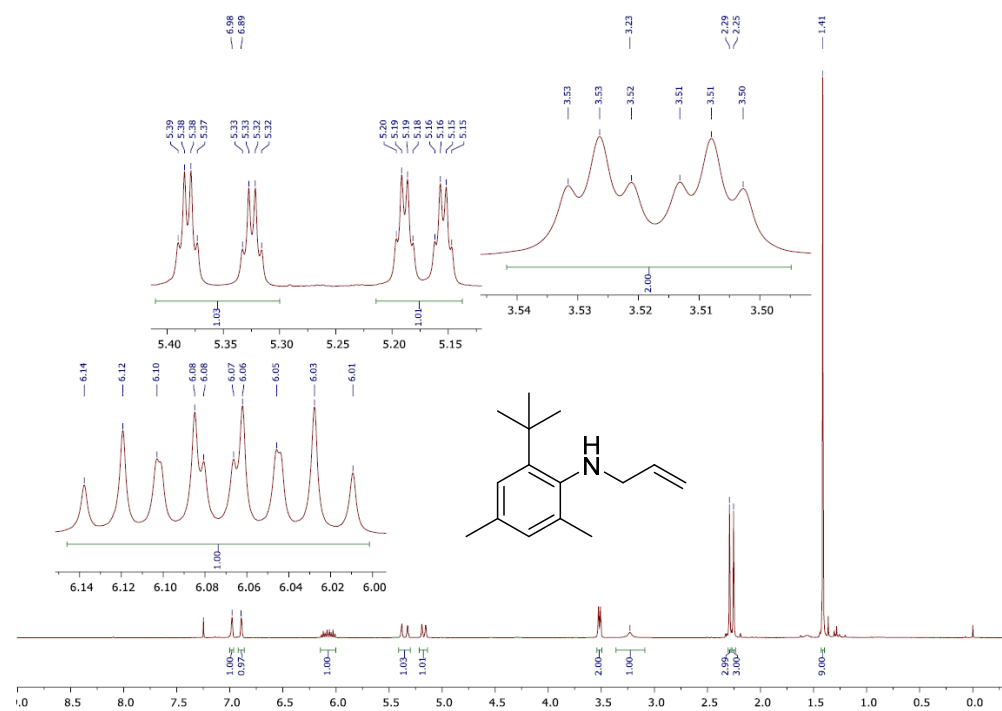^{1}H-NMR spectrum (300 MHz) of 4-*tert*-butyl-2,6-phenol **29** in CDCl₃.
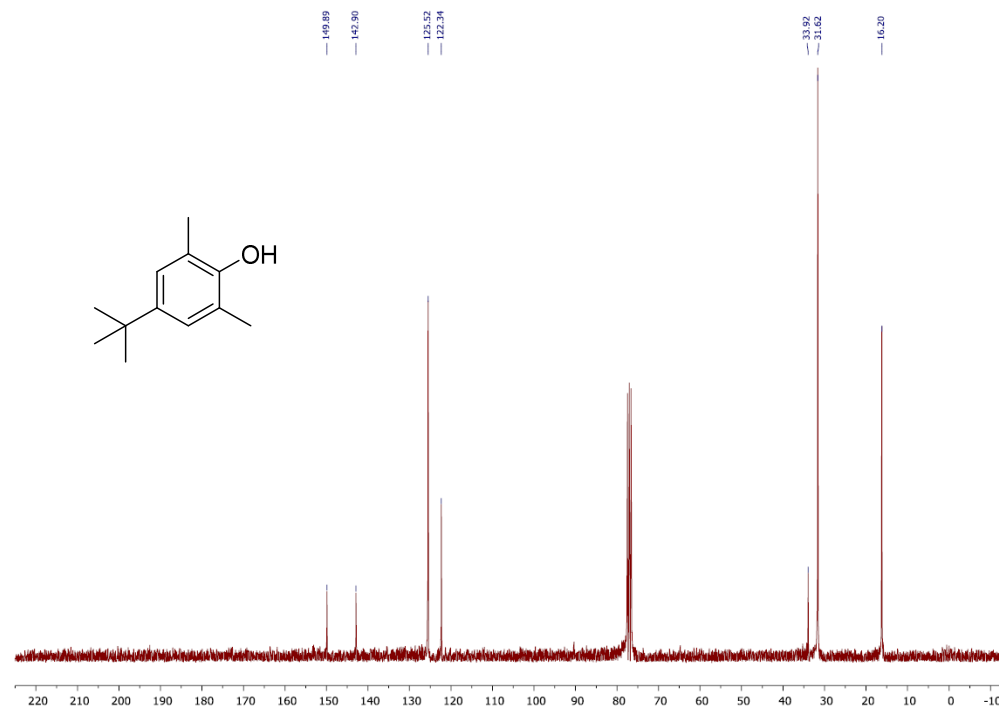
Figure 85
^{13}C-NMR spectrum (75 MHz) of 4-*tert*-butyl-2,6-phenol **29** in CDCl₃.
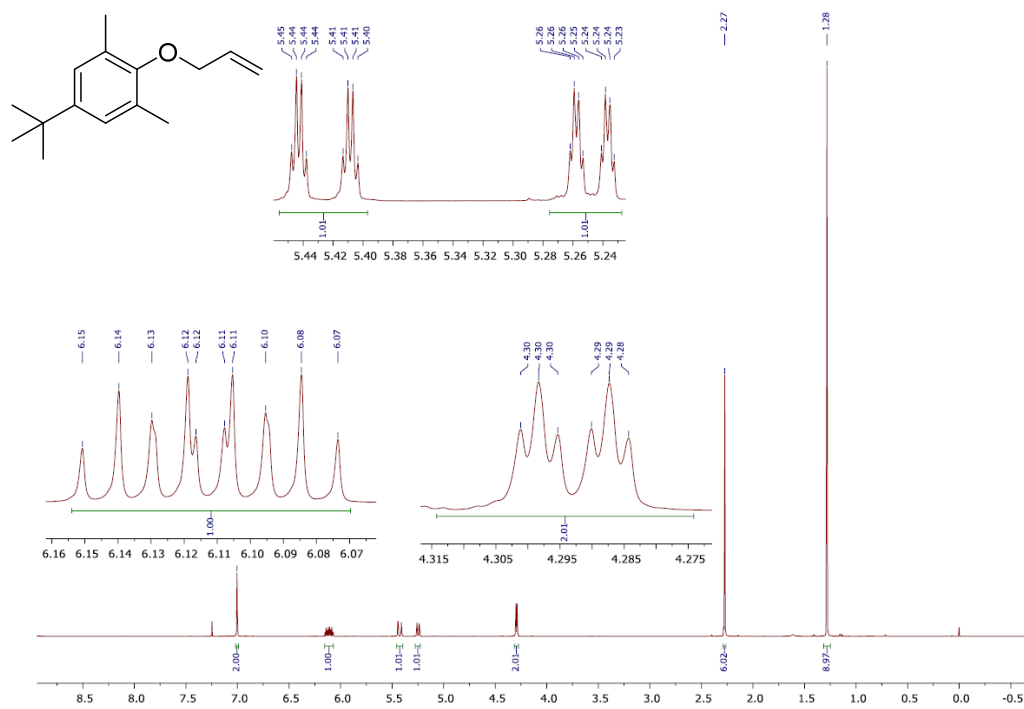
Figure 86

^{1}H-NMR spectrum (500 MHz) of allyl-2,4,6-trimethylphenylether **6** in CDCl$_3$.
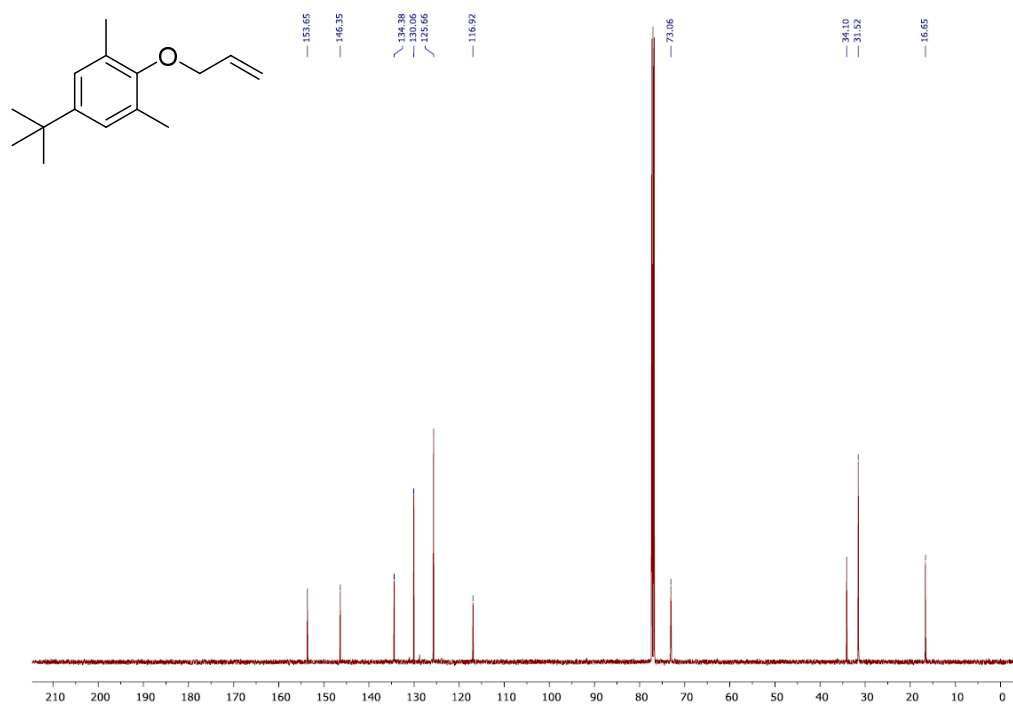
Figure 87

^{13}C-NMR spectrum (126 MHz) of allyl-2,4,6-trimethylphenylether **6** in CDCl$_3$.
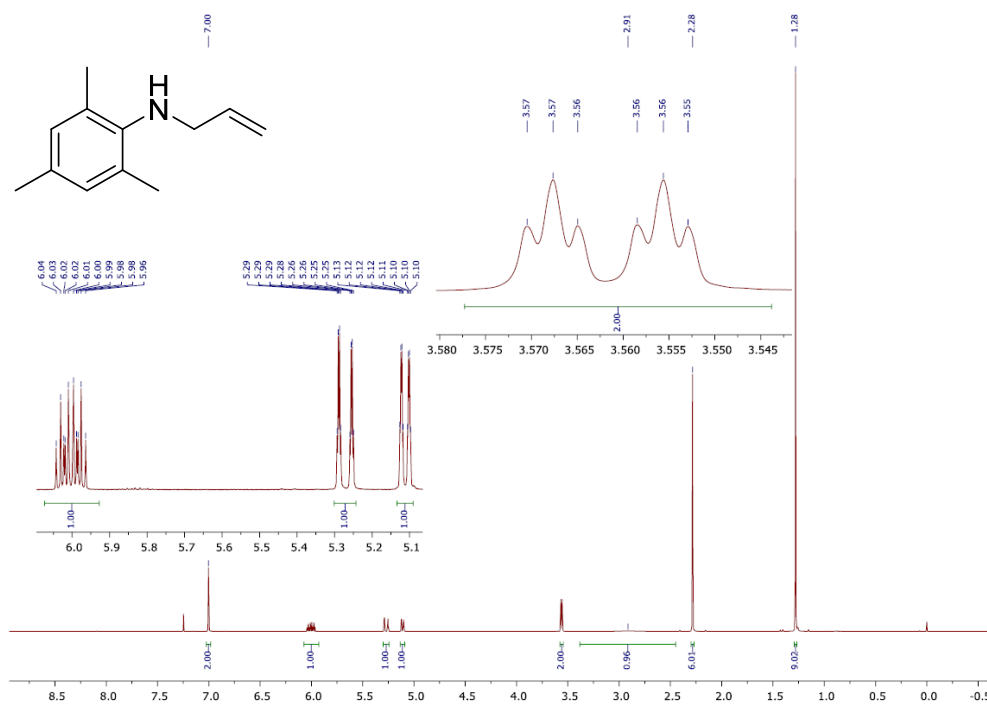
Figure 88
^{1}H-NMR spectrum (500 MHz) of *N*-allyl-2,4,6-trimethylaniline **17** in CDCl$_3$.
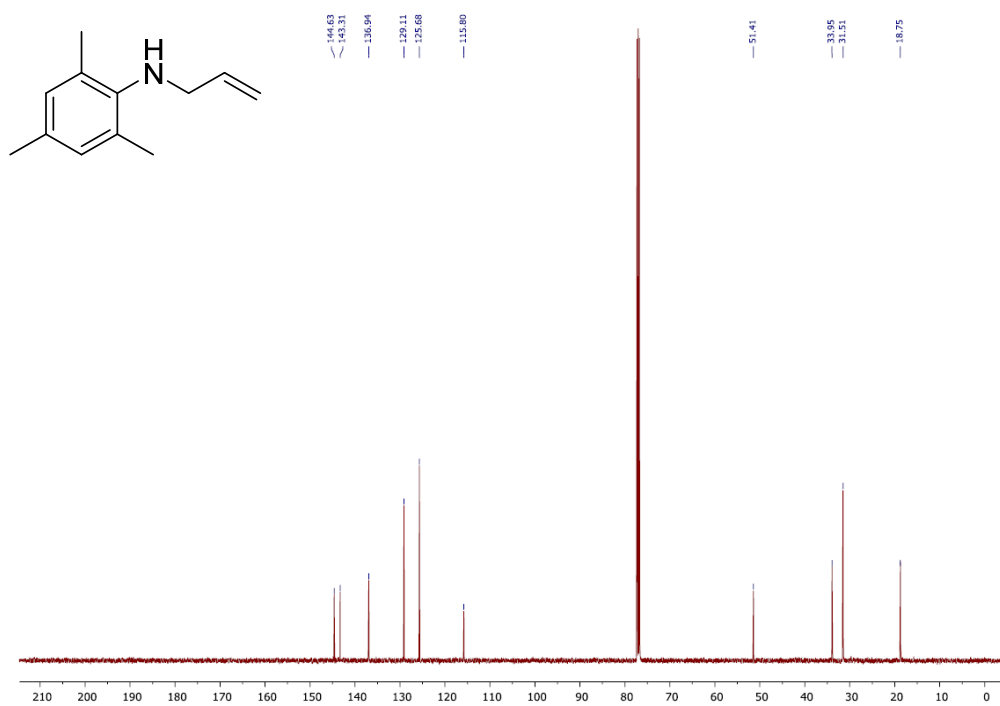
Figure 89
^{13}C-NMR spectrum (126 MHz) of *N*-allyl-2,4,6-trimethylaniline **17** in CDCl$_3$.
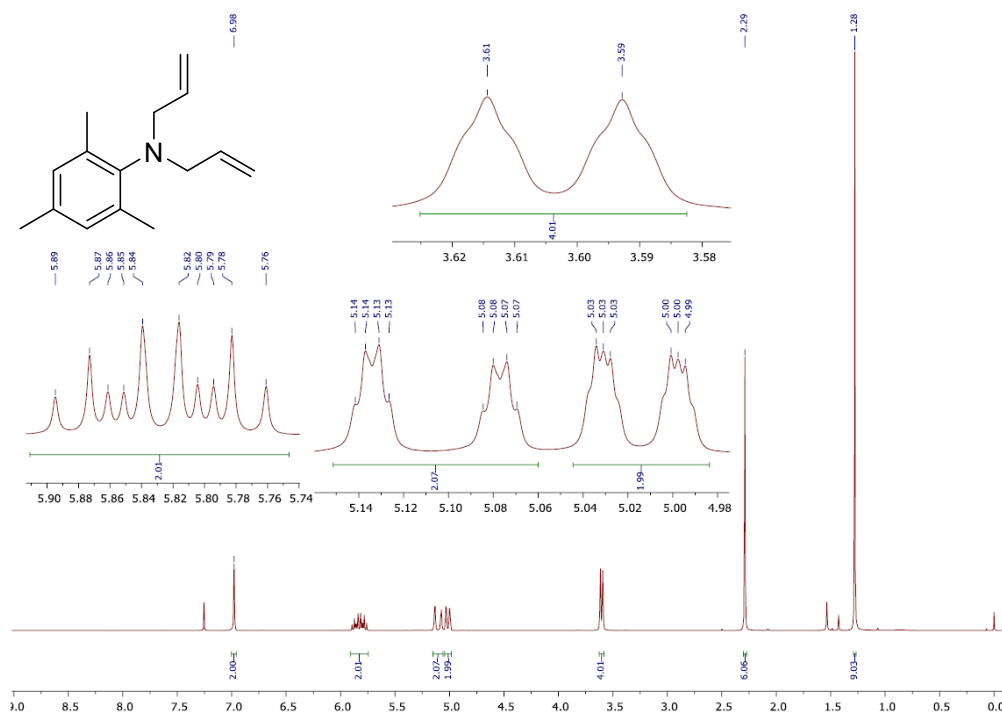
Figure 90
^{1}H-NMR spectrum (300 MHz) of *N,N*-diallyl-2,4,6-trimethylaniline **18** in CDCl$_3$.
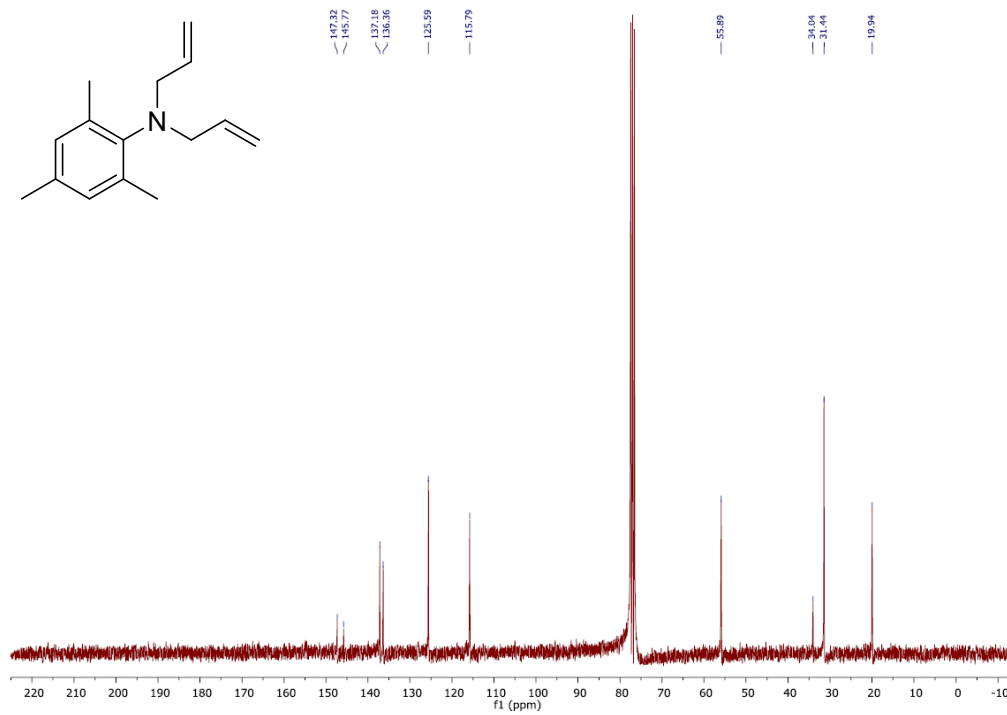
Figure 91
^{13}C-NMR spectrum (75 MHz) of *N,N*-diallyl-2,4,6-trimethylaniline **18** in CDCl$_3$.
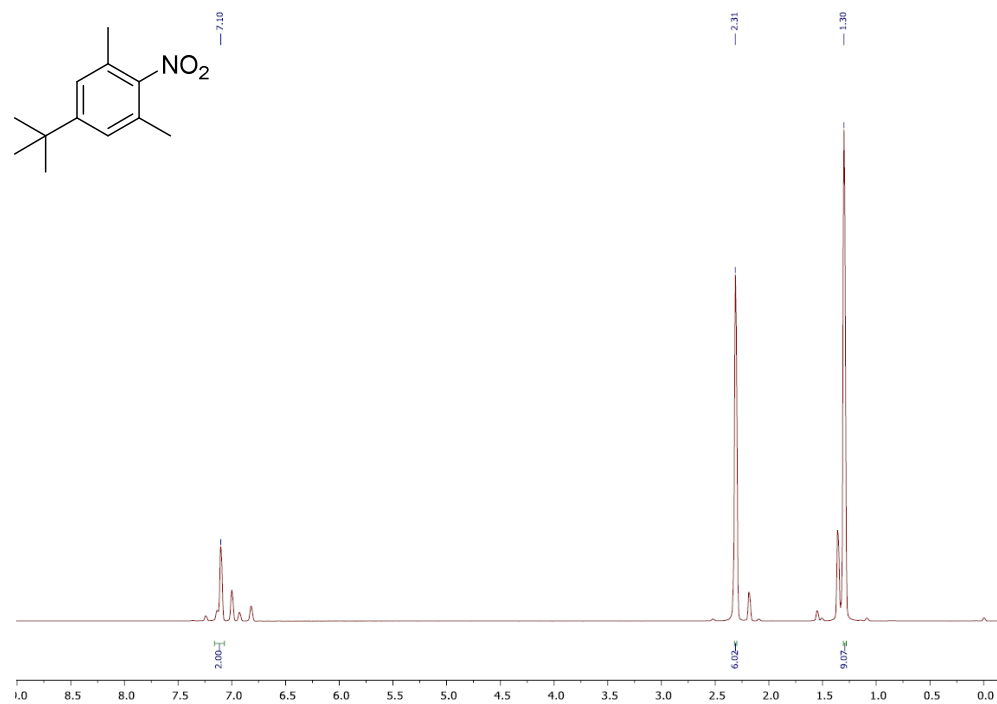
Figure 92

^{1}H-NMR spectrum (300 MHz) of 5-*tert*-butyl-1,3-dimethyl-2-nitrobenzene **33** in CDCl$_3$.
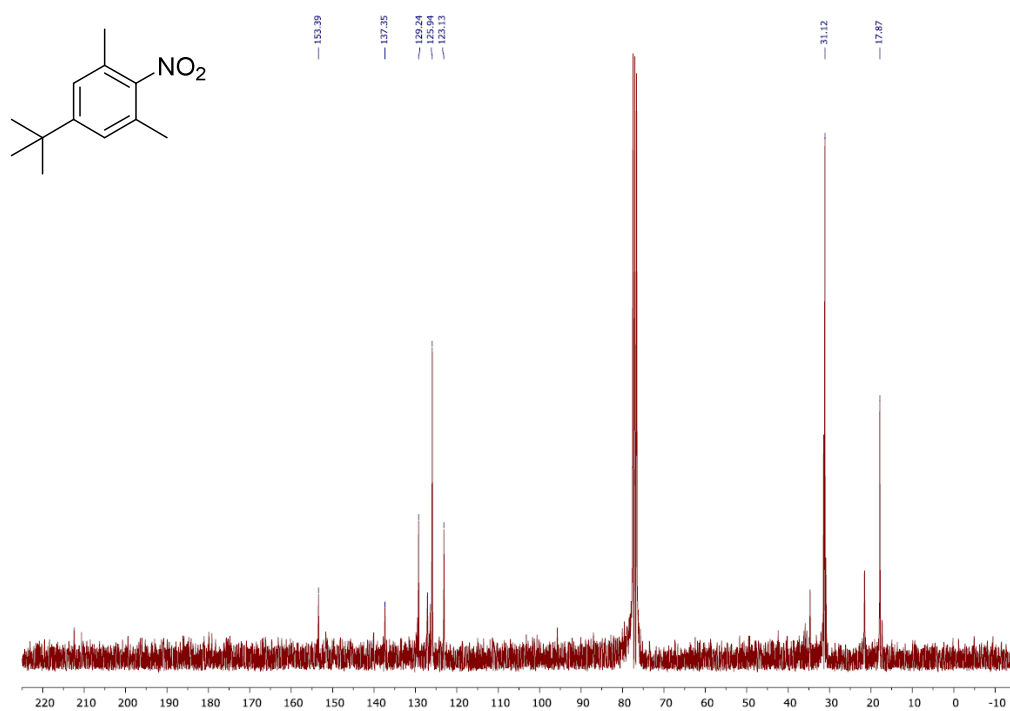
Figure 93

^{13}C-NMR spectrum (75 MHz) of 5-*tert*-butyl-1,3-dimethyl-2-nitrobenzene **33** in CDCl$_3$.
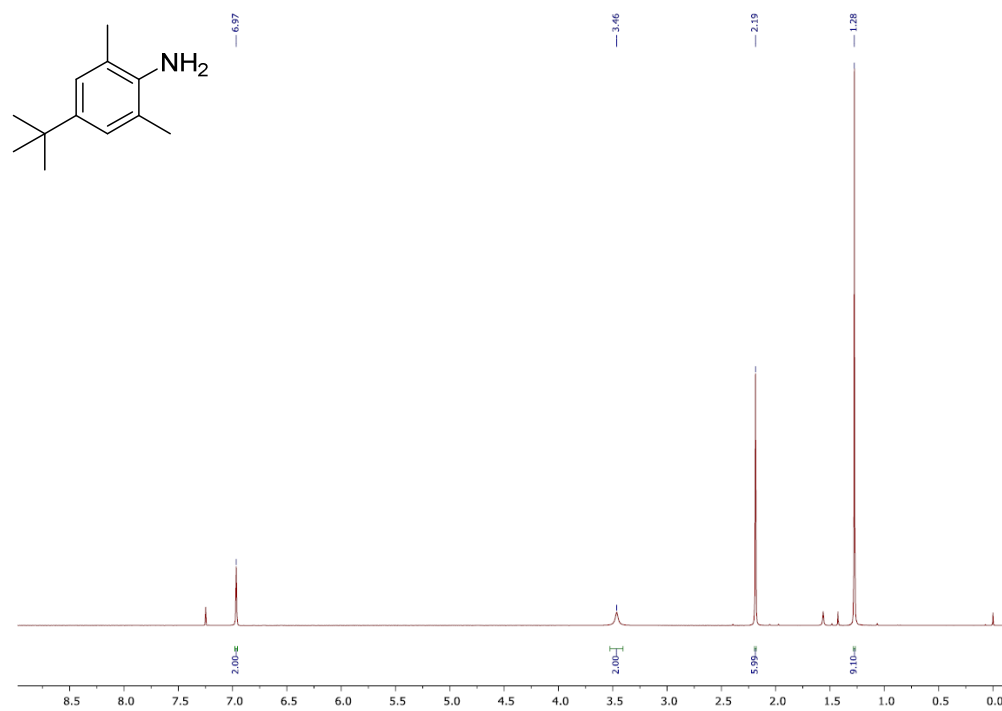
Figure 94
^{1}H-NMR spectrum (300 MHz) of 4-*tert*-butyl-2,6-dimethylaniline **34** in CDCl₃.
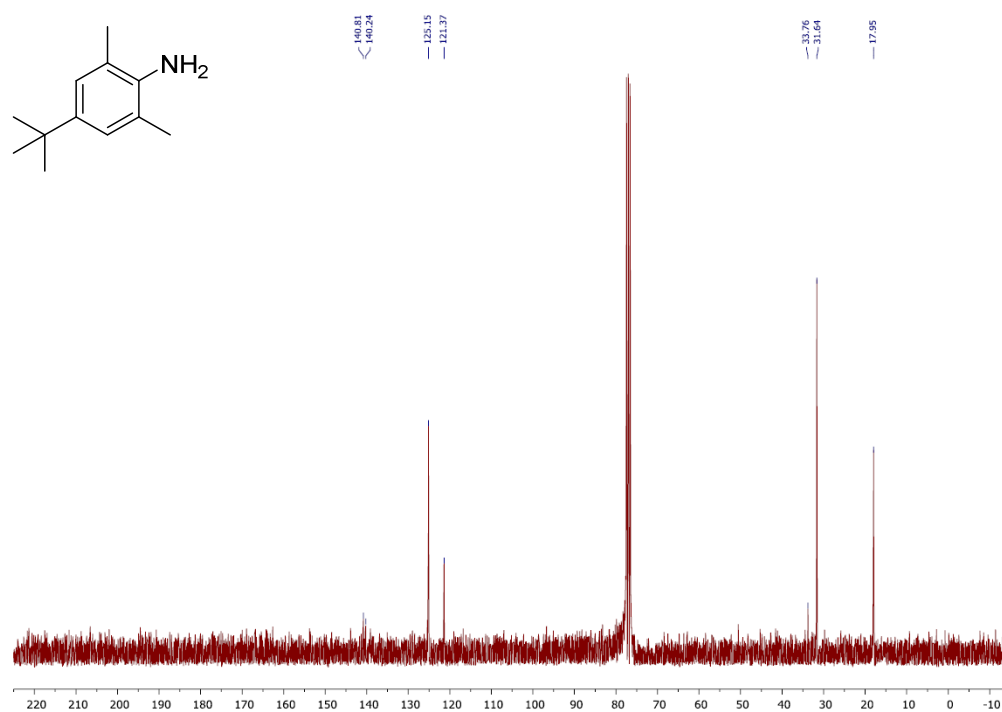
Figure 95
^{13}C-NMR spectrum (75 MHz) of 4-*tert*-butyl-2,6-dimethylaniline **34** in CDCl₃.
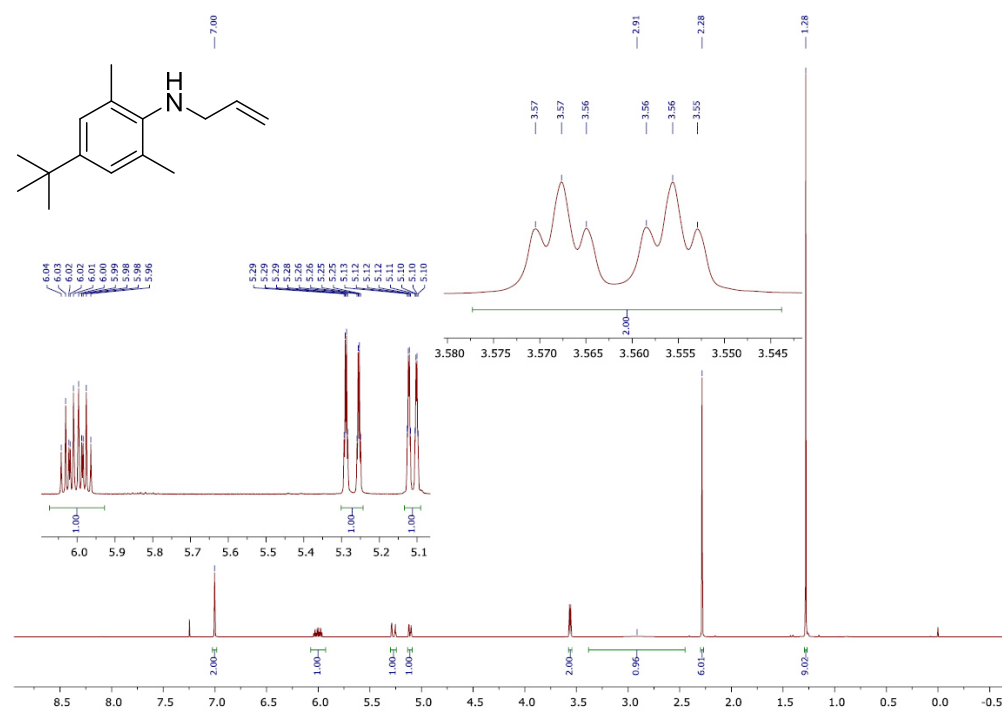
Figure 96
^{1}H-NMR spectrum (500 MHz) of *N*-allyl-2,6-dimethyl-4-*tert*-butylaniline **19** in CDCl3.
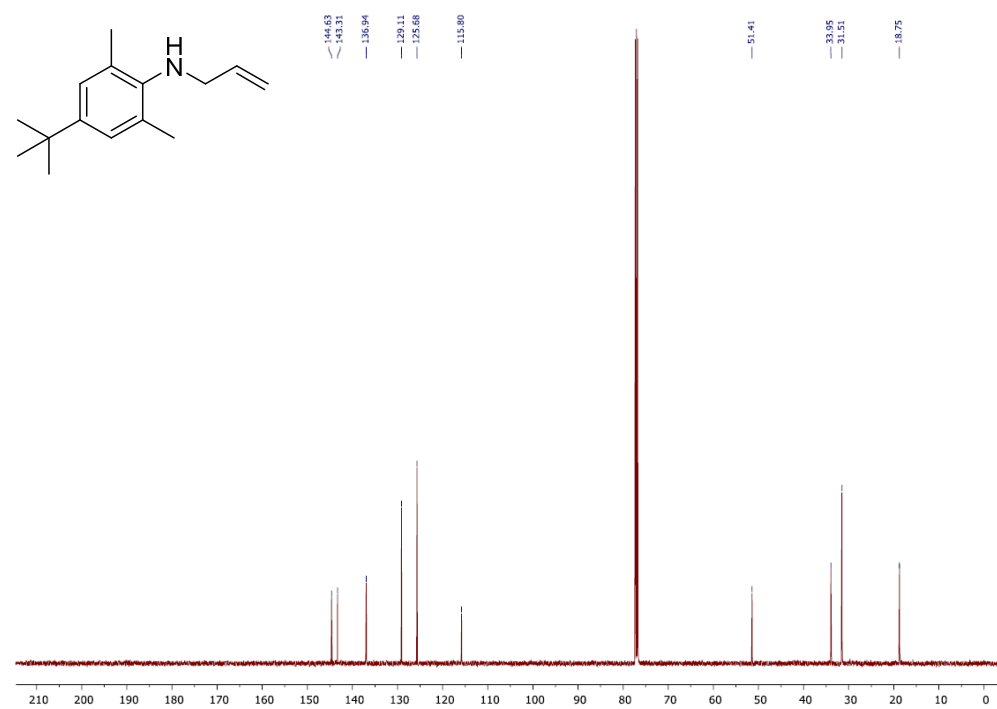
Figure 97
^{13}C-NMR spectrum (126 MHz) *N*-allyl-2,6-dimethyl-4-*tert*-butylaniline **19** in CDCl3.

Figure 98
^{1}H-NMR spectrum (300 MHz) of *N*-allyl-4,6-dimethyl-2-*tert*-butylaniline **20** in CDCl₃.
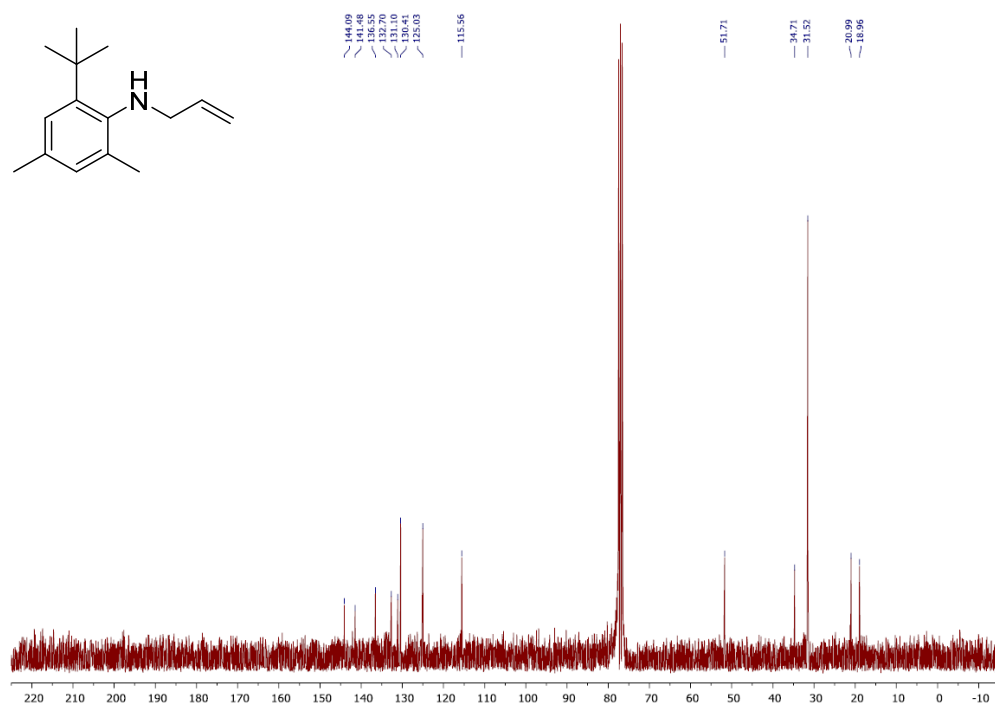
Figure 99
^{13}C-NMR spectrum (75 MHz) of *N*-allyl-4,6-dimethyl-2-*tert*-butylaniline **20** in CDCl₃.
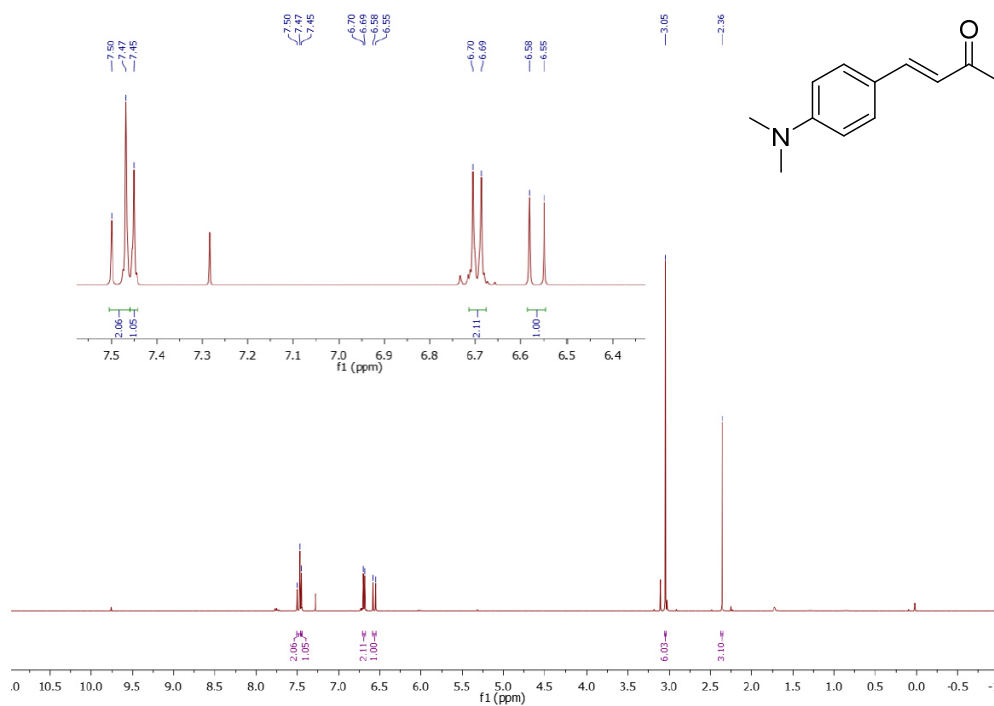
Figure 100
^{1}H-NMR spectrum (300 MHz) of (E)-4-(4-(dimethylamino)phenyl)but-3-en-2-one **38** in CDCl$_3$.
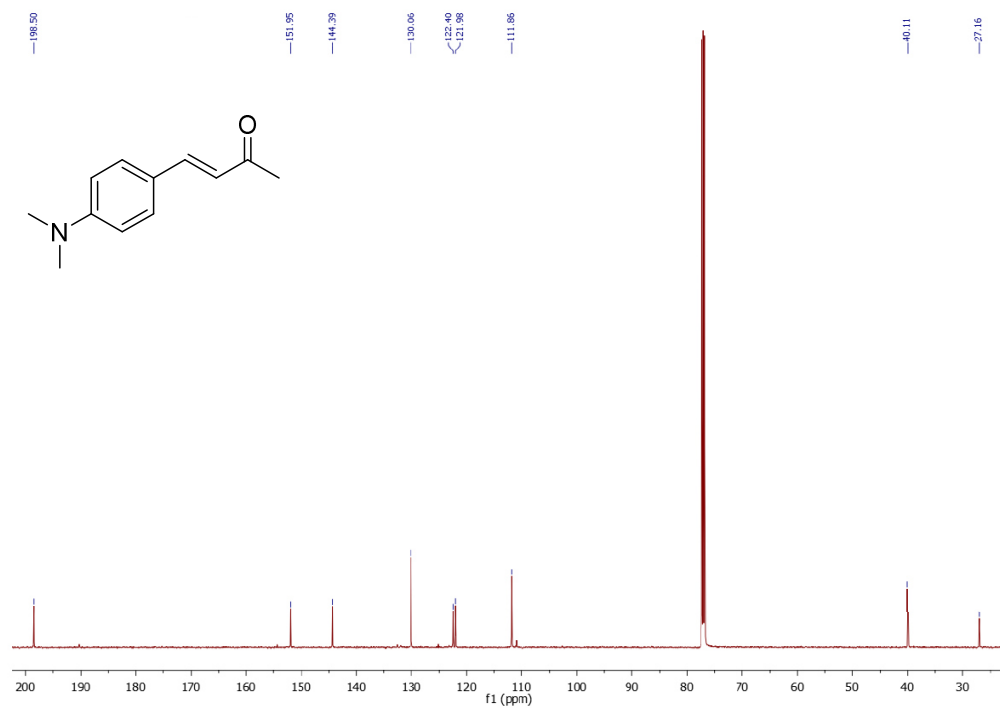
Figure 101
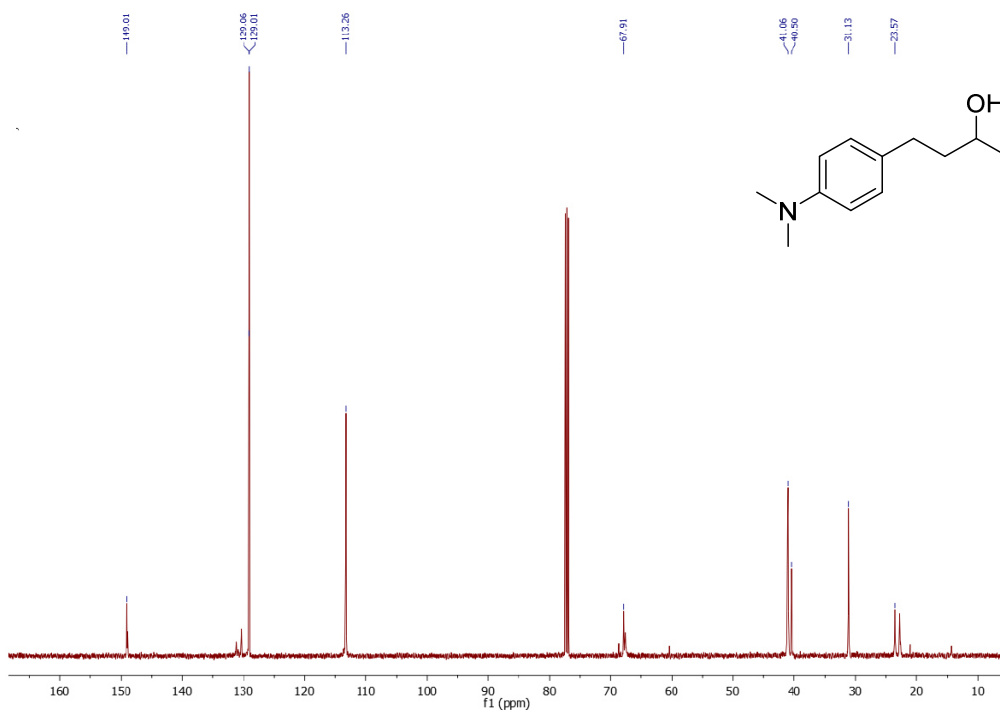^{13}C-NMR spectrum (75 MHz) of (E)-4-(4-(dimethylamino)phenyl)but-3-en-2-one **38** in CDCl$_3$.
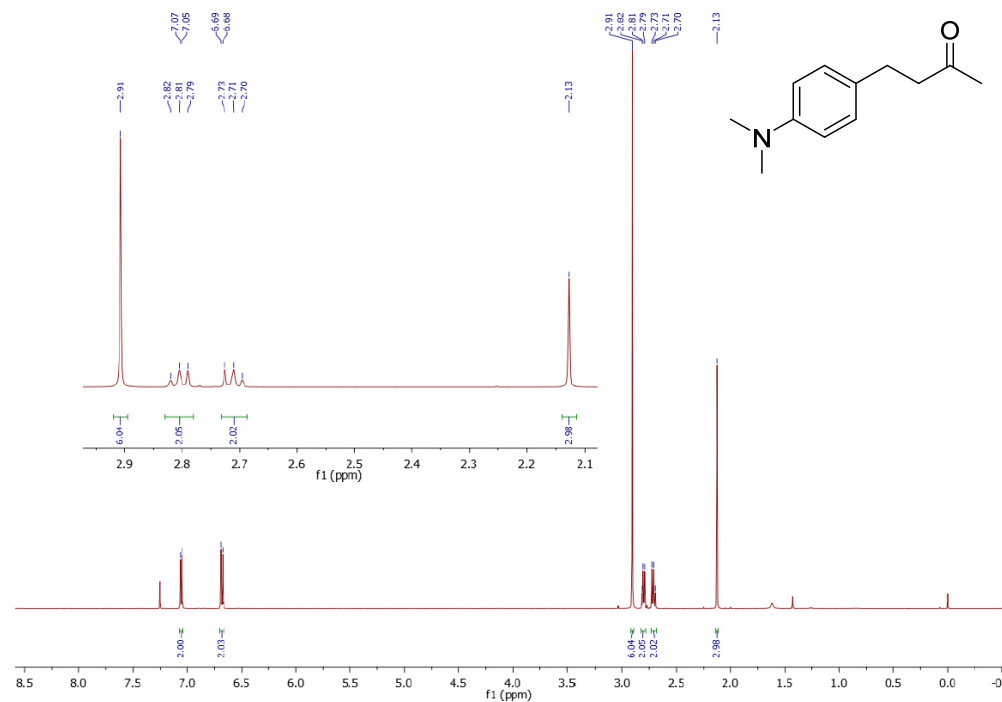
Figure 102

^{1}H-NMR spectrum (300 MHz) of 4-(4-(dimethylamino)phenyl)butan-2-one **39** in CDCl₃.
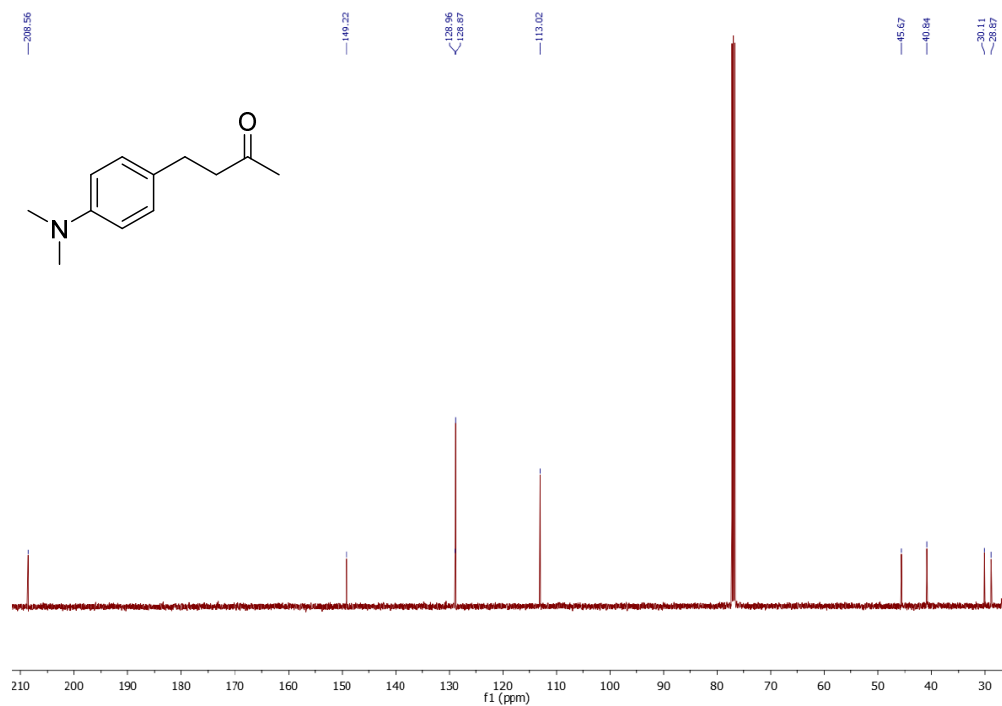
Figure 103

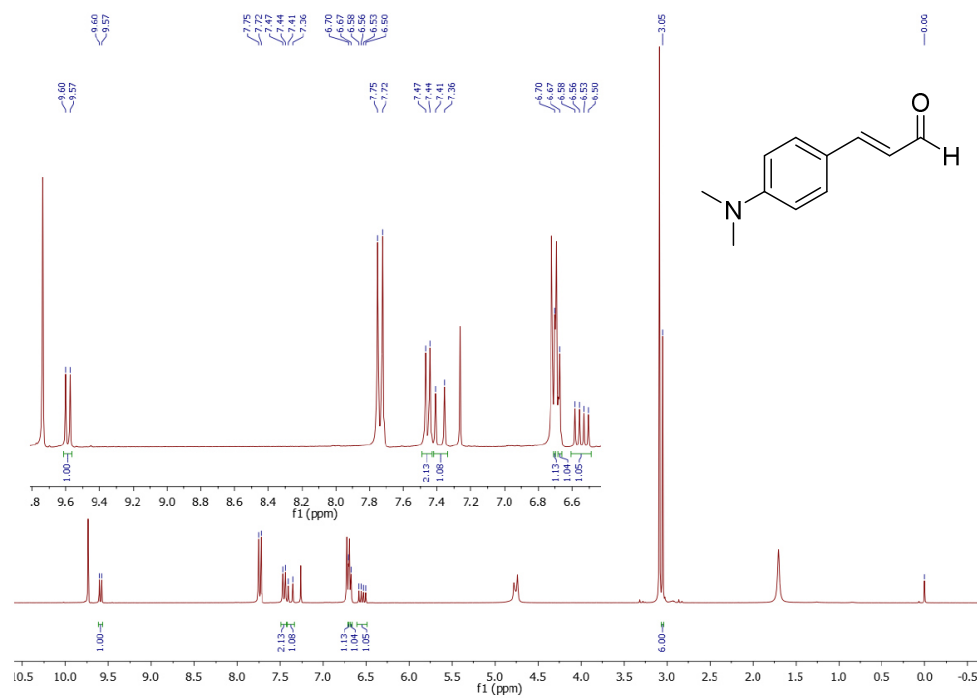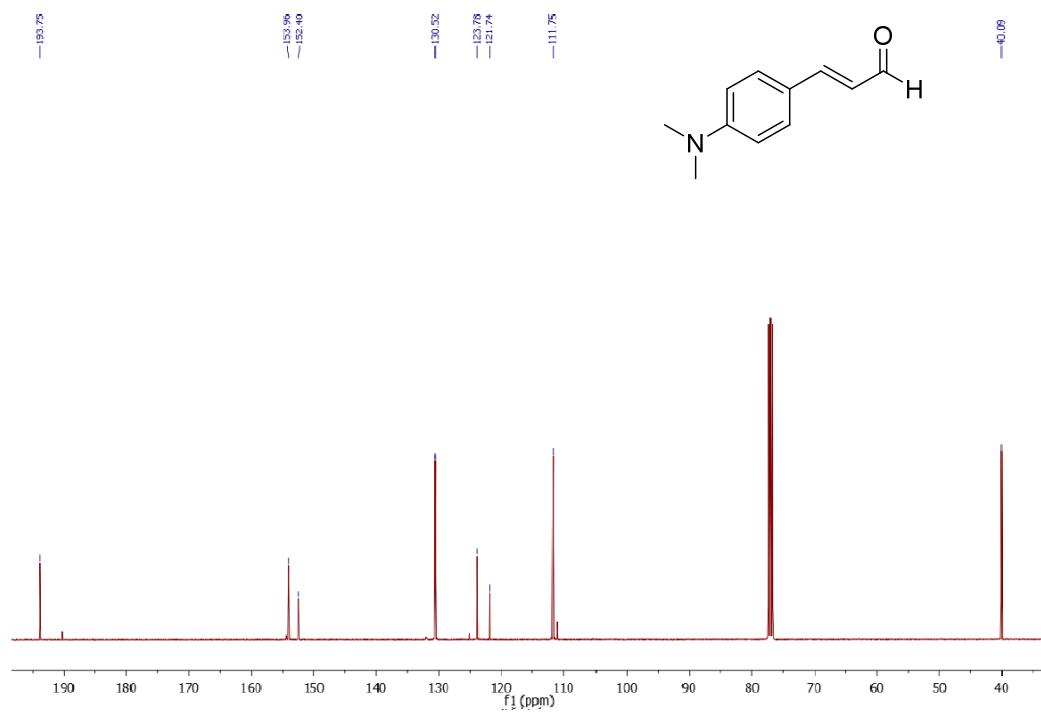^{13}C-NMR spectrum (75 MHz) of 4-(4-(dimethylamino)phenyl)butan-2-one **39** in CDCl₃.
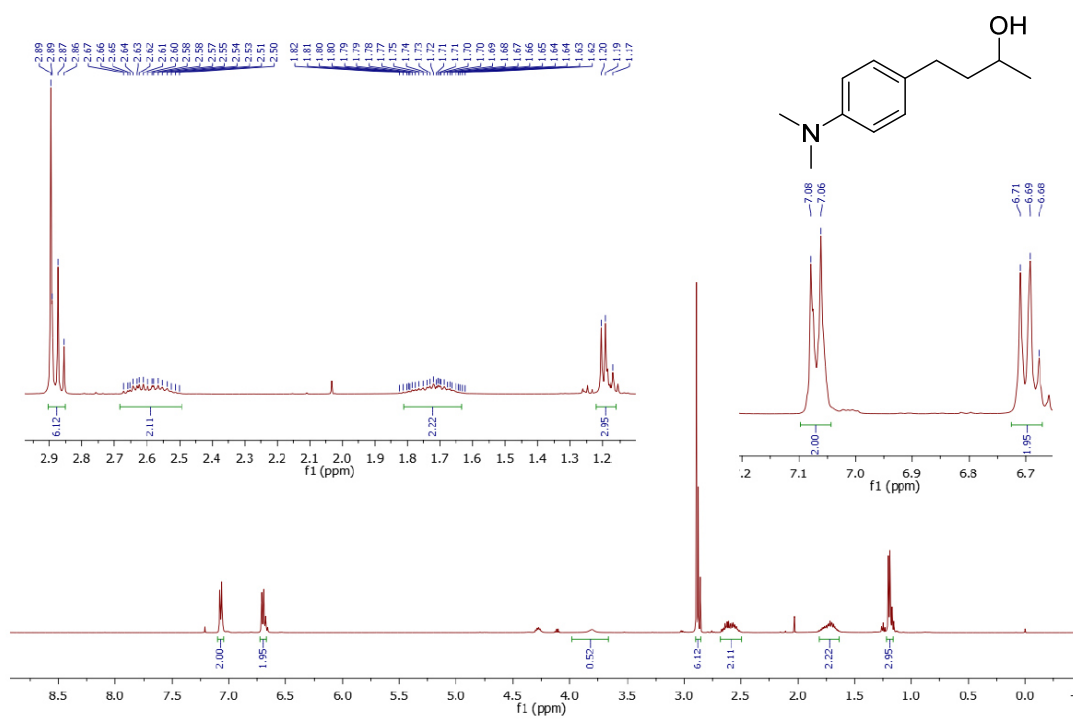
Figure 104
^{1}H-NMR spectrum (300 MHz) of 4-(4-*N*,*N*-dimethylaminophenyl)-2-butanol **14** in CDCl[3].
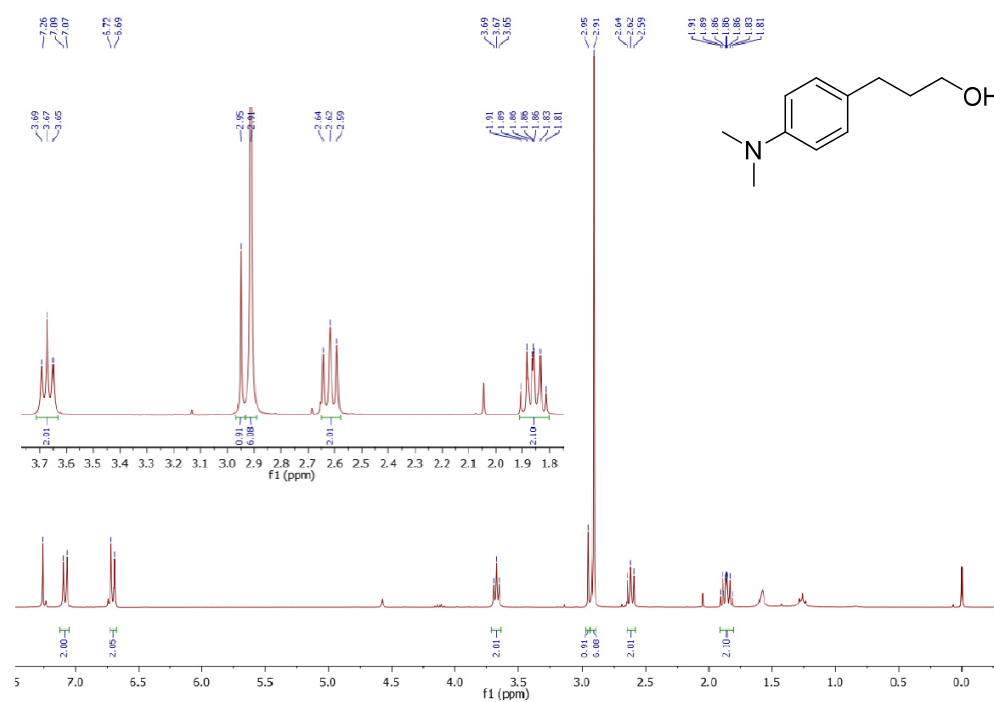

Figure 105
^{13}C-NMR spectrum (75 MHz) of 4-(4-*N*,*N*-dimethylaminophenyl)-2-butanol **14** in CDCl[3].
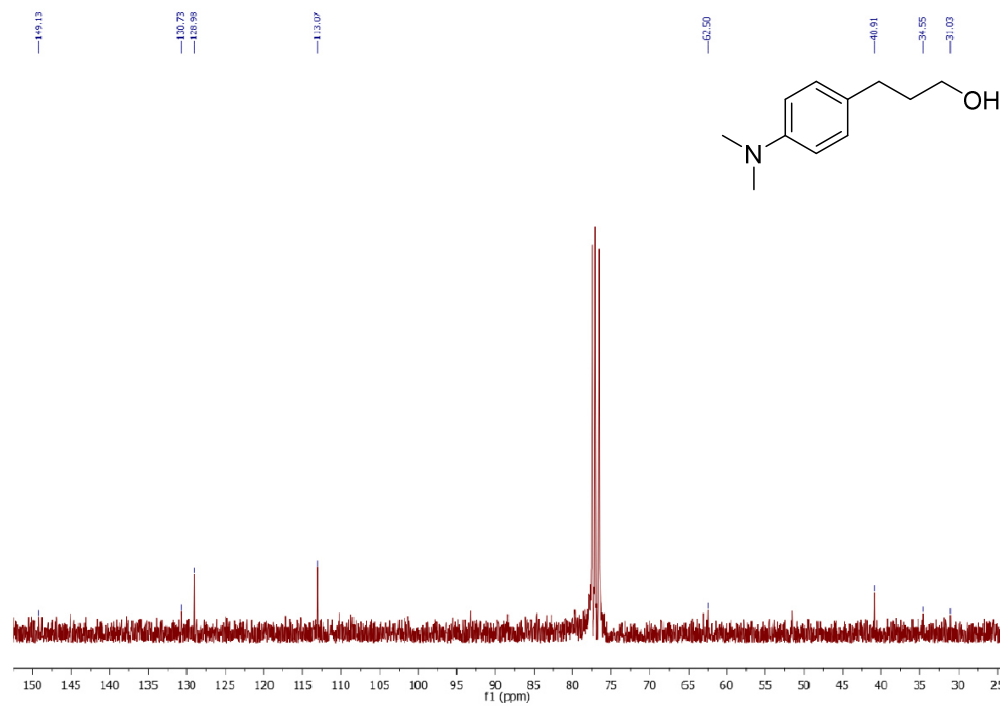
Figure 106
¹H-NMR spectrum (300 MHz) of (*E*)-3-(4-(dimethylamino)phenyl)acrylaldehyde **41** in CDCl₃.
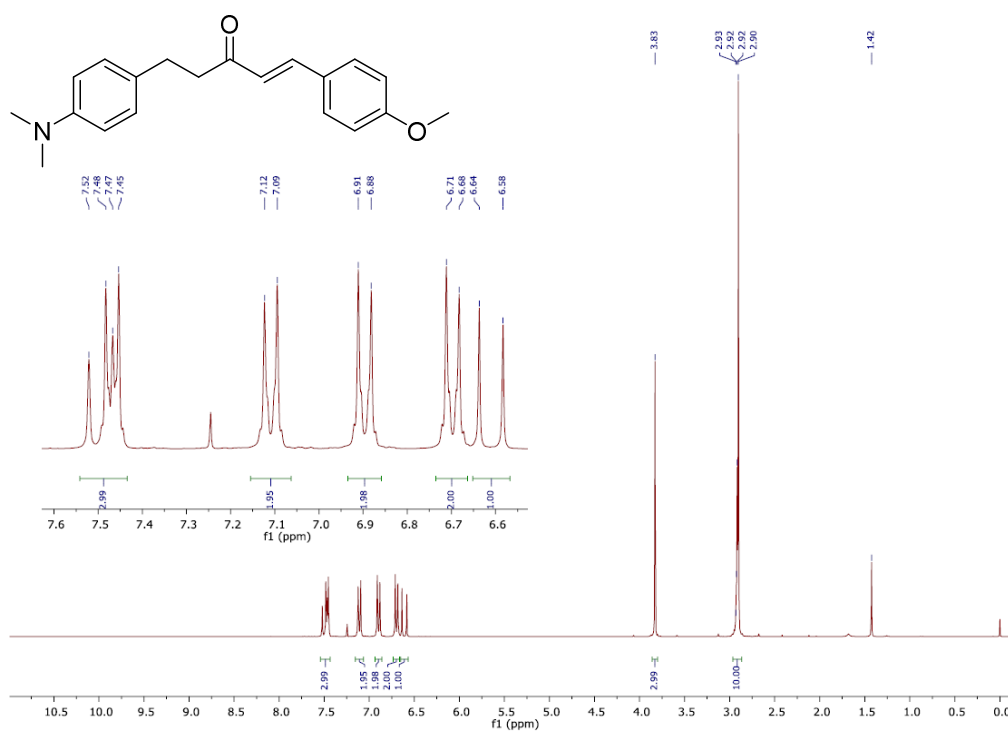

Figure 107
¹³C-NMR spectrum (75 MHz) of (*E*)-3-(4-(dimethylamino)phenyl)acrylaldehyde **41** in CDCl₃.
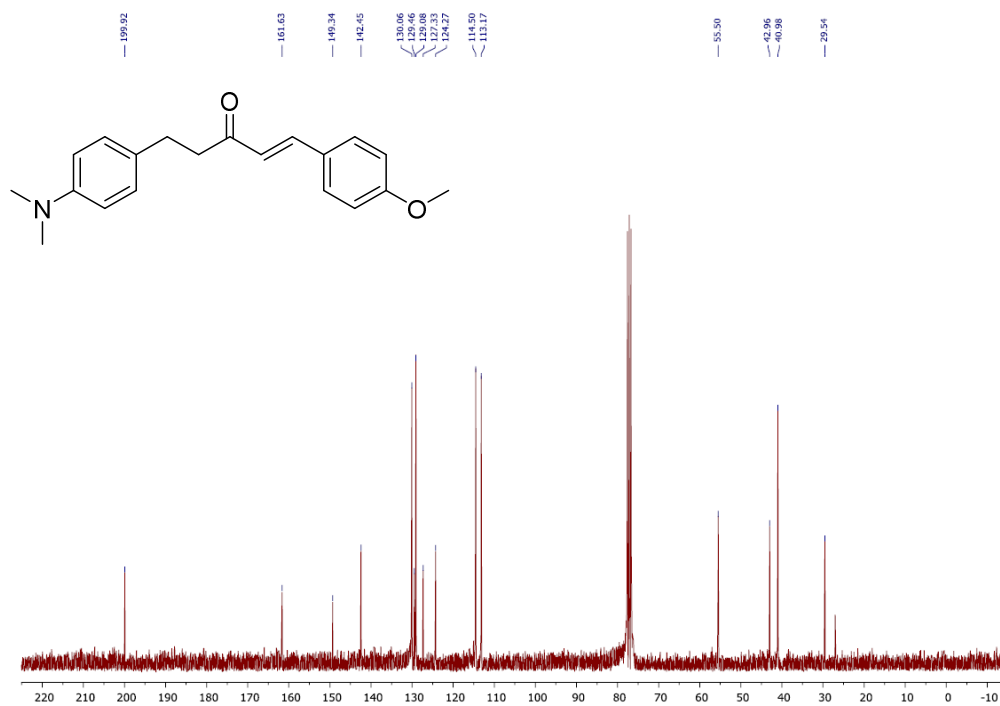
Figure 108
^{1}H-NMR spectrum (300 MHz) of 3-(4-*N*,*N*-dimethylaminophenyl)-1-propanol **15** in CDCl₃.

Figure 109
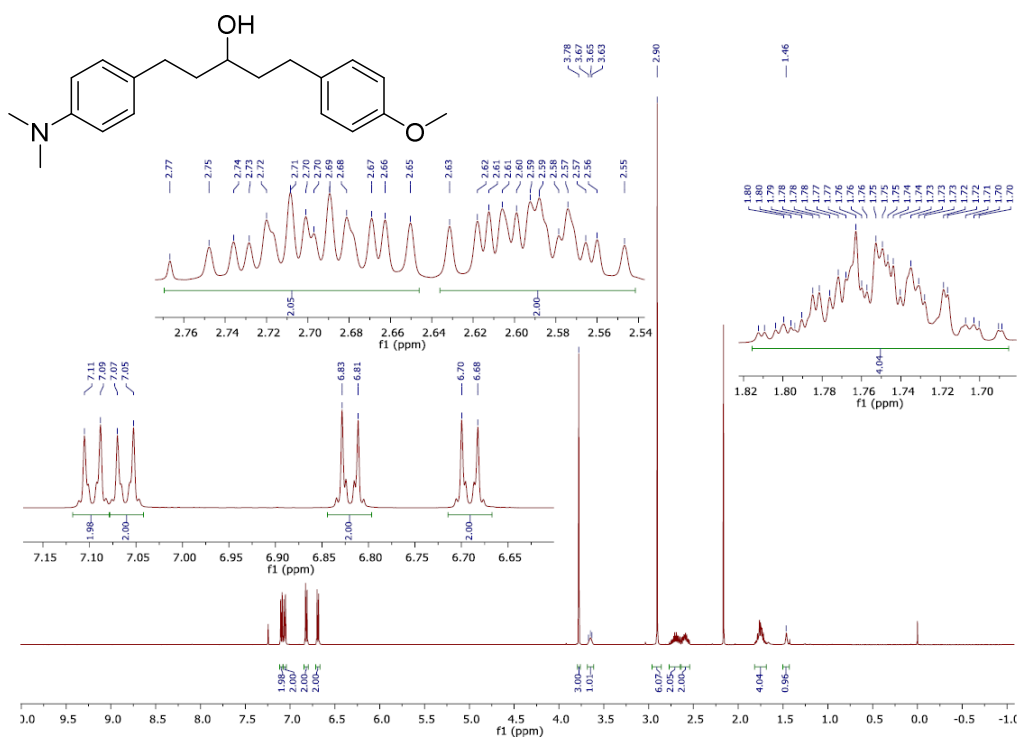^{13}C-NMR spectrum (75 MHz) of 3-(4-*N*,*N*-dimethylaminophenyl)-1-propanol **15** in CDCl₃.

Figure 110

^{1}H-NMR spectrum (300 MHz) of (*E*)-1-(4-methoxyphenyl)-5-(4-(dimethylamino)phenyl)-pent-1-en-3-one **43** in CDCl₃.

Figure 111

^{13}C-NMR spectrum (75 MHz) of (*E*)-1-(4-methoxyphenyl)-5-(4-(dimethylamino)phenyl)-pent-1-en-3-one **43** in CDCl₃.

Figure 112
^{1}H-NMR spectrum (300 MHz) of 1-(4-*N*,*N*-dimethylaminophenyl)-5-(4-methoxyphenyl)-3-pentanol **16** in CDCl[3].

Figure 113
^{13}C-NMR spectrum (75 MHz) of 1-(4-*N*,*N*-dimethylaminophenyl)-5-(4-methoxyphenyl)-3-pentanol **16** in CDCl[3].
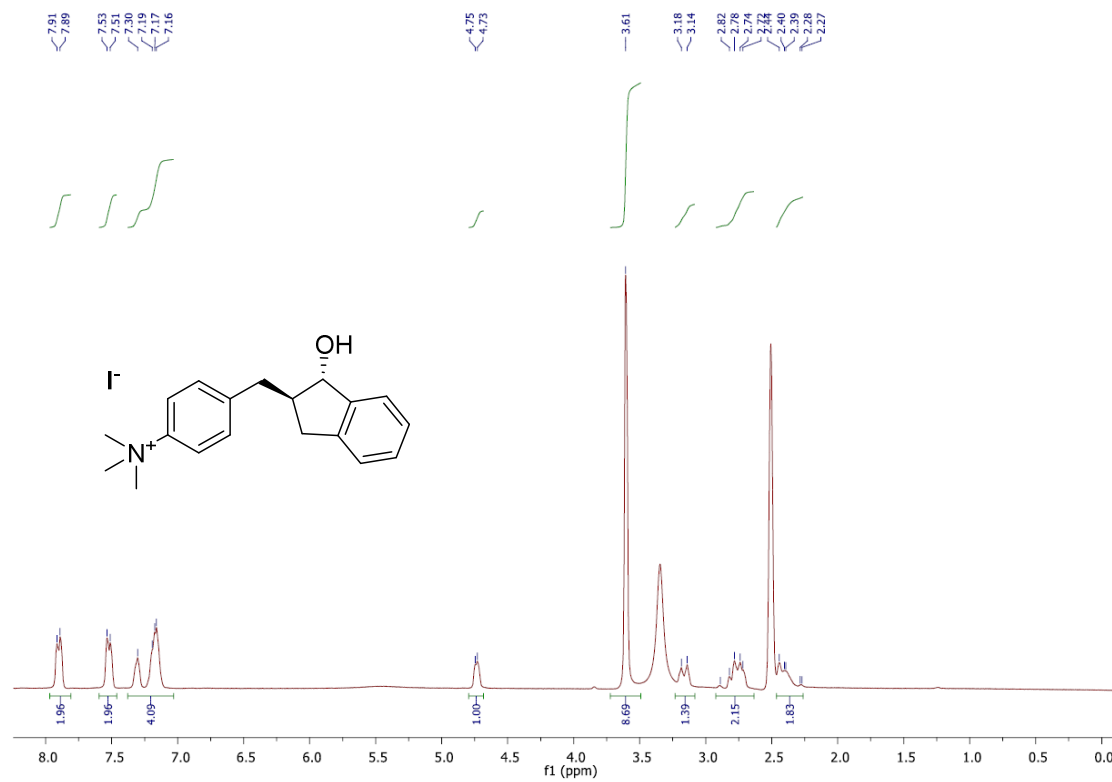
^{1}H-NMR spectrum (300 MHz) of *N*-(4-(((*trans*-1-hydroxyindan-2-yl)methyl)phenyl)-*N*,*N*,*N*-trimethylammonium iodide **12a** in DMSO-d$_6$.
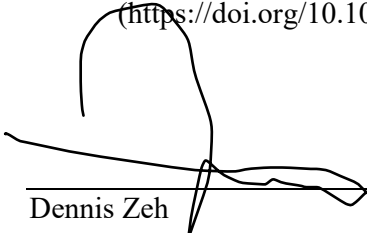
8.4 Eidesstattliche Erklärung

Hiermit versichere ich an Eides statt, dass ich die vorliegende Dissertation selbstständig und ohne die Benutzung anderer als der angegebenen Hilfsmittel und Literatur angefertigt habe. Alle Stellen, die wörtlich oder sinngemäß aus veröffentlichten und nicht veröffentlichten Werken dem Wortlaut oder dem Sinn nach entnommen wurden, sind als solche kenntlich gemacht. Ich versichere an Eides statt, dass diese Dissertation noch keiner anderen Fakultät oder Universität zur Prüfung vorgelegen hat; dass sie - abgesehen von unten angegebenen Teilpublikationen und eingebundenen Artikeln und Manuskripten - noch nicht veröffentlicht worden ist sowie, dass ich eine Veröffentlichung der Dissertation vor Abschluss der Promotion nicht ohne Genehmigung des Promotionsausschusses vornehmen werde. Die Bestimmungen dieser Ordnung sind mir bekannt. Darüber hinaus erkläre ich hiermit, dass ich die Ordnung zur Sicherung guter wissenschaftlicher Praxis und zum Umgang mit wissenschaftlichem Fehlverhalten der Universität zu Köln gelesen und sie bei der Durchführung der Dissertation zugrundeliegenden Arbeiten und der schriftlich verfassten Dissertation beachtet habe und verpflichte mich hiermit, die dort genannten Vorgaben bei allen wissenschaftlichen Tätigkeiten zu beachten und umzusetzen. Ich versichere, dass die eingereichte elektronische Fassung der eingereichten Druckfassung vollständig entspricht.

Teilpublikationen:

Zeh, D.; Bast, M.; *et al*., "Unidirectional Double and Triple Hydrogen Rearrangement Reactions Probed by Infrared Ion Spectroscopy", *Journal of the American Society for Mass Spectrometry*, **2022**. (https://doi.org/10.1021/jasms.2c00039)

Zeh, D.; Bast, M.; *et al*., "Cryogenic Messenger-IR Ion Spectroscopy Study of Phenol & Aniline Molecular Ions and of the common Fragment Ion $[C_5H_6]^{\bullet+}$ formed by EI-MS", *Journal of Molecular Spectroscopy*, **2021**, 378, 111453. (https://doi.org/10.1016/j.jms.2021.111453)

Dennis Zeh

Köln, September 2022

8.5 Curriculum Vitae Dennis Zeh

Date of birth: 21.10.1984	Address:
Place of birth: Herrenberg (Germany)	Weißenburgstr. 13
Phone: +49 172 7055587	50670 Köln
E-Mail: zeh.dennis@web.de	Germany

Education:

02/2019 – today	Enrolled and Employed (WHK) at the University of Cologne as PhD Candidate (Germany) Working on PhD thesis: ion/molecule reactions and infrared ion spectroscopy in the gas phase in a mass spectrometer
10/2018 – 12/2018	Working in the Ziegler Research Group at the Eberhard-Karls University Tübingen (Germany) Synthesis chemistry of carbohydrates and amino acids
08/31/2018	Awarded Master of Science Degree in Chemistry
01/2016 – 08/2018	Enrolled at the University of Massachusetts Boston (USA) Chemistry M.Sc. Program: development of a proteomic LC-MS platform and research on toxin induced differential protein expression in HeLa cells.
02/02/2015	Awarded Bachelor of Science Degree in Chemistry
10/2014 – 02/2015	Enrolled at the Eberhard-Karls University Tübingen (Germany) Chemistry B.Sc. Program (switched from the Diploma Program); researching and writing Bachelor Thesis.
10/2009 – 09/2014	Enrolled at the Eberhard-Karls University Tübingen (Germany) Chemistry Diploma Program (M.Sc. degree equivalent Program).
10/2007 – 09/2009	Enrolled at the Eberhard-Karls University Tübingen (Germany) Chemistry Pre-diploma Program (intermediate examination degree, 4 semesters); degree awarded on 23rd September 2009.
09/1995 – 07/2005	Attended Kepler Gymnasium Tübingen (Germany) Abitur (General Higher Education, degree to attend College or University); awarded on 21st June 2005.
09/1991 – 08/1995	Attended Elementary School Ammerbuch (Germany)

Professional Experience and Internships:

06/2016 – 08/2018	Working as Research Assistant in the Mass Spectrometry Proteomics Centre for the Centre for Personalized Cancer Therapy (CPCT), University of Massachusetts Boston (USA) Proteomics-based sample measurements on an Orbitrap Fusion Lumos mass spectrometer (Thermo Fisher Scientific), data processing and evaluation.
01/2016 – 05/2016 & 09/2017 – 12/2017	Working as Teaching Assistant for the Chemistry Department at the University of Massachusetts Boston (USA) Practical courses in general chemistry for Bachelor students; supervision, tutoring, and examination.
04/2008 – 01/2016	Working as Teaching Assistant for the Prof. Dr. Hubert Kahlbacher Research Group at the Interfaculty Institute of Biochemistry, Eberhard Karls University Tübingen (Germany) Practical courses in chemistry/biochemistry for medical students (approx. 200 students per semester); course preparation, supervision, tutoring, and examination.
11/2006 – 05/2007	Internship at the Department of Molecular Pathology, University Medical Center Tübingen (Germany) Molecular biological laboratory work.
06/2006 – 08/2006	Working as Administration Employee at the Comprehensive Cancer Center, University Medical Center Tübingen (Germany) Organizational, administrative, and EDP-related tasks.
09/2005 – 05/2006	Alternative Service (Zivildienst) at the the Comprehensive Cancer Center, University Medical Center Tübingen (Germany) Organizational, administrative, and EDP-related tasks.
08/2004 – 09/2004	Working at the Multek Europe Company (Board Manufacturer), Böblingen (Germany) Section for Solder Resist Mask.
09/2003	Social Work Internship at the Luise-Wetzel-Stift (Retirement Home); Tübingen (Germany) Care and maintenance tasks.
04/2001 & 07/2001	Internship at the Bank Company Marcard, Stein & Co. Bankiers, Hamburg (Germany) Transaction, exchange, customer support, account opening, bank/tax law, and IT-related tasks.